University of Alberta

Physics of water flow and solute transport across a soil horizon interface

by

Miles Franklin Dyck ©

A thesis submitted to the Faculty of Graduate Studies and Research
in partial fulfillment of the requirements for the degree of

Doctor of Philosophy

in

Soil Science

Department of Renewable Resources

Edmonton, Alberta
Fall, 2008

Canada

Dedication

To my parents, Ben and Muriel Dyck for their unwavering support and encouragement.

Abstract

Understanding of water flow and solute transport processes in field soils remains limited. By definition, soils have at least two horizons joined by the horizon interface. Because soil horizons (e.g.,, A and B horizons) have different average hydraulic properties and their boundaries are visually distinct, it is often assumed that soil horizons are independent layers and that the interface between soil horizons has no influence on the hydraulic behavior of the entire soil profile. Specific questions about the influence of the soil horizon interface on water flow and solute transport in field soils include: 1) At what scales, if any, does the nature of a soil horizon interface influence water flow and transport processes, and can we measure these processes? 2) Does the variability in water flow and transport caused at the scale of influence of soil horizon interfaces manifest at larger scales? and 3) Can the scale of influence of soil horizon interfaces be measured or predicted from simple field observations of soil horizon interface dimensions?

Time domain reflectometry (TDR) methodologies were developed to measure the spatial patterns of transient and steady state, local soil water flux above and below an A/B horizon interface, and implemented in field water flow and transport experiments. Results indicate the soil horizon interface is hydrologically significant. Specifically, the hydrological influence of the horizon interface was: 1) different for transient infiltration versus steady state flow (under constant water application); 2) dependent on the average rate of soil water flow; 3) scale (spatial) dependent; and 4) influenced by a spatial covariance of the interface shape and soil hydraulic properties (as expressed by the steady state soil water content). The research presented in this thesis contributes significantly to

the understanding of the physics of water flow and solute transport across soil horizon

interfaces.

Acknowledgements

Table of Contents

List of Tables

List of Figures

List of Symbols and Abbreviations

AMT	Adaptive Multitaper
C^f	Solute Flux Concentration
$C_{XY}(f)$	Cospectrum of Series X and Y
C_w	Soil Water Resident Solute Concentration
$\overline{C}_w$	Average Soil Water Resident Solute Concentration
CD	Convective Dispersive
CDE	Convective, Dispersive Equation
CLT	Convective, Lognormal Transfer Function
CS	Convective Stochastic
D	Coefficient of Dispersion
DPSSs	Discrete Prolate Spheroidal Sequences
$E(\cdot)$	Expectation Operator
EC	Electrical Conductivity
f^f	Solute Flux Travel Time Probability Density Function
$\left|H_{XY}(f)\right|^2$	Transfer Function of Series X and Y
K_s	Saturated Hydraulic Conductivity
$K(\cdot)$	Hydraulic Conductivity Function
K	Geometric TDR Probe Parameter
M	Total Solute Mass
PDF	Probability Density Function
q_w	Soil Water Flux Density
q_s	Solute Mass Flux Density
$Q_{XY}(f)$	Quadrature Spectrum of Series X and Y
$q_{w|tr}$	Transient Local Soil Water Flux
$q_{w|ss}$	Steady State Local Soil Water Flux
$R_{XY}(f)$	Coherency Spectrum of Series X and Y
$R_{XY|Z}$	Partial Coherency Spectrum of Series X and Y, given Series, Z
R_{XY}	Multiple Coherency Spectrum of Series X, and multiple Series, **Y**
REV	Representative Elementary Volume
$S_{XX}(f)$	Power Spectrum of Series, X
$S_{XY}(f)$	Cross Spectrum of Series, X and Y
$S_{XX|Z}$	Partial Power Spectrum of Series X, given Series, Z
SC	Stochastic Continuum
SMT	Simple Multitaper
STMs	Stochastic Stream Tube Models
$\bar{t}$	Mean Solute Travel Time
TDR	Time Domain Reflectometry
v	Convective Solute Velocity
$Var(\cdot)$	Variance Operator

W	Soil Water Storage
$Z^*(t)$	Position of Solute Front as a Function of Time
α	Capillary Length Scale[†]
	TDR Probe Intercept Calibration Parameter[‡]
β	TDR Probe Slope Calibration Parameter
$\delta(\cdot)$	Dirac Delta Function
ϕ	Soil Porosity
Φ	Hydraulic Potential
λ_i	Correlation Length Scale in the ith Direction[†]
	i^{th} Eigen Value[§]
$\mu.$	Lognormal Probability Density Function Mean Parameter
$\sigma.$	Lognormal Probability Density Function Variance Parameter[†]
	Electrical Conductivity[‡]
θ	Volumetric Water Content
$\bar{\theta}$	Average Soil Volumetric Water Content
ψ	Soil Water Potential

[†]Specific to Section 1.
[‡]Specific to Section 3.
[§]Specific to Section 4.

1. General Introduction

1.1. Background

Water and solute transport processes in soils are relevant to ecosystem functions and environmental integrity. From an environmental perspective, understanding water flow and solute transport is crucial to quantifying and mitigating the environmental risks associated with contaminants inadvertently introduced into soils (e.g., Pruess et al., 2002). The mineral matrix of soil (i.e., the parent material) is complex with particle/pore sizes spanning more than 3 orders of magnitude (10^{-6} to 10^{-3} m). Pedogenic processes acting over long periods of time have added to the original complexity and spatial variability of the parent material mostly through the formation of soil horizons.

Modeling of water flow and solute transport has focused on quantifying state transport properties (e.g., hydraulic conductivity, dispersivity) of soil. Because soil horizons (e.g., A, B and C horizons) have different average hydraulic properties and their boundaries are visually distinct, soils are sampled and parameterized by individual horizons. The implicit assumption in most models is that soil horizons are independent layers and the nature of the horizon interfaces has no influence on the bulk transport properties of the soil profile/pedon. Field solute transport experiments, however, have shown that soil horizons are likely not independent, and interfaces can have significant influence on transport through the entire pedon (Hamlen and Kachanoski, 1992; van Wesenbeeck and Kachanoski, 1994; Ellsworth and Jury, 1991).

To date, a variety of conceptual and mathematical models have been developed to incorporate, in a physically meaningful way, the observed statistical horizontal and vertical spatial variability of transport parameters into water and solute transport process

1

models. In general, model development of flow and transport in layered soils has outpaced fundamental understanding and measurements of processes occurring at soil horizon interfaces. In this chapter, a brief review of literature relevant to the physics of transport at soil layer interfaces is given, followed by a statement of the focus and objectives of this thesis. The relevant literature has been grouped into the following categories: 1) stochastic stream tube and continuum modeling; 2) scaling theory investigations and modeling; and 3) experimental observations of water and solute transport in field soils.

1.2. Stochastic stream tube and continuum modeling

Jury and Roth (1990) and Vereecken et al. (2007) define and distinguish stochastic stream tube models and stochastic continuum models. Stochastic stream tube models (STMs) conceptualize the soil as a series of vertical, parallel stream tubes. Water and solute transport parameters within each stream tube are usually constant and independent of all other parallel tubes. Transport within each stream tube (i.e., local scale transport) is described by process models such as Green and Ampt infiltration, piston flow, or convection/dispersion. Transport at larger scales (e.g., field scale) is described by the ensemble average transport within all stream tubes. Stochastic continuum models, on the other hand, incorporate observed horizontal and vertical variances and scale dependent interactions (e.g., autocorrelation) within and between transport parameters.

1.2.1. Stochastic stream tube models in vertically homogeneous soils

A useful and common practice to understand the physics of water flow and solute transport, and obtain transport parameters of interest, is to apply a conservative tracer to

the soil surface and track its movement through the soil under controlled boundary conditions. Controlled boundary conditions, such as quasi-steady state water application (surface flux), and quasi-steady state flow (zero matric potential gradients), simplify the physics of the system and help to ensure that experimental measurements are a result of the process of interest and not confounded by other processes (i.e., transient water flow). Under these assumptions, stochastic STMs provide a physical theoretical basis to describe observations that solute dispersion increases with mean transport depth. Examples of stochastic stream tube models are given by Dagan and Bresler (1979), Bresler and Dagan (1979), Jury et al. (1986), and Toride and Leij (1996a,b). The convective, lognormal transport (CLT) model of Jury et al (1986) is perhaps the most widely implemented stream tube model for describing field scale transport. The discussion presented here will focus on describing solute transport under a probabilistic framework. Under this framework, the CLT model developed by Jury et al. (1982) and the classical convective dispersive equation will be discussed because they represent important physical bounds for transport phenomena and were both further adapted to describe flow in layered soils (Jury and Roth, 1990; Jury and Utterman, 1992).

Stream tube models treat solute transport travel time (i.e., inverse net solute transport velocity) as a random variable. The connection between the physics of solute transport to probability theory will be presented here. Let q_w be defined as the quasi-steady soil water flux density (m^3 m^{-2} s^{-1}). The solute mass flux density (q_s, kg m^{-2} s^{-1}) is equal to the water flux density multiplied by the flux concentration (i.e., solute concentration of the flowing water, C^f, kg m^{-3}):

$$q_s(z,t) = q_w \cdot C^f(z,t)$$
[1-1].

Due to transport processes, C^f, and therefore q_s, are functions of depth (z; m) and time (t; s). Quasi-steady water flow is assumed, so q_w is constant. For a delta function (spike) input of solute at t = 0 the law of large numbers implies that the number or mass of ions passing a given depth at a given time, $q_s(t)$, relative to the total number or mass of ions applied, is equal to the travel time probability density function (i.e., the probability that a single ion/molecule applied at the surface would pass depth L after travel time t; Jury et al., 1986):

$$f^f(L,t) = \frac{q_s(L,t)}{M} \qquad [1\text{-}2]$$

where M is the total mass of solute ions applied per unit area (kg m^{-2}) at t = 0, and $f^f(L,t)$ has units of inverse time (s^{-1}).

The physical processes and soil properties affecting the spatial and temporal distribution of applied solute under quasi-steady water flux are reflected in the shape of the solute travel time probability density function (pdf) which is also called a solute breakthrough curve. The field average solute breakthrough curve at some depth z = L is then expressed as the convolution with time of the solute input at the soil surface $[C^f(0,t)]$ with the probability density function [pdf, $f^f(L,t)$] of stream tube travel times/velocites (Jury and Roth, 1990):

$$C^f(L,t) = \int_0^t C^f(0,t') \cdot f^f(L,t-t')dt' \qquad [1\text{-}3]$$

where the superscript, f, is associated either with flux concentrations, C^f (kg m^{-3}), or the flux travel time pdf, $f^f(z,t)$ (s^{-1}). According to Eq. [1-3], if the solute is introduced as an instantaneous spike (Dirac delta function) at the soil surface, then:

$$C^f(0,t) = \frac{M}{q_w} \delta(t), \qquad \text{and}$$

$$C^f(L,t) = \int_0^t \frac{M}{q_w} \cdot \delta(t') \cdot f^f(L,t-t')dt' = \frac{M}{q_w} \cdot f^f(L,t) \qquad [1\text{-}4]$$

where δ(t) is the Dirac delta function (unitless). Rearranging Eq. [1-4] to solve for

$f^f(L,t)$ and invoking conservation of mass yields:

$$f^f(L,t) = \frac{q_w C^f(L,t)}{M} = \frac{q_w C^f(L,t)}{\int_0^\infty C^f(L,t')q_w dt'} \qquad [1\text{-}5].$$

Under steady water flux (q_w), Eq. [1-5] simplifies to:

$$f^f(L,t) = \frac{C^f(L,t)}{\int_0^\infty C^f(L,t')dt'} = \frac{C^f(L,t)}{M} \qquad [1\text{-}6].$$

Thus, measurement of the solute breakthrough curve at some depth L, after a spike input

of solute at the surface, is essentially equivalent to measuring the solute travel time pdf

without having to assume a process model.

While not a STM as such, solutions to the CDE under similar boundary conditions

yield the solute travel time pdf for a convective dispersive process. The CDE for a

conservative solute under quasi-steady water flux is:

$$\frac{\partial C^f}{\partial t} = D\frac{\partial^2 C^f}{\partial z^2} - v\frac{\partial C^f}{\partial z} \qquad [1\text{-}7]$$

where v is the pore water velocity (m s^{-1}), and D is the coefficient of dispersion (m^2 s^{-1}).

The solution of Eq. [1-7] for a Dirac delta application of solute at the soil surface yields

the solute travel time pdf for a convective dispersive process (Jury and Roth, 1990):

5

$$C^f(z,t) = M \cdot f^f(z,t) = \frac{Mz}{2\sqrt{\pi Dt}} \exp\left[\frac{-(z-vt)^2}{4Dt}\right] \qquad [1\text{-}8]$$

Substitution of Eq. [1-8] into Eq. [1-3], therefore, describes the expected solute breakthrough curve for any arbitrary surface application of solute.

The CLT model of Jury et al. (1986) assumes a lognormal travel time pdf:

$$f^f(t) = \frac{1}{\sqrt{2\pi}\sigma t} \exp\left[\frac{-(\ln(t)-\mu)^2}{2\sigma^2}\right] \qquad [1\text{-}9]$$

where μ and σ^2 are the parameters used to calculated the mean (s) and variance (s^2) of the travel time pdf. Unlike the travel time pdf of the CDE (Eq. [1-8]), the lognormal pdf at a single depth does not provide any predictions of the solute breakthrough curves at unobserved depths. For prediction at other depths/times a model of transport must be assumed. For example, Jury and Roth (1990) modified the lognormal travel time pdf to include depth, using the following transformation:

$$f^f(z,t) = \frac{L}{z} f^f\left(L, t\frac{L}{z}\right) \qquad [1\text{-}10]$$

Equation [1-10] is a model of a solute transport process where the probability that a solute particle entering the soil surface will arrive at depth z at time t is the same as the probability that it will arrive at depth L at time $t\,L/z$; that is, a particle is assumed to have the same effective velocity at all depths. This was called a convective stochastic (CS) process, but is equivalent to a streamtube model. Substitution of Eq. [1-9] into Eq. [1-10] yields the solute travel time pdf for the convective stochastic CLT model (Jury and Roth, 1990):

$$f^f(z,t) = \frac{1}{\sqrt{2\pi}\sigma_L t} \exp\left[\frac{-\left(\ln\left(t\frac{L}{z}\right) - \mu_L\right)^2}{2\sigma_L^2}\right]$$ [1-11]

where μ_L and σ_L^2 are lognormal pdf parameters derived from a breakthrough curve

measured at a reference depth, L; that is, solute transport at any depth z is predicted using

the travel time pdf measured at depth L.

An important prediction of the CLT model is that the variance about the mean

travel time, $\text{Var}_z(t)$ (s^2), increases with the square of travel depth (Jury and Roth, 1990):

$$\text{Var}_z(t) = \left(\frac{z}{L}\right)^2 \text{Var}_L(t)$$ [1-12]

where $\text{Var}(\cdot)$ is the variance operator. The relationship between travel time variance and

depth in Eq. [1-12] is a result of the independent stream tube assumption, represented by

the probability relationship of Eq. [1-10]. Once a solute particle enters a stream tube at

the soil surface, it will remain in that stream tube (i.e., no mixing between stream tubes).

Field scale dispersion is a result of spatial variations in convective velocity only. In this

context, it is important to note that the convective dispersive equation represents a stream

tube model with convective transport within stream tubes, but perfect lateral mixing

between stream tubes. The perfect mixing results in all particles having the same average

velocity. Under these assumptions, the travel time variance of convective dispersive

(CD) breakthrough curves increases linearly with depth, z (Jury and Roth, 1990):

$$\text{Var}_z(t) = \frac{2Dz}{v^3}$$ [1-13].

In other words, for the CDE model, all of the particles are assumed to be traveling at the

same convective velocity. For any given depth increment, some particles travel slower or

faster than the average convective velocity because of dispersion processes. However, for any other depth interval, there is an equal probability for a given particle to be travelling faster or slower.

A number of mixed models have been developed. For example Toride and Leij (1996a,b) developed a CDE-based stochastic stream tube model where transport within each stream tube was described by the CDE and maintained independence between stream tubes (i.e., different average velocities between streamtubes, but no lateral mixing between stream tubes). For this situation, they showed that the travel time variance of the field scale BTC was proportional to both the first and second powers of depth.

1.2.2. Stochastic stream tube models for vertically heterogeneous soils

The discussion in section 1.2.1 summarized stream tube models where stream tubes are vertically homogeneous. Field soils have at least two pedogenic horizons in addition to any textural discontinuities resulting from depositional processes. Jury and Roth (1990) and Jury and Utterman (1992) derived stream tube models where stream tubes span two or more soil layers or horizons. The assumptions for these models are that the transport properties within each layer of each stream tube are vertically homogeneous and that there is an abrupt change in transport parameters at the interface between the two layers. Instead of one solute travel time pdf, each layer has a solute travel time pdf associated with it. Consider the simple case of a soil with two horizons. The depth of the bottom of the upper horizon is expressed as $z = L_1$ and the depth of the bottom of the lower horizon is expressed as $z = L_1 + L_2$. The solute travel time pdf to any depth $z > L_1$ is equal to (Jury and Utterman, 1992):

$$f^f(z,t) = \int_0^\infty \int_0^\infty \delta(t - t_1 - t_2) \cdot f_{12}^f(t_1, t_2) dt_1 dt_2 = \int_0^\infty f_{12}^f(t_1, t - t_1) dt_1 \qquad [1\text{-}14]$$

8

where $f_{12}^f(t_1, t_2)$ is the joint travel time pdf of layers 1 and 2. The joint travel time pdf of

a layered system like this one is a function of the travel time pdfs of the individual layers.

If the travel time pdfs of horizon 1 [$f_1^f(L_1, t_1)$] and horizon 2 [$f_2^f(L_2, t_2)$] are statistically

independent, then the joint pdf [$f_{12}^f(t_1, t_2)$] is:

$$f_{12}^f(t_1, t_2) = f_1^f(L_1, t_1) f_2^f(L_2, t_2) \qquad [1\text{-}15]$$

Substitution of Eq. [1-15] into Eq. [1-14] yields:

$$f^f(z, t) = \int_0^\infty f_1^f(L_1, t_1) f_2^f(z - L_1, t - t_1) dt_1 \qquad z > L_1 \qquad [1\text{-}16]$$

If the travel time pdfs of the 2 horizons are perfectly correlated (not statistically

independent) then the joint pdf is:

$$f_{12}^f(z, t_1, t_2) = f_1^f(L_1, t_1) \delta(t_2 - g(t_1)) \qquad [1\text{-}17]$$

where $g(t_1)$ is a functional dependence between the random variables t_1 and t_2. The

nature of the function $g(t_1)$ depends on the nature of the travel time pdfs of the individual

layers. If the travel time pdfs of the layers are lognormal, then t_2 and t_1 have a nonlinear

functional relationship:

$$t_2 = \exp\left[\mu_2 - \mu_1\left(\frac{\sigma_2}{\sigma_1}\right)\right] t_1^{(\sigma_2/\sigma_1)} = \alpha t_1^\beta \qquad [1\text{-}18]$$

where μ_1, σ_1, and μ_2, σ_2 are the parameters of the travel time pdfs for layers 1 and 2

respectively, $\alpha = \exp[\mu_2 - \mu_2(\sigma_2 / \sigma_1)]$, and $\beta = (\sigma_2 / \sigma_1)$. Substitution of Eqs [1-17] and

[1-18] into Eq. [1-14] yields:

$$f^f(z, t) = \int_0^\infty \delta(t - t_1 - \alpha t_1^\beta) f_1^f(L_1, t_1) dt_1 \qquad z > L_1 \qquad [1\text{-}19]$$

9

Statistical concepts of independence and correlation in the context of solute transport have specific physical interpretations; specifically, they define boundary conditions at soil layer interfaces. In Eq. [1-16], solute leaving layer 1 acts as a time distributed solute source entering layer 2. For the constraint of statistical independence to hold (Eq. [1-15]), the time distributed solute source is convoluted over all possible stream tubes in layer 2. In other words, a solute particle leaving layer 1 in a fast flowing stream tube will not necessarily enter into a fast stream tube in layer 2; that is, it has an equal probability of entering a slow, fast or medium flowing stream tube in layer 2. Physically, this implies perfect horizontal mixing between stream tubes or that the layer interface interrupts stream tube or pore space (but not solute flux) continuity. Put another way, if a solute particle has a travel time of t_1 through layer 1, and a travel time of t_2 through layer 2, the total travel time through layers 1 and 2 is $t_1 + t_2$, where there is no statistical relationship between t_1 and t_2. The layered CDE model of solute transport is representative of process model with independent travel time pdfs (Jury and Uttermann, 1992; Section 1.2.1).

In Eq. [1-19], solute leaving layer 1 again acts as a time distributed solute source entering layer 2. Now, however, the solute travel time pdf of layer 2 is a well defined function of the solute travel time pdf of layer 1 due to the statistical constraint of perfect correlation (Eqs. [1-17] and [1-18]). In other words, a solute particle leaving layer 1 in a fast stream tube, will enter a fast flowing stream tube in layer 2, or a solute particle leaving layer 1 in a slow flowing stream tube, will enter a slow flowing stream tube in layer 2 (assuming perfect positive correlation). Physically, this implies perfect isolation of stream tubes or that the layer interface does not interrupt stream tube or pore space (or

solute flux) continuity. Thus, if a solute particle has a travel time of t_1 through layer 1, its travel time through layer 2 is a function of (i.e., correlated to) t_1 (i.e., Eq. [1-18]). The layered CLT model of solute transport is representative of a process model with perfectly correlated travel time pdfs (Jury and Utterman, 1992; Section 1.2.1). Jury and Roth (1990) and Jury and Utterman (1992) go on to show that the travel time variance-depth relations shown in Eqs [1-12] and [1-13] are representative of perfect correlation between individual layer travel time pdfs (CS) and independent individual layer travel time pdfs (CD), respectively. Homogeneous soils could be conceptualized as being composed of many infinitesimally small layers. The CD model (e.g., CDE) is then conceptualized as representing solute transport in a soil where all infinitesimal layers are independent, and the CS model (e.g., CLT) is conceptualized as representing solute transport in a soil where all infinitesimal layers are perfectly correlated.

In summary, the CS, CLT model and the CD, CDE model represent two physical bounds of solute transport: perfectly isolated stream tubes and perfectly mixed stream tubes. Quasi-steady state solute transport, as it occurs in the field, falls somewhere between these two bounds. For example, at the field scale (tens or hundreds of meters), complete lateral mixing across all scales as in a CD process is unlikely. A more likely, and physically realistic, scenario is lateral mixing at some smaller, local scale (i.e., Pedon scale). Processes of this nature have been observed by van Wesenbeeck and Kachanoski (1994). These authors developed expressions showing that the large scale (field scale) travel time variance is the sum of the average local scale (stream tube) travel time variance and the variance(horizontal) of the local scale mean travel time between stream tubes (van Wesenbeeck and Kachanoski, 1991):

$$Var_{z,field}(t) = E[Var_{z,local}(t)] + Var[E_{z,local}(t)]$$ [1-20].

where E[·] is the expectation operator.

1.2.3. Stochastic continuum models

Discussion in section 1.2.1 and 1.2.2, while focusing on solute transport, indicates significant impact of the magnitude and variability of local soil water flux on solute transport. Indeed water flow and solute transport are coupled processes. Stochastic STMs assume constant water flux within stream tubes or at least within the individual layers of each stream tube, but do not specifically consider the impact of the variability of soil hydraulic properties such as K_s (saturated hydraulic conductivity), $K(\psi)$ (hydraulic conductivity as a function of soil water potential) and $\theta(\psi)$ (soil water content as a function of soil water potential) on field scale solute transport. The travel time pdfs of individual layers within stream tubes are correlated in the layered CLT model, but this does not imply any spatial cross correlation structure between layer water and solute transport properties in the geostatistical sense. Stochastic continuum (SC) models solve the appropriate governing partial differential equation for water or solute transport analytically or numerically within a stochastic framework. Numerous examples are present in the literature, including, but not limited to, Yeh et al. (1985a,b,c), Yeh (1989), Mantoglou (1992), Polmann et al. (1991), Mantoglour and Gelhar (1987a,b,c), and Green and Freyberg (1995) for unsaturated water flow, and Russo (1993), Russo (1995), and Dagan (1984) for solute transport.

In the SC approach, point estimates of transport parameters of the porous medium are isotropic. Anisotropy is introduced into the porous medium through directional dependent correlation length scales. For example, in a typical soil profile, horizons are

12

observed (at least visually) to be more horizontally continuous than vertically. It is therefore likely that the horizontal correlation length scale of transport parameters for the soil profile is greater than the vertical correlation length scale. As a result, the spatial structure of transport parameters for soil profiles with distinct horizons or layers is usually assumed to be well simulated by statistically anisotropic porous media. Like stochastic stream tube models, the goal of stochastic continuum models is to understand and describe the field scale behavior of water flow and solute transport given the observed statistical structure of transport parameters. In the context of flow and transport in layered soils, stochastic continuum models yield expressions for field scale, effective transport parameters. Overall, stochastic continuum simulations have contributed significantly to theoretical development of water and solute transport in vertically heterogeneous (layered) soils.

Stochastic continuum approaches applied to the Richards equation by Yeh et al. (1985a,b,c) and Polmann et al. (1991) have provided theoretical evidence for observed state dependent anisotropy in the unsaturated hydraulic conductivity tensor (e.g., McCord and Stephens, 1987; Stephens and Heerman, 1988; McCord et al., 1991a,b; Zhang et al., 2003; Raats et al., 2004). The Richards equation is the governing partial differential equation describing macroscopic, laminar water flow in porous media:

$$\frac{\partial}{\partial x_i}\left(K(\psi,x_i)\frac{\partial \Phi}{\partial x_i}\right) = \frac{\partial \theta}{\partial t} \qquad\qquad i = 1,2,3 \qquad\qquad [1\text{-}21]$$

where is the $K(\psi,x_i)$ is the soil hydraulic conductivity (m s^{-1}) as a function of soil water potential, Φ in the x_i direction ($\Phi = -x_1 - \psi$, where x_1 is the vertical direction, m), and θ is the volumetric water content (m^3 m^{-3}). The hydraulic conductivity function has been

modeled by many non-linear functions. A common and useful model was given by Gardner (1958):

$$K(\psi, x_i) = K_s(x_i)\exp(-\alpha(x_i)\psi) \qquad [1\text{-}22]$$

where $K_s(x_i)$ is the saturated hydraulic conductivity in the x_i direction, and α is a fitting parameter representing the decrease in the natural logarithm of hydraulic conductivity as a function of matric pressure head, ψ. Using the functional form of Eq. [1-22] for $K(\psi)$ in Eq. [1-21], allows the Richards equation to be linearized for a number of boundary conditions. Perturbation theory applied to Eqs. [1-21] and [1-22] transforms the Richards equation into a stochastic partial differential equation such that the statistical properties (mean, variance, and correlation length scale) of the hydraulic properties influence the solution (i.e., upscaling the Richards Equation). Solutions to the stochastic Richards equation are in the form of a mean and variance (i.e., the ensemble average soil water potential plus its variance) and are a function of the statistical properties of the hydraulic properties, and the imposed boundary conditions.

Within the stochastic continuum framework, effective hydraulic conductivity of the entire flow domain is the ratio of the ensemble average soil water flux, Q, and the ensemble average hydraulic gradient, J:

$$\hat{K}_{i,eff} = \frac{Q_i}{J_i} \qquad [1\text{-}23]$$

where, i, represents the direction of the coordinate vector. The terms in Eq. [1-23] are all interdependent, making calculation of effective hydraulic conductivity an iterative procedure (Vereecken et al., 2007). The work of Yeh et al. (1985b), for example,

provided some insight into saturation-dependent anisotropy in the hydraulic conductivity

tensor:

$$\frac{\hat{K}_{22}}{\hat{K}_{11}} = \exp\left[\frac{\sigma_f^2 + \sigma_a^2 H^2}{1 + \lambda_1 L_1 A}\right]$$
[1-24]

where $\hat{K}_{22}$ and $\hat{K}_{11}$ are the effective large-scale hydraulic conductivities in the directions

of the principle components of the unsaturated hydraulic conductivity tensor (in the case

of a layered soil, horizontal and vertical directions, respectively), σ_f^2 is the variance of

the log of the saturated hydraulic conductivity, σ_a^2 is the variance of Gardner's alpha, λ_1

is the correlation length in the vertical direction, L_1 is a spatial head gradient parameter,

A is the mean of Gardner's alpha and H is the mean soil water potential. The expression

in Eq. [1-24] is for the case where K_s and α are not correlated; expressions were also

derived for perfectly correlated K_s and alpha and include a covariance term within the

exponential. Equation [1-24] predicts that as the soil becomes more unsaturated, the

anisotropy ratio increases. Furthermore, the anisotropy ratio increases as the variance in

hydraulic properties increases. This suggests, that for a layered soil, the influence of the

layers on water flow (i.e., the macroscopic anisotropy ratio) should increase with

increasing differences in hydraulic properties between the layers and also increase as the

average soil water content decreases. Another property of these expressions is that they

are indirectly affected by hysteresis (Mantoglou and Gelhar, 1987a,b,c; Polmann et al.,

1991; Mantoglou, 1992). These authors noted that σ_f and σ_a are affected by the mean

change in matric potential with respect to time (dH/dt; i.e., whether the soil is wetting or

15

drying) through cross correlations between σ_f^2 and σ_H^2 and between σ_a^2 and σ_H^2 (Polmann et al., 1991).

The observed, theoretical anisotropy in the unsaturated hydraulic conductivity in the works above was attributed to the statistical anisotropy in the hydraulic properties of the porous medium. The imposed statistical anisotropy, when scaled up, resulted in unique, large-scale, hysteretic hydraulic conductivity-water potential relationships for the vertical and horizontal directions. Therefore, the ratio of the large scale vertical and horizontal hydraulic conductivities will be anisotropic, hysteretic and a function of water potential. The fact that hysteresis appeared at the large scale is surprising as it was not assumed at the local scale. The cause of hysteresis is often attributed to pore structure (i.e., "the ink bottle effect"). Mantoglou and Gelhar (1987c) provide a large scale analogue to "the ink bottle" effect that may occur in layered soils.

The influence of the spatial variability of soil hydraulic properties on solute transport has also been investigated through the development of stochastic continuum models for solute transport. In groundwater systems, the development of stochastic continuum models was motivated by field observations of increasing solute dispersion with increasing travel distance, and the sample size dependence of measured hydraulic conductivity (Dagan, 1984; Gelhar and Axness, 1983). Stochastic continuum solute transport investigations in unsaturated media were later carried out by Russo (1993), Russo (1995) and also Jury and Roth (1990; chapter 7). For groundwater systems, both Dagan (1984) and Gelhar and Axness (1983) found that the longitudinal macrodispersion coefficient (i.e., the scaled dispersion coefficient) increased with increasing travel time for mean travel distance less than or equal to the correlation length scales of the saturated

hydraulic conductivity field. The longitudinal macrodispersion coefficient

asymptotically reached a constant value for mean travel distances much greater than the

correlation length scale of the saturated hydraulic conductivity field. Jury and Roth

(1990) attributed the asymptotic behavior of the dispersion coeffient to increased mixing

across stream tubes with increasing travel time. In other words, solute transport

transitions from a CS to a CD process with increasing travel time.

In unsaturated systems, Russo (1993) predicted similar behavior of the

longitudinal macrodispersion coefficient. Russo (1995) investigated solute transport in

statistically anisotropic (i.e., layered) media. Not surprisingly, the results showed that the

asymptotic longitudinal macrodispersion coefficient was greatest when the orientation of

the principle axis of the porous media anisotropy tensor coincided with the orientation of

principle axis of the flux tensor, and decreased to a minimum when the principle axis of

the porous media and flow tensors were offset by 90 degrees.

1.3. Scaling theory investigations and modeling

The results from stochastic continuum simulations are valid only when the

simulated domain is an order of magnitude larger than the greatest correlation length

scale (Yeh et al., 1985a). Essentially, therefore, the stochastic continuum approaches are

up-scaling the appropriate governing transport equation. The governing equations were

developed at the representative elementary volume (REV) scale. As a result, the

simulated correlation length scales would be applied to REV scale estimates of the

appropriate transport parameters. Typical correlation length scales for transport and

hydraulic parameters are generally not readily available (e.g., Ward and Zhang, 2007),

making it difficult to determine exactly which scales the stochastic continuum results are

relevant for. If the REV scale is assumed to be well represented by a soil core with a diameter of 10 cm, for example, stochastic continuum simulations may be representative of scales of several meters (i.e., the pedon scale). As mentioned earlier, REVs in the stochastic continuum approach are assumed to be isotropic. Therefore, the stochastic continuum approach may not be applicable for soils which are anisotropic at the pore and REV scale (Ursino et al., 2000).

Ursino et al. (2000) used Miller-Miller scaling to investigate the effects of pore scale anisotropy on REV scale transport properties. Anisotropy at the microscopic or pore scale was simulated by one of following three models: (1) direction-dependent average number of pores; (2) direction-dependent pore size distribution; and (3) direction-dependent number of pores and pore size distribution. Each of these microscopic models had a microscopic anisotropy factor based on the ratios of Miller-similar characteristic lengths (Miller and Miller, 1956). The microscopic anisotropy factors for each model are: (1) the ratio of the direction-dependent characteristic length of particle sizes (i.e., oblate particles); (2) a tension-dependent microscopic anisotropy factor representative of direction depend pore size distributions; and (3) a combination of the first two factors. REV anisotropy ratios of the hydraulic conductivity as a function of saturation were derived from the microscopic anisotropy factors using Miller-Miller scaling (Miller and Miller, 1956). Statistically isotropic random fields of these REV anisotropy ratios were generated and applied to elements of a numerical model with domains dimensions of 5 by 6.25 m to simulate water flow via the Richards equation and solute transport with a particle tracking method. Results from the particle tracking simulations were used to map particle trajectories.

Results of the simulations by Ursino et al. (2000) corroborated the following earlier results by Roth (1995) and Roth and Hammel (1996): 1) the simulations produced a complex network of flow channels; 2) the structure of the flow network is a function of the degree of water saturation; 3) asymptotic dispersion is reached after an average travel depth that is 10 times the correlation length of the random field; and 4) the asymptotic longitudinal dispersivity is dependent on the magnitude of the water flux. A further observation was that the simulated pedon-scale porous medium constructed using pore-scale anisotropy behaved either as a series of columns if the direction of higher conductivity was parallel to the flow direction (vertical) or a series of layers otherwise. Furthermore, when the microscopic anisotropy factor was made to be saturation dependent (in the case of anisotropic pore size distributions) the simulated soil would behave either like a series of columns or like a series of layers depending on the magnitude of the steady state water flux (i.e., degree of saturation); that is, the direction of maximum hydraulic conductivity switches at a critical saturation. In contrast, the direction of maximum hydraulic conductivity in the simulations of Yeh et al. (1985c) and Mantaglou and Gelhar (1987) were always in the same direction as the maximum correlation length scale.

Another investigation of note is the work of Zhang et al. (2003). Miller-similar media, 1 m^3 in volume, were constructed by Zhang et al. (2003) by conditional simulation of Miller-Miller scaling factors for a statistically anisotropic correlation structure. Water transport was simulated in the Miller-similar media using the STOMP numerical model (White and Oostrom, 2004), and up-scaled hydraulic properties for the 1 m^3 media were estimated with inverse procedures. Like the results of Yeh et al. (1985c)

and Mantaglou and Gelhar (1987), the direction of maximum hydraulic conductivity always coincided with the direction of maximum correlation length scale.

1.4.   Experimental observations of water and solute transport in field soils

Significant experimental efforts to understand water and solute transport processes as they occur in field soils have been undertaken by Biggar and Nielsen (1976), Ward et al. (1995), van Wesenbeeck and Kachanoski (1994), Hamlen and Kachanoski (1992), Butters et al. (1989); Butters and Jury (1989), Ellsworth and Jury (1991), Roth et al. (1991), Hammel et al. (1999), Starr et al. (1986), Derby and Knighton (2001), Javaux and Vanclooster (2004a,b), Garrido et al. (2001), Coquet et al. (2005), Dyck et al. (2003), Dyck et al. (2005), Woods et al. (2006) and Ward and Zhang (2007). While each of the experiments were carried out under different conditions on different soils, common themes have emerged from the results.

The most common theme to arise from field transport experiments is that soil horizon/layer interfaces are focal points for local scale three-dimensional flow and redistribution of mass (van Wesenbeeck and Kachanoski, 1994; Hammel et al., 1999; Starr et al., 1986; Dyck et al., 2005; Butters et al., 1989; Ellsworth and Jury, 1991; Javaux and Vanclooster, 2004b Garrido et al., 2001). In cases where there are large textural differences between soil horizons and a fine-over-coarse texture configuration, local three-dimensional flow and redistribution of mass at soil horizon interfaces has been manifested by fingered flow (Starr et al., 1986; Javaux and Vanclooster, 2004b; and Garrido et al., 2001). Van Wesenbeeck and Kachanoski (1994) Hammel et al. (1999), Dyck et al. (2005), Butters et al. (1989) and Ellsworth and Jury (1991), however,

observed significant redistribution of water and solute mass near soil horizon interfaces that did not exhibit fingered flow.

Vereecken et al. (2007) reviewed field and laboratory experiments intended to verify stochastic continuum theory. The studies of McCord et al. (1991a) and Ursino et al. (2001) confirmed, in a qualitative sense, the existence of saturation-dependent anisotropy in the hydraulic conductivity tensor. Wildenschild and Jensen (1992) found that effective hydraulic properties derived by an inverse model of observed water flow in a sand tank matched those derived by perturbation theory. Jensen and Mantiglou (1992) incorporated stochastic continuum estimations of effective hydraulic properties into a finite difference representation of the large-scale Richards equation, and compared the results to a flow experiment executed at a field site in Denmark. Effective hydraulic properties estimated with continuum methods were used to update the numerical model at each time step. Statistical properties (mean, variance, and correlation lengths) of the hydraulic properties were determined from samples in the field. Jensen and Mantiglou (1992) reported good agreement between spatially averaged observations and simulated results.

1.5. Discussion and synthesis

Based on the summaries in sections 1.2 and 1.3, it may be concluded that, while STMs and SC methods have gone a long way to develop the theory of transport in realistic, simulated soils, the assumptions the models make do not allow them to accurately describe field observations of three-dimensional flow and redistribution of mass at soil horizon interfaces. For example, the homogeneous or layered CLT models are able to incorporate lateral variability in stream tube water flux, but require that the

local water flux established at the tube inlet remain constant for the duration of transport (Jury and Roth, 1990). The CDE as conceptualized by Jury and Roth requires perfect solute mixing between stream tubes, but the end result of such a process would be equal solute and water mass between stream tubes. Stochastic continuum efforts go a long way to describe behavior of layered soil profiles, pedons or even fields, depending on the statistical structure of the random field, but it is unclear whether these large scale results honour smaller scale processes occurring at the soil horizon interfaces (pore or REV scale; Ursino et al., 2000; Vanderborght et al., 2006) which may be environmentally signficant. Pore scale approaches using Miller similar media (Ursino et al., 2000; Zhang et al., 2003) are also enlightening, but still problematic as it is unclear whether real soils are Miller similar (Jury and Roth, 1990) or have direction-dependent pore scale properties. A major issue is that there are few field studies that have measured (with appropriate spatial/temporal resolution) water flow and chemical transport across soil layer interfaces.

Recently, physical and practical problems associated with upscaling of hydraulic properties have been identified. Vogel and Ippisch (2008) investigated the effects of spatial discretization on numerical solutions to the Richards equation. They found that, when simulating transient phenomena such as infiltration or drainage, there is a critical upper limit of the spatial discretization for solving the Richards equation on the order of millimeters to decimeters. Exceeding this critical limit essentially violates the assumption of local equilibrium between water content and water potential, and results either in a lack of convergence, biased results (i.e., poor mass balance) or both. Roth (2008) further elaborates on the implicit assumption of local equilibrium behind the

Richards equation and demonstrates that the Richards and groundwater flow equations are based on a stationary (i.e., local equilibrium) approximation of the Navier-Stokes equation. Therefore, in order for the macroscopic flow equations (i.e., Richards equation) to hold, the assumption of local equilibrium must be honoured at the REV or discretization scale. In a practical sense, the time scale of the forcing function (i.e., boundary conditions) must be larger than the internal dynamics of the system. Therefore, using upscaled hydraulic parameters which allow for larger discretization of the Richards equation may only be valid for very long-term (i.e., quasi-steady state) problems, where soil water balance approaches are likely much more practical. In fact, it may be that local variability in soil transport properties and layer dimensions may have little impact on long term processes (Woods et al., 2006).

The identification of the appropriate REV and the upscaling issues raised by Roth (2008) need to be reconciled with soil classification systems (e.g., USA, Canada) based on the concept of a pedon: the smallest 3-dimensional unit that constitutes a soil unit. A pedon is usually describes as having lateral dimensions large enough to encompass all of the local variability of soil horizon thickness/properties. Quantification of these dimensions, however, is usually somewhat subjective.

1.5.1. Motivation, framework, and objectives of this PhD research

Three questions emerge from the above discussion:

1) At what scales, if any, does the nature of a soil horizon interface influence water flow and transport processes, and can we measure these processes?

2) Does the variability in water flow and transport caused at the scale of influence of a soil horizon interfaces manifest at larger scales?

23

3) Can the scale of influence of soil horizon interfaces be measured or predicted

from simple field observations of soil horizon interface dimensions?

The rest of this section will be devoted to developing a theoretical and experimental

framework motivated by the above three questions.

Stochastic theory allows natural variability of soil and porous materials to be

accounted for while honouring the physics of hydrological processes (Gelhar, 1993).

Consider a field soil with two horizons (A and B horizons) as shown in Figure 1-1. The

depth to the horizon interface varies about a stationary mean depth, and the variance is

constant over the scale of observation (i.e., a polypedon scale). Under steady water

application, water flow and solute transport within this soil may be conceptualized by a

stream tube model where stream tubes within each horizon are independent, but scale

dependent horizontal redistribution and mixing of water and solute mass occurs at the

horizon interface; that is, water and solute flux density across the interface at the local,

stream tube scale may be discontinuous while still maintaining conservation of mass at

larger scales. To investigate the scale of influence of the horizon interface and better

understand processes occurring at the interface, experimental methods are developed in

this thesis to measure effective one-dimensional, local, vertical water and solute flux

within each stream tube above and below the horizon interface. The measured spatial

patterns of local stream tube water flux in the A and B horizons are treated as single

realizations of separate yet possibly related stochastic processes. The ergodic hypothesis

is invoked; that is, the mean and variance of a single realization are assumed to be

representative of the ensemble mean and variance of the stochastic process. Furthermore,

it is assumed that the realization of the water and solute transport processes are determined by and are representative of the underlying transport parameters of the soil.

The conceptual model above is a combination of three separate yet related trajectories of this PhD research: 1) it is a description of a stochastic STM different from those currently in the literature (i.e., it allows redistribution of mass at soil horizon interfaces as has been observed in the reviewed field experiments); 2) it is a hypothesis of how water and solute transport processes may occur in field soils and 3) it is a description of field measurements required to address the three questions stated at the beginning of this section. Therefore, within this framework and motivation the objectives of this PhD research are:

1) Develop methodology to measure (at the pedon scale) the spatial patterns of local water and solute fluxes above and below a soil horizon interface in a field soil.

2) Quantify the influence of the soil horizon interface on the spatial scale dependence of water and solute transport.

3) Develop theory to describe and predict the scale dependent effect of soil horizon interfaces on water and solute transport.

1.6. References

Biggar, J. W. and D. R. Nielsen. 1976. Spatial variability of the leaching characteristics of a field soil. Water Resour. Res. 12:78-84.

Bresler, E., and G. Dagan. 1979. Solute dispersion in unsaturated heterogeneous soil at field scale: II. Applications. Soil Sci. Soc. Am. J. 43:497-472.

Butters, G. L., W. A. Jury, and F. F. Ernst. 1989. Field scale transport of bromide in unsaturated soil. 1. Experimental methodology and results. Water Resour. Res. 25:1575-1581.

Butters, G. L., and W. A. Jury. 1989. Field scale transport of bromide in an unsaturated soil. 2. Dispersion modeling. Water Resour. Res. 25:1583-1589.

Coquet, Y., C. Coutadeur, C. Labat, P. Vachier, M. Th. van Genuchten, J. R. Roger-Estrade, and J. Šimůnek. 2005. Water and solute transport in a cultivated silt loam soil: 1. Field observations. Vadose Zone J. 4:573-586.

Dagan. G. 1984. Solute transport in heterogeneous porous formations. J. Fluid Mech. 145:151-177.

Dagan, G., and E. Bresler. 1979. Solute dispersion in unsaturated heterogeneous soil at field scale: I. Theory. Soil Sci. Soc. Am. J. 43: 461-467.

Derby, N. E., and R. E. Knighton. 2001. Field-scale preferential transport of water and chloride trace by depression-focused recharge. J. Environ. Qual. 30: 194-199.

Dyck, M. F., R. G. Kachanoski, and E. de Jong. 2003. Long-term movement of a chloride tracer under transient, semi-arid conditions. Soil Sci. Soc. Am. J. 67:471-477.

Dyck, M. F., R. G. Kachanoski, and E. de Jong. 2005. Spatial variability of long-term chloride transport under semiarid conditions: Pedon Scale. Vadose Zone J. 4:915-923.

Ellsworth, T. W., and W. A. Jury. 1991. A three-dimensional field study of solute transport through unsaturated, layered, porous media: 2. Characterization of vertical dispersion. Water Resour. Res. 27:967-981.

Gardner, W. R. 1958. Some steady state solutions of the unsaturated moisture flow equation with applications to evaporation from a water table. Soil Sci. 85:228-232.

Garrido, F., M. Ghodrati, C. G. Campbell, and M. Chendorain. 2001. Detailed characterization of solute transport in a heterogeneous field soil. J. Environ. Qual. 30:573-583.

Gelhar, L. W. and C. L. Axness. 1983. Three-dimensional stochastic analysis of macrodispersion in aquifers. Water Resour. Res. 19:161-180.

Gelhar, L. W. 1993. Stochastic subsurface hydrology. Prentice Hall, New Jersey.

Green, T. R., and D. L. Freyberg. 1995. State-dependent anisotropy: Comparison of quasi-analytical solutions with stochastic results for steady gravity drainage. Water Resour. Res. 31:2201-2211.

Hammel, K., J. Gross, G. Wessolek, and K. Roth. 1999. Two-dimensional Simulation of Bromide Transport in a Heterogeneous Filed Soil with Transient Unsaturated Flow. Eur. J. of Soil Sci. 50:633-647.

Hamlen, C. J., and R. G. Kachanoski. 1992. Field solute transport across a soil horizon boundary. Soil Sci. Soc. Am. J. 56:1716-1720.

Javaux, M. and M. Vanclooster. 2004a. In situ long-term chloride transport through a layered, non-saturated subsoil. 1. Data set, interpolation methodology, and results. Vadose Zone J. 3:1322-1330.

Javaux, M. and M. Vanclooster. 2004b. In situ long-term chloride transport through a layered, nonsaturated subsoil. 2. Effect of layering on solute transport processes. Vadose Zone J. 3:1331-1339.

Jensen, K. H., and A. Mantiglou. 1992. Application of stochastic unsaturated flow theory, Numerical simulations, and comparisons to field observations. Water Resour. Res. 28: 269-284.

Jury, W. A., G. Sposito, and R. W. White. 1986. A transfer function model of solute transport through soil. 1. Fundamental concepts. Water Resour. Res. 22:243-247.

Jury, W. A., and J. Utermann. 1992. Solute transport through layered soil profiles: Zero and perfect travel time correlation models. Transp. Porous Media: 8:277-297.

Jury, W. A., and K. Roth. 1990. Transfer functions and solute movement through soil: Theory and applications. Birkhäuser Verlag, Boston.

Mantoglou, A., and L. W. Gelhar. 1987a. Stochastic modeling of large-scale transient unsaturated flow systems. Water Resour. Res. 23:37-46.

Mantoglou, A., and L. W. Gelhar. 1987b. Capillary tension head variance, mean soil moisture content, and effective specific soil moisture capacity of transient unsaturated flow in stratified soils. Water Resour. Res. 23:47-56.

Mantoglou, A., and L. W. Gelhar. 1987c. Effective hydraulic conductivities of transient unsaturated flow in stratified soils. Water Resour. Res. 23:57-67.

Mantoglou, A. 1992. A theoretical approach for modeling unsaturated flow in spatially variable soils: effective flow models in finite domains and nonstationarity. Water Resour. Res. 28:251-267.

Miller, E. E., and R. D. Miller. 1956. Physical theory for capillary flow phenomena. J. App. Phys. 27:324-332.

McCord, J. T., and D. B. Stephens. 1987. Lateral moisture flow beneath a sandy hillslope without an apparent impeding layer. Hydrol. Proc. 1:225-238.

McCord, J. T, D. B. Stephens, and J. L. Wilson. 1991a. Hysteresis and state-dependent anisotropy in modeling unsaturated hillslope hydrologic processes. Water Resour. Res. 27:1501-1518.

McCord, J. T., D. B. Stephens, and J. L. Wilson. 1991b. Towards validating state-dependent macroscopic anisotropy in unsaturated media: Field experiments and modeling considerations. J. Cont. Hydrol. 7:145-175.

Polmann, D. J., D. McLaughlin, S. Luis, L. W. Gelhar, and R. Ababou. 1991. Stochastic modeling of large-scale flow in heterogeneous unsaturated soils. Water Resour. Res. 27:1447-1458.

Pruess, K, S. Yabusaki, C. Steefel, and P. Lichtner. 2002. Fluid flow, heat transfer and solute transport at nuclear waste storage tanks in the Hanford vadose zone. Vadose Zone J. 1:68-88.

Raats, P. A. C., Z. F. Zhang, and A. L. Ward. 2004. The relative connectivity-tortuosity tensor for conduction of water in anisotropic unsaturated soils. Vadose Zone J. 3:1471-1478.

Roth, K. 1995. Steady state flow in an unsaturated, two-dimensional, macroscopically homogeneous Miller-similar medium. Water Resour. Res. 31:2127-2140.

Roth, K. 2008. Scaling of water flow through porous media and soils. Eur. J. of Soil Sci. 59: 125-130.

Roth, K. and K. Hammel. 1996. Transport of conservative chemical through an unsaturated two-dimensional Miller-similar medium with steady state flow. Water Resour. Res. 32:1653-1663.

Roth, K., W. A. Jury, H. Flühler, and W. Attinger. 1991. Transport of chloride through an unsaturated field soil. Water Resour. Res. 27:2533-2541.

Russo, D. 1993. Stochastic modeling of macrodispersion for solute transport in a heterogeneous unsaturated porous formation. Water Resour. Res. 29:383-397.

Russo, D. 1995. Stochastic analysis of the velocity covariance and the displacement covariance tensors in partially saturated heterogeneous anisotropic porous formations. Water Resour. Res. 31:1647-1658.

Starr, J. L., Y. Parlange, and C. R. Frink. 1986. Water and chloride movement through a layered field soil. Soil Sci. Soc. Am. J. 50:1384-1390.

Stephens, D. B., and S. Heermann. 1988. Dependence of anisotropy on saturation in a stratified sand. Water Resour. Res. 24:770-778.

Toride, N. and F. J. Leij. 1996a. Convective-dispersive stream tube model for field-scale solute transport: I. Moment analysis. Soil Sci. Soc. Am. J. 60:342-352.

Toride, N. and F. J. Leij. 1996b. Convective-dispersive stream tube model for field scale solute transport: II. Examples and calibration. Soil Sci. Soc. Am. J. 60:352-361.

Ursino, N., K. Roth, T. Gimmi, and H. Flühler. 2000. Upscaling of anisotropy in unsaturated Miller-similar porous media. Water Resour. Res. 36:421-430.

Vanderborght, J., R. Kastell, and H. Vereecken. 2006. Stochastic continuum transport equations for field-scale solute transport: Overview of theoretical and experimental results. Vadose Zone J. 5: 184-203.

van Wesenbeeck, I. J., and R. G. Kachanoski. 1991. Spatial scale dependence of in situ solute transport. Soil Sci. Soc. Am. J. 55:3-7.

van Wesenbeeck, I. J., and R. G. Kachanoski. 1994. Effect of variable horizon thickness on solute transport. Soil Sci. Soc. Am. J. 58:1307-1316.

Vereecken, R., J. Kasteel, J. Vanderborght, and T. Harter. 2007. Upscaling hydraulic properties and soil water flow processes in heterogeneous soils: A review. Vadose Zone J. 6:1-28.

Vogel, H. J., and O. Ippisch. 2008. Estimation of a critical spatial discretization limit for solving Richards' equation at larger scales. Vadose Zone J. 7: 112-114.

Ward, A. L., R. G. Kachanoski, A. P. von Bertoldi, and D. E. Elrick. 1995. Field and undisturbed column measurements for predicting transport in unsaturated, layered soil. Soil Sci. Soc. Am. J.: 59:52-59.

Ward, A. L., and Z. F. Zhang. 2007. Effective hydraulic properties determined from transient unsaturated flow in anisotropic soils. Vadose Zone J. 6:913-924.

White, M. D., and M. Oostrom. 2004. User's guide of STOMP-Subsurface transport over multiple phases. Version 3.1. PNNL-14478. Pacific Northwest Natl. Lab., Richland, WA.

Wildenschild, D., and K. H. Jensen. 1999. Laboratory investigations of effective flow behavior in unsaturated heterogeneous sands. Water Resour. Res. 35:17-27.

Woods, S. A., R. G. Kachanoski, and M. F. Dyck. 2006. Long-term solute transport under semi-arid conditions: Pedon to field scale. Vadose Zone J. 5:365-376.

Yeh, T. C. J. 1989. One-dimensional steady state infiltration in heterogeneous soils. Water Resour. Res. 25:2149-2158.

Yeh, T. C. J., L. W. Gelhar and A. L. Gutjahr. 1985a. Stochastic analysis of unsaturated flow in heterogeneous soils: 1. Statistically isotropic media. Water Resour. Res. 21:447-456.

Yeh, T. C. J., L. W. Gelhar and A. L. Gutjahr. 1985b. Stochastic analysis of unsaturated flow in heterogeneous soils: 2. Statistically anisotropic media with variable α. Water Resour. Res. 21:457-464.

Yeh, T. C. J., L. W. Gelhar and A. L. Gutjahr. 1985c. Stochastic analysis of unsaturated flow in heterogeneous soils: 3. Observations and applications. Water Resour. Res. 21:465-471.

Zhang, Z. F., A. L. Ward, and G. W. Gee. 2003. A tensorial connectivity-tortuosity concept to describe the unsaturated hydraulic properties of anisotropic soils. Vadose Zone J. 2:313-321.
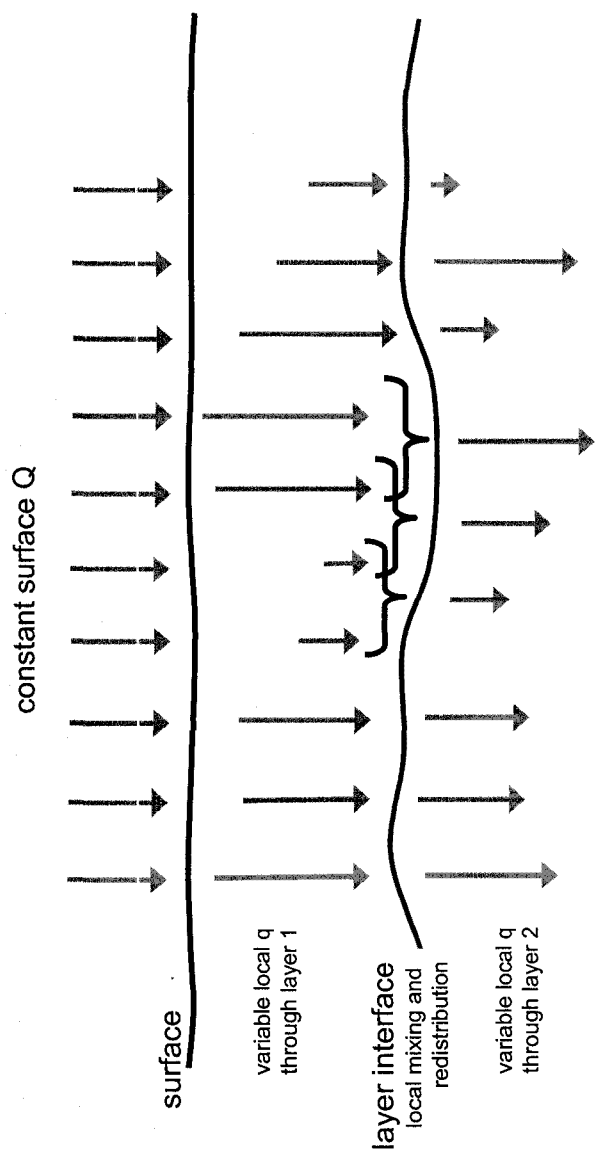
Figure 1-1: Conceptual model of water and solute transport through layered soils (pedon scale).

2.   Measurement of the spatial pattern of local soil water flux above and below a soil horizon interface: I. Transient, local soil water flux

2.1.   Introduction

Understanding of water flow and solute transport processes in field soils remains limited. By definition, soils have at least two horizons separated by a horizon interface. Because soil horizons (e.g., A and B horizons) have different average hydraulic properties and their boundaries are visually distinct, it is often assumed that soil horizons are independent layers and that the interface between soil horizons has no influence on the hydraulic behavior of the entire soil profile. Soil horizons and soil horizon interfaces, however, have been formed by pedogenic processes driven by environmental gradients; these processes are spatially variable and scale dependent. The basic unit of soil, the pedon, is described as the minimum, three-dimensional unit of soil representative of the variability of soil horizon dimensions and morphology. Within the context of field water flow and solute transport then, soil horizons and soil horizon interfaces are spatially variable, scale dependent, and likely influence flow and transport at local (stream tube), pedon (meters) and field scales (10s, 100s of meters).

Major contributions to flow and transport theory in spatially-variable, vertically heterogeneous soils are presented in stochastic stream tube (i.e Jury and Utterman, 1992) or stochastic continuum frameworks (i.e., Yeh et al., 1985a,b,c). Recent, comprehensive reviews of these frameworks are available (Vereecken et al., 2007; Vanderborght et al., 2006). Theoretical developmen t, however, seems to have outpaced experimental observations. Many field experiments have indicated that local, vertical flux continuity assumptions of stream tube models do not hold (e.g., van Wesenbeeck and Kachanoski,

1994; Roth et al., 1991). Ward and Zhang (2007) indicate that significant sampling and hydraulic property characterization efforts are required for the stochastic continuum approach. Furthermore, the scaling of hydraulic properties inherent to stochastic continuum frameworks may not be physically reasonable during short-term transient processes such as infiltration (Roth, 2008; Vogel and Ippisch, 2008).

Understanding flow and transport processes in spatially variable, vertically homogeneous field soils requires experimental observations of the horizontal and vertical variability of water and solute fluxes in field soils. In this chapter, a TDR method using vertically installed probes is developed that measures the transient, local vertical soil water flux above and below spatially-variable soil horizon interfaces. Parkin et al. (1995) and Si and Kachanoski (2003) developed a time domain reflectometry TDR method to measure local soil water flux in soils without distinct horizonation during infiltration under constant flux surface boundary conditions. The objective of this section is to extend this method to soils with distinct horizons/layers. This method measures the spatial pattern of local soil water flux above and below a soil horizon interface during infiltration under quasi constant surface water application. Even though the surface water application is approximately constant, the infiltration process under these conditions is still designated as transient because the water content of the soil changes as the wetting front progresses through the soil.

2.2. Theory

2.2.1. Local soil water flux through soil horizons during constant flux infiltration

In this section, the methods of Si and Kachanoski (2003) and Parkin et al. (1995) are extended to soils with at least two distinct horizons. The theory is developed for a soil with two horizons (i.e., A and B horizons).

The method involves some *a priori* knowledge of the depth of the soil horizons, which can easily be obtained from initial coring. At each measurement location on the soil surface, two TDR probes are inserted vertically into the soil such that one probe spans the surface horizon (i.e., A horizon), and the other probe spans both the A and B horizons (Figure 2-1). The probes are inserted in a cross pattern so that their sampling volumes partially overlap. As the wetting front passes through the soil during constant flux infiltration, average water content ($\bar{\theta}$; cm^3 cm^{-3}) measurements from the vertical TDR probes can be used to determine water storage (W; cm^3 cm^{-2}) along the length of the probe with time (Si and Kachanoski, 2003):

$$W_L(t) = \bar{\theta}_L(t)L \qquad\qquad [2\text{-}1]$$

where L is the length of the vertical TDR probe (cm). For the probe configuration in Fig. 2-1, let L_A (cm) be the length of the probe that spans the A horizon and L (cm) be the length of the probe that spans both the A and B horizon. Then the water storage (cm^3 cm^{-2}) as a function of time along the length of the probe that spans the A horizon is:

$$W_{L_A}(t) = \bar{\theta}_A(t)L_A \qquad\qquad [2\text{-}2]$$

and the water storage (cm) as a function of time along the length of the probe that spans both the A and B horizons is:

$$W_L(t) = \bar{\theta}_{AB}(t)L \qquad\qquad [2\text{-}3].$$

where $L = L_A + L_B$.

The one-dimensional continuity equation is:

$$\frac{d\theta}{dt} = -\frac{dq_w}{dz}$$

[2-4]

where θ is volumetric water content (cm^3 cm^{-2}), t is time (days), and q_w is soil water flux (cm^3 cm^{-2} day^{-1}), and z is depth (m). Integrating both sides of Eq. [2-4] with respect to depth between $z = 0$ and $z = L_A$ gives:

$$\frac{d}{dt}\int_0^{L_A}\theta dz = -\int_0^{L_A}\frac{dq_w}{dz}dz = \frac{dW_{L_A}(t)}{dt} = q_w(0) - q_w(L_A)$$

[2-5]

Assuming $q_w(L_A) = 0$, Si and Kachanoski (2003) and Parkin et al. (1995) showed that the change in water storage along the length of the probe, L, with respect to time before the wetting front has reached the ends of the probe is equal to the soil water flux at the surface:

$$q_{w|0} = \frac{dW_L(t)}{dt} \qquad t < t_L$$

[2-6].

where $q_{w|0}$ is defined as the local water flux at the soil surface (cm day^{-1}), and t_L is the time (days) at which the leading edge of the wetting front reaches the end of the probe. Although, it is the surface water flux that causes the change in water storage along the length of the probe, Eq. [2-6] may be said to represent the average (effective) vertical soil water flux through the soil from the soil surface to the depth of the wetting front under the following conditions: 1) the soil is initially sufficiently dry such that $q_w(L_A) = 0$; 2) the wetting front is sharp enough (i.e., high water application rates) such that the water flux just below the wetting front may be assumed to be zero; and 3) due to the tortuous

35

nature of soil pores, water from adjacent stream-tubes may enter and leave the sampling volume of the TDR probe during infiltration.

Assuming the probe configuration in Fig. 2-1, local soil water flux from the soil surface to the A/B horizon interface (i.e., local soil water flux through the A horizon) may be estimated from the change in soil water storage with respect to time before the leading edge of the wetting front has reached the interface between the A and B horizons (t_{L_A}):

$$q_{w|A,tr} = \frac{dW_{L_A}(t)}{dt} \qquad\qquad t < t_{L_A} \qquad\qquad [2\text{-}7].$$

Furthermore, the local soil water flux below A/B horizon interface (i.e., the local water flux through the B horizon) may be estimated from the change in soil water storage with respect to time after the wetting front has reached the A/B horizon interface but before the leading edge of the wetting from has reached the end of the probe spanning both horizons (t_L):

$$q_{w|B,tr} = \frac{dW_L(t)}{dt} \qquad\qquad t_{L_A} < t < t_L \qquad\qquad [2\text{-}8].$$

Equation [2-8] assumes that there no change in water content in the A horizon after the wetting front has entered the B horizon and that $q_w(L) = 0$.

2.3. Materials and methods

The proposed methods were tested for proof-of-principle under laboratory conditions in soil columns where one-dimensional transport could be confidently assumed, and then implemented in the field. For both field and laboratory experiments, a quasi constant flux boundary condition (pulsed water application at regular time intervals) was imposed at the soil surface. Furthermore, all field and laboratory

experiments were executed on relatively dry soil (initial $\theta \leq 0.15$) to fulfill the assumptions of the method stated in section 2.2.

Laboratory experiments were carried out on a repacked soil column. Two types of sand with different particle size distributions were packed into a sectioned, 1.6 m high PVC column, 15 cm i.d., similar to the set-up of Nissen et al., (2000). The two types of sand were packed in the column to create a medium-over-fine, layered profile. The fine sand (Sil Industrial Minerals, Edmonton, AB, Sil 1) consisted of particles ranging from 75 to 425 μm in diameter (200 – 40 mesh) with a median diameter of 175 μm. The medium sand (Sil Industrial Minerals, Edmonton, AB, Sil 7) consisted of particles ranging from 180 to 1200 μm in diameter (80 – 16 mesh) with a median diameter of 400 μm. The medium sand layer was 25 cm thick and the fine sand layer was 135 cm thick. Both horizontal and vertical TDR probes were installed. Vertical, two-rod probes with lengths of 24.5 cm and 45 cm were installed to measure local soil water flux in the medium and fine sand layers. In this case, the vertical probes were not installed in the cross pattern as in Fig. 2-1, but were separated by 7.5 cm. The horizontal probes were part of a different, simultaneous solute transport experiment, and are not relevant to rest of this section.

Probes for the disturbed column were constructed from stainless steel TIG welding rod (diameter 1.6 mm) coupled to RG-58U coaxial cable using crimp connectors. The crimped joints were insulated with liquid plastic (Plasti Dip International, Blaine MN, USA). Probe rods were spaced 16 to 18 mm apart. These construction methods allowed thin, flexible probe handles that minimized interference with the applied water. The other end of the coaxial cable was fitted with crimp type BNC connectors.

Water application rates were controlled with a programmable syringe pump (Harvard Apparatus model PhD 2000). The pump was programmed to deliver a known volume of water to the soil at regular time intervals. Manifolds with narrow bore (0.2 mm i.d.) tygon tubing and hypodermic needles were constructed to partition the water flow evenly over the soil surface. The manifold partitioned flow to 61, 27 gauge, hypodermic needles (38 mmin length) with approximately 1 needle per 2.9 cm^2 of soil surface. Water applied to the soil columns contained 5 mg/L $AgCl_2$ and thymol to inhibit microbial and fungal growth.

Field experiments were executed in a pasture 75 km north of Edmonton, Alberta, Canada (54°2'11" Latitude; 113°30'12" Longitude) in the summers of 2006 and 2007. The field had not been cultivated for at least 15 years (Ray Pelletier, landowner, personal communication). Soils at the site are mapped as 80% Orthic Gray Luvisols (Brightbank series) and 20% Orthic Dark Gray Chernozems (Redwater series) developed on sandy (texture sandy loam) aeolian parent material. A suitable plot was chosen to set up a greenhouse (10 m long by 5 m wide) containing a water application system to run water and solute transport experiments. The soil at this location displayed a distinct Ah-Bm horizon sequence indicative of a Chernozemic soil. Prior to setting up the greenhouse, a narrow trench 1 meter deep was dug around the perimeter of the plot to assess the dimensions of the horizons without disturbing the soil in the area where the transport experiments were to be executed. Perimeter trench observations determined that the average depth to the A/B horizon interface was 25 cm (CV = 21%).

Figure 2-2 shows a schematic diagram of the experimental setup. Because only the average depth to the A/B horizon interface was known, 25- and 60-cm-long, two rod

TDR probes were constructed with 4.8 mm diameter stainless steel TIG welding rod. The 25 cm long probes were assumed to span the A horizon, and the 60 cm long probes were assumed to span both the A and B horizon. The probes were installed into the soil according to the configuration in Fig. 2-1, every 15 cm along a 6.75 m transect (46 25-cm probes and 46 60-cm probes) in the center of the greenhouse. An additional 45 60-cm probes were installed between each dual-probe nest giving a total of 91 60-cm probes at 7.5 cm spacing along the transect. TDR rods were pushed into the soil through a jig that ensured straight, parallel installation with 50 mm separation between the center of the rods. Coaxial cables (RG-58U) were coupled to the rods using female stereo jacks after they had been pushed into the soil, and conducting silver epoxy was used to ensure a secure connection between the TDR rods and coaxial cables (MG chemicals; www.mgchemicals.com). The other end of the coaxial cables were fitted with BNC crimp connectors, which were then secured in rows on a panel according to their transect location. These panels were used to manually and systematically switch between probes.

Tensiometer and thermocouple nests were installed along a second transect, offset by 40 cm, but parallel to the TDR probe transect (Fig. 2-2). Tensiometer nests consisted of three tensiometers installed such that the cups were 10, 25, and 60 cm below the soil surface. Matric suction was measured with a Tensimeter (Soil Measurement Systems, Tucson, Arizona). Copper-constantan thermocouple nests were constructed by drilling holes at 18 cm intervals in 1 cm i.d. PVC tubing. The thermocouple wire was fed down the center of the PVC tubes and pushed through the holes such that the thermocouple was on the outside of the tubing and would be in contact with the soil. Liquid foam insulation was used to fill the center of the PVC tubes after the thermocouples had been constructed

and tested. Thermocouple nests were installed such that temperature measurements were available for 10, 28, 46, 64, and 82 cm below the soil surface.

An Andpro Spray Rite Watering Boom™ (www.agroponic.com) system was used to establish a quasi constant flux boundary condition at the soil surface. The system uses an electronic drive train that runs along a single rail suspended from the roof of the greenhouse to move a spray boom back and forth over the soil surface. Water application rates were set by adjusting the cycling frequency and speed of the spray boom, nozzle flow capacity and water pressure. Spray booms 1.5 meters wide, with 4 or 5 evenly spaced spray nozzles (FloodJet® wide angle flat spray deflector nozzles) were constructed out of 1 cm i.d. PVC pipe. The spray booms were constructed such that the spray pattern of adjacent nozzles overlapped which helped to achieve uniform water application. Spatial variability of water application rates with the system was low (CV = 5%). The greenhouse/water application system was able to apply water to a 1.5 m wide by 8.0 m long area. A Goulds JetPump attached to a pressure regulator supplied water to the spray boom from 5000 liter storage tanks outside of the greenhouse.

For all lab and field transport experiments, apparent dielectric permittivity was estimated from TDR waveforms sampled by Tektronix 1502B or 1502C cable testers controlled by the TACQ BETA software (Evett, 2000). In the laboratory, Dynamax multiplexers were used to switch between probes. In the field, probes were switched manually, but the TACQ software was still used to log the waveforms to the hard drive of a laptop computer every 1 to 3 hours depending on water application rate. It was found that manual switching could be performed fast enough to accurately log the TDR waveforms with the TACQ software. Logging the waveforms electronically allowed for

consistent post-processing. Undisturbed 10 cm i.d. cores 27 cm long (N = 4) and 65 cm

long (N = 4) were brought back to the laboratory to test the apparent dielectric

permittivity-volumetric water content calibration. For the 60-cm probes, the calibration

equation measured by Topp et al. (1980) was accurate, but seemed to over estimate the

volumetric water content for the 25-cm probes. Therefore, apparent permittivity

measured from the 25-cm probes was converted to volumetric water content using a site-

specific calibration (Appendix D).

To characterize the hydraulic properties of the soil horizons, 128 soil cores were

taken from a transect along the west wall of the greenhouse, well away from the TDR

transect. Aluminum cores, 60 cm in length, were hammered into the soil. Prior to

extracting the core, the depth of the A/B horizon interface directly adjacent to each core

was determined with a hand auger. The aluminum cores were split at the depth of the

horizon interface, and then each horizon was split into 5 cm subsamples. Four-point

moisture retention curves were measured on each 5 cm subsample with standard pressure

plate methods (Reynolds and Topp, 2008). Saturated hydraulic conductivity was

measured on the 5 cm subsamples from half of the sampling locations under constant

head boundary conditions (Reynolds, 2008). The van Genuchten (1980) moisture

retention model was fit to moisture retention measurements, and these parameters were

used predict the hydraulic conductivity function (van Genuchten 1980). Average A and

B horizon hydraulic properties are summarized in Table 2-1 and Figure 2-3.

2.4.   Results and Discussion

A summary of transient local soil water flux measurements and water application

rates are presented in Table 2-2. The proof-of-principle laboratory experiments were

only replicated once for each water application rate so standard deviations were not calculated. For the field experiments, the results presented in Table 2-2 are the average of 46 probes along the 6.75 m transect. The spatial variability (represented as CV in Table 2-2) of the measured water flux was similar to that measured by Si and Kachanoski (2003). Mass recovery as displayed in Table 2-2 is the ratio of measured flux local soil water flux to the application rate. Over all, measured local soil water flux agreed well with the application rate with mass recoveries ranging from 87 to 118%.

For the disturbed column in the laboratory (Figure 2-4), the difference between measured local soil water flux in the medium (top) and fine (bottom) sand layers is small which is expected for these conditions as flow was forced to be one-dimensional. Although water application conditions were set up in the field such that flow would be effectively one-dimensional, there were no impermeable boundaries forcing one-dimensional flow like a laboratory soil column. Therefore, vertical probes in the field measured the effective, vertical local soil water flux. In all measurements of water storage versus time from the field experiments (Figures 2-5, 2-6 and 2-7), a linear increase in soil water storage with time was measured during transient infiltration, indicating effective one-dimension flow within individual soil horizons. Changes in transient, local soil water flux were observed, however, as the wetting front moved across the soil horizon interface, indicating that the interface between soil horizons is a focal point of three dimensional flow under these conditions. Figures 2-5B, 2-6B and 2-7B show examples of the change in soil water storage with time $dW_{L_{AB}}(t)/dt$ measured by the 60-cm probes (spanning both A and B horizons) remaining relatively constant, decreasing and increasing as the wetting front moved across the A/B soil horizon

interface, respectively. Therefore, it would seem that soil horizon interfaces are focal

points for three-dimensional redistribution of mass as noticed by others (e.g., van

Wesenbeeck and Kachanoski, 1994; Ellsworth et al., 1991; Dyck et al., 2005).

The transient local water flux measured at early times ($t < t_{L_A}$) by the probe

spanning the A and B horizons was very similar to the local flux measured at early times

by the probe spanning only the A horizon (Fig. 2-5, 2-6 and 2-7). Because the two

probes are close together and measure similar volumes of soil at early times, it is

expected that local soil water flux estimated with the probe spanning the A horizon,

should be similar to local soil water flux estimated with the probe spanning the A and B

horizon. The two, independent measurements of local A horizon flux for each location

along the 6.75 transect are presented in Figure 2-8 and agree well with each other;

Pearson correlation coefficients, r, are greater than 0.94 and highly significant (P < 0.001)

for all water application rates. The excellent agreement between the two independent

measurements of transient, local water flux in essentially the same volume of soil

indicates that the observed spatial pattern and variability is real and not an artifact of

measurement error. It also indicates that the TDR probes and methodology are sensitive

enough to measure changes in local soil water flux as the wetting front encounters layer

interfaces.

Given the sensitivity and repeatability of the method, physical interpretations of

the observed spatial patterns of transient, local soil water flux above and below the A/B

horizon interface are possible. Possible mechanisms explaining the redistribution of mass

at the soil horizon interfaces observed during these experiments and experiments by

others (e.g., van Wesenbeeck and Kachanoski, 1994; Ellsworth et al., 1991; Dyck et al.,

2005) are: 1) water entry potential discontinuities across the horizon interface (e.g., for a fine-over-coarse texture interface); or 2) a greater reduction in hydraulic conductivity across the interface (vertical direction) than along the interface (horizontal direction; e.g., anisotropy). Van Wesenbeeck and Kachanoski (1994) showed that the spatial pattern of solute mass recovery after steady state solute transport closely matched the spatial pattern of a Bm-Ck horizon interface (fine over coarse interface). Ellsworth et al. (1991) noted that the presence of thin loam-textured layer compressed and laterally shifted a solute pulse travelling through an otherwise sandy soil. Dyck et al. (2005) also observed significant three-dimensional long-term solute transport at the interface between two sedimentary layers. Examples of three-dimensional flow attributed to state-dependent anisotropy in soil hydraulic properties have been provided by Stephens and Heerman (1988), Ursino et al. (2000), and Glass et al. (2005). Numerical simulations have shown that three dimensional flow in anisotropic soils is possible whether the underlying anisotropy is statistical (e.g., anisotropy in the correlation length scales of hydraulic properties as in Yeh et al. (1987a,b,c)) or capillary in nature (e.g., anisotropic pore size distributions as in Ursino et al., 2000). These studies indicate that layered soils may exhibit state-dependent anisotropy, but didn't explicitly discuss processes localized at horizon interfaces.

The spatial patterns of transient local soil water flux above and below the A/B horizon interface can be used to quantify the scale of influence of the horizon interface. The spatial-scale-dependent variability and correlation of the horizon interface and local water fluxes is examined in detail with Fourier domain spatial spectral and coherency techniques in Section 4. A few overall observations, however, are also given here.

Overall, the measurements of transient, local soil water flux within each horizon displayed somewhat consistent spatial patterns across all water application rates. The A horizon flux estimates are significantly correlated to each other at all water application rates, as are the spatial patterns of B horizon flux estimates are (Table 2-3).The transient, local soil water flux through/across the A and B horizons are also significantly correlated, but the correlation is weak (e.g., r = 0.29; P<0.01; Table 2-3). Although weakly correlated, the fact that the correlation coefficient between the A and B horizon fluxes is still statistically significant indicates that the soil horizons do not behave as independent layers, and that the interface between the horizons is a hydrologically significant component of the soil profile at this average soil water flux. The continuity/correlation of local soil water flux across the horizon interface measured by individual TDR probes (i.e local, stream tube scale) is likely scale (spatial) dependent and must be interpreted within a larger context: three-dimensional flow processes at some larger scale are influencing TDR measurements at the local, stream-tube scale. As a result, the average correlation between local, stream-tube scale A and B horizon transient fluxes is weak, but may be much stronger at other scales.

The correlation between the spatial pattern of A and B horizon, transient local water fluxes also appears to be flux dependent (Table 2-3). At low average, transient soil water flux, correlation coefficients are higher (r=0.38; P<0.01, for the 1.3 cm day^{-1} experiment) than at high average, transient soil water flux (r=0.20; P>0.05 for the 10.6 cm day^{-1} experiment). This suggests that the hydraulic response of the horizon interface appears to be flux-dependent: as the average transient soil water flux increases, the horizon interface disrupts the local scale, vertical continuity of soil water flux to a greater

extent. Conceptually, this behavior appears to be physically reasonable. Under higher water application rates, then, sharper wetting fronts and, therefore, greater vertical and horizontal hydraulic gradients localized at the wetting front, can be expected. The spatially variable pattern of A horizon transient soil water flux (i.e., spatially variable wetting front velocity) coupled with a spatially variable horizon interface would result in the wetting front reaching the interface relatively earlier at some spatial locations compared to others. Any change in pore size distribution or pore continuity that may be associated with the horizon interface may enhance localized three-dimensional flow as the wetting front hits the interface, because water-conducting-pores within the A horizon (horizontally) may be more continuous than across the interface into the B horizon (vertically).

Quantification of the pedon-scale hydrological influence of soil horizon interfaces is a potentially important hydrological property of the soil profile that is not yet explicitly recognized by hydrological models or pedotransfer functions. Recalling that the definition of the pedon is the smallest three dimensional unit of soil capturing the variability of the profile's horizons, the flux dependence of the continuity/correlation of local soil water flux across the horizon interface (and possibly spatial-scale-dependent nature of the correlation) raises interesting and important issues in the development of quantitative, process based definition of a Pedon. It also makes the relationship between the definition/dimensions of a pedon and the REV required for valid definition of macroscopic hydraulic properties (e.g., Roth, 2008) more complex.

2.5. Conclusion

A TDR method to measure the spatial patterns of transient, local soil water flux above and below soil horizon interfaces was developed and tested in laboratory and field. Water mass recovery in field and laboratory experiments ranged between 87 and 118%, indicating that the methods yield estimates consistent with the actual local water flux in the soil. Furthermore, the excellent agreement of spatial patterns of two independent measurements of local, transient flux through the A horizon (for 4 different surface water application rates) suggests that the method is very sensitive to changes in local soil water flux as the advancing wetting front encounters different soil horizons, and soil horizon interfaces, and that local A and B horizon water fluxes can be measured by one probe spanning two horizons. The water flow measurements indicate that the interface between the A and B horizons is a hydrologically significant component of the soil profile. Further, the hydrologic response of the interface appears to be flux dependent. A full analysis of the spatial patterns of the influence of the soil horizon interface on the pattern of transient, local soil water fluxes is the subject of Sections 3 and 4.

2.6. References

Dyck, M. F., R. G. Kachanoski, and E. de Jong. 2005. Spatial variability of long-term chloride transport under semiarid conditions: Pedon scale. Vadose Zone J. 4:915-923.

Ellsworth, T. W., W. A. Jury, F. F. Ernst and P. J. Shouse. 1991. A three-dimensional field study of solute transport through unsaturated, layered, porous media: 1. Methodology, mass recovery, and mean transport. Water Resour. Res. 27:951-965.

Evett. S. R. 2000. The TACQ computer program for automatic time domain reflectometry measurements: I. Design and operating characteristics. Trans. ASAE 43:1939-1946.

Glass, R. J., J. R. Brainard, and T. C. Jim Yeh. 2005. Infiltration into unsaturated layered fluvial deposits at Rio Bravo: Macroscopic anisotropy and heterogeneous transport. Vadose Zone J. 4:22-31.

Jury, W. A., and J. Utermann. 1992. Solute transport through layered soil profiles: Zero and perfect travel time correlation models. Transp. Porous Media: 8:277-297.

Nissen, H. H., P. Moldrop, and R. G. Kachanoski. 2000. Time domain reflectometry measurements of solute transport across a soil layer boundary. Soil Sci. Soc. Am. J. 64:62-74.

Parkin, G. W., R. G. Kachanoski, D. E. Elrick, and R. G. Gibson. 1995. Unsaturated hydraulic conductivity measured by time domain reflectometry under a rainfall simulator. Water Resour. Res. 31:447-454.

Reynolds, W. D. 2008. Saturated hydraulic properties: Laboratory methods. p. 1013-1024. *In* M. R. Carter and E. G. Gregorich (ed.) Soil Sampling and Methods of Analysis, Second Edition, CRC, Boca Raton, FL.

Reynolds, W. D., and G. C. Topp. 2008. Soil water desorption and imbibition: Tension and pressure techniques. p. 981-998. *In* M. R. Carter and E. G. Gregorich (ed.) Soil Sampling and Methods of Analysis, Second Edition, CRC, Boca Raton, FL.

Roth, K., W. A. Jury, H. Flühler, and W. Attinger. 1991. Transport of chloride through an unsaturated field soil. Water Resour. Res. 27:2533-2541.

Roth, K. 2008. Scaling of water flow through porous media and soils. Eur. J. of Soil Sci. 59: 125-130.

Si, B. C., and R. G. Kachanoski. 2003. Measurement of local soil water flux during field solute transport experiments. Soil Sci. Soc. Am J. 67:730-736.

Stephens, D. B., and S. Heermann. 1988. Dependence of anisotropy on saturation in a stratified sand. Water Resour. Res. 24:770-778.

Topp, G. C., J. L. Davis, and A. P. Annan. 1980. Electromagnetic determination of soil water content measurements in coaxial transmission lines. Water Resour. Res. 16:574-582.

Ursino, N., K. Roth, T. Gimmi, and H. Flühler. 2000. Upscaling of anisotropy in unsaturated Miller-similar porous media. Water Resour. Res. 36:421-430.

Vanderborght, J., R. Kastell, and H. Vereecken. 2006. Stochastic continuum transport equations for field-scale solute transport: Overview of theoretical and experimental results. Vadose Zone J. 5: 184-203.

van Genuchten, M. Th. 1980. A closed form equation for predicting the hydraulic conductivity of unsaturated soils. Soil Sci. Soc. Am. J. 44:892-898.

van Wesenbeeck, I. J., and R. G. Kachanoski. 1994. Effect of variable horizon thickness on solute transport. Soil Sci. Soc. Am. J. 58:1307-1316.

Vereecken, R., J. Kasteel, J. Vanderborght, and T. Harter. 2007. Upscaling hydraulic properties and soil water flow processes in heterogeneous soils: A review. Vadose Zone J. 6:1-28.

Vogel, H. J., and O. Ippisch. 2008. Estimation of a critical spatial discretization limit for solving Richards' equation at larger scales. Vadose Zone J. 7: 112-114.

Ward, A. L., and Z. F. Zhang. 2007. Effective hydraulic properties determined from transient unsaturated flow in anisotropic soils. Vadose Zone J. 6:913-924.

Yeh, T. C. J., L. W. Gelhar and A. L. Gutjahr. 1985a. Stochastic analysis of unsaturated flow in heterogeneous soils: 1. Statistically isotropic media. Water Resour. Res. 21:447-456.

Yeh, T. C. J., L. W. Gelhar and A. L. Gutjahr. 1985b. Stochastic analysis of unsaturated flow in heterogeneous soils: 2. Statistically anisotropic media with variable α. Water Resour. Res. 21:457-464.

Yeh, T. C. J., L. W. Gelhar and A. L. Gutjahr. 1985c. Stochastic analysis of unsaturated flow in heterogeneous soils: 3. Observations and applications. Water Resour. Res. 21:465-471.

Table 2-1: Average hydraulic properties for A and B horizons

matric potential (-cm)	measured θ (cm^3 cm^{-3})		C.V. %	
	A horizon[†]	B horizon[‡]	A horizon	B horizon
1	0.41	0.39	12	18
20	0.36	0.35	14	12
100	0.20	0.17	25	26
300	0.15	0.13	33	29
Ks (cm day^{-1})	120	151	123	113
VG§ θs	0.42	0.39		
VG α	0.041	0.037		
VG n	1.43	1.52		
VG θr	0.001	0.003		

† N=298

‡ N=381

§ van Genuchten (VG) parameters for average moisture retention curve

Table 2-2: Summary of local soil water flux estimates under quasi steady infiltration

Experiment	Application rate	Measured flux			Standard deviation† ($cm\ day^{-1}$)	Coefficient of variation† (%)
		Layer	Estimate	Mass recovery (%)		
Laboratory disturbed column	2.3 cm hour^{-1}	medium	2.0	87		
		fine	2.0	87		
	6.7	medium	6.5	97		
		fine	6.4	96		
	13.2	medium	12.7	96		
		fine	12.8	97		
Field	1.3 cm day^{-1}	A horizon	1.53	118	0.2	12.4
		B horizon	1.42	109	0.2	15.5
	2.7	A horizon	2.45	91	0.3	12.0
		B horizon	2.75	102	0.5	19.1
	7.0	A horizon	7.12	102	0.7	9.2
		B horizon	7.14	102	0.7	9.4
	10.6	A horizon	10.82	102	1.0	9.3
		B horizon	11.34	107	1.0	8.9

† Laboratory experiments were not replicated

Table 2-3: Correlation matrix for transient, local soil water flux estimates across four water application rates

	$q_{w|A,tr}(1.3)$	$q_{w|B,tr}(1.3)$	$q_{w|A,tr}(2.7)$	$q_{w|B,tr}(2.7)$	$q_{w|A,tr}(7.0)$	$q_{w|B,tr}(7.0)$	$q_{w|A,tr}(10.6)$	$q_{w|B,tr}(10.6)$
$q_{w|A,tr}(1.3)$	1							
$q_{w|B,tr}(1.3)$	0.38**	1						
$q_{w|A,tr}(2.7)$	0.48***	0.26	1					
$q_{w|B,tr}(2.7)$	0.45**	0.68***	0.31*	1				
$q_{w|A,tr}(7.0)$	0.5***	0.33*	0.63***	0.12	1			
$q_{w|B,tr}(7.0)$	0.32*	0.54***	0.23	0.62***	0.29*	1		
$q_{w|A,tr}(10.6)$	0.44**	0.24	0.66***	0.13	0.77***	0.21	1	
$q_{w|B,tr}(10.6)$	0.28	0.56***	0.21	0.41**	0.35*	0.64***	0.20	1

* Significant at the 0.05 probability level
** Significant at the 0.01 probability level
*** Significant at the 0.001 probability level
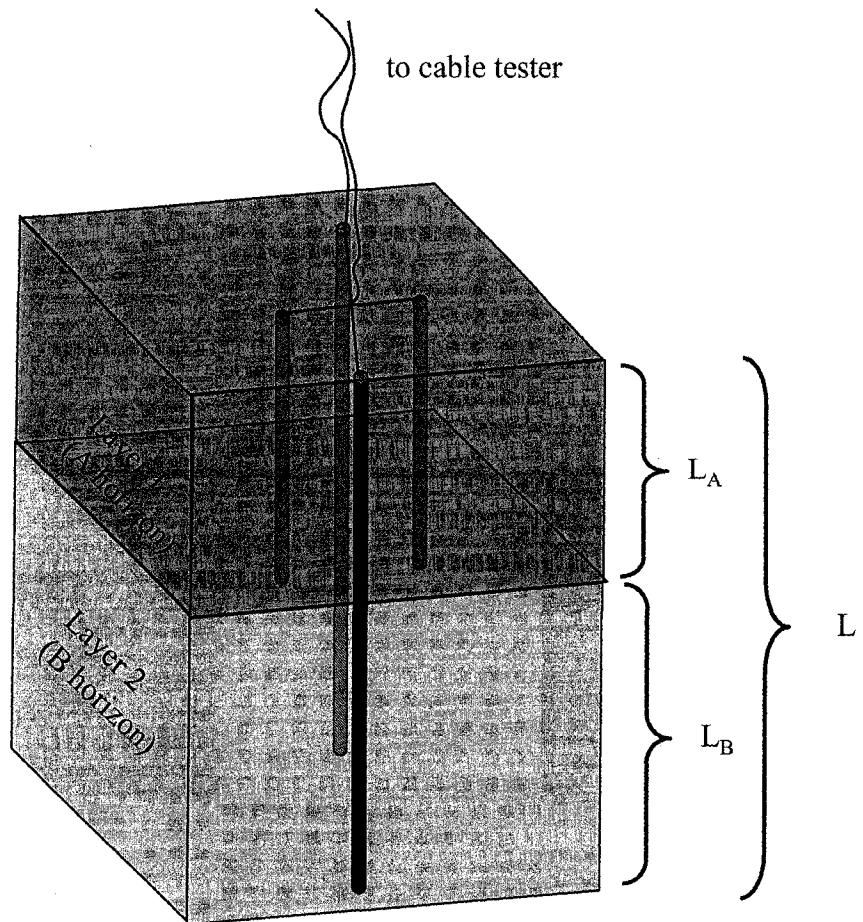
Figure 2-1: Configuration of vertical TDR probes for measurement of local soil water flux in layered soils (single location).
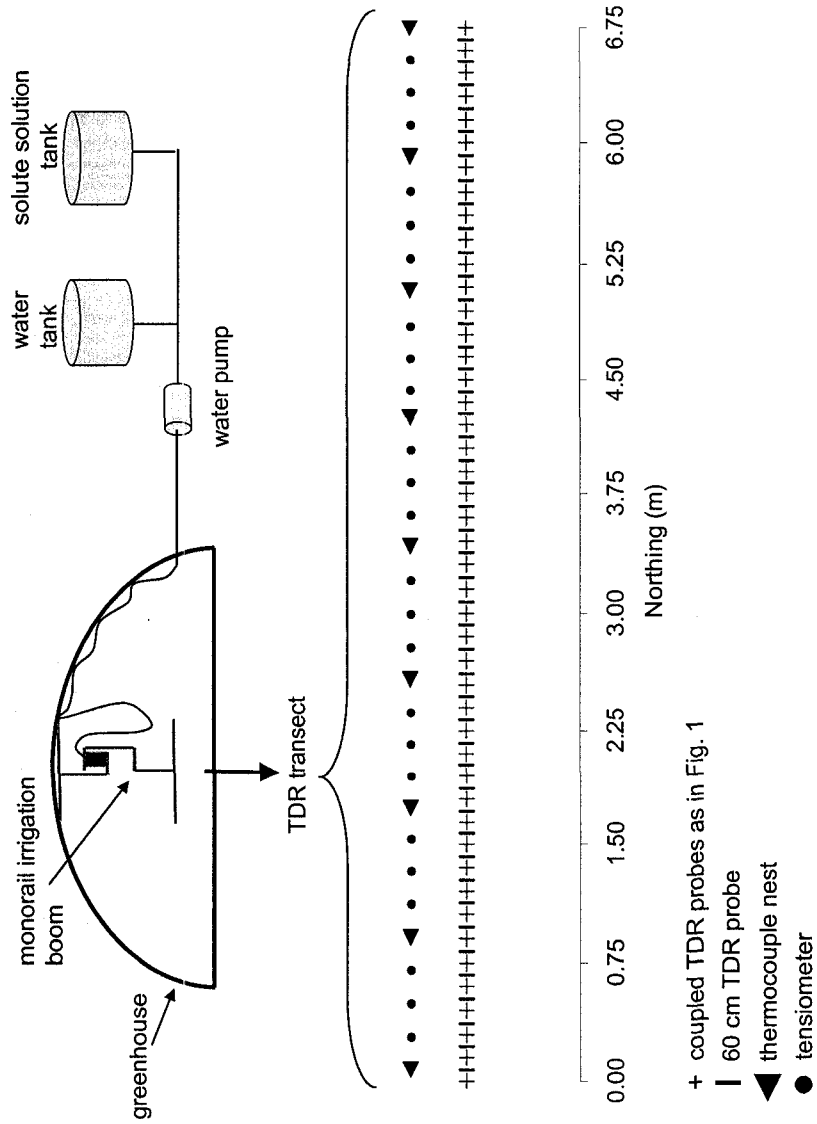
Figure 2-2: Schematic diagram of experimental setup for field water and solute transport experiments
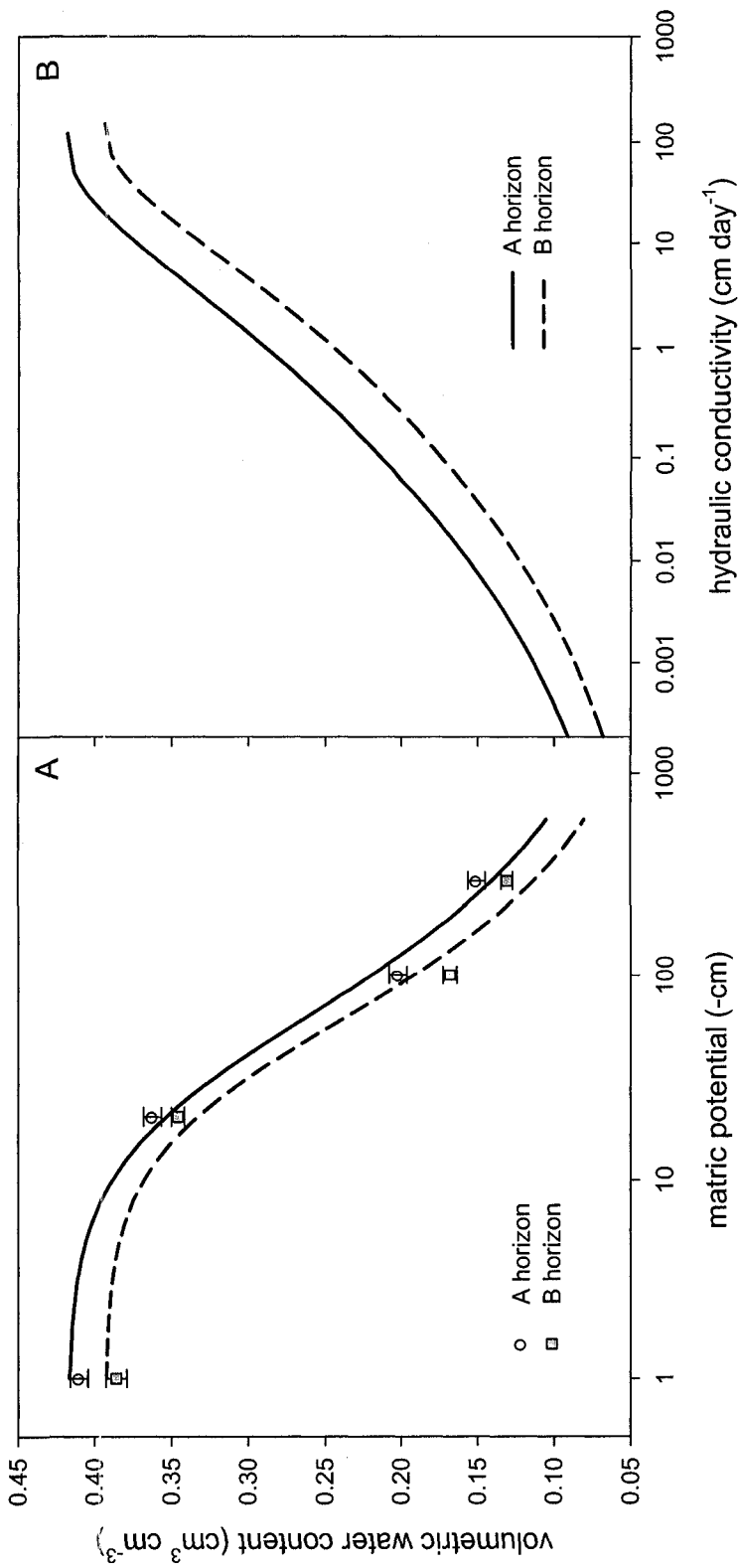
Figure 2-3: Average hydraulic properties of the A and B horizons: A) moisture retention curve measurements (symbols) and best fit van Genuchten model (lines); B) predicted hydraulic conductivity based on van Genuchten moisture retention parameters, measure saturated hydraulic conductivity, and Mualem capillary model.
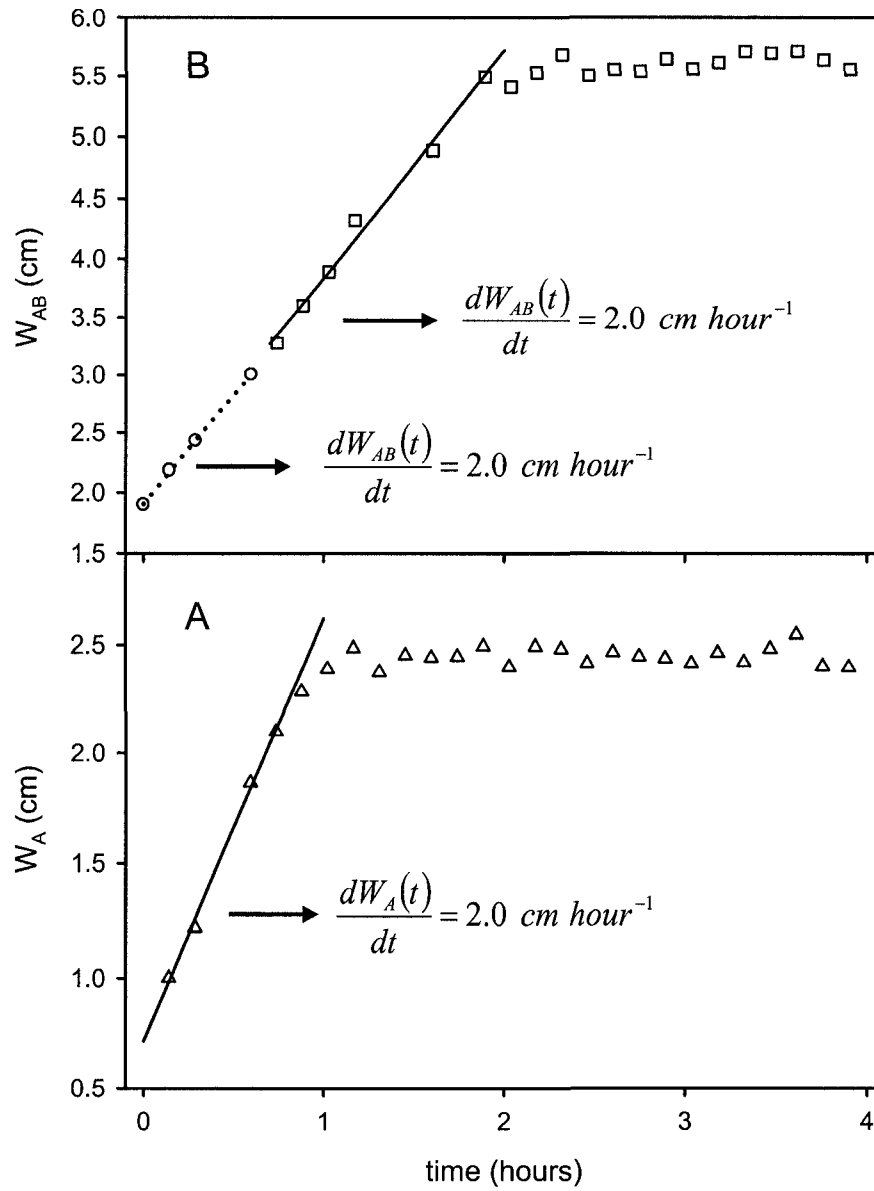
Figure 2-4: Soil water storage versus time during the 2.3 cm hour^{-1} laboratory experiment for A) the probe in the top medium sand layer ($L_A = 24.5$ cm); and B) the probe spanning both medium and fine sand layers ($L_{AB} = 45$ cm)
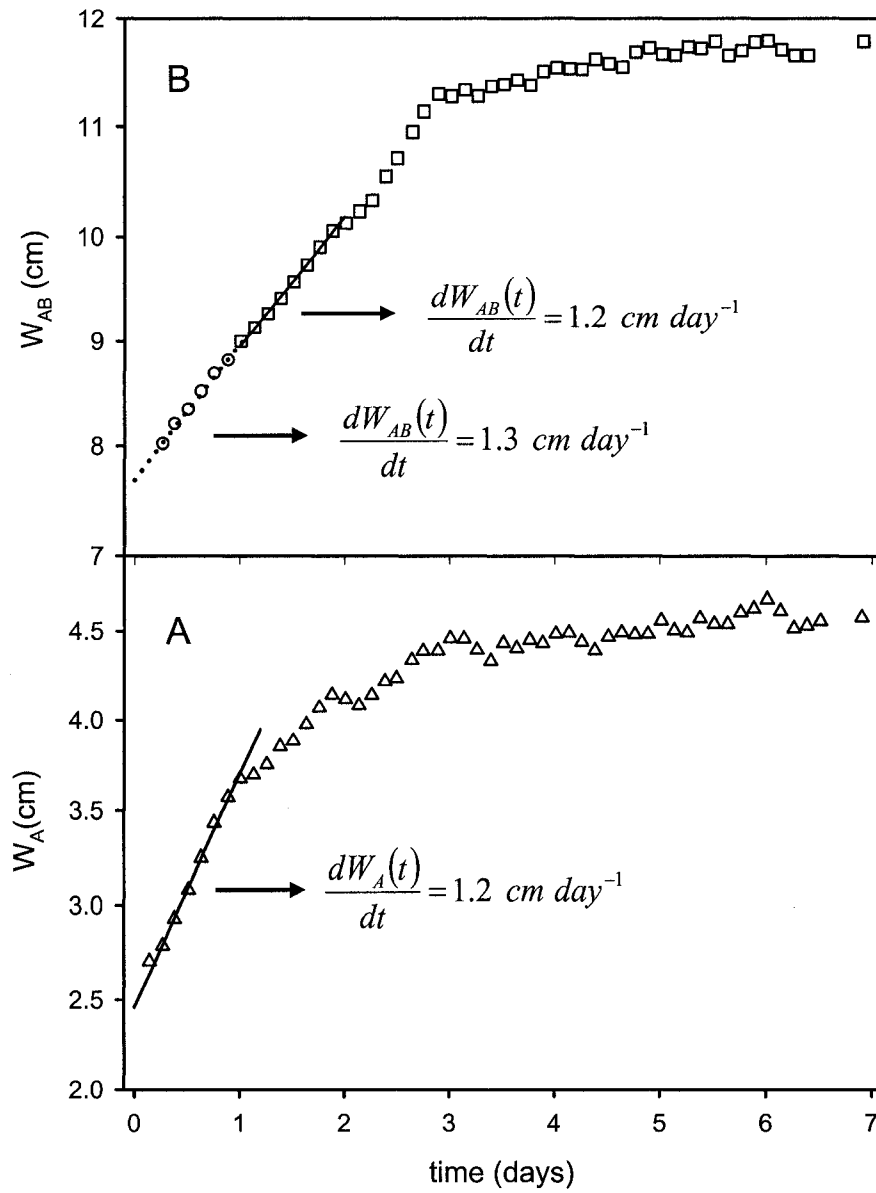
Figure 2-5: Example showing relatively little change in transient soil water flux across the horizon interface. Soil water storage versus time measured at the 0.15 m transect location during the 1.3 cm day^{-1} field experiment
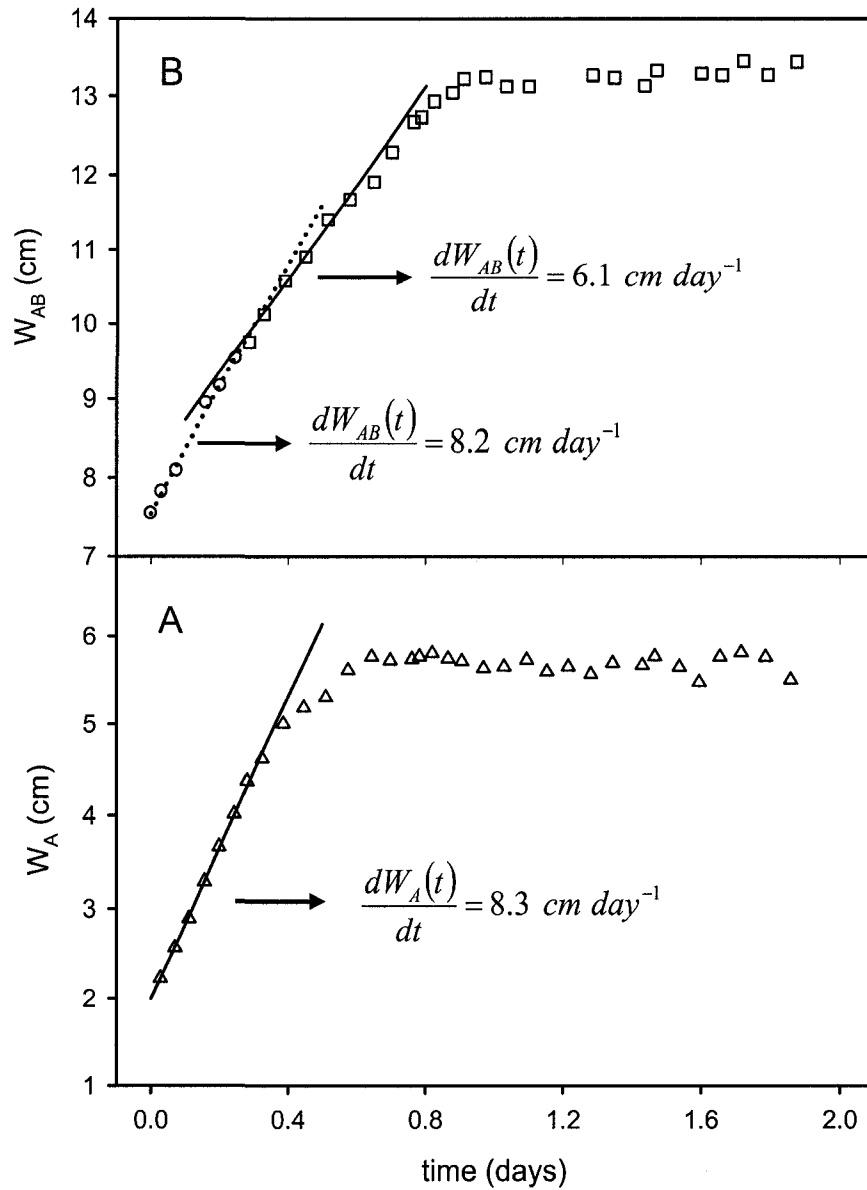
Figure 2-6: Example showing a measured decrease in water flux across the horizon interface. Soil water storage versus time measured at the 5.25 m transect location during the 7.0 cm day^{-1} field experiment
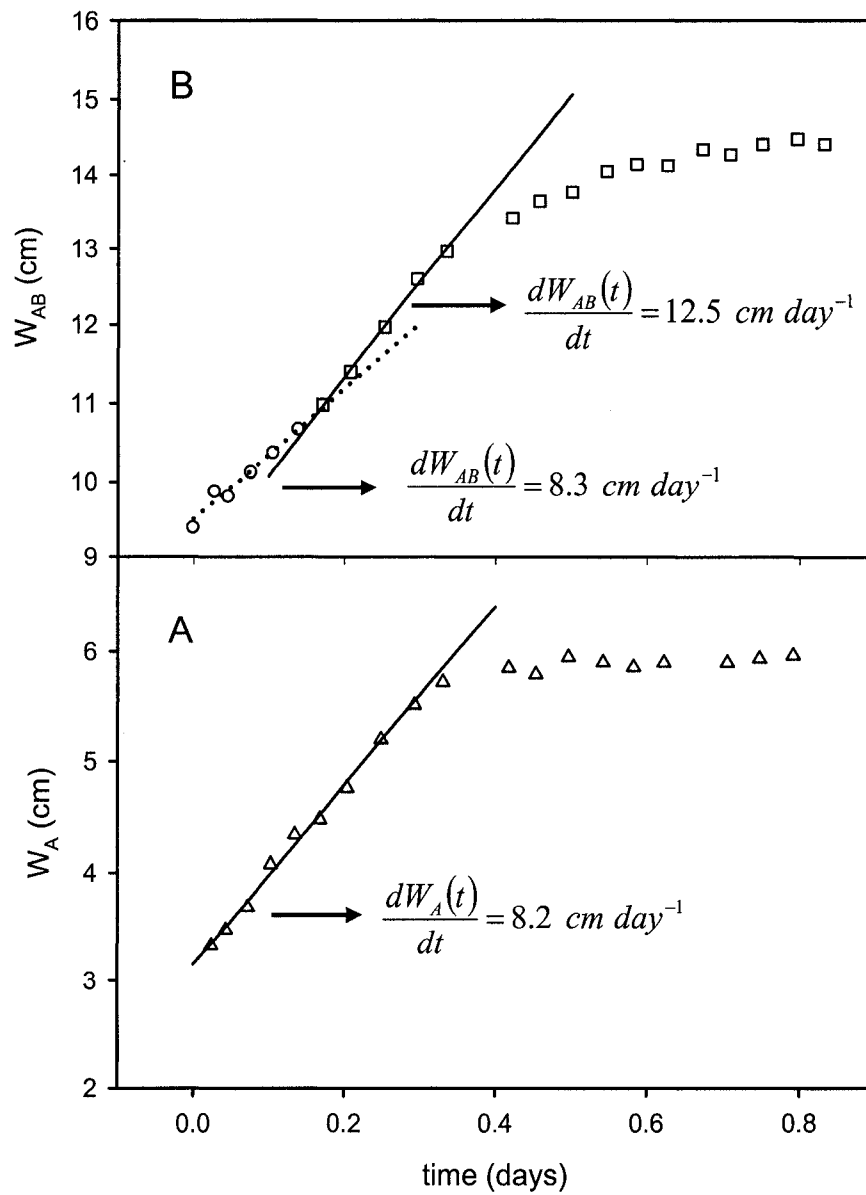
Figure 2-7: Example showing a measured water flux increase across the horizon interface. Soil water storage versus time measured at the 6.75 m transect location during the 10.6 cm day^{-1} field experiment
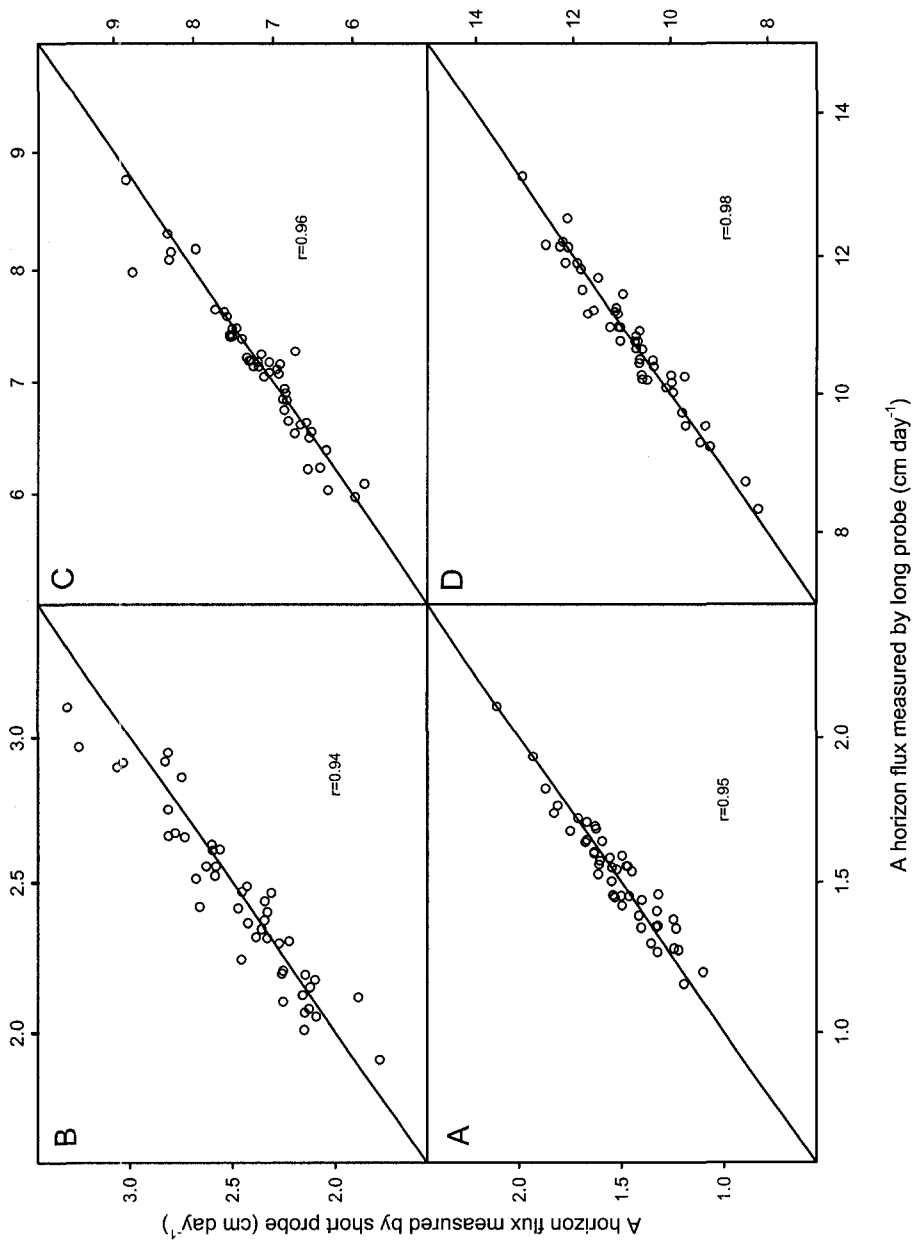
Figure 2-8: Comparison of A horizon local soil water flux measured with probes spanning A and B horizons (x axis) and probes spanning A horizons only (y axis) for A) 1.3 cm day^{-1}; B) 2.7 cm day^{-1}; C) 7.0 cm day^{-1} and D) 10.6 cm day^{-1} water application rates.

3. Measurement of the spatial pattern of local soil water flux above and below a soil horizon interface: II. Steady state, local soil water flux

3.1. Introduction

A number of solute transport experiments in field soils have shown that soil horizon interfaces are focal points for local three-dimensional flow and redistribution of water and solute mass (van Wesenbeeck and Kachanoski, 1994; Hammel et al., 1999; Ellsworth and Jury, 1991; and Dyck et al., 2005). Mechanisms for localized redistribution of mass at soil horizon interfaces vary, but these experimental observations suggest that soil horizon interfaces are hydrologically significant. The transport experiments of Ellsworth and Jury (1991) and van Wesenbeeck and Kachanoski (1994) examined the spatial distribution of resident solute concentration at a single time(s) under steady state conditions at one water application rate (2.0 cm day^{-1} and 4.0 cm day^{-1}, respectively). Solute transport for the experiments of Hammel et al. (1999) and Dyck et al. (2005) were subject to transient, environmental boundary conditions. It remains unclear whether the hydrologic response of soil horizon interfaces is sensitive to varying boundary conditions (i.e., different water application rates; steady state versus transient conditions).

Basic water flow and transport theory predicts the hydrological or transport response of the soil subject to external and internal boundary conditions, given state hydraulic and transport properties. External boundary conditions such as water application rate, depth to water table and solute mass additions or subtractions are imposed on the external boundaries of the soil domain. Internal boundary conditions, such as continuity of mass flux across soil horizon interfaces are imposed internally, or

inside the soil domain. Because direct measurement of state hydraulic and transport properties is often practically difficult and time consuming, soil hydraulic and transport properties are often identified using inverse procedures. Inverse procedures use the sensitivity of the hydraulic or transport response of the soil to the imposed boundary conditions to identify hydraulic and transport properties. Therefore, execution of water flow and solute transport experiments in field soils under varying, but well defined external boundary conditions is required to quantify the hydrologic response and influence of soil horizon interfaces, and test assumptions about internal boundary conditions.

Si and Kachanoski (2003) developed a TDR method to measure steady state local soil water flux in soils without distinct horizonation during solute transport under constant flux surface boundary conditions. The objective of this section is to extend the method of Si and Kachanoski (2003) to soils with distinct horizons/layers to measure the spatial pattern of steady state, local soil water flux above and below a soil horizon interface. This method, coupled with the transient method presented in Section 2, provides a means of quantifying the sensitivity of the hydrological influence of soil horizon interfaces to varying internal boundary conditions (i.e., transient versus steady state).

3.2   Theory

The method as presented here involves the same probe configuration presented in Fig. 2-1. TDR probes are inserted vertically in the soil such that one TDR probe spans the A horizon and a longer TDR probe spans the A and B horizons.

Ferré et al. (2000) showed that TDR-measured bulk electrical conductivity (EC) is a length-weighted average of the actual soil bulk EC spanned by the probe:

$$EC_{TDR} = K \frac{\sum_i L_i \sigma_{b,i}}{\sum_i L_i} \qquad [3\text{-}1]$$

where $\sigma_{b,i}$ is the actual bulk soil EC (dS m^{-1}) of soil segment i, L_i is the length of soil segment i (m), and K is a calibration constant depending on probe geometry. Under stable mineralogical conditions, σ_b is a function of the EC of the soil water, σ_w (dS m^{-1}), the EC of the soil minerals, σ_s (dS m^{-1}) and the volumetric water content (Ferre et al., 2000):

$$\sigma_b = \sigma_w \theta^n \phi^{m-n} + \sigma_s \qquad [3\text{-}2]$$

where θ is the volumetric water content (m^3 m^{-3}), ϕ is the soil porosity (m^3 m^{-3}), and m and n are fitting parameters. Under steady state flow conditions, θ remains constant, and, therefore, σ_b depends only on σ_w multiplied by a calibration constant, c:

$$\sigma_b = c\sigma_w + \sigma_s \qquad [3\text{-}3].$$

Many authors (e.g., Barthel et al., 1980) have shown that, for simple electrolytes, solute concentration is linearly proportional to σ_w:

$$\sigma_w = bC_w + a \qquad [3\text{-}4]$$

where C_w is the liquid solute concentration (kg m^{-3}) of the added electrolyte, b is a calibration constant, and a represents the background conductivity of the water in which the solute is dissolved. Substitution of Eq. [3-4] and [3-3] into Eq. [3-1] gives:

$$EC_{TDR} = \frac{\sum_i L_i \left[Kbc_i C_{w,i} + Kac_i + K\sigma_{s,i} \right]}{\sum_i L_i} \qquad [3\text{-}5],$$

which may be simplified to:

$$EC_{TDR} = \frac{\sum_i L_i \beta_i C_{w,i}}{\sum_i L_i} + \alpha \qquad [3\text{-}6]$$

where $\beta_i = Kbc_i$ and $\alpha = \sum_i L_i \big[ac_i K + K\sigma_{s,i}\big] \Big/ \sum_i L_i$ are lumped calibration constants.

Because steady state θ in each segment may vary (i.e., a layered soil), the β calibration constant is placed inside the summation in Eq. [3-6]. The α constant in Eq. [3-6] represents the TDR-measured EC of the soil without any added solute, and is proportional to the EC of the ambient soil solution and soil minerals. Thus, EC_{TDR} is linearly proportional to the length-weighted average liquid solute concentration in the soil water.

Now the theory will be specified for a soil during steady state solute transport with A horizon and B horizons. If we assume, the horizons are distinct soil segments, then, for a vertical TDR probe spanning both A and B horizons, Eq. [3-6] may be expressed as:

$$EC_{TDR,L} = \overline{C}_{w,A} \frac{L_A}{L} \beta_A + \overline{C}_{w,B} \frac{L_B}{L} \beta_B + \alpha \qquad [3\text{-}7]$$

where $EC_{TDR,L}$ is the TDR-measured EC of a probe spanning the lengths of the A and B horizons ($L = L_A + L_B$), L_A and L_B are the lengths of the A and B horizons, β_A and β_B are the calibration constants of the A and B horizons, and α represents the TDR measured EC without any added solute.

Now consider a steady state solute transport experiment with a step change of solute at $t = t_i$. Let $Z^*(t)$ represent the effective depth of the advancing solute front (m) as a function of time (Kachanoski et al., 1994). Now the TDR-measured EC is a function of

time because, as the solute front travels along the TDR rods, the average solute

concentration in the soil spanned by the TDR probe increases. At times when the solute

front is between the soil surface and the A/B horizon interface ($Z^*(t) < L_A$), it is only the

increase in solute mass in the A horizon that is influencing the TDR measured EC. The

solute concentration in the B horizon is zero, $\overline{C}_{w,B} = 0$. So, from Eq. [3-7]:

$$EC_{TDR,L}(t) = \frac{L_A}{L}\beta_A \overline{C}_{w,A}(t) + \alpha \qquad\qquad Z^*(t) < L_A \qquad\qquad [3\text{-}8],$$

where $\overline{C}_{w,A}(t)$ is the average applied solute concentration in the A horizon which can be

estimated by:

$$\overline{C}_{w,A}(t) = \frac{C_0 Z^*(t)\overline{\theta}_A}{\theta_A L_A} \qquad\qquad Z^*(t) < L_A \qquad\qquad [3\text{-}9],$$

where C_0 is the solute concentration in the applied solute step, $Z^*(t)$ is the effective depth

of the solute front (Kachanoski et al., 1994) $\overline{\theta}_A$ is the average volumetric water content in

the A horizon, and α is the TDR-measured EC prior to any solute being added to the soil.

Substitution of Eq. [3-9] into Eq. [3-8] yields:

$$EC_{TDR,L}(t) = C_0 \frac{Z^*(t)}{L}\beta_A + \alpha \qquad\qquad Z^*(t) < L_A \qquad\qquad [3\text{-}10].$$

When the effective depth of the solute front is equal to the depth of the A/B

horizon interface, $Z^*(t) = L_A$:

$$EC_{TDR,L}(t) = C_0 \frac{L_A}{L}\beta_A + \alpha \qquad\qquad Z^*(t) = L_A \qquad\qquad [3\text{-}11].$$

At times when the average depth of the solute front, $Z^*(t)$, is greater than L_A, but less than

L, it is only the advance of the solute front in the B horizon that changes the TDR-

measured EC:

$$EC_{TDR,L}(t) = C_0 \frac{L_A}{L} \beta_A + \frac{L_B}{L} \beta_B \overline{C}_{w,B} + \alpha \qquad\qquad L_A < Z^*(t) < L \qquad [3\text{-}12].$$

where $\overline{C}_{w,B}$ is the average concentration of applied solute in the B horizon, which can be estimated by:

$$\overline{C}_{w,B} = \frac{C_0 [Z^*(t) - L_A] \overline{\theta}_B}{L_B \overline{\theta}_B} \qquad\qquad L_A < Z^*(t) < L \qquad [3\text{-}13].$$

Substitution of Eq. [3-13] into Eq. [3-12] yields:

$$EC_{TDR,L}(t) = C_0 \frac{L_A}{L} \beta_A + C_0 \frac{Z^*(t) - L_A}{L} \beta_B + \alpha \qquad\qquad L_A < Z^*(t) < L \qquad [3\text{-}14].$$

Finally, when the solute front has passed the ends of the TDR rods:

$$EC_{TDR,L}(t)\Big|_{Z(t)>L} = C_0 \frac{L_A}{L} \beta_A + C_0 \frac{L_B}{L} \beta_B + \alpha \qquad\qquad Z^*(t) > L \qquad [3\text{-}15]$$

which is consistent with Eq. [3-7]. Equations [3-11] and [3-15] give the following useful calibration relationships.

$$\beta_A = \frac{L}{L_A C_0} \left[EC_{TDR,L}(t_{L_A}) - \alpha \right] \qquad\qquad [3\text{-}16]$$

$$\beta_B = \frac{L}{L_B C_0} \left[EC_{TDR,L}(t_L) - EC_{TDR,L}(t_{L_A}) \right] \qquad\qquad [3\text{-}17].$$

where $EC_{TDR,L}(t_{L_A})$ is the TDR-measured EC when $Z^*(t) = L_A$, and $EC_{TDR,L}(t_L)$ is the TDR measured EC when $Z^*(t) > L$.

Equations [3-10] and [3-14] can be used to derive expressions for the local steady state water flux during a step change solute transport experiment. Taking the first derivative with respect to time of Eq. [3-10]:

$$\frac{dEC_{TDR,L}(t)}{dt} = \frac{\beta_A C_0}{L} \frac{dZ^*(t)}{dt} \qquad\qquad Z^*(t) < L_A \qquad [3\text{-}18].$$

Solving Eq. [3-18] for $dZ^*(t)/dt$:

$$\frac{dZ^*(t)}{dt} = \frac{L}{\beta_A C_0} \frac{dEC_{TDR,L}(t)}{dt} \qquad Z^*(t) < L_A \qquad [3\text{-}19].$$

Substituting Eq. [3-16] into Eq. [3-19]:

$$\frac{dZ^*(t)}{dt} = \frac{L_A}{EC_{TDR,L}(t_{L_A}) - \alpha} \frac{dEC_{TDR,L}(t)}{dt} \qquad Z^*(t) < L_A \qquad [3\text{-}20].$$

Assuming that $dZ^*(t)/dt$ is equal to the solute velocity, v, and that water flux, q = vθ, multiplying Eq. [3-20] by the water content of the A horizon, yields an estimate of the steady state water flux through the A horizon:

$$q_{w|A,ss} = \frac{L_A \bar{\theta}_A}{EC_{TDR,L}(t_{L_A}) - \alpha} \frac{dEC_{TDR,L}(t)}{dt} \bigg|_{Z^*(t) < L_A} \qquad [3\text{-}21]$$

which is similar to Eq. [12] of Si and Kachanoski (2003). It should also be noted that:

$$\bar{t}_A = \frac{1}{EC_{TDR,L}(t_{L_A}) - \alpha} \frac{dEC_{TDR,L}(t)}{dt} \bigg|_{Z^*(t) < L_A} \qquad [3\text{-}22]$$

where $\bar{t}_A$ is an estimate of the mean solute travel time (days) through the A horizon. Thus Eq. [3-21] is equivalent to the steady state soil water storage along a streamtube in the A horizon divided by the mean solute travel time through the A horizon (in the same streamtube). In a similar manner, the following expressions can be derived to estimate steady state local soil water flux in the B horizon:

$$\frac{dEC_{TDR,L}(t)}{dt} = \frac{\beta_B C_0}{L} \frac{dZ^*(t)}{dt} \qquad L_A < Z^*(t) < L \qquad [3\text{-}23]$$

which is the first derivative with respect to time of Eq. [3-14]. Solving for $dZ^*(t)/dt$ and multiplying by the average steady state water content in the B horizon gives the following

expression to estimate steady state, local soil water flux along a stream-tube in the B

horizon:

$$q_{w|B,ss} = \frac{L_B \bar{\theta}_B}{EC_{TDR,L}(t_L) - EC_{TDR,L}(t_{L_A})} \left. \frac{dEC_{TDR,L}(t)}{dt} \right|_{L_A < Z(t) < L}$$ [3-24].

The presence of a short probe spanning only the A horizon can be used with the

long probe spanning both horizons to calculate $\bar{\theta}_A$ and $\bar{\theta}_B$. Equation [12] of Si and

Kachanoski (2003) can be used to obtain another estimate of local water flux in A

horizon using the short probe spanning only the A horizon.

3.3. Materials and Methods

Detailed descriptions of the laboratory and field experiments are given in Section

2.3. In the laboratory, proof-of-principle experiments were carried out on the layered, re-

packed column described in Section 2.3 after steady state conditions had been reached.

Instantaneous step increase or decrease of solute concentrations in the applied water were

achieved by replacing the manifold applying solute free water with another manifold

connected to a reservoir containing a 5 g L^{-1} $CaCl_2 \cdot 2H_2O$ solution and *vice versa*. In the

field experiments, time restrictions did not allow for both step increase and step decrease

solute applications, and only step decrease experiments were run. During the transient

experiments described in Chapter 2, the applied water had a constant concentration of

either KCl (1.0 g L^{-1}) or $CaCl_2$ (0.5 g L^{-1}). After steady state conditions had been reached

(i.e., at the end of the transient experiment), a step decrease in solute concentration in the

applied water was achieved by switching source tanks (see Fig. 2-2). The plumbing of

the water application system was then quickly flushed with the different source water and

then application of water to the soil surface continued.

68

All steady state field experiments were completed by September 2007. Following completion of the field experiments, a trench with dimension 7.5 by 0.60 by 0.60 m was dug centered on the TDR probe transect (see Fig. 2-2). At each probe location (every 7.5 cm along the transect), the depth to the A/B horizon interface was recorded at 20 cm on either side of the probe and between the probe rods to get a small scale three dimensional shape of the soil layer interface. The depths to the interface were used for the L_A and L_B parameters in Section 3-2.

As indicated in Eqs [3-6], [3-10] and [3-14], TDR-measured EC is linearly proportional to the average applied solute concentration, and the geometric calibration constant, K, is effectively lumped in with all other calibration constants. Therefore, for all laboratory and field experiments, EC_{TDR} was estimated as:

$$EC_{TDR,L} = \frac{1}{R_L - R_{cable}}$$

[3-25]

where R_L is the TDR-measured resistance (ohms, Ω) of the entire circuit (soil, cables and connectors), and R_{cable} (ohms, Ω) is the resistance of the cables and connectors. For all field and laboratory experiments, the TACQ BETA program (Evett, 2000), estimates R_L as:

$$R_L = 50\left(\frac{1 + \rho_\infty}{1 - \rho_\infty}\right)$$

[3-26]

where ρ_∞ is the reflection coefficient (dimensionless) or the ratio of incident and reflected wave (e.g., Giese and Tiemann, 1975; Lin et al., 2007). The cable resistance is also estimated with Eq. [3-26], but ρ_∞ is determined when the probe is short circuited

($\rho_{\infty,SC}$ in Lin et al., 2007). All $EC_{TDR,L}$ measurements were corrected for temperature according to Noborio et al. (2006).

Due to practical constraints, the length of the TDR probes spanning the A horizon was kept constant (25 cm) at all locations on the TDR transect (Fig. 2-2). In locations where the actual depth of the horizon interface was less than 25 cm, the water content measured by a 25 cm TDR probe will be influenced by the water content in the B horizon, resulting in a small error in steady state A horizon water content. To reduce these errors at locations where the depth of the A/B horizon interface was less than 25 cm, the following iterative algorithm was used to estimate A and B horizon steady state water content:

1) starting with the steady state water content measurements from a pair of 25-cm and 60-cm TDR probes, the initial estimate of B horizon steady state water content was set to the steady state water content in the 25 to 60 cm depth:

$$\overline{\theta}_{B,guess} = \frac{60\overline{\theta}_{60} - 25\overline{\theta}_{25}}{35}$$

2) $\overline{\theta}_{B,guess}$ was then used to calculate the initial guess of the A horizon water content:

$$\overline{\theta}_{A,guess} = \frac{25\overline{\theta}_{25} - (25 - L_A)\overline{\theta}_{B,guess}}{L_A}$$

3) $\overline{\theta}_{A,guess}$ was then used to update the B horizon estimate, $\overline{\theta}_B^{(1)} = \frac{60\overline{\theta}_{60} - L_A\overline{\theta}_{A,guess}}{60 - L_A}$

4) $\overline{\theta}_B^{(1)}$ was used to update the A horizon estimate, $\overline{\theta}_A^{(1)} = \frac{25\overline{\theta}_{25} - (25 - L_A)\overline{\theta}_B^{(1)}}{L_A}$

5) Steps 3) and 4) were repeated until the water content estimates didn't change within a specified tolerance

70

3.4.   Results and Discussion

Summaries of steady state, local soil water flux estimates for field and proof-of-principle laboratory experiments are presented in Table 3-1. It should be noted that steady state component of the 1.3 cm day^{-1} water application rate (see Table 2-1) was not completed due to equipment failure. Mass recovery (measured local water flux divided by applied water flux) estimates for the steady state experiments are comparable to those for the transient flux estimates in Section 2. For the field experiments, the coefficient of variations (CV) of the steady state local water flux patterns was generally higher than the transient patterns, ranging from 15 – 33% for the steady state estimates versus 9 – 19% for the transient estimates (Table 2-1). Si and Kachanoski (2003) indicated mass recoveries ranging from 90 – 110% for local, steady state water flux estimates, but CVs were consistent between transient and steady state flux estimates.

Measured steady-state average travel times to the end of the 60-cm TDR probe were 4.42 days, 2.05 days, and 1.32 days for the 2.7 cm day^{-1}, 7.0 cm day^{-1}, and 10.6 cm day^{-1} application rates respectfully. This is very similar to the predicted travel times based on piston flow and mass balance using the applied water application rates and the measured steady state water contents (i.e., 4.39 days, 1.85 days, and 1.33 days for the 2.7 cm day^{-1}, 7.0 cm day^{-1}, and 10.6 cm day^{-1} application rates, respectfully). This indicates that, on average, the assumption that the measured solute front velocity equals the water flow velocity seems valid for this soil. It also suggests that on average, the proposed methodology resulted in good mass balance during the steady state experiments as it did with the transient experiments. Examples of $EC_{TDR,L}(t)$ measured during the field and laboratory experiments are presented in Figures 3-1, 3-2, 3-3 and 3-4. Parameters used to

71

calculate the steady state, local water flux from these figures are summarized in Table 3-2. The medium and fine sand layers in the proof-of-principle experiment (Table 3-1, 3-2 and Fig. 3-1) respectively correspond to A and B horizons in all the equations in Section 3.2. For all experiments, steady state, local soil water flux was estimated by graphically estimating travel times to $z = L_A$ ($\bar{t}_A$) and $z = L$ ($\bar{t}_{AB}$) and the steady state soil water storage of the A and B horizons.

Under conditions where flow is forced to be 1-D as in the proof of principle laboratory experiments, $EC_{TDR,L}(t)$ displays a distinct change in slope ($dEC_{TDR,L}/dt$) which corresponds to the time when the solute front is moving past the end of the probe spanning only the top, medium sand layer (Fig. 3-1A and B). Therefore, it would seem that the probe spanning both the medium and fine sand layers (i.e., A and B horizons) is sensitive to solute transport in both layers. The intersection point of the best fit linear relationship through the early and late time $EC_{TDR,L}(t)$ measurements can be used to estimate the mean travel time through the top, medium sand layer ($\bar{t}_A$ in Fig. 3-1). This intersection point may also be used to estimate $EC_{TDR,L}(t_{L_A})$ in Eq. [3-21], but because of the relationship between $\bar{t}_A$ and $EC_{TDR,L}(t_{L_A})$ shown in Eq. [3-22], either $\bar{t}_A$ or $EC_{TDR,L}(t_{L_A})$ can be used to calculate the steady state, local soil water flux through the A horizon. The intersection point between the best fit line through the late time $EC_{TDR,L}(t)$ measurements and final TDR measured EC represent to total travel time through the A and B horizons ($\bar{t}_{AB}$ in Fig. 3-1).

Despite the change in $dEC_{TDR,L}/dt$ shown in Fig. 3-1B at the time the solute front enters the B horizon (t = 1.0 – 1.1 hours), the water flux estimates for both layers are very

close for both step increase and decrease solute applications (Tables 3-1 and 3-2).

Equations [3-18] and [3-23] indicate that $dEC_{TDR,L}/dt$ is sensitive to the calibration

coefficients of the separate horizons, β_A and β_B, and the effective solute velocity,

$dZ^*(t)/dt$. In this case, $\overline{\theta}_A < \overline{\theta}_B$, and as a result, the solute velocity, $dZ^*(t)/dt$, through

the B horizon would decrease relative to the A horizon under constant flux conditions.

Since $dEC_{TDR,L}/dt$ is larger through the underlying fine sand layer (late time $EC_{TDR,L}(t)$

measurements in Fig. 3-1A, B), but the water flux is essentially constant across the layer

boundary, the calibration constant β_B must be greater β_A. This is consistent with the

higher water content of the underlying fine sand layer.

Examples of $EC_{TDR,L}(t)$ measure during field experiments (Figures 3-2 and 3-3)

also show a change in slope as the solute front passed from the A horizon into the B

horizon. In the field, however, flow was not forced to be one dimensional as in the proof-

of-principle column experiments (Fig. 3-1). In other words, in the field, steady state,

local soil water flux may not be continuous across soil horizon interfaces. Furthermore,

the differences in texture, organic matter and porosity between horizons are likely greater

in the field which effect β_A and β_B in addition to volumetric water content (Eqs. [3-2]

and [3-5]). Thus, even when the average volumetric water contents of the A and B

horizons and soil water fluxes through the A and B horizons are similar for a single

location, there is still a measurable change in $dEC_{TDR,L}/dt$ as the solute front crosses the

soil horizon interface (Fig. 3-2). The advantage to measuring a change in $dEC_{TDR,L}/dt$ is

that the intersection point of the best fit lines through the early (squares in Figs. 3-2 and

3-3) and late (triangles in Figs. 3-2 and 3-3) $EC_{TDR,L}(t)$ measurements can be used to

estimate the mean travel time through the A horizon ($\bar{t}_A$ in Figs. 3-2 and 3-3).

Figures 3-1, 3-2 and 3-3 show examples with distinct changes in $dEC_{TDR,L}/dt$ as

the solute front crosses the soil horizon interface due to changes in either β, $dZ^*(t)/dt$ or

$q_{w,ss}$. A different type of behavior in $EC_{TDR,L}(t)$ measurements was observed at some

locations during the field experiments (e.g., Figure 3-4). In this example, the depth to

A/B horizon interface (L_A) was observed to be 26 cm. The length of the probe used to

measure $EC_{TDR,L_A}(t)$ is 25 cm (represented by circles in Fig. 3-4), suggesting that $\bar{t}_A$

measured with this probe is very close to the actual travel time through the 26 cm thick A

horizon. Observations from the probe spanning both A and B horizons, however, show a

noticeable change in $dEC_{TDR,L}/dt$ at times less than $\bar{t}_A$. Closer inspection of the 25 cm

probe observations also show a slight change in slope prior to $\bar{t}_A$. Observations from this

probe showed a similar pattern for the 2.7 cm day^{-1} experiment, but not for the 10.6 cm

day^{-1} experiment. The number of probes displaying this type of pattern varied from 10

for the 10.6 cm day^{-1} experiment to 17 for the 7.0 cm day^{-1} experiment.

Possible mechanisms for the type of behavior shown in Fig. 3-4 are: 1) the depth

of the layer interface estimated by direct observation of change in color between A and B

horizons is incorrect; or 2) water and solute from adjacent areas are moving laterally into

the sampling volume of the TDR probe (i.e., localized three-dimensional flow at the soil

horizon interface). The lack of water flux continuity across the interface at this site

during transient conditions (Section 2), and the lack of consistency in this type of

behavior across different water application rates suggests that flux-dependent localized

three dimensional flow may be the more plausible explanation. This is consistent with previous experimental observations by van Wesenbeeck and Kachanoski (1994) and Ellsworth and Jury (1991),

Figures 3-1, 3-2, 3-3 show example locations where the estimates of the mean travel time through the A horizon made with independent observations from the 25- and 60-cm probes are similar. The confounding effects of localized three-dimensional flow shown in Fig. 3-4, result in two different estimates of $\bar{t}_A$ from the 60-cm probe, one of which is closer to the $\bar{t}_A$ estimated with the 25-cm probe. Comparing estimates of mean travel time through the A horizon made with the 25- and 60-cm probes become more complicated for locations where the observed depth of the soil horizon interface (L_A) is significantly different than 25 cm. In such cases, $\bar{t}_A$ estimated with the 25-cm probe must be corrected. The actual depth of the horizon interface varied from 15 to 35 cm. In locations where the actual depth of the interface was greater than 25 cm, $\bar{t}_A$ estimated with the 25-cm probe was extrapolated to the actual depth of the interface, L_A by assuming the effective solute velocity stayed constant until the solute front reached the depth of the interface. For locations where the depth of the horizon interface was less than 25 cm, distinct changes in $dEC_{TDR,L}/dt$ from the 25-cm probe observations were confounded by solute dispersion; that is, the leading edge of the solute front started to move below 25 cm before, or shortly after, any changes in $dEC_{TDR,L}/dt$ were observable. Thus, like those locations where $L_A > 25$ cm, the best solution was to adjust $\bar{t}_A$ estimated with the 25 cm probe to the actual depth of the interface L_A assuming the solute velocity was constant over the 25-cm depth.

Steady state, local soil water flux estimates calculated using adjusted $\bar{t}_A$ values

from the 25-cm probes are compared to those calculated with estimates of $\bar{t}_A$ observed

with the 60-cm probes in Fig. 3-5. For all three water application rates, Pearson

correlation coefficients showed a highly significant relationship between the two

independent estimates ($0.76 \leq r \leq 0.91$; $P < 0.001$; Fig. 3-5). It is interesting to note that

the correlation between the two steady state, local A horizon flux estimates decreased

with increase water application rates. This may be due to increasing uncertainty with

increasing solute velocity when adjusting $\bar{t}_A$ estimated with the 25-cm probes, or an

increase in very local scale spatial variability of soil water flux/solute travel times.

A correlation matrix for the paired transient and steady state soil water flux

estimates, the steady-state soil water contents, and measured horizon interface depth is

presented in Table 3-3. As for the transient experiments (Section 2), steady state A

horizon water fluxes are significantly correlated to each other across all water application

rates. Steady state B horizon fluxes are also significantly correlated to each other across

all water application rates.

Spatial patterns in steady state soil water contents within soil horizons were very

consistent ($r > 0.94$) for all water application rates (Fig. 3-7). Also, most transient A

horizon fluxes are significantly positively correlated to steady state A horizon fluxes

(Table 3-3), and most transient B horizon fluxes are significantly positively correlated to

steady state B horizon fluxes across all water application rates (Table 3-3).

The correlation between steady state A and B horizon local soil water flux has

changed from positive under transient conditions to negative under steady state

conditions. The strength of the negative correlation is dependent on the average water

flux with r = -0.51 (P<0.001), r = -0.39 (P<0.001), and r = -0,28 (P<0.01), for the 2.7 cm day^{-1}, 7.0 cm day^{-1}, and 10.6 cm day^{-1} water applications rates, respectively. Therefore, it would seem that the hydrological influence of the soil horizon interface is also a function of the how conditions at the interface change as average flow increases. The negative correlation between A and B horizon steady state, local soil water fluxes indicates that the A/B horizon interface would not only disrupt the continuity of steady state vertical mass flux across the interface, but it would reverse some of the influence of the spatial variability of convective flow in the A horizon on the variance of larger scale water/solute travel times at depths below the interface. Locations with relatively higher local water flux approaching the interface would tend to have relative lower local water flux below the interface and *vice versa*.

Since the physics governing the flow of water with an advancing wetting front (transient infiltration) are different than after wetting and steady state conditions, it is reasonable to expect that the influence of the interface might be quite different under transient versus steady state flow conditions. Under transient conditions, it is likely the interaction between a spatially variable wetting front, variable hydraulic gradients and a spatially variable soil horizon interface affecting the continuity and spatial pattern of vertical water flux. Under steady state conditions, there is no sharp advancing wetting front creating significant local 3-D hydraulic gradients, and the influence of hydraulic property heterogeneity on water flow can be different or opposite (e.g., areas with water entry capillary effects that would initially impede/re-direct an advancing wetting front are areas of higher conductivity after wetting).

The similarity in average steady state soil water contents and average soil hydraulic properties (Table 2-1) in A and B horizon suggests that the primary influence of the horizon interface will be expressed through (1) the spatial covariance relationships between the hydraulic properties above and below the horizon interface, and (2) the spatial covariance relationships between the horizon interface shape parameters (depth, curvature) which could accentuate or buffer the effects of any difference/similarities in local hydraulic properties at or across the interface. These spatial covariant relationships are likely scale-dependent, so the correlations need to be examined and partitioned as a function of spatial scale to better understand the influence of the horizon interface. Thus, the remaining section focuses on using advance spatial statistical methods to quantify the scale (spatial) dependent covariant relations to understand and develop a conceptual model to explain the changes in the spatial patterns of water flux and the different flux-dependent correlations between the measured A and B horizon fluxes under transient and steady state boundary conditions.

3.5. Conclusions

The analysis of the data from the steady state and transient experiments indicate that the proposed methods for measuring transient and steady state soil water flux across a soil horizon interface/boundary are sensitive, accurate, and repeatable. This is illustrated by

1. Measurements of the spatial patterns of transient soil water fluxes within soil horizons (A, B) were significantly correlated across all applied water applications, and very highly correlated with independent measurements (short versus long TDR probes) at the same water application rates.

2. Measurements of the spatial patterns of steady state soil water fluxes and steady state soil water contents within soil horizons (A, B) were significantly correlated across all applied water applications, and very highly correlated with independent measurements (short versus long TDR probes) at the same water application rates

3. There was very good mass balance (applied water application rate versus average measured water flow rates) for both transient and steady state measurements.

The influence of the horizon interface on spatial patterns on water flow above and below the interface was significant, dependent of average water flux, and different under transient versus steady state flow conditions. Since average hydraulic properties in the A and B horizon are similar, the influence of the interface is attributed to the spatial covariance relationships of hydrologic properties within and between horizons, and their joint spatial covariance with the shape of the horizon interface

3.6. References

Barthel, J., F. Feuerlein, R. Neueder, and R. Wachter. 1980. Calibration of conductances cells at various temperatures. J. Solution Chem. 9:189-199.

Dyck, M. F., R. G. Kachanoski, and E. de Jong. 2005. Spatial variability of long-term chloride transport under semiarid conditions: Pedon scale. Vadose Zone J. 4:915-923.

Ellsworth, T. W., and W. A. Jury. 1991. A three-dimensional field study of solute transport through unsaturated, layered, porous media: 2. Characterization of vertical dispersion. Water Resour. Res. 27:967-981.

Evett. S. R. 2000. The TACQ computer program for automatic time domain reflectometry measurements: I. Design and operating characteristics. Trans. ASAE 43:1939-1946.

Ferré, P. A., D. L. Rudolph, and R. G. Kachanoski. 2000. Identifying conditions amenable to the determination of solute concentrations with time domain reflectometry. Water Resour. Res. 36:633-636.

Giese, K., and R. Tiemann. 1975. Determination of the complex permittivity from thin sample time domain reflectometry improved analysis of the step response waveform. Adv. Mol. Rel. Proc. 7:45-59

Hammel, K., J. Gross, G. Wessolek, and K. Roth. 1999. Two-dimensional Simulation of Bromide Transport in a Heterogeneous Filed Soil with Transient Unsaturated Flow. Eur. J. of Soil Sci. 50:633-647.

Kachanoski, R. G., J. L. Thony, M. Vauclin, G. Vachaud, and R. Laty. 1994. Measurement of solute transport during constant infiltration from a point source. Soil Sci. Soc. Am. J. 58:304-309.

Lin, C. P., C. C. Chung, and S. H. Tang. 2007. Accurate time domain reflectometry, measurement of electrical conductivity accounting for cable resistance and recording time. Soil Sci. Soc. Am. J. 71:1278-1287.

Noborio, K., R. G. Kachanoski, and C. S. Tan. 2006. Solute transport measurement under transient field conditions using time domain reflectometry. Vadose Zone J. 5:412-418.

Si, B. C., and R. G. Kachanoski. 2003. Measurement of local soil water flux during field solute transport experiments. Soil Sci. Soc. Am J. 67:730-736.

van Wesenbeeck, I. J., and R. G. Kachanoski. 1994. Effect of variable horizon thickness on solute transport. Soil Sci. Soc. Am. J. 58:1307-1316.

Table 3-1: Summary of local soil water flux estimates under quasi steady solute transport

Experiment	Application rate	Measured flux		$\bar{\theta}_{ss}$ (cm^3 cm^{-3})‡	Mass recovery (%)	Standard deviation† (cm day^{-1})	Coefficient of variation† (%)
		Layer	Estimate				
Laboratory disturbed column	2.3 cm hour^{-1}	medium	2.3 cm hour^{-1}	0.10	100		
		fine	2.1	0.14	91		
	6.8	medium	6.4	0.11	94		
		fine	6.5	0.17	96		
	13.6	medium	13.5	0.12	99		
Step increase		fine	13.3	0.21	98		
	2.3	medium	2.1	0.10	91		
		fine	2.0	0.14	87		
	6.8	medium	6.9	0.11	101		
		fine	7.0	0.17	103		
	13.6	medium	13.5	0.12	99		
Step decrease		fine	13.3	0.21	98		
Field step decrease only	2.7 cm day^{-1}	A horizon	2.7 cm day^{-1}	0.20	100	0.5	19
		B horizon	3.1	0.20	115	1.0	33
	7.0	A horizon	6.6	0.22	94	1.0	15
		B horizon	6.5	0.22	93	1.5	24
	10.6	A horizon	10.8	0.24	101	1.8	17
		B horizon	11.4	0.23	108	2.9	25

† Laboratory experiments were not replicated

‡ Steady state water content

Table 3-2: Summary of parameters for steady state, local soil water flux calculations in Figures 3-1 to 3-4

Figure	$\bar{\theta}_A$ (cm³ cm⁻³)	$\bar{\theta}_B$ (cm³ cm⁻³)	L_A (cm)	L (cm)	L_B (cm)	$\bar{t}_A$	$\bar{t}_{AB}$	$\bar{t}_B = \bar{t}_{AB} - \bar{t}_A$	$q_{w|A,ss}$	$q_{w|B,ss}$
3-1 A†	0.095	0.135	24.5	45.7	21.2	1.04	2.44	1.4	2.3	2.1
3-1 B†	0.095	0.135	24.5	45.7	21.2	1.13	2.57	1.44	2.1	2.0
3-2‡	0.23	0.23	27	60	33	1.94	4.16	2.22	3.2	3.4
3-3‡	0.25	0.27	27	60	33	0.54	1.24	0.70	12.5	12.7
3-4‡	0.20	0.21	26	60	34	1.03	2.17	1.14	6.0	6.3

† Time units are in hours and flux units are cm hour⁻¹

‡ Time units are days and flux units are cm day⁻¹

82

Table 3-3: Correlation matrix for paired transient and steady state, local soil water flux estimates

	$q_{w|A,tr}(2.7)$	$q_{w|B,tr}(2.7)$	$q_{w|A,tr}(7.0)$	$q_{w|B,tr}(7.0)$	$q_{w|A,tr}(10.6)$	$q_{w|B,tr}(10.6)$	$q_{w|A,ss}(2.7)$	$q_{w|B,ss}(2.7)$	$q_{w|A,ss}(7.0)$	$q_{w|B,ss}(7.0)$	$q_{w|A,ss}(10.6)$	$q_{w|B,ss}(10.6)$
$q_{w|A,tr}(2.7)$	1											
$q_{w|B,tr}(2.7)$	0.25	1										
$q_{w|A,tr}(7.0)$	0.63***	0.12	1									
$q_{w|B,tr}(7.0)$	0.23	0.62***	0.29*	1								
$q_{w|A,tr}(10.6)$	0.66***	0.13	0.77***	0.21	1							
$q_{w|B,tr}(10.6)$	0.21	0.41**	0.35*	0.64***	0.2	1						
$q_{w|A,ss}(2.7)$	0.49***	0.17	0.34*	0.02	0.46**	0.05	1					
$q_{w|B,ss}(2.7)$	-0.04	0.26	0.01	0.33*	0.01	0.23	-0.44**	1				
$q_{w|A,ss}(7.0)$	0.27	-0.18	0.33*	-0.1	0.42**	-0.02	0.58***	-0.21	1			
$q_{w|B,ss}(7.0)$	0.32*	0.51***	0.23	0.58***	0.21	0.45**	-0.12	0.52***	-0.3*	1		
$q_{w|A,ss}(10.6)$	0.3*	0.06	0.46**	0.15	0.4**	0.22	0.55***	-0.13	0.51***	-0.16	1	
$q_{w|B,ss}(10.6)$	0.22	0.35*	0.13	0.49***	0.14	0.41*	-0.1	0.56***	-0.09	0.67***	-0.23	1

* Significant at the 0.05 probability level
** Significant at the 0.01 probability level
*** Significant at the 0.001 probability level

83
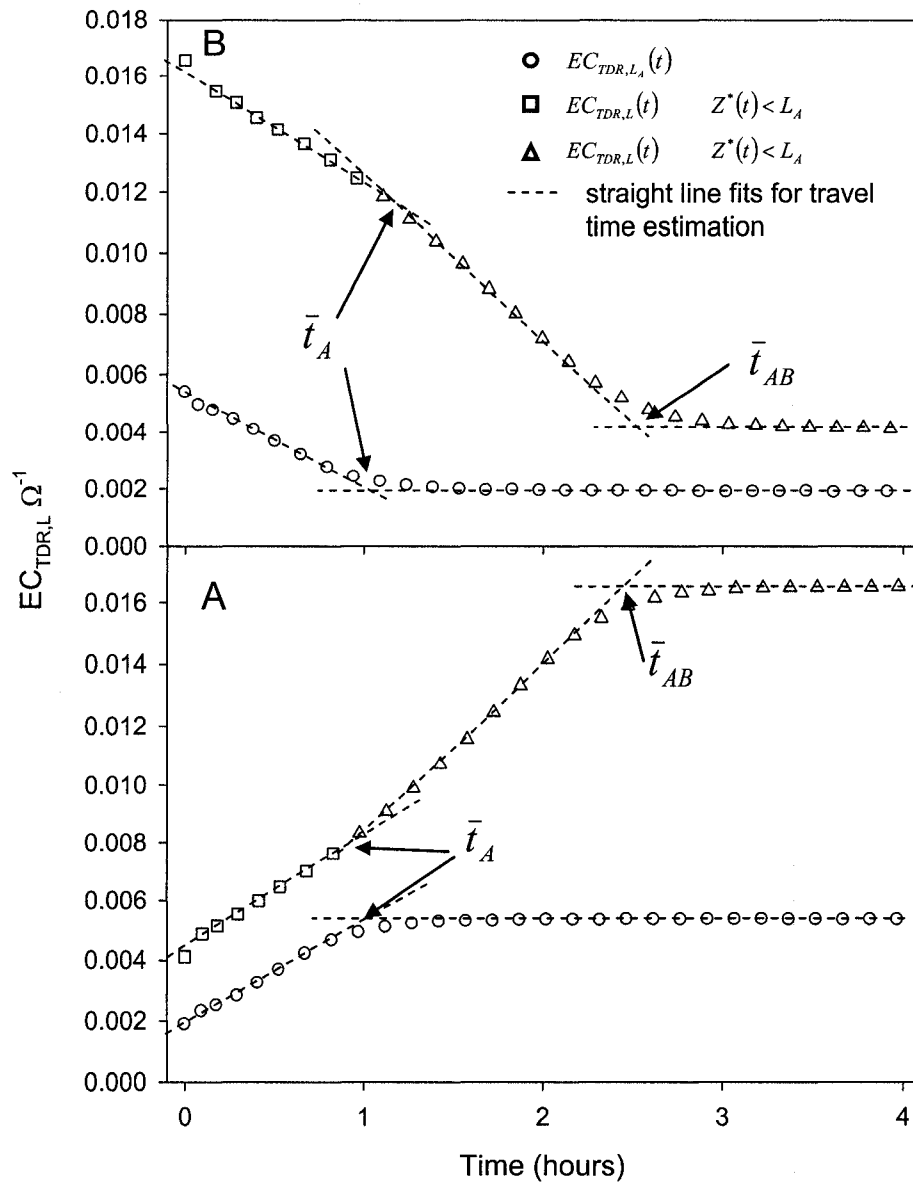
Figure 3-1: TDR measured EC versus time during the 2.3 cm hour^{-1} laboratory experiment for step increase (A) and step decrease (B) solute applications
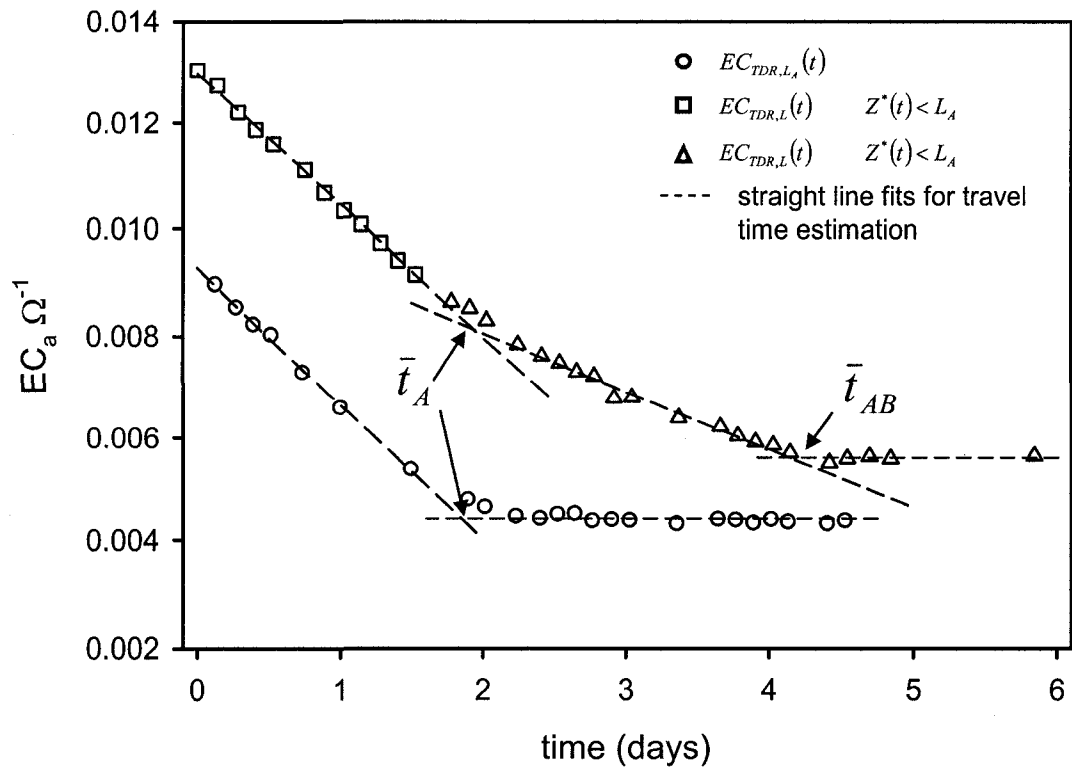
Figure 3-2: TDR measured EC versus time at the 0.75 m transect location during the 2.7 cm day^{-1} field experiment.
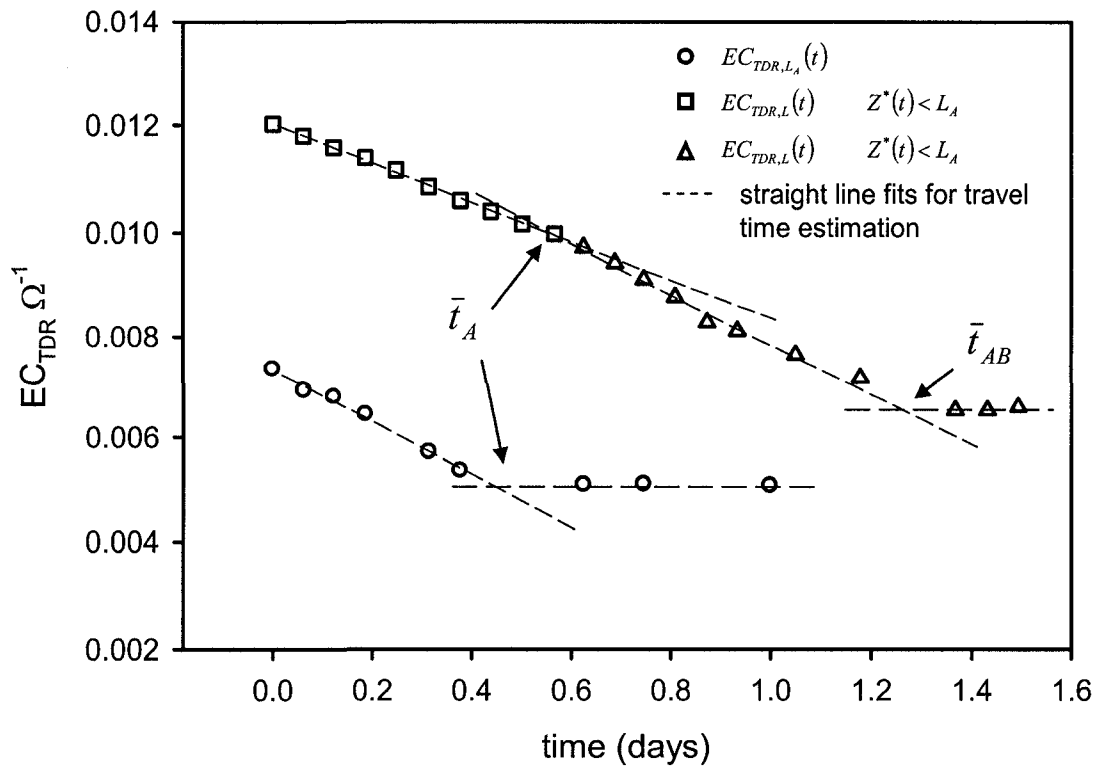
Figure 3-3: TDR measured EC versus time at the 6.60 m transect location during the 10.6 cm day^{-1} field experiment.
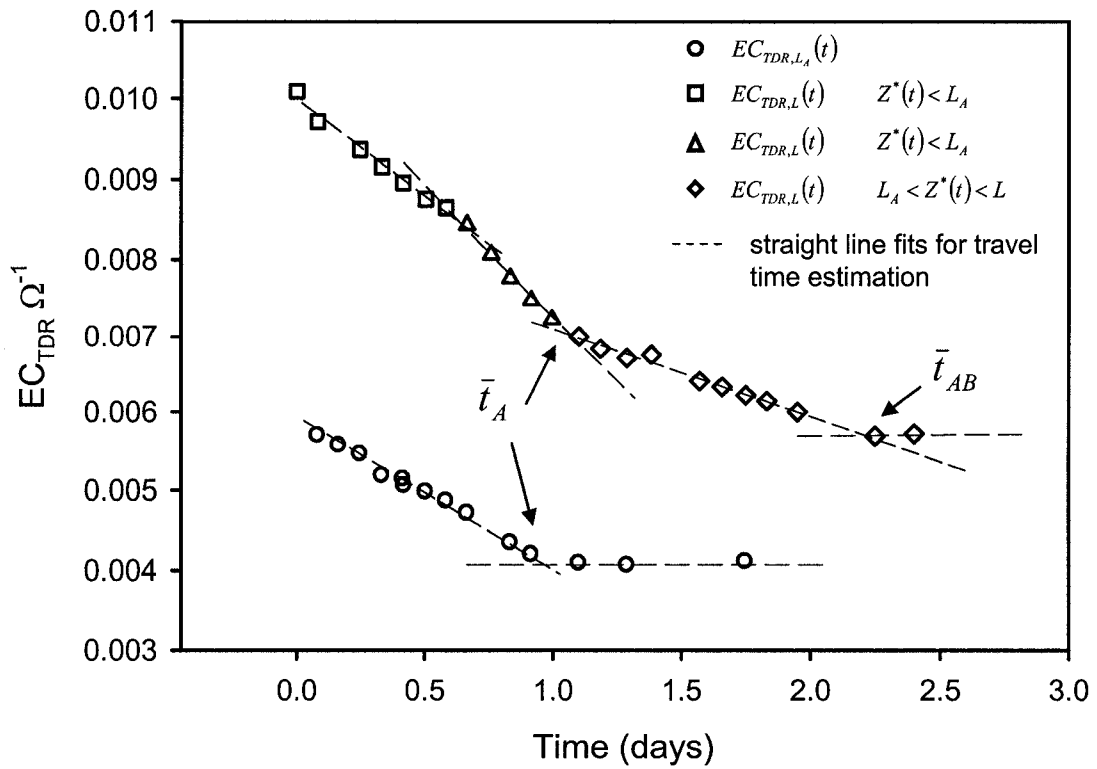
Figure 3-4: TDR measured EC versus time at the 3.75 m transect location during the 7.0 cm day^{-1} field experiment.
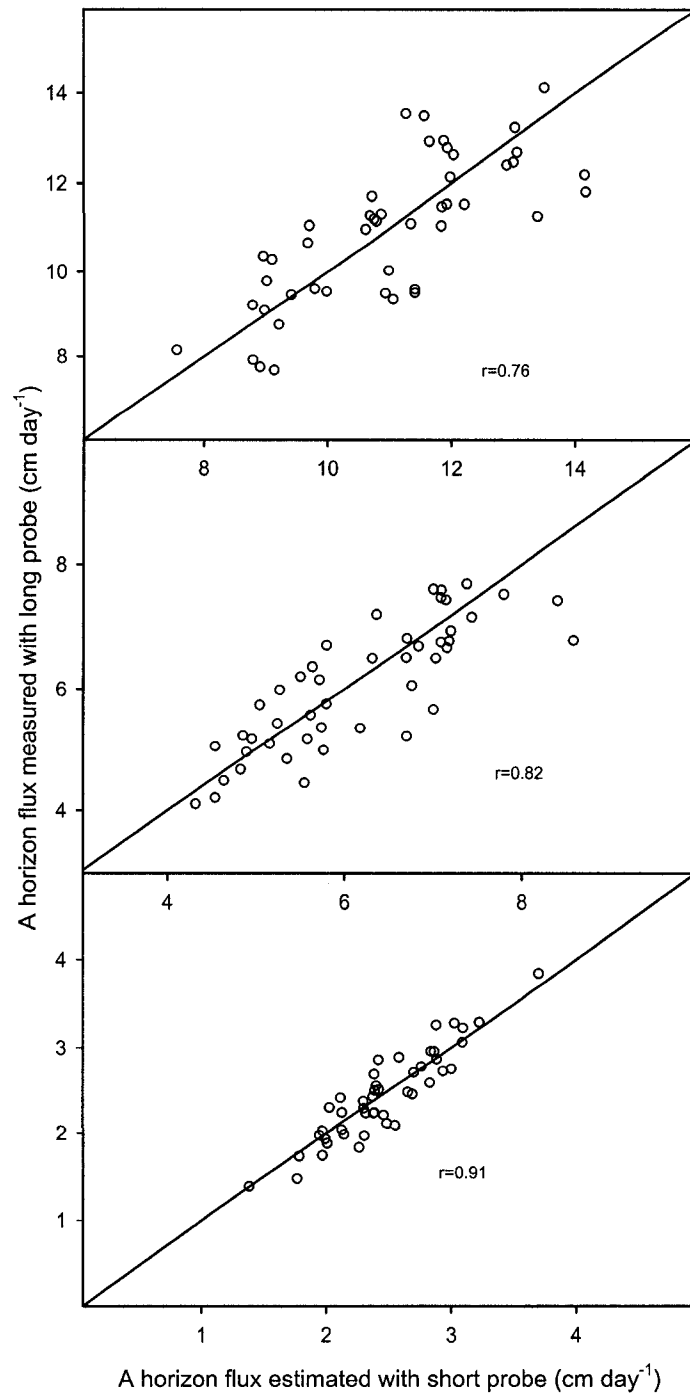
Figure 3-5: Comparison of A horizon flux estimates calculated with the short probes spanning only the A horizon, and long probes, spanning both the A and B horizon.
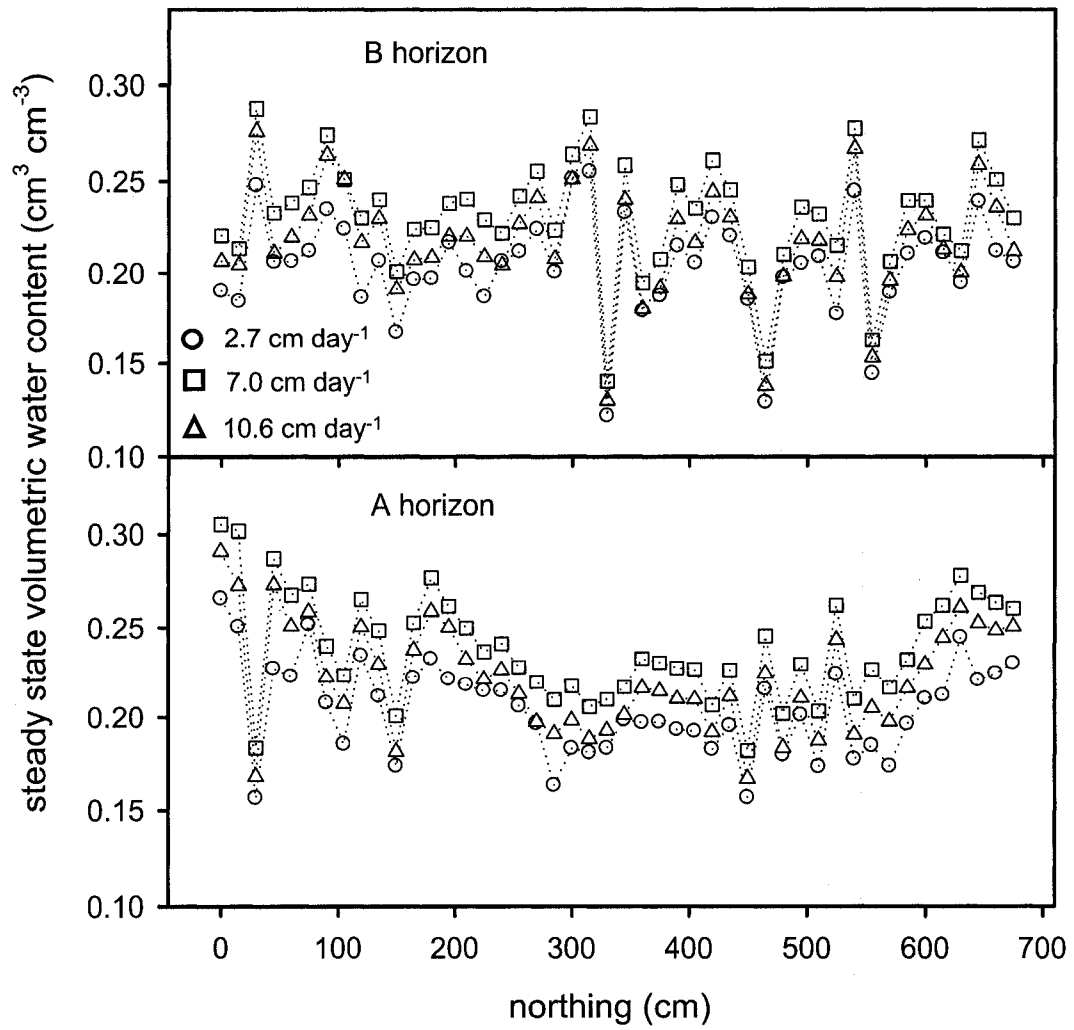
Figure 3-6: Summary of the spatial pattern of steady state volumetric water content for the three solute transport experiments

4. Spatial scale dependent variability of local soil water flux above and below a soil horizon interface

4.1. Introduction

Investigation of the influence of the spatial variability and spatial structure of soil hydraulic properties on water flow and solute transport has been the focus of much of the theoretical development of water flow and solute transport in layered soils over the past 20 years (e.g., Yeh et al., 1985a,b,c; Russo and Dagan, 1991, Roth and Hammel, 1996; and Ursino et al., 2000). Due to practical constraints associated with field experiments, the majority of the investigations have been carried out in simulated porous media using simulation models. While the convenience and utility of such simulations should not be overlooked, ultimately, investigation of water flow and solute transport processes in field soils using experimental measurements is required for theory validation and to support decisions about the direction of future research. Furthermore, the practical constraints associated with field experiments have also led to a variety of innovative and novel field methods to measure and develop theory of transport processes in field soils (e.g., Si and Kachanoski, 2003; Kachanoski et al., 1994 ; Noborio et al., 2006; Clothier et al., 1992)

In field soils, horizons develop over time as a result of pedogenic processes. The result is a soil profile with spatially-variable horizon dimensions. The nature of this variability is included in the most basic unit of the soil profile, the pedon. The pedon is defined as the minimum three-dimensional unit of soil required to account for the variability in the dimensions of the soil horizons. Because soil horizons are visually distinct, they are often assumed to have different average hydraulic properties and are sampled accordingly. Soil horizons, however, are most often developed from the same

90

parent material over the course of soil genesis. Initial heterogeneities in the original

parent material likely interact with pedogenic processes in a complex way during soil

genesis, resulting in the observed spatially-variable soil profiles. Therefore, there are

likely to be complex scale-dependent spatial covariance relationships between soil

hydraulic properties above and below soil horizon interfaces. The influence of soil

hydraulic properties on water flow and solute transport processes in soils would then

suggest complex, scale-dependent patterns in measure soil transport processes.

In Sections 2 and 3, a TDR method was developed to measure the spatial patterns

of transient and steady state, local soil water flux above and below a soil horizon

interface in-situ. Therefore, the objectives of this Section are: 1) to investigate the

potentially spatial-scale-dependent nature of a soil horizon interface; and 2) to investigate

the potentially scale dependent covariance between the spatial pattern of measured local

soil water flux and the horizon interface.

4.2.   Theory

Using the methods outlined in Sections 2 and 3, spatial series of local, vertical soil

water flux estimates above and below the A/B horizon interface, $q_{w|A,n\Delta x}$, $q_{w|B,n\Delta x}$

(n=1,2,...N) were measured. Using a signal processing analogy, the spatial series of

local soil water flux above the horizon interface (A horizon flux) may be likened to the

input signal. The soil horizon interface itself modifies the input signal, and the spatial

series of local soil water flux below the horizon interface (B horizon flux) is the resultant

output signal. To quantify the scale dependency of the spatial variance of a variable, and

the scale-dependent spatial co-variance between variables, spectral (spatial) analysis is

used. The power spectrum of the spatial series/signal, X, partitions the total variance into

the N/2 Fourier frequencies ($f = K/N$; $K = 1,2\ldots N/2$):

$$S_{XX}(f) = \left\langle S_{XX}^{(p)}(f) \right\rangle = \left\langle \frac{1}{N} \left| \sum_{t=1}^{N} X_n e^{-2\pi ft} \right|^2 \right\rangle \qquad \text{[4-1]},$$

where $S_{XX}(f)$ is the power spectrum of series X, $S_{XX}^{(p)}(f)$ is the periodogram, $|a|^2 = a^*a$,

and the asterisk denotes the complex conjugate (Percival and Walden, 1993). The

periodogram, $S_{XX}^{(p)}(f)$, is a naïve estimator (i.e., only 2 degrees of freedom per estimated

value) of the power spectrum, and must be averaged in some way to estimate $S_{XX}(f)$ as

indicated by the expectation operator, $\langle \cdot \rangle$, in Eq. [4-1]. Specific details of spectrum

estimation are given in Section 4.3. Power spectra give an independent estimate of

variance at each spatial frequency. The power spectrum may also be interpreted as the

frequency domain representation of the autocovariance function (Duffy and Gelhar,

1985). Spatial frequencies range between $1/N\,\Delta x$ to $1/2\,\Delta x$ corresponding to maximum

spatial periods/scales of $N\Delta x$ (the transect length) to a minimum spatial period/scale

of $2\Delta x$ (twice the sampling interval).

Comparison of the power spectra of the spatial series, $q_{w|A,n\Delta x}$ and $q_{w|B,n\Delta x}$ is an

indication of how the horizon interface changes the spatial pattern of the input signal,

$q_{w|A,n\Delta x}$. The horizon interface may be modeled in the frequency domain with the transfer

function:

$$|H_{XY}(f)|^2 = \frac{S_{YY}(f)}{S_{XX}(f)} \qquad \text{[4-2]}$$

where $S_{YY}(f)$ is the power spectrum of the output signal (i.e., $q_{w|B,n\Delta x}$) and $S_{XX}(f)$ is the power spectrum of the input signal (i.e., $q_{w|A,n\Delta x}$). This approach likens the horizon interface to an amplitude filter (Duffy and Gelhar, 1985). The changes in the spatial power spectrum indicate how the spatial variance has changed as a function of spatial scale (period/frequency). For example, if the soil horizon interface results in local (i.e., small scale relative to transect length) horizontal re-distribution and mixing/averaging of soil water flow, then this would be expressed as a low-pass filter were large scale (low frequency) spatial variance in water flow remains intact, but small scale (high frequency) variance is reduced.

The influence of the spatial pattern of the A/B horizon shape and dimensions and the A and B horizon local soil water fluxes may also be assessed with spatial coherency analysis (Kachanoski and de Jong, 1988). Covariance between two spatial series as a function of spatial scale, is quantified with the cross spectrum:

$$S_{XY}(f) = S_{XX}(f)S_{YY}^{*}(f)$$ [4-3]

where * denotes the complex conjugate. The cross spectrum consists of in-phase and out-of-phase covariance components:

$$S_{XY}(f) = C_{XY}(f) - iQ_{XY}(f)$$ [4-4]

where $C_{XY}(f)$ is the cospectrum (in-phase covariance) and $Q_{XY}(f)$ is the quadrature spectrum (out-of-phase covariance). Linear correlation between input signals as a function of spatial scale is then quantified with the squared coherency spectrum, $R_{XY}(f)$:

$$R_{XY}(f) = \frac{|S_{XY}(f)|^{2}}{S_{XX}(f)S_{YY}(f)}$$ [4-5]

In addition to coherency, multiple and partial coherency spectra be calculated. Multiple coherency examines the scale-dependent linear relationship between the spatial series of the dependent variable with the spatial series of two or more independent variables. Partial coherency may be calculated to estimate the scale-dependent correlation between two spatial series, given one ore more series of covariates. In this manner, multivariate models, with different scale-dependent effects of variables, can be assessed.

Construction of the n x n cross spectral matrix of the independent variables is the primary operation in calculating multiple and partial coherency spectra (Shumway, 1988):

$$\mathbf{S}_{ZZ}(\mathbf{f}) = \begin{bmatrix} S_{Z_1 Z_1}(f) & S_{Z_1 Z_2}(f) & \cdots & S_{Z_1 Z_n}(f) \\ S_{Z_2 Z_1}(f) & S_{Z_2 Z_2}(f) & \cdots & S_{Z_2 Z_n}(f) \\ \vdots & \vdots & \ddots & \vdots \\ S_{Z_n Z_1}(f) & S_{Z_n Z_2}(f) & \cdots & S_{Z_n Z_n}(f) \end{bmatrix} \qquad [4\text{-}6]$$

where $\mathbf{S}_{ZZ}(\mathbf{f})$ is the cross spectral matrix of the independent variables, Z_1, Z_2...Z_n, with the convention that $S_{Z_2 Z_1}(f) = S_{Z_1 Z_2}^{*}(f)$. Next, the n x 1 cross spectral vector of the dependent and independent variables is constructed:

$$\mathbf{S}_{XZ}(\mathbf{f}) = \begin{bmatrix} S_{XZ_1}(f) & S_{XZ_2}(f) & \cdots & S_{XZ_n}(f) \end{bmatrix} \qquad [4\text{-}7].$$

The multiple coherency between series X, and n series of independent variables, $\mathbf{Z}$, $R_{XZ}(f)$, is then calculated as Shumway (1988):

$$R_{XZ}(f) = \frac{\mathbf{S}_{XZ}(\mathbf{f}) \, \mathbf{S}_{ZZ}^{-1}(\mathbf{f}) \, \mathbf{S}_{XZ}'(\mathbf{f})}{S_{XX}(f)} \qquad [4\text{-}8].$$

where the prime ' superscript represents simultaneous complex conjugate and transpose operations on the vector in question. The partial coherency between spatial series X and Y given n covariate series, $\mathbf{Z}$, $R_{XY|\mathbf{Z}}(f)$, is defined as (Brillinger, 1981; Halliday et al., 1995):

$$R_{XY|\mathbf{Z}}(f) = \frac{\left|S_{XY|\mathbf{Z}}(f)\right|^2}{S_{XX|\mathbf{Z}}(f)S_{YY|\mathbf{Z}}(f)} \qquad [4\text{-}9]$$

where $S_{XY|\mathbf{Z}}(f)$ is the partial cross spectrum between X and Y given $\mathbf{Z}$, and $S_{XX|\mathbf{Z}}(f)$ and $S_{YY|\mathbf{Z}}(f)$ are the partial auto spectra for X and Y given $\mathbf{Z}$, respectively. Partial cross and auto spectra are defined as (Halliday et al., 1995):

$$S_{XY|\mathbf{Z}}(f) = S_{XY}(f) - \mathbf{S_{XZ}}(\mathbf{f})\ \mathbf{S_{ZZ}^{-1}}(\mathbf{f})\ \mathbf{S'_{YZ}}(\mathbf{f}) \qquad [4\text{-}10]$$

$$S_{XX|\mathbf{Z}}(f) = S_{XX}(f) - \mathbf{S_{XZ}}(\mathbf{f})\ \mathbf{S_{ZZ}^{-1}}(\mathbf{f})\ \mathbf{S'_{XZ}}(\mathbf{f}) \qquad [4\text{-}11]$$

$$S_{YY|\mathbf{Z}}(f) = S_{YY}(f) - \mathbf{S_{YZ}}(\mathbf{f})\ \mathbf{S_{ZZ}^{-1}}(\mathbf{f})\ \mathbf{S'_{YZ}}(\mathbf{f}) \qquad [4\text{-}12]$$

where $\mathbf{S_{YZ}}(\mathbf{f})$ is constructed as in Eq. [4-7].

4.3. Materials and Methods

Spatial series of local, transient and steady state soil water flux were measured according to the methods presented in Sections 2 and 3. In Section 2, transient, soil water flux was measured at 46 locations along a 6.75 m transect with paired 25- and 60-cm TDR probes (A and B horizon local soil water flux). Based on the results in Sections 2, it appears there is enough information to estimate transient, local soil water flux through the A and B horizon with only the 60-cm probes. Therefore, the additional 45 60-cm probes situated between the 46 pairs of 25- and 60-cm TDR probes (Fig. 2-2) were used to estimate transient, local soil water flux according to the methods in Section 2. As a

result, the spatial series consisted of 91 transient, local soil water flux estimates above and below the horizon interface along the 6.75 m transect for each water application rate (0.075 m sampling interval; Fig. 2-2).

Spatial series of steady state, local soil water flux estimates (estimated according to Section 3) were also expanded to 91 point series by using the additional 45 60-cm TDR probes located between the paired 25- and 60-cm probes (Fig. 2-2). In order to estimate the steady state, local soil water flux through the A horizon at the 45 locations without 25-cm probes, however, the steady state water content in the 0- to 25-cm layer was estimated with the average of the 2 adjacent 25-cm probes. For the cases where the actual depth of the horizon interface was less than 25 cm, the steady state water contents of the A and B horizons were estimated using the iterative technique outlined in Section 3.3.

As mentioned in Section 3, the depth to the A/B horizon interface (DEPTH) was measured at each probe location along three, parallel transects centered on the TDR probe transect. This allowed for a three-dimensional representation of the horizon interface. Interface curvature was quantified by fitting the following three-dimensional polynomial to each 3 by 3 grid of interface depth measurements centered around each TDR probe (Young and Evans, 1978; Kachanoski et al., (1985); Pennock et al., 1987):

$$z = ax^2 + by^2 + cxy + dx + ey + f \qquad [4\text{-}13]$$

where x, y and z are the easting, northing, and depth coordinates respectively, and a, b, c, d, e, and f are least squares coefficients. Young and Evans (1978) derived expressions to quantify the slope aspect, gradient, profile and plan curvature of a three-dimensional surface using the least squares coefficients. For this study the profile (PROF) and plan

(PLAN) curvature of the horizon interface were quantified. Profile curvature is the rate of change of the gradient of the 3D surface in the direction of maximum gradient. Plan curvature is the rate of change of the gradient of the 3D surface perpendicular to the direction of maximum gradient. The convention is that negative curvature represents concave shapes and positive curvature represents convex shapes.

Power spectra were estimated non-parametrically using multitaper spectral methods (Thomson, 1982; Percival and Walden, 1993). Transformation of data into the Fourier domain without data tapering usually results in biased spectral estimates (Thomson, 1982; Percival and Walden, 1993). Tapering data with a suitable taper prior to transformation into the Fourier domain reduces bias and increases resolution in the power spectrum at discrete frequencies. The decreased bias and increased resolution are offset, however, by a loss in degrees of freedom. Slepian (1978) and Thomson (1982) developed multi-taper methods that did not result in a loss of degrees of freedom. Multi-taper methods involve tapering the original data set with a set of K independent tapers to get K independent estimates of the power spectra. The K estimates of the power spectra are then averaged (arithmetic or weighted) to get the final spectral estimate. If the K tapers are orthogonal to each other in both time/space and frequency domains (i.e., doubly orthogonal), the K spectral estimates are independent of each other (a proof is given in Percival and Walden, 1993, Ch. 7). The final average spectral estimate at each frequency will have $\leq 2K$ degrees of freedom.

Slepian (1978) introduced discrete, prolate, spheroidal sequences (DPSSs) as a suitable set of data tapers doubly orthogonal to each other. These sequences are the

discrete realization of the continuous, prolate, spheroidal wave functions. The set of K, DPSSs are obtained with the solution to the following eigenvalue problem:

$$\sum_{n'=0}^{N-1} \frac{\sin\left[2\pi \frac{p}{N}(n-n')\right]}{\pi(n-n')} h_{n',k}(N,p) = \lambda_k(N,p) h_{n',k}(N,p) \qquad \begin{array}{l} k = 0,1\ldots K-1 \\ n = 0,1\ldots N-1 \end{array} \qquad [4\text{-}14]$$

where $h_{n,k}(N,p)$ is the kth data taper, $\lambda_k(N,p)$ is the kth eigenvalue, N is the length of the data series, K is the number of tapers, and p is a parameter that defines the bandwidth of the taper. The solution of Eq. [4-14] will yield K eigenvectors of length N, $h_{n',k}(N,p)$, which are the DPSSs. In addition to being doubly orthogonal, the DPSSs have good variance conservation characteristics; that is, very little variance from the data series is lost outside of the taper bandwidth. The fractional amount of variance lost from the data sequence as a result of tapering is estimated by (Thomson, 1982):

$$1 - \lambda_k(N,p) \cong \frac{\sqrt{2\pi}}{k!} \left[\frac{8N\sin\left(\pi\frac{p}{N}\right)}{\cos^2\left(\pi\frac{p}{N}\right)} \right]^{k+\frac{1}{2}} \left[\frac{1-\sin\left(\pi\frac{p}{N}\right)}{1+\sin\left(\pi\frac{p}{N}\right)} \right]^N \qquad [4\text{-}15]$$

For K < 2p, the first K eigenvalues ($\lambda_k(N,p)$) are very close to 1, or almost zero variance loss. With p=3.5, the first 5 eigenvalues are > 0.98. Thus, for the spectrum estimates in this work, p=3.5, K=5, and N=91.

The DPSSs were estimated using the tridiagonal formulation given in Slepian (1978) and Percival and Walden (1993). Slepian (1978) showed that all DPSSs satisfy the following difference equation:

$$\frac{n(N-n)h_{n-1,k}(N,p)}{2}$$

$$+\left[\left(\frac{|N-1-2n|}{2}\right)^2\cos\left(2\pi\frac{p}{N}\right)-\theta_k(N,p)\right]h_{n,k}(N,p) \qquad [4\text{-}16]$$

$$+\frac{(n+1)(N-1-n)h_{n+1,k}(N,p)}{2}=0$$

Equation [4-16] simplifies to the following eigenvalue problem:

$$\mathbf{A}\mathbf{v}_k(N,p)=\zeta_k\mathbf{h}_k(N,p) \qquad [4\text{-}17]$$

where the DPSSs, $\mathbf{h}_k(N,p)$, are now eigenvectors of matrix $\mathbf{A}$, and $\zeta_k(N,p)$ are the eigenvalues of matrix, A (different from $\lambda_k(N,p)$). Matrix $\mathbf{A}$ is a tridiagonal matrix with diagonal elements equal to:

$$\left(\frac{|N-1-2n|}{2}\right)^2\cos\left(2\pi\frac{p}{N}\right) \qquad n=0,1\ldots N-1 \qquad [4\text{-}18]$$

and off-diagonal elements equal to:

$$\frac{n(N-t)}{2} \qquad n=1,2\ldots N-1 \qquad [4\text{-}19]$$

Eigenvector problems for tridiagonal matrices can be solved numerically with a variety of available software packages and computer code. The DPSS tapers were calculated for this work with a QR/QL algorithm coded in Delphi (Bochkanov, 2007) and implemented in Free Pascal for Windows (Gábor et al., 2006). Each taper is then normalized such that $\sum_t(h_{t,k})^2=1$ (Percival and Walden, 1993).

Each of the K tapers is used to calculate K eigen spectra:

$$\hat{S}_{k,XX}(f)=\frac{1}{N}\left|\sum_{t=1}^{N}\tilde{h}_{t,k}\tilde{X}_t e^{-i2\pi ft}\right|^2 \qquad [4\text{-}20]$$

where $\hat{S}_{k,XX}(f)$ is the kth eigen spectra (or periodogram), f are the Fourier frequencies, $\tilde{h}_{t,k}$ is the kth normalized data taper, and $\tilde{X}_t = X_t - \bar{X}$, is the data series with the mean subtracted. The simple multi-taper spectrum, $\hat{S}_{XX}^{(smt)}(f)$, is the arithmetic average of the K eigen spectra (Percival and Walden, 1993):

$$\hat{S}_{XX}^{(smt)}(f) = \frac{1}{K} \sum_{k=0}^{K-1} \hat{S}_{k,XX}(f)$$

[4-21]

which has 2K degrees of freedom at each frequency and does not require additional smoothing (Thomson, 1982).

Unequal weights can be used to derive an adaptive multi-taper spectrum, $\hat{S}_{XX}^{(amt)}(f)$ (Percival and Walden, 1993):

$$\hat{S}_{XX}^{(amt)}(f) = \frac{\sum_{k=0}^{K-1} b_k^2(f) \lambda_k \hat{S}_{k,XX}(f)}{\sum_{k=0}^{K-1} b_k^2(f) \lambda_k}$$

[4-22]

where $b_k(f)$ are adaptive weights for each of the K eigen spectra at each frequency, and λ_k are the eigenvalues from Eq. [4-15]. The adaptive weights are estimated with:

$$b_k(f) = \frac{\sqrt{\lambda_k} S_{XX}(f)}{\lambda_k S_X(f) + \sigma^2 (1 - \lambda_k)}$$

[4-23]

where $S_{XX}(f)$ is the true spectrum and σ^2 is the variance of the data series. Equation [4-23] has two unknowns, $b_k(f)$ and $S_{XX}(f)$, so the adaptive weights must be determined iteratively using the following algorithm:

1) the initial guess for $S_{XX}(f)$ is calculated as the arithmetic average of the first two eigen spectra (i.e., Eq. [4-21] with K = 2)

2) substituting the initial guess for $S_{XX}(f)$ into Eq. [4-23]; the first estimate of adaptive weights are calculated

3) the weights calculated in 2) are substituted into Eq. [4-22]

4) the result from 3) is substituted for $S_{XX}(f)$ in Eq. [4-23] and a second estimate of the adaptive weights is calculated.

5) Steps 3) and 4) are repeated until $\hat{S}_{XX}^{(amt)}(f)$ in Eq. [4-22] does not change within a specified tolerance

The rational behind determining adaptive weights with Eq. [4-23] is that, for a white noise process, $S_{XX}(f)$ is equal to σ^2 at each frequency so each of the $b_k(f)$ weights would be equal to 1 and the adaptive spectral estimate in Eq. [4-22] converges to the simple spectral estimate in Eq. [4-21] (Percival and Walden, 1993). For non-white noise processes, the adaptive spectral estimate gives more weight to the lower order eigenspectra with the best variance conservation characteristics. As a result, the adaptive spectral estimate at each frequency has <2K degrees of freedom which are a function of the adaptive weights, $b_k(f)$:

$$v(f) = \frac{2\left(\sum_{k=0}^{K-1} b_k^2(f)\lambda_k\right)^2}{\sum_{k=0}^{K-1} b_k^4 \lambda_k^2} \qquad [4\text{-}24]$$

where $v(f)$ are the effective degrees of freedom as a function of frequency. As in Shumway (1988), for example, the 1-α/2 confidence interval for the power spectrum estimate at each frequency may be calculated with the chi-squared distribution:

$$\log\left[\hat{S}_{XX}(f)\right] - \log\left[\frac{\chi_{v,\alpha/2}^2}{v}\right] \leq \log\left[\hat{S}_{XX}(f)\right] \leq \log\left[\hat{S}_{XX}(f)\right] - \log\left[\frac{\chi_{v,1-\alpha/2}^2}{v}\right] \qquad [4\text{-}25]$$

where $\chi^2_{v,\alpha/2}$ and $\chi^2_{v,1-\alpha/2}$ are the values of the chi-squared distribution with v degrees of freedom ($v(f)$ for adaptive estimates) at $\alpha/2$ and $1-\alpha/2$ probabilities. The estimated power spectra for the input signal, $\hat{S}_{XX}(f)$, and the output signal, $\hat{S}_{YY}(f)$, can now be used to estimate the transfer function (Eq. [4-2]), $\left|\hat{H}_{XY}(f)\right|^2$.

Eigen cross spectra for two series, X and Y, $\hat{S}_{k,XY}(f)$, can be calculated by substituting the eigen power spectra calculated with Eq. [4-20] for series X and Y, and substituted into Eq. [4-3] (Thomson, 1982). Similar to the simple spectral estimate, a simple cross spectral estimate can be calculated by substituting eigen cross spectra, $\hat{S}_{k,XY}(f)$, into Eq. [4-21]. An adaptive estimate of the cross spectrum may also be calcuated using the weights derived from Eq. [4-23] (Vernon, 1994):

$$\hat{S}_{XY}^{(amt)} = \frac{\sum_{k=0}^{K-1}\lambda_k b_{k,XX}(f)S_{k,XX}b_{k,YY}(f)S^*_{k,YY}}{\left[\sum_{k=0}^{K-1}\lambda_k b^2_{k,XX}(f)\right]^{\frac{1}{2}}\left[\sum_{k=0}^{K-1}\lambda_k b^2_{k,YY}(f)\right]^{\frac{1}{2}}} \qquad [4\text{-}26]$$

where $b_{k,XX}(f)$, and $b_{k,YY}(f)$ are the weights used to calculate $\hat{S}_{XX}^{(amt)}(f)$ and $\hat{S}_{YY}^{(amt)}(f)$, respectively. The coherency spectrum can now be estimated by substituting the simple or adaptive cross spectrum and power spectra estimates ($\hat{S}_{XY}^{(amt)}, \hat{S}_{XX}^{(amt)}(f)$ and $\hat{S}_{YY}^{(amt)}(f)$; or $\hat{S}_{XY}^{(smt)}, \hat{S}_{XX}^{(smt)}(f)$ and $\hat{S}_{YY}^{(smt)}(f)$)) into Eq. [4-5]. Coherency estimates using adaptive cross and power spectra may be difficult to interpret because the adaptive cross spectrum and power spectrum estimates may have different degrees of freedom at each frequency. In- and out-of-phase correlation as a function of frequency may also be calculated using the

102

cospectra and quadrature spectra derived from either the simple or adaptive cross and power spectra estimates:

$$\hat{r}_{IN,XY} = \frac{\hat{C}_{XY}}{\sqrt{\hat{S}_{XX}\hat{S}_{YY}}} \qquad [4\text{-}27]$$

and

$$\hat{r}_{OUT,XY} = \frac{\hat{Q}_{XY}}{\sqrt{\hat{S}_{XX}\hat{S}_{YY}}} \qquad [4\text{-}28]$$

In accordance with Brillinger (1981), Kachanoski et al. (1985), and Si (2008), the critical value for $\hat{R}_{XY}(f)$ is:

$$\rho_{XY} = 1 - (1-\alpha)^{[2/(v-2)]} \qquad [4\text{-}29]$$

where α is the significance level, and v is the degrees of freedom. Multiple coherency spectra may be calculated by substituting simple or adaptive multitaper auto or cross spectra estimates into Eqs. [4-6] – [4-8]. The critical value for multiple coherency, $R_{XZ}(f)$ is (Si, 2008):

$$\rho_{XZ} = 1 - (1-\alpha)^{[2/(v-2n)]} \qquad [4\text{-}30]$$

where n is the length of cross spectral vector, Eq. [4-7]. Partial coherency spectra are calculated by substituting either simple or adaptive multitaper auto or cross spectra estimates into Eqs. [4-9] – [4-12]. Critical values for partial coherency, are calculated by (Brillinger, 1981; Winterhalder et al., 2005):

$$\rho_{XY|Z}(f) = 1 - (1-\alpha)^{[2/(v-2n-2)]} \qquad [4\text{-}31]$$

4.4. Results and Discussion

4.4.1. Nature and Description of Soil Horizon Interface

As indicated in Table 2-1, the average hydraulic properties of the A and B horizon are quite similar. Thus, the primary influence of the horizon interface must be in the difference/similarities of the spatial patterns of the hydraulic properties (i.e their spatial covariance relationships) and the relationship of this spatial covariance with the shape of the interface. For a uniform soil with no layers under constant water application and steady state conditions, the soil water content is a reflection of unit gradient conditions with $q_w = K(\theta)$. Thus, the soil water content, θ, will increase until the hydraulic conductivity K is equal to the soil water flux, q_w. For soil with variable hydraulic properties, the relationship between local water flux and local steady state water content has been used to estimate in-situ $K(\theta)$ functions. (Si and Kachanoski, 2003). Thus, the spatial pattern of volumetric water content is a reflection of the underlying static spatial pattern of hydraulic properties. Yeh (1989) and Srivastava and Yeh (1991) have shown that, for a layered soil under constant water application and steady state conditions, the steady state soil water content of the underlying soil layer (layer B) is also a reflection of unit gradient conditions with $q_B = K_B(\theta_B)$, where the subscript B refers to layer B. They also showed that the steady state matric pressure head ψ_B of the underlying layer (from the $\theta_B(\psi_B)$ relationship) acts as a lower boundary condition for the upper layer. So, in the upper layer, the steady state water content transitions from $\theta_A(\psi_A = \psi_B)$ at the layer interface to the steady state soil water content reflecting unit gradient conditions in the upper layer with $q_A = K_A(\theta_A)$. The transition distance in layer A depends on the water flux and on the difference/similarity of the hydraulic functions of the 2 layers. For

somewhat similar hydraulic functions, the transition distance is quite short (a few cm above the layer interface).

Given the above discussion, it is reasonable to assume that, for soils with relatively thick layers and similar (but spatially variable) hydraulic properties, the spatial pattern of steady state soil water contents will be a reflection of the underlying static spatial pattern of hydraulic properties. This assumption is consistent with the work of Dagan and Bresler (1979) and Russo and Dagan (1991), who used the spatial variability/pattern of saturated water content and scaling/covariant relationships of hydraulic parameters to predict the ensemble (macro-scale) spatial variance of local steady state water flow and travel times in heterogeneous soil as a function of average flow rate. In this manner, the spatial pattern of steady state soil water content in the B horizon can be viewed as a function of the spatially-variable local $q_{w,B|ss}$ and local $K_B(\theta_B)$ relationships with the internal steady state boundary condition $q_{w,B|ss} = K_B(\theta_B)$.

The resultant spatial pattern in the B horizon serves as a spatially variable lower boundary condition for the A horizon (through the spatial pattern and covariance of the local $\theta_B(\psi_B)$ and $\theta_A(\psi_A = \psi_B)$ relationship). The spatial pattern of the A horizon steady state soil water contents are primarily a reflection of the spatial pattern/variability of local q_A and local $K_A(\theta_A)$ relationships, and the steady state internal boundary condition $q_{w,A|ss} = K_A(\theta_A)$. This spatial pattern then transitions over a relatively short distance to the spatial pattern of the lower boundary condition (controlled by the spatial pattern in the B horizon).

For the A/B horizon interface under consideration, spatial series of DEPTH, PROF, and PLAN are presented in Fig. 4-1, and a 3-D representation of the interface is presented in Fig. 4-2. The correlation matrix in Table 4-1 indicates that depth (DEPTH) of the horizon interface is significantly negatively correlated to both profile (PROF; $r = -0.47$; P<0.001) and plan curvature (PLAN; $r = -0.24$; P < 0.05). Therefore, on average, locations with greater depth to the interface tend to be concave (negative PROF) and convergent (negative PLAN) areas, which would accumulate any water flow being re-directed at an interface. Locations with shallow interfaces would tend to be convex (positive PROF) and divergent (positive PLAN), which would tend to shed any water that might be redirected by an interface. At any specific location, the interface may or many not redirect vertical water flow depending on the difference in local hydraulic properties above (A horizon) and below (B horizon) the interface.

Spatial series of A and B horizon steady state soil water content and storage are presented in Fig. [4-3] and Fig. [4-4]. Both steady state water content and storage showed remarkable consistency across water application rates. Spatial series of A and B horizon water contents were significantly correlated to themselves across all water application rates ($r \geq 0.94$; P<0.001; Table 4-1). Similarly, spatial series of A and B horizon soil water storage were significantly correlated to each other across all water application rates ($r \geq 0.96$; P<0.001; Table 4-1). A and B horizon water contents, however, were not correlated to each other at all water application rates ($r < 0.03$; Table 4-1). No significant correlation was found between horizon depth and steady state A horizon soil water content. In the B horizon, however, steady state soil water content was significantly correlated to the horizon depth at all water flow rates ($r = 0.25$; P< 0.05;

Table 4-1). This indicates that B horizon water contents were relatively lower when the depth to the interface was less than 25 cm (the average depth to the interface), and relatively higher when the depth was greater than 25 cm. The very high consistency in the spatial patterns of observed steady state A and B horizon water contents across flow rates is an indication that they are primarily reflecting the underlying static spatial distributions of the state hydraulic functions ($K_A(\theta_A)$, $K_B(\theta_B)$).

Consistency in spatial series of steady state A and B horizon water contents is further expressed in the power spectra of steady state A and B horizon water contents (Fig. 4-5). Both A and B steady state water contents show very similar spectra across all water application rates. The spectra for A and B horizon water contents indicate significant, but different autocorrelated patterns in A and B horizon steady state water content. Power spectra of the DEPTH, PROF, and PLAN, give more information about the spatial pattern of the morphology of the horizon interface (Fig. 4-6). Both DEPTH and PROF show similar spatial patterns at scales ranging from 0.3 to 6.75 m, but there is relatively more variance at local scale (spatial scales < 0.3 m) in PROF than DEPTH. Plan curvature shows relatively high variability at all scales except for a small range of local scales around 0.17 m.

The significant (but relatively low) positive correlation between B horizon steady state water content and DEPTH may also be examined as a function of scale with coherency and in- and out-of-phase covariance spectra (Fig. 4-7). The co-spectrum (i.e., in phase covariance) indicates positive covariance across all/most scales and this positive covariance generally increases as the spatial scale increases. The quad spectrum (i.e., out of phase covariance) indicates that there is also very significant covariance between B

horizon steady state water content and DEPTH at intermediate spatial scales (0.3 m to 1.0 m), but the covariance is negative and out of phase. With respect to a conceptual model of the influence of the interface shape, the negative out-of-phase covariance is consistent with positive in-phase covariance. It suggests that, on average, locations with greater depth to the interface, which also tend to be concave (negative PROF) and convergent (negative PLAN) areas, are areas of higher steady-state soil water contents (i.e., significant positive in-phase covariance) and these are also areas with adjacent lower soil water content (ie, significant negative out-of phase covariance). Conversely, locations with shallow interfaces, which tend to be convex (positive PROF) and divergent (positive PLAN), are locations of lower steady-state soil water contents (i.e., significant positive in-phase covariance) and these are also areas with adjacent higher soil water content (ie, significant negative out-of-phase covariance). It is important to note that the significant (but relatively low) correlation between B horizon steady state water content and DEPTH is an expression of only the integral of the in-phase co-spectrum, and does not account for the out-of-phase covariance of the Quad spectrum. Thus, the influence of the depth/shape of the interface on the spatial pattern of soil water content is greater than what is suggested by the standard correlation coefficient.

4.4.2. Steady State Soil Water Flux

Based on the discussion above, the influence of the horizon interface on local steady state water flow would be related to the spatially-scale-dependent covariance relationships between the hydraulic properties of the horizons, and the variable depth/curvature of the interface causing spatial variability in the lower A horizon boundary condition. The interface influence would be primarily expressed through local

water redistribution in the thin transition zone above the interface (i.e., in the A horizon), which creates a subsequent different spatial pattern of $q_{w,B|ss}$.

The observed complex spatial covariance between the depth/curvature of the horizon interface and the steady state B horizon water content (i.e., Fig. 4-7), along with our understanding of pedogenic processes creating the horizons/interface, can account for a moderate negative correlation between the spatial patterns of local steady state water flux in the A versus B horizon (r =-0.28 to -0.51; P<0.01; Table 4-1). Pedogenic weathering/dissolution/transport (e.g., oxides), and translocation of material (e.g., clay) from the A horizon coupled with subsequent precipitation and deposition of this material to the B horizon) could result in a negative spatial covariance between hydraulic properties at the local scale. Local areas of increased weathering in the A horizon (i.e., areas of deeper A horizons with concave convergent curvature) would tend to have relatively more porosity, lower percentage of small pores, and higher hydraulic conductivity ,and directly below (along the same flow pathway) the B horizon which receives this material would have relatively lower porosity, higher percentage of small pores, and generally lower hydraulic conductivity. Depending on the nature of the parent material and the local $K_A(\theta_A)$ and $K_B(\theta_B)$ curves, these processes, acting over a long period of time, may create a local scale covariance between hydraulic properties which is flux dependent which could potential result in a flux- and scale-dependent covariance between steady state water flux across the horizon interface.

Figure 4-8 shows in- and out-of-phase correlation spectra between steady state local A and B horizon soil water flux. As indicated by the average negative correlations in Table 4-1, and predicted by the conceptual model, there is a negative in-phase

correlation between steady state, local A and B horizon water flux at spatial scales less than 1.0 m, with the exception of the 0.4 – 0.5 m scale at the 10.6 cm day^{-1} flow rate. The average correlation between $q_{w,A|ss}$ and $q_{w,B|ss}$ at the 10.6 cm day^{-1} rate was the lowest out of the all of the flow rates (r = -0.28; P<0.01; Table 4-1). Furthermore, as average water application rate increases, the average steady state soil water flux pattern would converge to the pattern in saturated hydraulic conductivity of the A and B horizon, which may be different than the unsaturated hydraulic conductivity.

The influence of the B horizon (as a lower boundary condition) on steady state water flux in the A horizon at local scales is apparent in the comparison of the scale dependent in-phase correlations between $q_{w,A|ss}$ and $\overline{\theta}_{B,ss}$, and between $q_{w,B|ss}$ and $\overline{\theta}_{B,ss}$ (Fig. 4-9). For all water application rates, $q_{w,B|ss}$ and $\overline{\theta}_{B,ss}$ are positively correlated in-phase across all spatial scales. For most local, spatial scales (i.e., < 1 meter), $q_{w,A|ss}$ and $q_{w,B|ss}$ show opposite in-phase correlations to $\overline{\theta}_{B,ss}$ (negative for $q_{w,A|ss}$ and positive for $q_{w,B|ss}$). It is interesting to note, however, that at the intermediate (0.4-0.5 m) spatial scale, the in phase correlation between $q_{w,A|ss}$ and $\overline{\theta}_{B,ss}$ shifts from slightly negative at the 2.7 cm day^{-1} water application rate to moderately positive at the 10.6 cm day^{-1} water application rate. It was the 0.5 m scale that $q_{w,A|ss}$ was positively correlated (in-phase) to $q_{w,B|ss}$ at the 10.6 cm day^{-1} water application rate (Fig. 4-8). This was also the scale at which a negative out-of-phase correlation between horizon depth and $\overline{\theta}_{B,ss}$ was observed (Fig. 4-7). The 0.5 m scale is also the scale at which spectra in DEPTH, PROF, and $\overline{\theta}_{B,ss}$ have relatively larger variances indicating, once again, the influence of the spatially scale

110

dependent covariance relationships between the hydraulic properties of the horizons, and

the influence of the shape of the interface on the spatial pattern of the lower A horizon

boundary condition, and its influence on $q_{w,A|ss}$.

The change in the scale-dependent correlation between $q_{w,A|ss}$ and $\bar{\theta}_{B,ss}$ (i.e., from

negative at the 0.5 m scale at the 2.7 cm day^{-1} rate to positive at the 10.6 cm day^{-1} rate) is

consistent with the conceptual model because the spatial patterns of $K_A(\bar{\theta}_{A,ss})$ and

$K_B(\bar{\theta}_{B,ss})$ are non-linear functions. Figure 4-10 compares the relationship between $q_{w,A|ss}$

and $\bar{\theta}_{A,ss}$, and the relationship between $q_{w,B|ss}$ and $\bar{\theta}_{B,ss}$. At higher water application

rates, the slope of the $q_{w,B|ss}$ *versus* $\bar{\theta}_{B,ss}$ relationship is much more dependent on the

average applied water than the slope of $q_{w,A|ss}$ *versus* $\bar{\theta}_{A,ss}$ relationship, indicating that

the lower boundary condition at the A/B horizon interface is not only spatially variable

and scale dependent, but is also flux dependent according to the spatial pattern in state

hydraulic properties of the B horizon.

4.4.3. Transient Soil Water Flux

The spatial patterns of A and B horizon transient flux show a different average

covariance (positive) to each other than the steady state patterns (negative). The influence

of the interface on the spatial patterns of transient, local A and B horizon flux is expected

to be different than the observed influence at steady state. There are likely slight

hydraulic gradients localized at the soil horizon interface under steady state conditions

due to spatial-variability in the depth and curvature of the interface. Under transient

conditions, advancement of a spatially-variable wetting front with spatially-variable

velocity through the A horizon and across the A/B horizon interface, likely results in

111

stronger spatially- and temporally-variable hydraulic gradients than under steady state conditions. As mentioned in Section 2.4, during transient infiltration, either water entry or hydraulic conductivity discontinuities above and below the horizon interface at any given location can result in local, three-dimensional flow and redistribution of mass. The combination of forcing from above the wetting front (surface flux boundary condition) and pulling at and below the wetting front (hydraulic gradients) likely diminishes (but does not eliminate) the influence of the spatial patterns the A and B horizon hydraulic properties (i.e their spatial covariance relationships) on the pattern of transient flow compared to steady state flow. In addition, the spatially scale dependent interaction of the advancing wetting front with the horizon interface would further influence the relationship between the patterns of transient local A and B horizon flux.

Spatial series of transient, local A and B horizon soil water flux are presented in Figure 4-11. Significant correlations between A horizon fluxes measured under different water application rates indicate some consistency in the spatial pattern of the input signal at different average fluxes (Table 4-1). It is interesting to note, however, that the strength of the correlation between A horizon flux patterns decreases with increasing difference between water application rates. For example, the spatial pattern of A horizon flux at the 1.3 cm day^{-1} application rate is more similar to the spatial pattern of A horizon flux at the 2.7 cm day^{-1} rate (r = 0.43; P<0.001; Table 4-1) than at the 10.6 cm day^{-1} rate (r = 0.37; table 4-1). In addition, the correlation between successive spatial patterns of flux increased with increasing water application rates. The correlation between the 10.6 cm day^{-1} A horizon flux pattern and the 7.0 cm day^{-1} A horizon flux pattern is 0.64 (P<0.001; Table 4-1) while the correlation between the 7.0 cm day^{-1} A horizon flux pattern and the

2.7 cm day^{-1} A horizon flux pattern is 0.57 (P<0.001; Table 4-1). The increasing

consistency between successive A horizon flux patterns as a function of water application

rate is presented in Fig. 4-12 for the full (N = 91) and limited (N = 46) series. As the

water application rate increased, the spatial pattern of the A horizon flux converged to the

spatial pattern of the 10.6 cm day^{-1} water application rate. This observed increasing

consistency/correlation between A horizon flux patterns with increasing water application

rate suggests that the spatial pattern of the A horizon flux appears to be converging to the

spatial pattern of the saturated hydraulic conductivity of the A horizon. A similar

observation was reported by Si (1998).

The increasing consistency between successive A horizon flux patterns as average

water flux increased was not observed in the B horizon flux patterns. The correlation

coefficients between B horizon flux patterns varied between r = 0.4 and r = 0.61 and did

not show any trends with average flow rate.

The flux-dependent correlation between the spatial patterns of A and B horizon

transient flux observed in Section 2 (N = 46) is still apparent and somewhat stronger in

the full spatial series (N = 91). As average transient water flux increased, the positive

correlation between the patterns of A and B horizon transient flux patterns decreased

from r = 0.50 (P<0.001) for the 1.3 cm day^{-1} rate to r = 0.19 (P>0.05) for the 10.6 cm day^{-1} water application rate (Table 4-1). It is also interesting to note that the A horizon flux

pattern for the 1.3 cm day^{-1} application rate has a stronger correlation to the B horizon

flux patterns at all other rates compared to the A horizon flux patterns at those rates (Fig.

4-13). This indicates that (1) the spatial patterns of successive transient flux

measurement in the A horizon and B horizon were more alike as the average flow

decreased, and (2) the B horizon flux patterns were more persistent across different flow rates than the A horizon flux patterns. In other words, as average flow rate increased, the spatial pattern of the A horizon transient flux was converging to a stable pattern that was increasingly different than the spatial pattern of water flux in the B horizon. This indicates a hydrologically significant, flux-dependent influence of the soil horizon interface during transient infiltration.

As mentioned in Section 2 and at the beginning of this section, the flux-dependent correlation between A and B horizon flux patterns is conceptually consistent with the physics of a spatially-variable wetting front encountering a spatially-variable soil horizon interface. The correlation coefficients presented in Table 4-1, however, represent an average correlation between two spatial series at all scales. Spatial resolution in the correlation between two series is gained through coherency spectra, which provide insight as to the scales at which processes are occurring.

Coherency and in- and out-of-phase correlation spectra comparing $q_{w,A|tr}(1.3)$ with $q_{w,B|tr}(1.3)$, $q_{w,A|tr}(1.3)$ with $q_{w,B|tr}(10.6)$, and $q_{w,A|tr}(10.6)$ with $q_{w,B|tr}(10.6)$ are presented in Figs. 4-14, 4-15 and 4-16 respectively. The significant scale dependent correlation between the spatial patterns of A and B horizon transient water flux is evident at the 1.3 cm day^{-1} application rate. Even though the correlation between $q_{w,A|tr}(1.3)$ and $q_{w,B|tr}(1.3)$ is only 0.50 on average, the coherency and in-phase correlation/covariance (Fig. 4-14.) are very high (r ~ 0.9) at large scales (1.0 – 6.75 m) and around r = 0.6-0.7 at medium (0.38 – 0.5 m) spatial periods/scales (Fig. 4-6). Coherency is not statistically significant at all other scales. The coherency spectrum between $q_{w,A|tr}(1.3)$ and

$q_{w,B|tr}(10.6)$ (Fig. 4-15) has a similar shape to that in Fig. 4-14, but because the average

correlation between $q_{w,A|tr}(1.3)$ and $q_{w,B|tr}(10.6)$ (r = 0.29) is somewhat less than the

correlation $q_{w,A|tr}(1.3)$ and $q_{w,B|tr}(1.3)$ (r = 0.50), the strength of the linear relationship at

the 1.0 – 6.75 m and 0.38 – 0.5 m spatial scales is weaker. Comparison of $q_{w,A|tr}(10.6)$

and $q_{w,B|tr}(10.6)$ (Fig. 4-16) again reflects the weaker average correlation (r = 0.19)

between these two patterns with significant coherency at only that the very local, 0.15 m

scale (Fig. 4-16).

The spatial patterns of A and B horizon transient flux are not significantly

correlated to any of the horizon interface parameters (DEPTH, PROF, PLAN), except for

a weak correlation between $q_{w,A|tr}(7.0)$ and depth (Table 4-1). Partial coherency spectra,

however, indicate there are some significant relationships between B horizon flux

patterns and layer parameters once the covariance between the A horizon flux (input flux)

and layer parameters is accounted for. Figure 4-17 shows examples of the coherency

between $q_{w,B|tr}$ and DEPTH given $q_{w,A|tr}$ and $q_{w,B|tr}$ and PLAN given $q_{w,A|tr}$ for the 1.3

and 10.6 cm day^{-1} water application rates. Coherency between $q_{w,B|tr}$ and DEPTH

increases slightly at the 1.0 – 6.75 m spatial scales as the water application rate increases

from 1.3 to 10.6 cm day^{-1} (Fig. 4-17A). Coherency between $q_{w,B|tr}$ and PLAN increases

significantly at the 0.38 – 0.50 m spatial scales as the water application rate increases

from 1.3 to 10.6 cm day^{-1} (Fig. 4-17B). In fact the, average coherency between $q_{w,B|tr}$

and DEPTH for 1.0 – 6.75 m spatial scales, and the average coherency between $q_{w,B|tr}$

and PLAN at the 0.38 – 0.5 m spatial scales increases with increase water application rate (Fig. 4-18).

It would appear that two separate yet related flux-dependent phenomena are occurring: 1) convergence of the pattern of $q_{w,A|tr}$ to the spatial pattern of saturated hydraulic conductivity of the A horizon with increasing water application rate; and 2) increased modification of the input pattern, $q_{w,A|tr}$, as the wetting front moves across the soil horizon interface, resulting in a relatively more stable pattern of $q_{w,B|tr}$ compared to $q_{w,A|tr}$ at all water application rates. These changes in spatial patterns were scale dependent. Comparison of A and B horizon fluxes across and within different water application rates revealed a loss of coherency between A and B horizon water flux between spatial scales of 1.0 – 6.75m and 0.38 – 0.50 m. Simultaneously, coherency between $q_{w,B|tr}$ and DEPTH and $q_{w,B|tr}$ and PLAN increased at the frequencies where the coherency between $q_{w,A|tr}$ and $q_{w,B|tr}$ decreased. As mentioned in Section 2, the flux-dependent behavior of the horizon interface is physically consistent. Water entry or anisotropic effects occurring at the interface disrupt the continuity of transient water flux across the interface, but forcing from above, and pulling at the wetting front result in positive correlations between A and B horizon flux patterns. Spectral methods allow quantification of the scale at which these physical processes are occurring. Based on this analysis, it would appear that the horizon interface has the most influence at spatial scales of 0.38 – 0.5 m (Fig. 4-17B), the same as the scales at which the interface influenced steady state flow patterns. At larger scales (1.0 – 6.75 m), the influence of the soil horizon interface is less apparent (Fig. 4-17A), and the changes in transient flux patterns

likely reflect differences in patterns of underlying hydraulic properties. However, it is also possible that the influence of the interface at smaller scales may, in turn, influence the spatial pattern of soil water flux at larger scales, accounting for the loss of coherency between A and B horizon flux patterns at large scales (Fig. 4-16).

It was suggested in Section 4.2 that a transfer function is the appropriate model for the soil horizon interface. The complex interaction between different shape parameters of the soil horizon interface, soil hydraulic properties, and the input water flux from the A horizon would suggest that the transfer function is a reflection of the multivariate interactions between the A horizon flux and horizon interface shape parameters. Transfer functions for the transient and steady state experiments are summarized in Appendix E. Multiple coherency of the B horizon local water flux with A horizon local water flux, and layer parameters averaged across all flow rates are presented in Fig. 4-19. A relatively high proportion of the variability in the B horizon soil water flux at all scales is accounted for by the spatial patterns of A horizon flux and layer shape parameters. This suggests that, while the 0.4 to 0.5 m scales showed the highest amounts of variability in the soil horizon shape, the horizon interface also has larger scale influences. Furthermore, a multivariate scale-dependent model with layer shape parameters and A horizon input flux appears to be very appropriate for describing the scale-dependent spatial variability in the B horizon soil water flux.

4.5. Conclusion

The influence of a soil horizon interface on the spatially-covariant patterns of transient and steady state local soil water flux was examined in detailed using advanced spatial statistical/spectral methods. Methods for analyzing surface landform/topographic

shape were used to characterize the physical shape of horizon interface. The spatial

correlation of horizon interface shape parameters (depth, profile curvature, plan

curvature) suggests that the shape of the interface should have significant influence on

water flow. Locations with greater depth to the interface tended to be concave (negative

PROF) and convergent (negative PLAN) areas, which would accumulate any water flow

being re-directed at an interface. Locations with shallow interfaces tended to be convex

(positive PROF) and divergent (positive PLAN), which would tend to shed any water that

might be redirected by an interface.

The spatial pattern of the soil horizon interface shape had significant influence on

the continuity of soil water flow across the interface. The influence of the horizon

interface shape was: 1) different for transient infiltration versus steady state flow (under

constant water application); 2) dependent on the average soil water flow; 3) dependent on

spatial scale; and 4) influenced by a spatial covariance of the interface shape and soil

hydraulic properties (as expressed by the steady state soil water content).

The analysis of the measurements: 1) validates the sensitivity of the proposed

methods in Sections 2 and 3 in that measured patterns of local soil water fluxes are

consistent with conceptual models of water flow in layered soils and soil genesis; and 2)

indicates the need for in-depth spatial- and scale-dependent analysis of local soil water

flux patterns to discern the scale(s) at which soil horizon interfaces influence soil water

flow in the field. The consistency of the observed patterns of water flow with conceptual

models of soil genesis is particularly important for soil horizon interfaces. Soil horizons

are different than geological layers, for example, in that the interface or boundary

between two horizons (i.e., A and B) is a result of pedogenic processes such as

weathering and translocation of pedogenic salts and clays, rather than a more abrupt

change in depositional environment or sediments. For this particular soil, the average

hydraulic properties in the A and B horizons are very similar, but it is likely pedogenic

processes that have created to the spatial covariance between A and B horizon hydraulic

properties and the shape of the soil horizon interface. These type of complex, scale-

dependent spatial covariance patterns between soil horizons are not presently accounted

for by pedotransfer functions.

Finally, the measured spatial covariant relationships indicate that the nature of the

soil horizon interface will significantly influence solute transport including (in particular)

the validity of interpretation of measured solute travel time probability density functions

(pdfs) and the estimation of pedon-scale travel time pdfs. This is illustrated in Table 4.2

which shows an inverse relationship between the ratio of average solute travel times (0-

25 cm depth versus 0-60 cm depth) and the ratio of travel time variance for the same

depth increments. The travel time data could be interpreted (incorrectly) as a transition

from a convection-dispersion process at low flow rates to stochastic-convective process

at high flow rates. The inverse relationship is a result of the flux-dependent negative

correlation (spatial) between water flux in the A and B horizon with convective stochastic

flow dominating in all flow rates. The significant flux dependent negative covariance of

travel time velocity/soil water flux across the horizon interface would not be predicted (or

accounted for in pedo-transfer function models) given the similarity of the A and B

horizon average soil hydraulic properties and similarity in average steady state soil water

contents. This effect is an interface property governed by the spatial pattern/shape of the

interface and its spatial covariance with soil hydraulic properties above and below the

interface.

4.6. References

Bochkanov, S. 2007. TDEVD unit coded in Delphi. http://www.alglib.net/eigen /symmetric/tdevd.php

Brillinger, D. R. 1981. Time series: Data analysis and theory, 2nd Edition. Holden Day, San Francisco.

Clothier, B. E., M. B. Kirkham, and J. E. McLean. 1992. In situ measurement of the effective transport volume for solute moving through soil. Soil Sci. Soc. Am. J. 56:733-736.

Dagan, G, and E. Bresler. 1979. Solute dispersion in unsaturated heterogeneous soil at field scale: I. Theory. Soil Sci. Soc. Am J. 43:461-467.

Duffy, C. J., and L. W. Gelhar. 1985. A frequency domain approach to water quality modeling in groundwater: Theory. Water Resour. Res. 21: 1175-1184.

Gábor, B., P. Muller, and P. Vreman. 2006. Free Pascal version 2.0.4.i386. http://www.freepascal.org/

Halliday, D. M., J. R. Rosenberg, A. M. Amjad, P. Breeze, B. A. Conway, and S. F. Farmer. 1995. A framework for the analysis of mixed time series/point process data – theory and application to the study of physiological tremor, single motor unit discharges and electrograms. Prog. Biophys. Molec. Biol. 64:237-278.

Kachanoski, R. G. and E. de Jong. 1988. Scale dependence and the temporal persistence of spatial patterns of soil water storage. Water Resour. Res. 24:85-91.

Kachanoski, R. G., D. E. Rolston, and E. de Jong. 1985. Spatial and spectral relationships of soil horizon properties and microtophography. I. Density and thickness of A horizon. Soil Sci. Soc. Am. J. 49:804-812.

Kachanoski, R. G., J. L. Thony, M. Vauclin, G. Vachaud, and R. Laty. 1994. Measurement of solute transport during constant infiltration from a point source. Soil Sci. Soc. Am. J. 58:304-309.

Noborio, K., R. G. Kachanoski, and C. S. Tan. 2006. Solute transport measurement under transient field conditions using time domain reflectometry. Vadose Zone J. 5:412-418.

Pennock, D. J., B. J. Zebarth, and E. de Jong. 1987. Landform classification and soil distribution in hummocky terrain, Saskatchewan, Canada. Geoderma 40:297-315.

Percival, D. B., and A. T. Walden. 1993. Spectral analysis for physical applications: Multitaper and conventional univariate techniques. Cambridge University Press, New York.

Roth, K. and K. Hammel. 1996. Transport of conservative chemical through an unsaturated two-dimensional Miller-similar medium with steady state flow. Water Resour. Res. 32:1653-1663.

Russo, D, and G. Dagan. 1991. On solute transport in a heterogeneous formation under saturated and unsaturated water flows. Water Resour. Res. 27:285-292.

Shumway, R. H. 1988. Applied statistical time series analysis. Prentice Hall, Englewood Cliffs.

Si, B. C. 1998. Constant flux infiltration and drainage in unsaturated heterogeneous soils. Ph.D. diss. Univ. of Guelph, Guelph, ON, Canada.

Si, B. C. 2008. Spatial scaling analyses of soil physical properties: A review of spectral and wavelet methods. Vadose Zone J. 7:547-562.

Si, B. C., and R. G. Kachanoski. 2003. Measurement of local soil water flux during field solute transport experiments. Soil Sci. Soc. Am J. 67:730-736.

Slepian, D. 1978. Prolate spheroidal wave functions, Fourier analysis and uncertainty: V. The discrete case. Bell System Technical Jour. 57:1371-1430.

Srivastava, R., and T. C. J. Yeh. 1991. Analytical solutions for one-dimensional, transient infiltration toward the water table in homogeneous and layered soils. Water Resour. Res. 27:753-762.

Thomson, D. J. 1982. Spectrum estimation and harmonic analysis. IEEE Proc. 70(9): 1055-1096.

Ursino, N., K. Roth, T. Gimmi, and H. Flühler. 2000. Upscaling of anisotropy in unsaturated Miller-similar porous media. Water Resour. Res. 36:421-430.

Vernon, F. L. 1994. Jackknifed multiple-window spectra and coherence applied to seismic data. IEEE ICASSP-94 Proc. VI: VI93 – VI96.

Yeh, T. C. J. 1989. One-dimensional steady state infiltration in heterogeneous soils. Water Resour. Res. 25:2149-2158.

Yeh, T. C. J., L. W. Gelhar and A. L. Gutjahr. 1985a. Stochastic analysis of unsaturated flow in heterogeneous soils: 1. Statistically isotropic media. Water Resour. Res. 21:447-456.

Yeh, T. C. J., L. W. Gelhar and A. L. Gutjahr. 1985b. Stochastic analysis of unsaturated flow in heterogeneous soils: 2. Statistically anisotropic media with variable α. Water Resour. Res. 21:457-464.

Yeh, T. C. J., L. W. Gelhar and A. L. Gutjahr. 1985c. Stochastic analysis of unsaturated flow in heterogeneous soils: 3. Observations and applications. Water Resour. Res. 21:465-471.

Young, M., and I. S. Evans. 1978. Statistical characterization of altitude matrices. Report No. 5. Grant DA-ERO-591-7.-G0040, Dept. of Geog., University of Durham, England.

Winterhalder, M., B. Schelter, W. Hesse, K. Schwab, L. Leistritz, D. Klan, R. Bauer, J. Timmer, and H. Witte. 2005. Comparison of linear signal processing techniques to infer directed interactions in multivariate neural systems. Signal Processing. 85:2137-2160.

Table 4-1: Correlation matrix of transient, local soil water fluxes and horizon interface morphology (N=91)

	DEPTH	PROF	PLAN	$q_{w|A,tr}(1.3)$	$q_{w|B,tr}(1.3)$	$q_{w|A,tr}(2.7)$	$q_{w|B,tr}(2.7)$
DEPTH	1						
PROF	-0.47***	1					
PLAN	-0.24*	0.17	1				
$q_{w|A,tr}(1.3)$	0.16	-0.2	0.18	1			
$q_{w|B,tr}(1.3)$	0	0.07	0.03	0.5***	1		
$q_{w|A,tr}(2.7)$	0.13	-0.05	-0.12	0.43***	0.35***	1	
$q_{w|B,tr}(2.7)$	-0.11	-0.01	-0.01	0.45***	0.54***	0.33**	1
$q_{w|A,tr}(7.0)$	0.25*	-0.17	0.14	0.4***	0.38***	0.57***	0.15
$q_{w|B,tr}(7.0)$	0.04	-0.01	0.02	0.34**	0.55***	0.33**	0.52***
$q_{w|A,tr}(10.6)$	0.13	-0.2	-0.01	0.37***	0.34***	0.61***	0.3**
$q_{w|B,tr}(10.6)$	-0.08	0.05	0.1	0.29**	0.45***	0.16	0.4***
$\bar{\theta}_{A,ss}(2.7)$	-0.02	0.04	-0.13	0.14	0.17	0.52***	0.26*
$\bar{\theta}_{B,ss}(2.7)$	0.24*	-0.08	-0.01	0.27**	0.43***	0.31**	0.51***
$\bar{\theta}_{A,ss}(7.0)$	-0.12	0.05	-0.12	0.17	0.15	0.48***	0.28**
$\bar{\theta}_{B,ss}(7.0)$	0.25*	-0.04	0.01	0.27*	0.44***	0.37***	0.46***
$\bar{\theta}_{A,ss}(10.6)$	-0.13	0.06	-0.13	0.14	0.13	0.47***	0.27**
$\bar{\theta}_{B,ss}(10.6)$	0.24*	-0.06	0.02	0.27**	0.45***	0.37***	0.46***
$W_{A,ss}(2.7)$	0.62***	-0.1	-0.15	0.25*	0.17	0.42***	0.11
$W_{B,ss}(2.7)$	-0.3**	0.03	0.04	0.14	0.36***	0.24*	0.53***
$W_{A,ss}(7.0)$	0.56***	-0.08	-0.16	0.29**	0.18	0.44***	0.15
$W_{B,ss}(7.0)$	-0.29**	0.08	0.06	0.14	0.38***	0.31**	0.49***
$W_{A,ss}(10.6)$	0.59***	-0.09	-0.17	0.27**	0.17	0.42***	0.13
$W_{B,ss}(10.6)$	-0.32**	0.06	0.07	0.13	0.38***	0.3**	0.48***
$\bar{t}_{A,ss}(2.7)$	0.19	-0.11	-0.03	-0.11	0	-0.09	0.05
$\bar{t}_{B,ss}(2.7)$	-0.11	0.05	0.02	0.07	-0.06	-0.05	-0.04
$\bar{t}_{A,ss}(7.0)$	0.23*	-0.16	-0.25*	0.14	0.18	0.13	0.25*
$\bar{t}_{B,ss}(7.0)$	-0.25*	0.12	0.17	-0.22*	-0.22*	-0.24*	-0.23*
$\bar{t}_{A,ss}(10.6)$	0.27*	-0.11	-0.16	-0.11	-0.11	0.03	-0.06
$\bar{t}_{B,ss}(10.6)$	-0.22*	0.17	-0.04	-0.2	-0.23*	-0.21*	-0.25*
$q_{w|A,ss}(2.7)$	0.27**	0.03	-0.1	0.32**	0.17	0.41***	0.1
$q_{w|B,ss}(2.7)$	-0.07	-0.05	-0.01	0.02	0.22*	0.14	0.35***
$q_{w|A,ss}(7.0)$	0.28**	0.03	0.06	0.11	-0.02	0.23*	-0.11
$q_{w|B,ss}(7.0)$	0	-0.06	-0.1	0.26*	0.42***	0.38***	0.48***
$q_{w|A,ss}(10.6)$	0.15	0.05	0.01	0.32**	0.25*	0.3**	0.17
$q_{w|B,ss}(10.6)$	0	-0.13	0.06	0.18	0.34***	0.25*	0.38***

* Significant at the 0.05 probability level
** Significant at the 0.01 probability level
*** Significant at the 0.001 probability level

Table 4-1 Continued

	$q_{w|A,tr}(7.0)$	$q_{w|B,tr}(7.0)$	$q_{w|A,tr}(10.6)$	$q_{w|B,tr}(10.6)$	$\bar{\theta}_{A,ss}(2.7)$	$\bar{\theta}_{B,ss}(2.7)$	$\bar{\theta}_{A,ss}(7.0)$
DEPTH							
PROF							
PLAN							
$q_{w|A,tr}(1.3)$							
$q_{w|B,tr}(1.3)$							
$q_{w|A,tr}(2.7)$							
$q_{w|B,tr}(2.7)$							
$q_{w|A,tr}(7.0)$	1						
$q_{w|B,tr}(7.0)$	0.3**	1					
$q_{w|A,tr}(10.6)$	0.64***	0.3**	1				
$q_{w|B,tr}(10.6)$	0.11	0.61***	0.19	1			
$\bar{\theta}_{A,ss}(2.7)$	0.22*	0.24*	0.36***	0.08	1		
$\bar{\theta}_{B,ss}(2.7)$	0.27**	0.51***	0.19	0.38***	0.03	1	
$\bar{\theta}_{A,ss}(7.0)$	0.2	0.18	0.37***	0.08	0.94***	0.01	1
$\bar{\theta}_{B,ss}(7.0)$	0.32**	0.51***	0.23*	0.35***	0.05	0.96***	0
$\bar{\theta}_{A,ss}(10.6)$	0.18	0.16	0.37***	0.07	0.94***	0	0.99***
$\bar{\theta}_{B,ss}(10.6)$	0.34***	0.54***	0.25*	0.37***	0.07	0.96***	0.02
$W_{A,ss}(2.7)$	0.32**	0.23*	0.29**	0.04	0.66***	0.19	0.52***
$W_{B,ss}(2.7)$	0.12	0.42***	0.15	0.35***	0.04	0.79***	0.11
$W_{A,ss}(7.0)$	0.34**	0.2	0.32**	0.04	0.7***	0.18	0.64***
$W_{B,ss}(7.0)$	0.17	0.43***	0.19	0.33**	0.06	0.78***	0.1
$W_{A,ss}(10.6)$	0.32**	0.18	0.31**	0.03	0.67***	0.18	0.6***
$W_{B,ss}(10.6)$	0.18	0.45***	0.2	0.35***	0.07	0.75***	0.12
$\bar{t}_{A,ss}(2.7)$	-0.06	0.26*	-0.02	0.01	0.17	0.14	0.1
$\bar{t}_{B,ss}(2.7)$	0.01	-0.24*	-0.07	-0.04	-0.21*	-0.07	-0.15
$\bar{t}_{A,ss}(7.0)$	0.04	0.19	0.05	0.06	0.13	0.27**	0.07
$\bar{t}_{B,ss}(7.0)$	-0.25*	-0.35***	-0.25*	-0.16	-0.11	-0.13	-0.08
$\bar{t}_{A,ss}(10.6)$	-0.03	-0.08	-0.05	-0.17	0.27*	0.12	0.23*
$\bar{t}_{B,ss}(10.6)$	-0.14	-0.38***	-0.13	-0.25*	-0.2	-0.38***	-0.18
$q_{w|A,ss}(2.7)$	0.3**	-0.02	0.28**	0.03	0.38***	0.04	0.35***
$q_{w|B,ss}(2.7)$	0.03	0.41***	0.13	0.23*	0.2	0.47***	0.18
$q_{w|A,ss}(7.0)$	0.24*	-0.02	0.2	-0.01	0.45***	-0.09	0.44***
$q_{w|B,ss}(7.0)$	0.3**	0.52***	0.31**	0.31**	0.1	0.61***	0.11
$q_{w|A,ss}(10.6)$	0.28**	0.25*	0.3**	0.23*	0.26*	0.03	0.24*
$q_{w|B,ss}(10.6)$	0.17	0.46***	0.21*	0.34***	0.16	0.62***	0.18

Table 4-1 Continued

	$\bar{\theta}_{B,ss}(7.0)$	$\bar{\theta}_{A,ss}(10.6)$	$\bar{\theta}_{B,ss}(10.6)$	$W_{A,ss}(2.7)$	$W_{B,ss}(2.7)$	$W_{A,ss}(7.0)$	$W_{B,ss}(7.0)$
DEPTH							
PROF							
PLAN							
$q_{w|A,tr}(1.3)$							
$q_{w|B,tr}(1.3)$							
$q_{w|A,tr}(2.7)$							
$q_{w|B,tr}(2.7)$							
$q_{w|A,tr}(7.0)$							
$q_{w|B,tr}(7.0)$							
$q_{w|A,tr}(10.6)$							
$q_{w|B,tr}(10.6)$							
$\bar{\theta}_{A,ss}(2.7)$							
$\bar{\theta}_{B,ss}(2.7)$							
$\bar{\theta}_{A,ss}(7.0)$							
$\bar{\theta}_{B,ss}(7.0)$	1						
$\bar{\theta}_{A,ss}(10.6)$	-0.01	1					
$\bar{\theta}_{B,ss}(10.6)$	0.99***	0.01	1				
$W_{A,ss}(2.7)$	0.23*	0.51***	0.24*	1			
$W_{B,ss}(2.7)$	0.73***	0.1	0.74***	-0.29**	1		
$W_{A,ss}(7.0)$	0.2	0.63***	0.21*	0.97***	-0.24*	1	
$W_{B,ss}(7.0)$	0.79***	0.09	0.79***	-0.24*	0.96***	-0.22*	1
$W_{A,ss}(10.6)$	0.21	0.59***	0.21*	0.97***	-0.27*	1***	-0.24*
$W_{B,ss}(10.6)$	0.76***	0.11	0.77***	-0.26*	0.97***	-0.23*	0.99***
$\bar{t}_{A,ss}(2.7)$	0.12	0.1	0.14	0.28**	0	0.24*	-0.03
$\bar{t}_{B,ss}(2.7)$	-0.07	-0.13	-0.1	-0.26*	0.02	-0.22*	0.03
$\bar{t}_{A,ss}(7.0)$	0.3**	0.07	0.29**	0.3**	0.07	0.28**	0.11
$\bar{t}_{B,ss}(7.0)$	-0.18	-0.07	-0.19	-0.28**	0.03	-0.27*	-0.01
$\bar{t}_{A,ss}(10.6)$	0.13	0.23*	0.13	0.4***	-0.08	0.4***	-0.06
$\bar{t}_{B,ss}(10.6)$	-0.36***	-0.18	-0.38***	-0.28**	-0.22*	-0.28**	-0.21*
$q_{w|A,ss}(2.7)$	0.09	0.34***	0.07	0.5***	-0.17	0.52***	-0.11
$q_{w|B,ss}(2.7)$	0.42***	0.16	0.45***	0.05	0.51***	0.04	0.47***
$q_{w|A,ss}(7.0)$	-0.1	0.43***	-0.09	0.52***	-0.27**	0.57***	-0.29**
$q_{w|B,ss}(7.0)$	0.65***	0.09	0.66***	0.03	0.61***	0.04	0.67***
$q_{w|A,ss}(10.6)$	0.02	0.23*	0.03	0.33**	-0.1	0.35***	-0.11
$q_{w|B,ss}(10.6)$	0.61***	0.18	0.64***	0.04	0.63***	0.06	0.63***

Table 4-1 Continued

	$W_{A,ss}(10.6)$	$W_{B,ss}(10.6)$	$\bar{t}_{A,ss}(2.7)$	$\bar{t}_{B,ss}(2.7)$	$\bar{t}_{A,ss}(7.0)$	$\bar{t}_{B,ss}(7.0)$	$\bar{t}_{A,ss}(10.6)$
DEPTH							
PROF							
PLAN							
$q_{w|A,tr}(1.3)$							
$q_{w|B,tr}(1.3)$							
$q_{w|A,tr}(2.7)$							
$q_{w|B,tr}(2.7)$							
$q_{w|A,tr}(7.0)$							
$q_{w|B,tr}(7.0)$							
$q_{w|A,tr}(10.6)$							
$q_{w|B,tr}(10.6)$							
$\bar{\theta}_{A,ss}(2.7)$							
$\bar{\theta}_{B,ss}(2.7)$							
$\bar{\theta}_{A,ss}(7.0)$							
$\bar{\theta}_{B,ss}(7.0)$							
$\bar{\theta}_{A,ss}(10.6)$							
$\bar{\theta}_{B,ss}(10.6)$							
$W_{A,ss}(2.7)$							
$W_{B,ss}(2.7)$							
$W_{A,ss}(7.0)$							
$W_{B,ss}(7.0)$							
$W_{A,ss}(10.6)$	1						
$W_{B,ss}(10.6)$	-0.26*	1					
$\bar{t}_{A,ss}(2.7)$	0.24*	-0.02	1				
$\bar{t}_{B,ss}(2.7)$	-0.21*	0.01	-0.76***	1			
$\bar{t}_{A,ss}(7.0)$	0.28**	0.09	0.27*	-0.16	1		
$\bar{t}_{B,ss}(7.0)$	-0.27*	0	-0.3**	0.38***	-0.56***	1	
$\bar{t}_{A,ss}(10.6)$	0.41***	-0.07	0.36***	-0.13	0.4***	-0.15	1
$\bar{t}_{B,ss}(10.6)$	-0.27**	-0.22*	-0.32**	0.34***	-0.34**	0.44***	-0.47***
$q_{w|A,ss}(2.7)$	0.52***	-0.14	-0.66***	0.48***	0.01	0.05	-0.02
$q_{w|B,ss}(2.7)$	0.02	0.49***	0.68***	-0.79***	0.16	-0.28**	0.06
$q_{w|A,ss}(7.0)$	0.56***	-0.27**	-0.04	-0.02	-0.61***	0.27*	0
$q_{w|B,ss}(7.0)$	0.02	0.66***	0.19	-0.24*	0.48***	-0.73***	0.05
$q_{w|A,ss}(10.6)$	0.34***	-0.11	-0.19	-0.02	-0.19	-0.04	-0.69***
$q_{w|B,ss}(10.6)$	0.05	0.65***	0.2	-0.23*	0.23*	-0.3**	0.34***

126

Table 4-1 Continued

	$\bar{t}_{B,ss}(10.6)$	$q_{w|A,ss}(2.7)$	$q_{w|B,ss}(2.7)$	$q_{w|A,ss}(7.0)$	$q_{w|B,ss}(7.0)$	$q_{w|A,ss}(10.6)$	$q_{w|B,ss}(10.6)$
DEPTH							
PROF							
PLAN							
$q_{w|A,tr}(1.3)$							
$q_{w|B,tr}(1.3)$							
$q_{w|A,tr}(2.7)$							
$q_{w|B,tr}(2.7)$							
$q_{w|A,tr}(7.0)$							
$q_{w|B,tr}(7.0)$							
$q_{w|A,tr}(10.6)$							
$q_{w|B,tr}(10.6)$							
$\bar{\theta}_{A,ss}(2.7)$							
$\bar{\theta}_{B,ss}(2.7)$							
$\bar{\theta}_{A,ss}(7.0)$							
$\bar{\theta}_{B,ss}(7.0)$							
$\bar{\theta}_{A,ss}(10.6)$							
$\bar{\theta}_{B,ss}(10.6)$							
$W_{A,ss}(2.7)$							
$W_{B,ss}(2.7)$							
$W_{A,ss}(7.0)$							
$W_{B,ss}(7.0)$							
$W_{A,ss}(10.6)$							
$W_{B,ss}(10.6)$							
$\bar{t}_{A,ss}(2.7)$							
$\bar{t}_{B,ss}(2.7)$							
$\bar{t}_{A,ss}(7.0)$							
$\bar{t}_{B,ss}(7.0)$							
$\bar{t}_{A,ss}(10.6)$							
$\bar{t}_{B,ss}(10.6)$	1						
$q_{w|A,ss}(2.7)$	0.09	1					
$q_{w|B,ss}(2.7)$	-0.4***	-0.51***	1				
$q_{w|A,ss}(7.0)$	0.07	0.42***	-0.12	1			
$q_{w|B,ss}(7.0)$	-0.44***	-0.11	0.51***	-0.39***	1		
$q_{w|A,ss}(10.6)$	0.26*	0.43***	-0.03	0.43***	-0.04	1	
$q_{w|B,ss}(10.6)$	-0.85***	-0.14	0.52***	-0.16	0.62***	-0.28**	1

Table 4-2: Summary of solute travel times and travel time variance for each water application rate.

Applied Water (cm day^{-1})	Average travel time			Travel time variance		
	0-25 cm[†]	0-60 cm[‡]	ratio	0-25 cm	0-60 cm	ratio
2.7	1.91	4.42	2.31	0.0707	0.1032	1.46
7.0	1.03	2.05	2.05	0.0109	0.0242	2.22
10.6	0.70	1.32	1.89	0.0055	0.0165	3.00

† measured with short (25 cm) TDR probe

‡ measured with long (60 cm) TDR probe
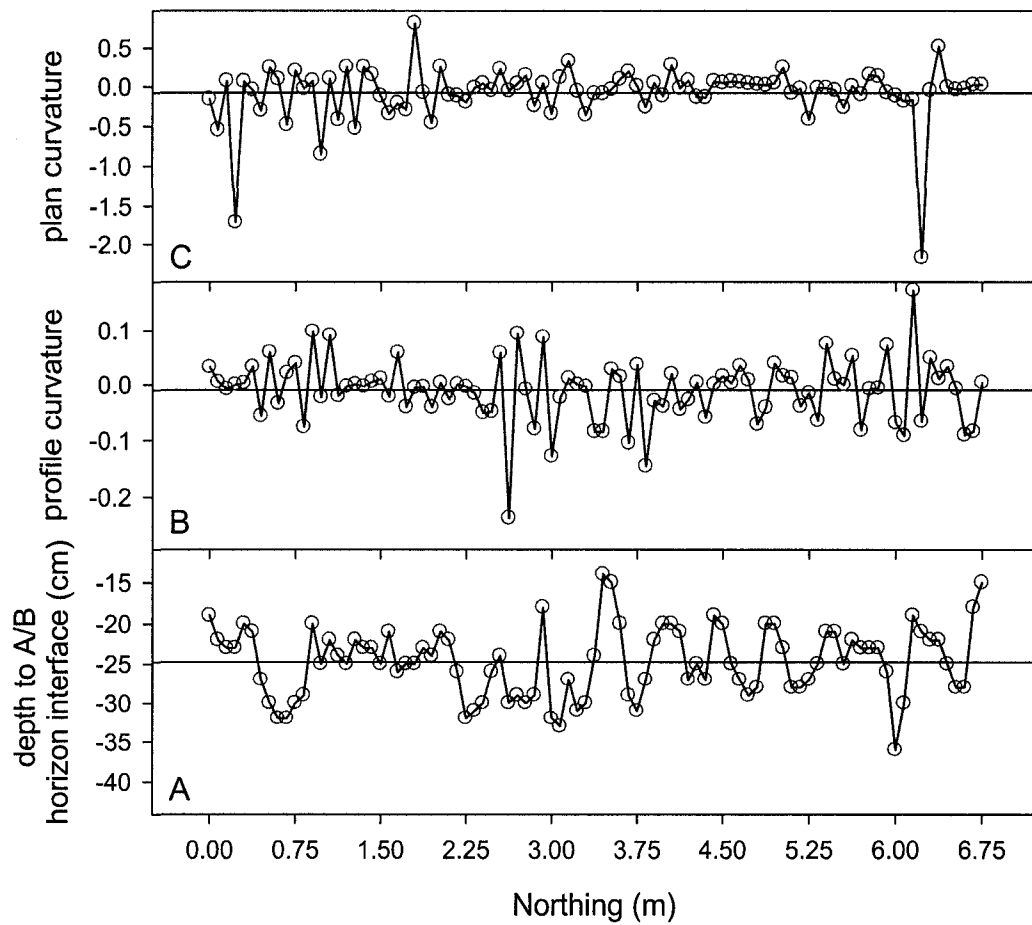
Figure 4-1: Spatial pattern of A/B horizon interface morphology: A) depth to horizon interface along the TDR probe transect (zero = soil surface); B) interface profile curvature (negative = concave curvature; positive = convex curvature); C) interface plan curvature (negative = concave curvature; positive = convex curvature. The horizontal reference lines indicate the mean of the series.
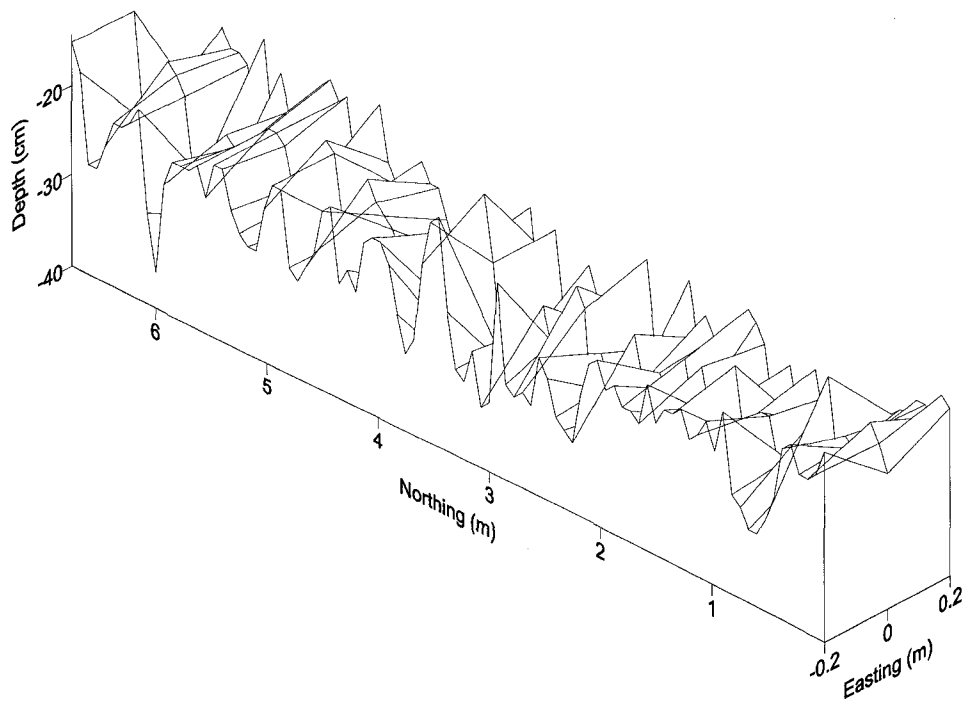
Figure 4-2: Three dimensional representation of the A/B horizon interface
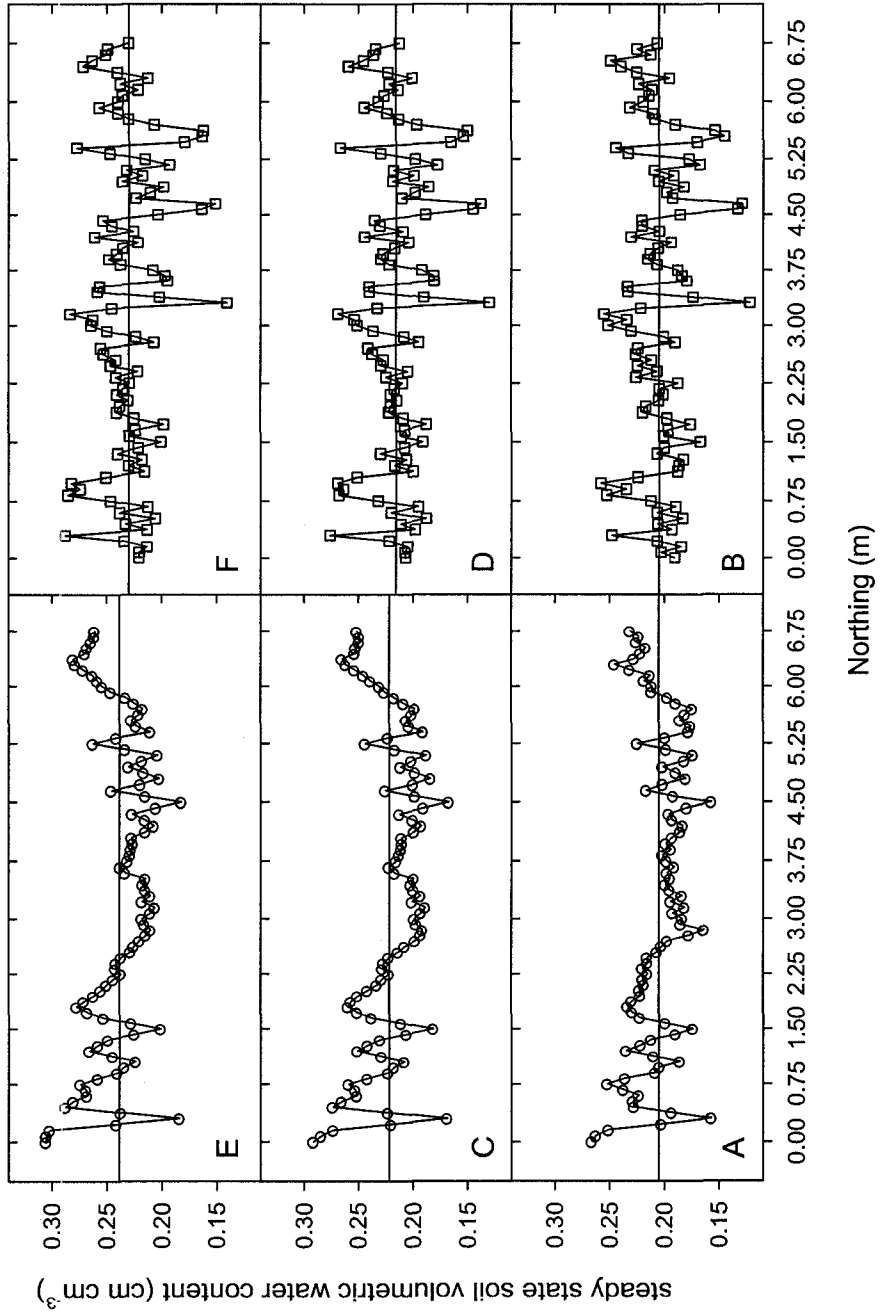
Figure 4-3: Spatial pattern of A and B horizon steady state average volumetric water content. A) & B) A and B horizon 2.7 cm day^{-1} water application rate; C) & D) A and B horizon 7.0 cm day^{-1} water application rate; E) & F) A and B horizon 10.6 cm day^{-1} water application rate.

131
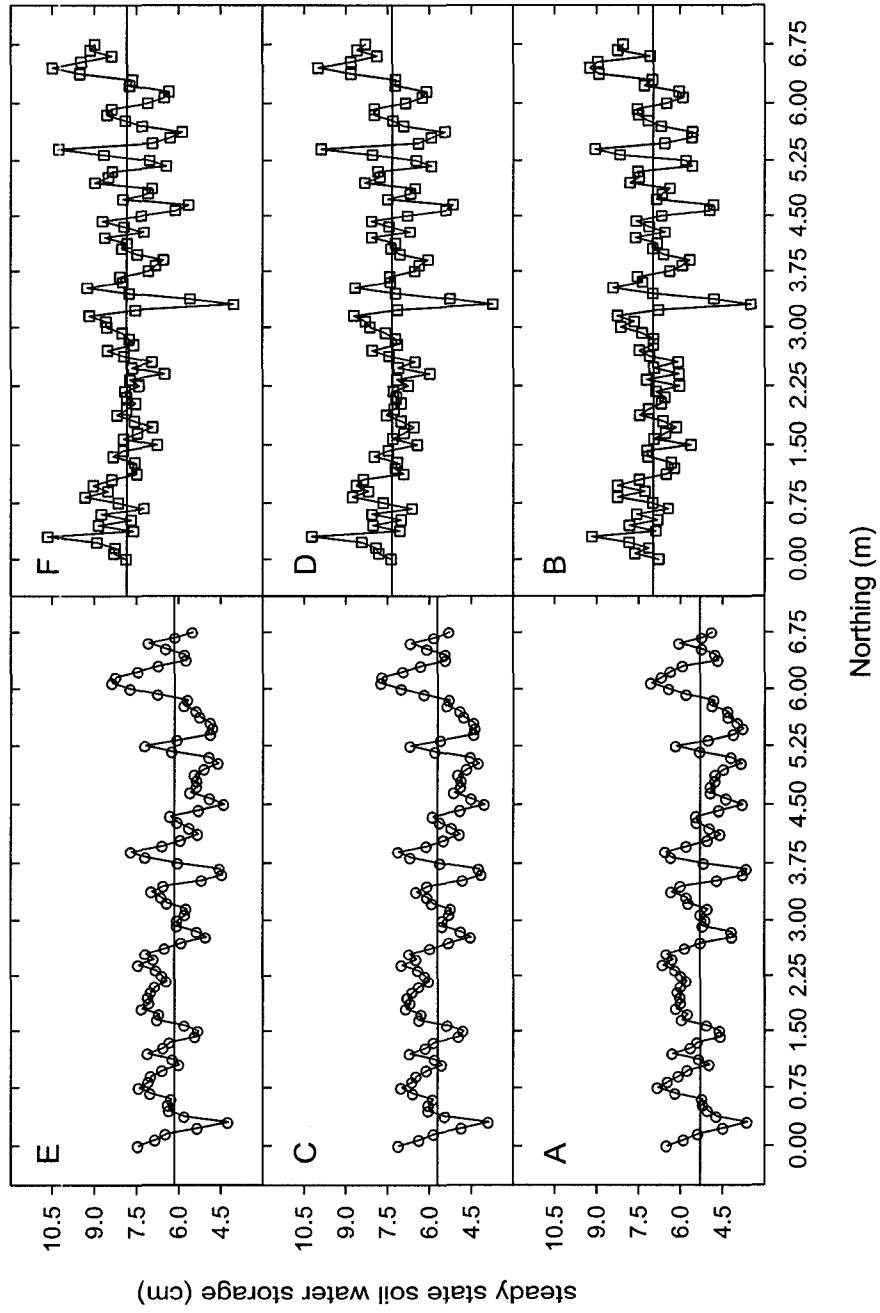
Figure 4-4: Spatial pattern of A and B horizon steady state soil water storage. A) & B) A and B horizon 2.7 cm day^{-1} water application rate; C) & D) A and B horizon 7.0 cm day^{-1} water application rate; E) & F) A and B horizon 10.6 cm day^{-1} water application rate.

132
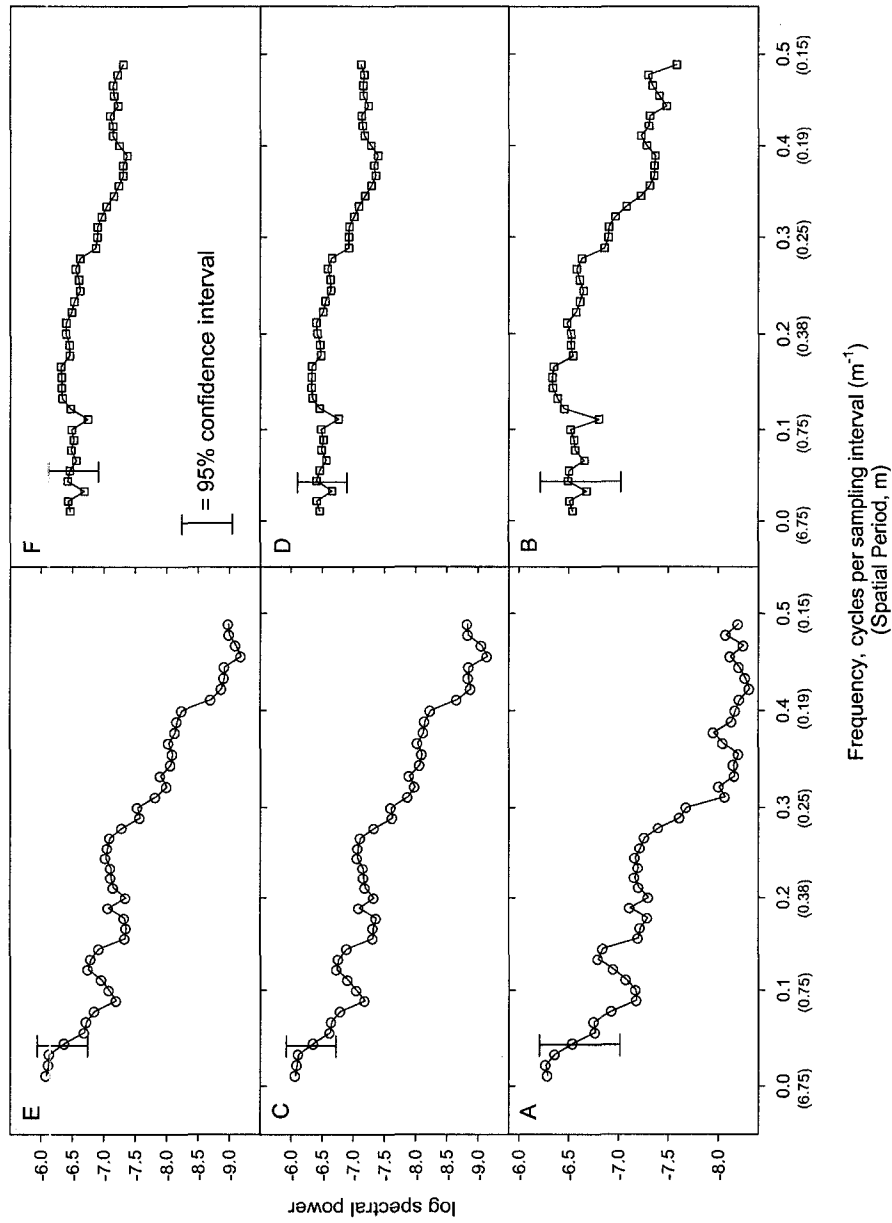
Figure 4-5: Simple multitaper power spectra of A and B horizon steady state local soil water content. A) & B) A and B horizon 2.7 cm day^{-1} water application rate; C) & D) A and B horizon 7.0 cm day^{-1} water application rate; E) & F) A and B horizon 10.6 cm day^{-1} water application rate.

133
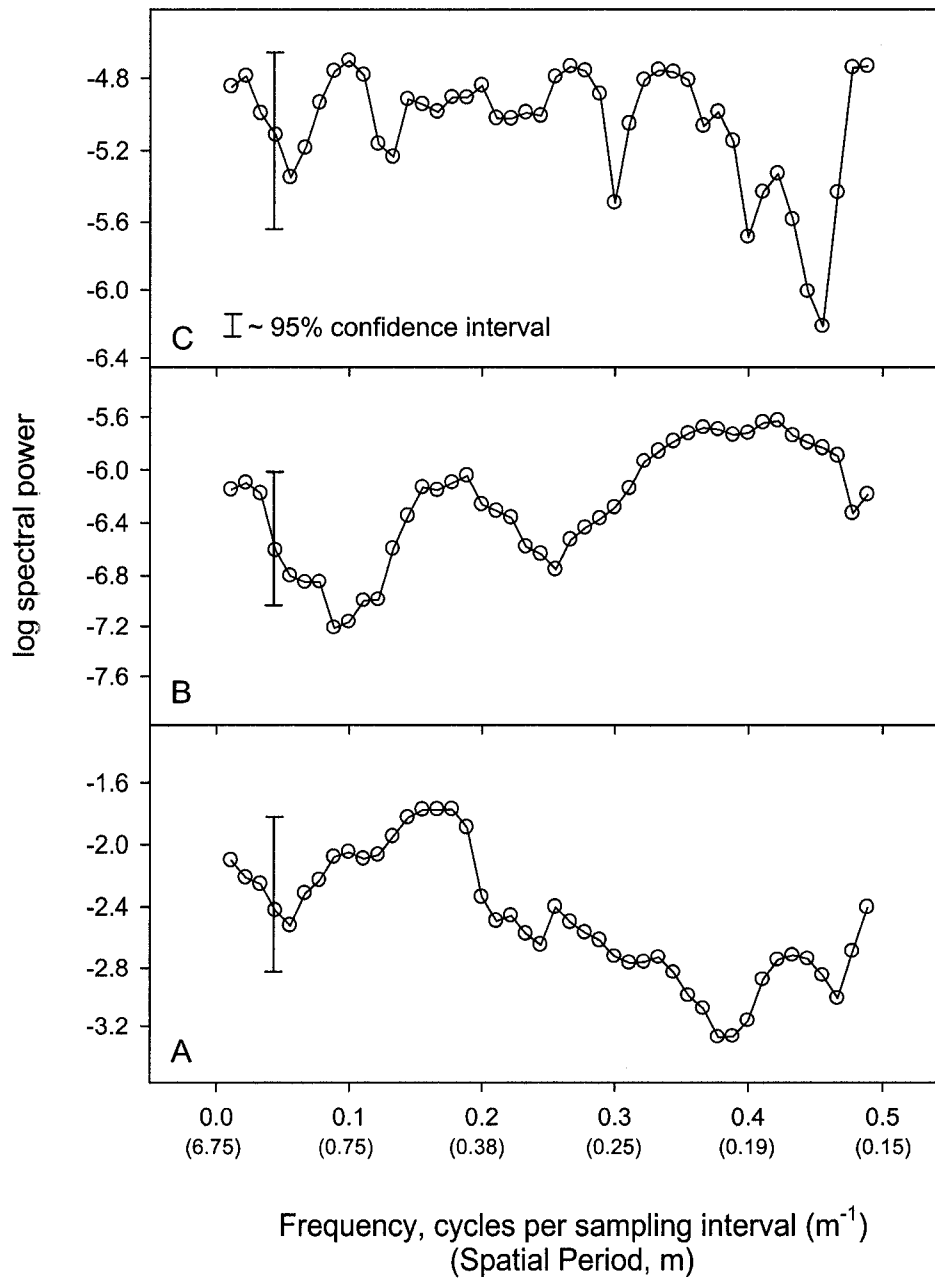
Figure 4-6: Adaptive multitaper power spectra of A/B horizon interface morphology: A) depth to horizon interface, TDR transect; B) profile curvature and C) plan curvature. Adaptive degrees of freedom did not vary appreciably across frequencies and so approximate 95% confident intervals are displayed on the figures.
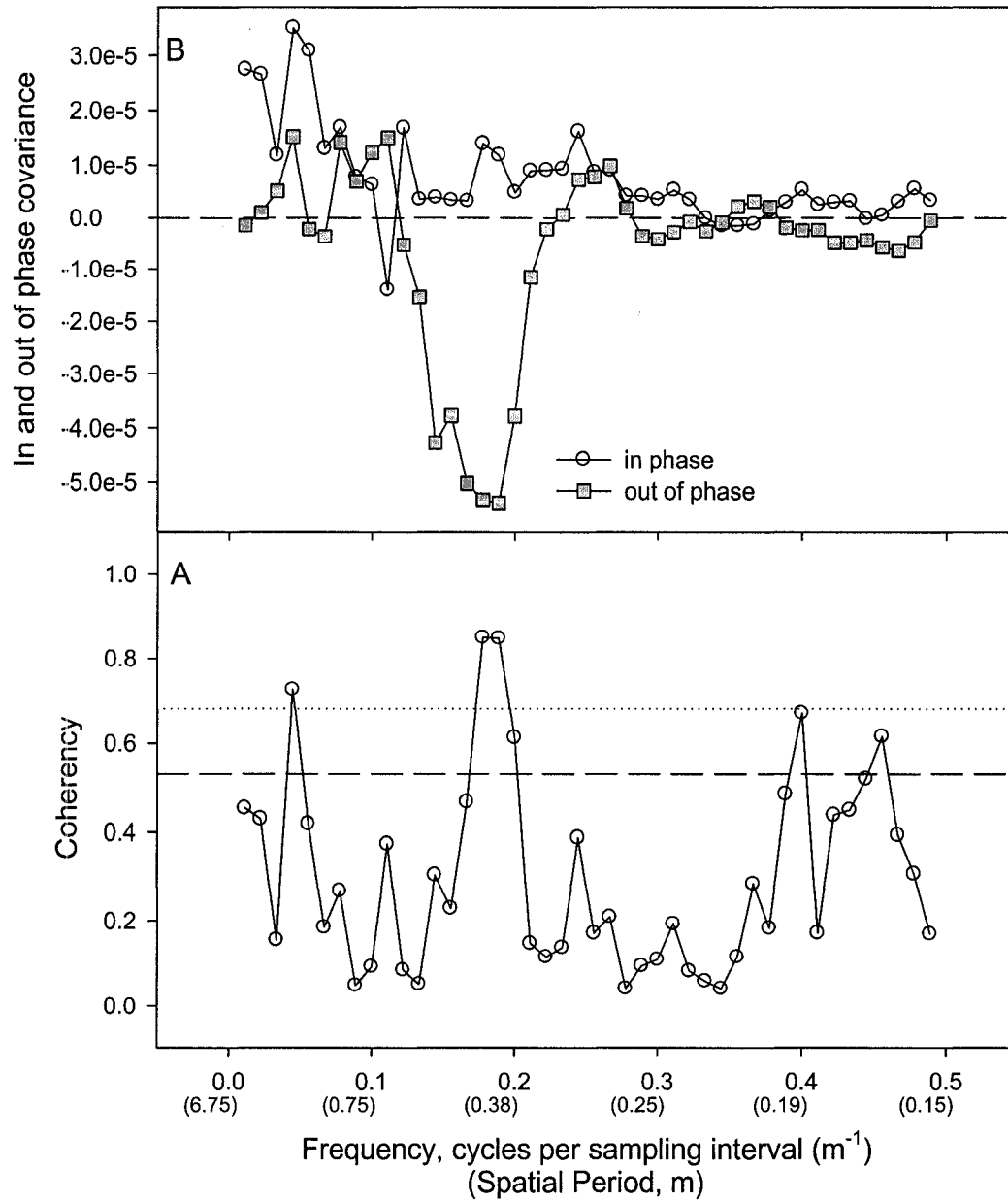
Figure 4-7: Example of coherency and in phase and out of phase covariance spectra examining the scale dependent relationship between A/B horizon interface depth and steady state B horizon water content. Spectra shown are for the 2.7 cm day^{-1} water application rate, but do not change appreciably for other rates due to the consistency in $\overline{\theta}_{B,ss}$ across all flow rates.
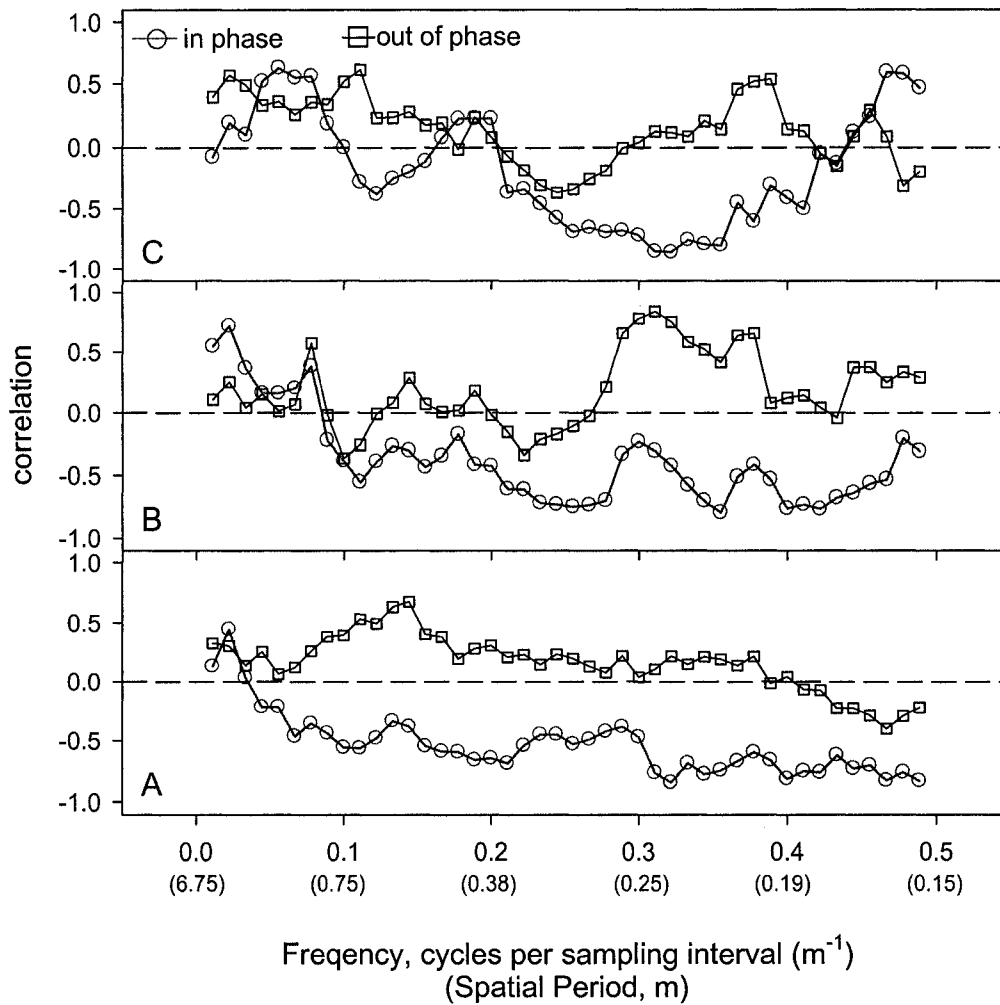
Figure 4-8: In- and out-of-phase correlation between A and B horizon steady state, local soil water flux for A) 2.7 cm day^{-1}; B) 7.0 cm day^{-1}; and C) 10.6 cm day^{-1} water application rates. Zero correlation is marked as a reference. Calculated with simple multitaper cross spectra.
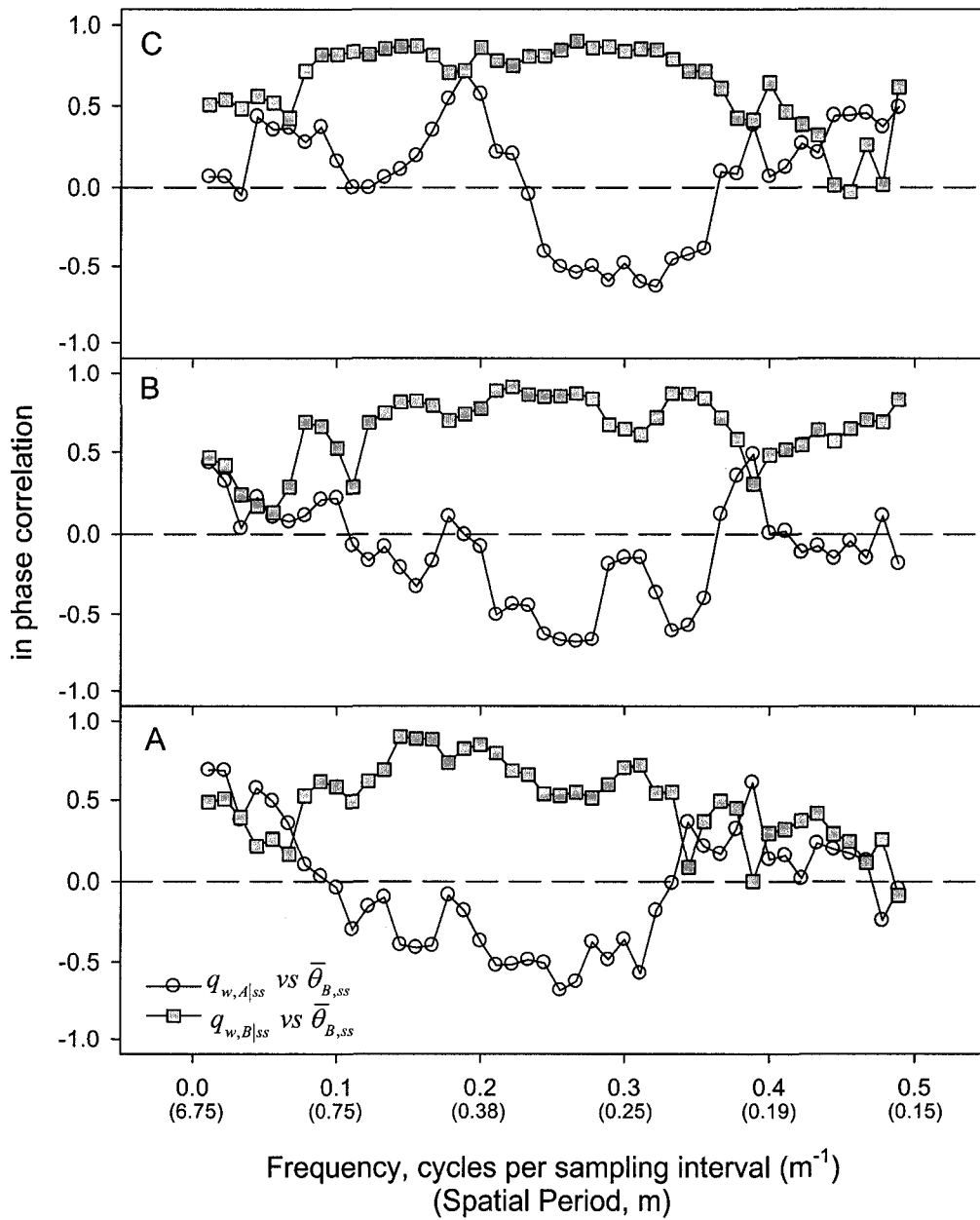
Figure 4-9: In-phase correlation as a function of scale between $q_{w,A|ss}$ and $\overline{\theta}_{B,ss}$ (circles) and $q_{w,B|ss}$ and $\overline{\theta}_{B,ss}$ (squares).
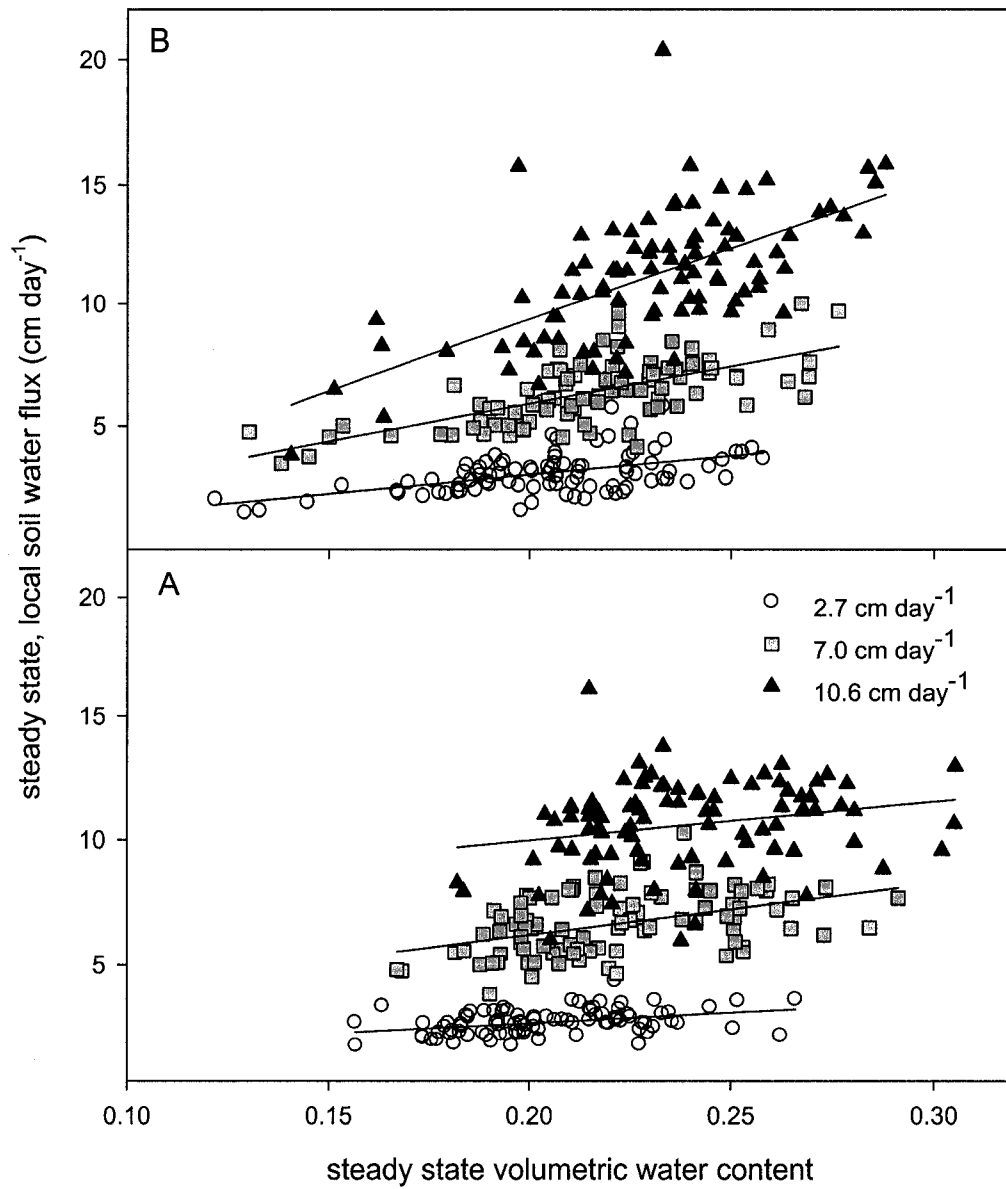
Figure 4-10: Summary of steady state local soil water flux versus steady state soil water contents, A) $q_{w,A|ss}$ *versus* $\bar{\theta}_{A,ss}$; and B) $q_{w,B|ss}$ *versus* $\bar{\theta}_{B,ss}$
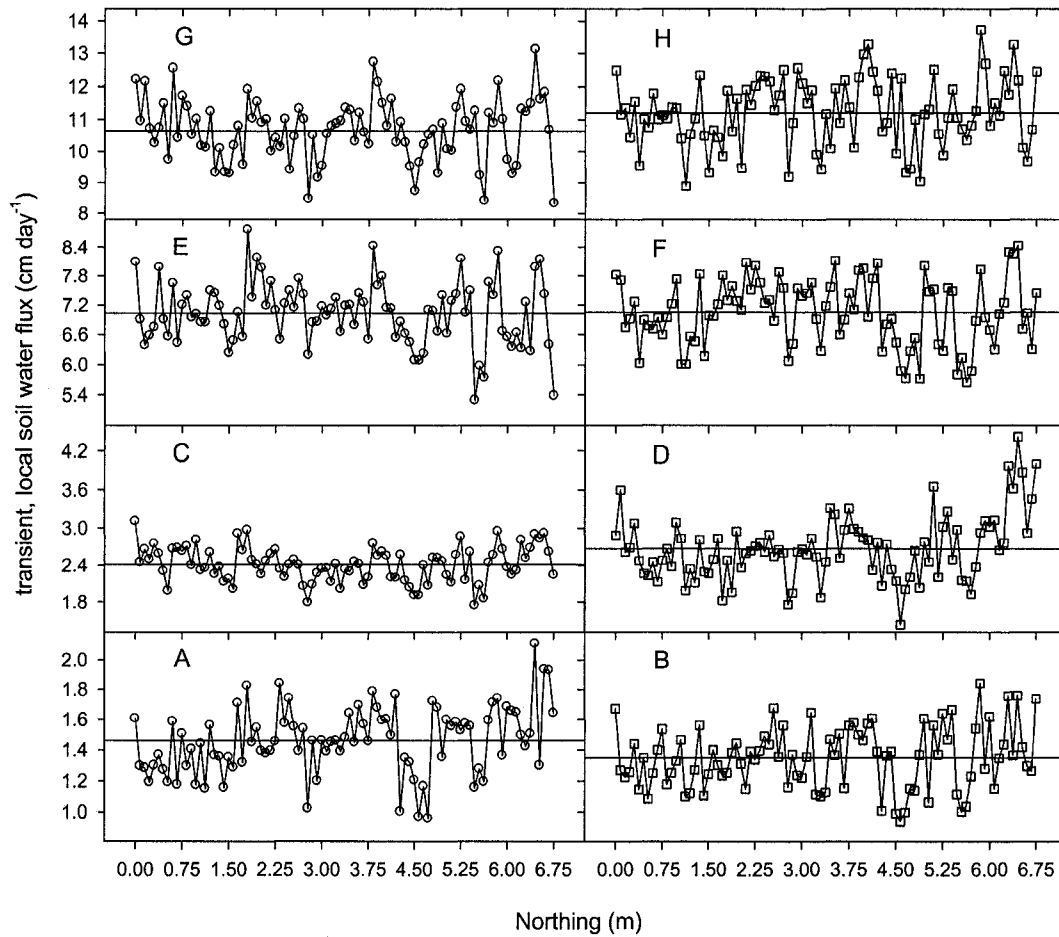
Figure 4-11: Spatial pattern of transient, local soil water fluxes: A) & B) A and B horizon fluxes for the 1.3 cm day^{-1} application rate, respectively; C) & D) A and B horizon fluxes for the 2.6 cm day^{-1} application rate; E) & F) A and B horizon fluxes for the 7.0 cm day^{-1} application rate; G) & H) A and B horizon fluxes for the 10.6 cm day^{-1} application rate. The horizontal reference lines indicate the mean of the series.
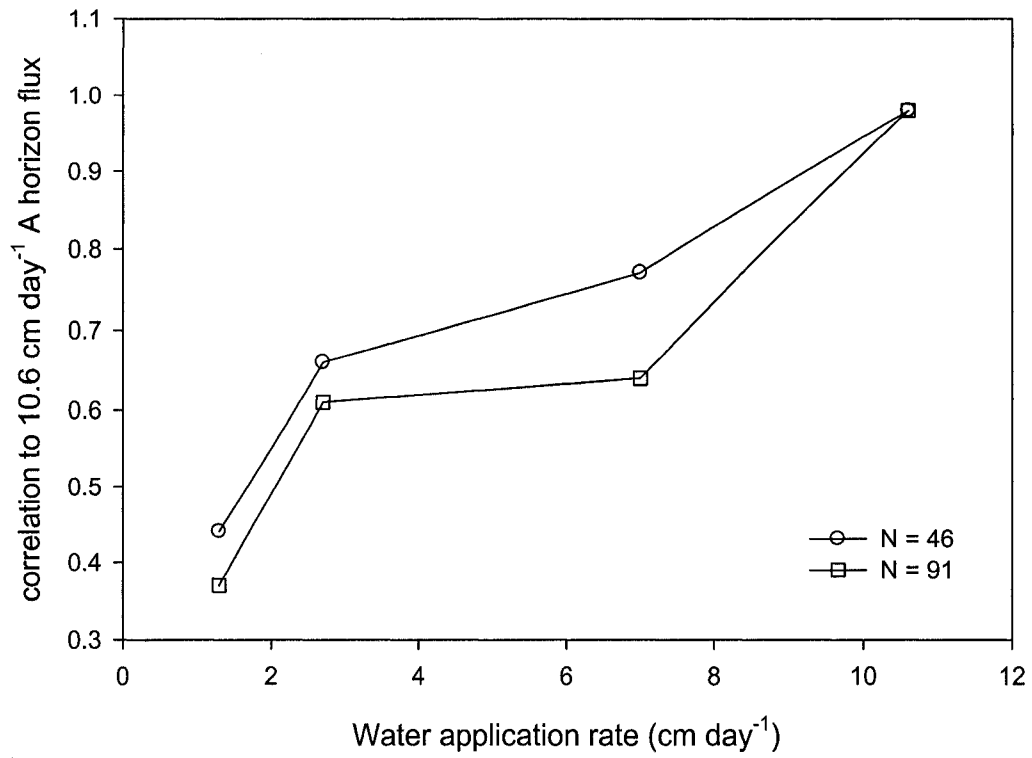
Figure 4-12: Flux dependent correlation between spatial pattern of 10.6 cm day^{-1} transient A horizon flux spatial pattern and A horizon flux patterns of all other water application rates.
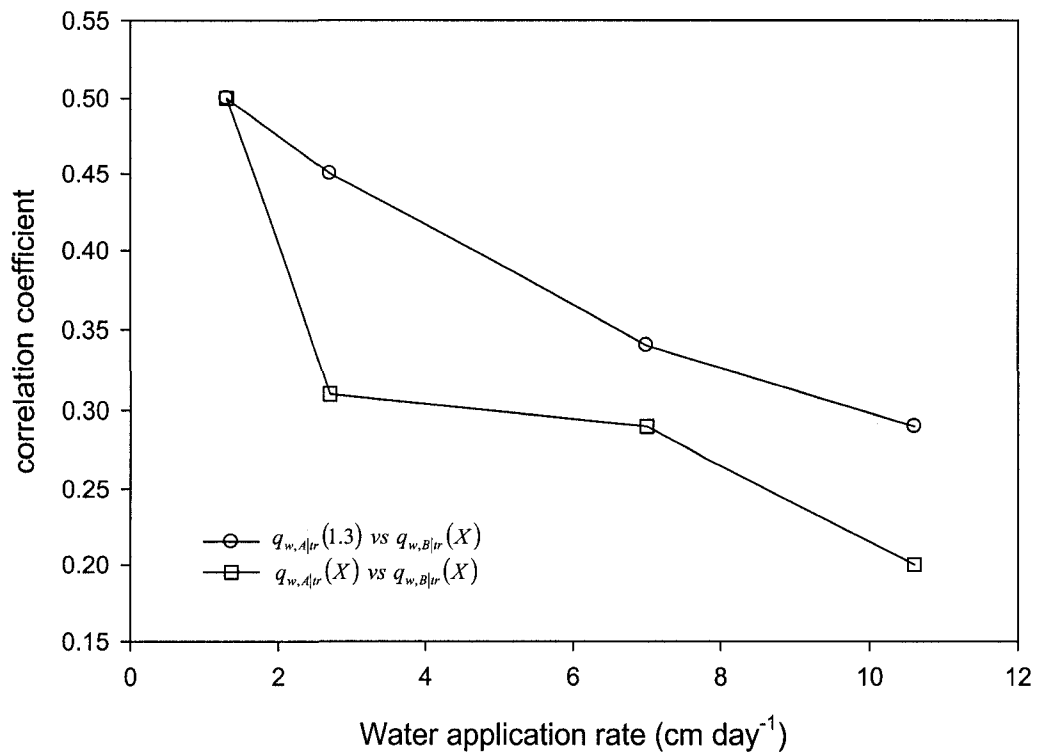
Figure 4-13: Flux dependent correlation between spatial pattern of A and B horizon transient, local soil water flux. Circles represent the correlation between the spatial pattern of the 1.3 cm day^{-1} A horizon flux pattern to the B horizon flux pattern at all other water application rates. Squares represent the correlation between the spatial patterns of A and B horizon fluxes at each water application rate.
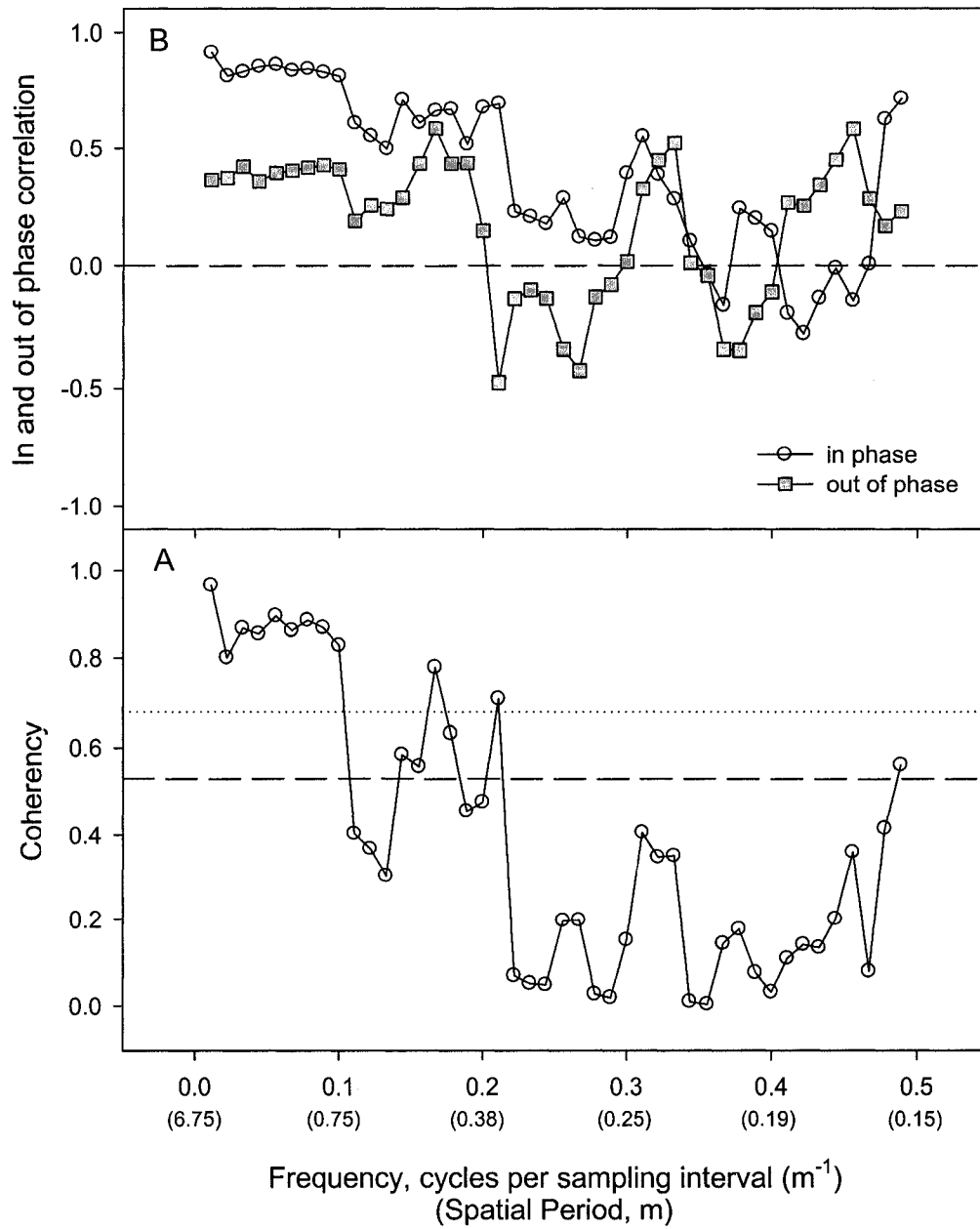
Figure 4-14: Coherency (A), in phase and out phase correlation (B) spectra between $q_{w,A|tr}(1.3)$ and $q_{w,B|tr}(1.3)$
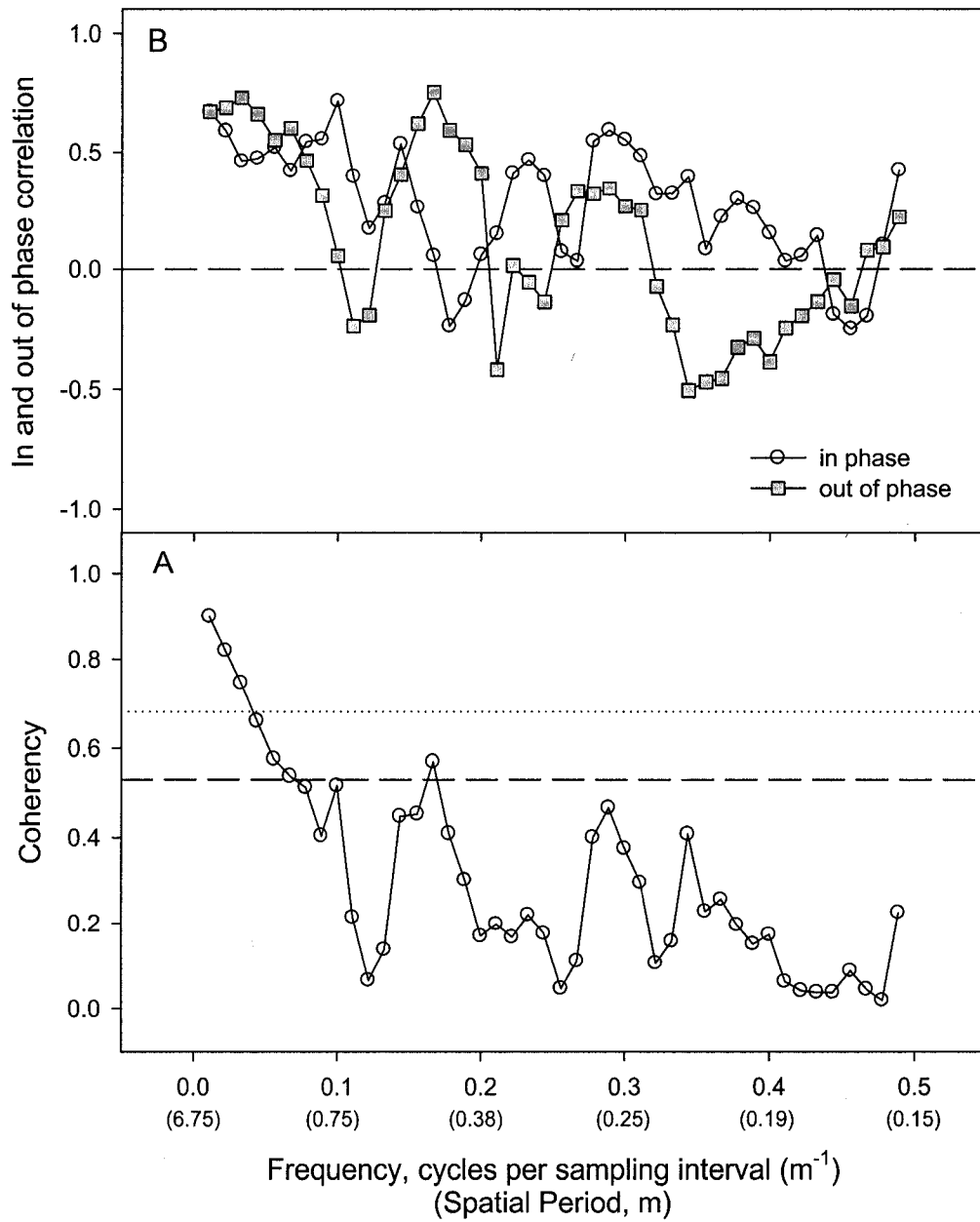
Figure 4-15: Coherency (A), in phase and out phase correlation (B) spectra between $q_{w,A|tr}(1.3)$ and $q_{w,B|tr}(10.6)$
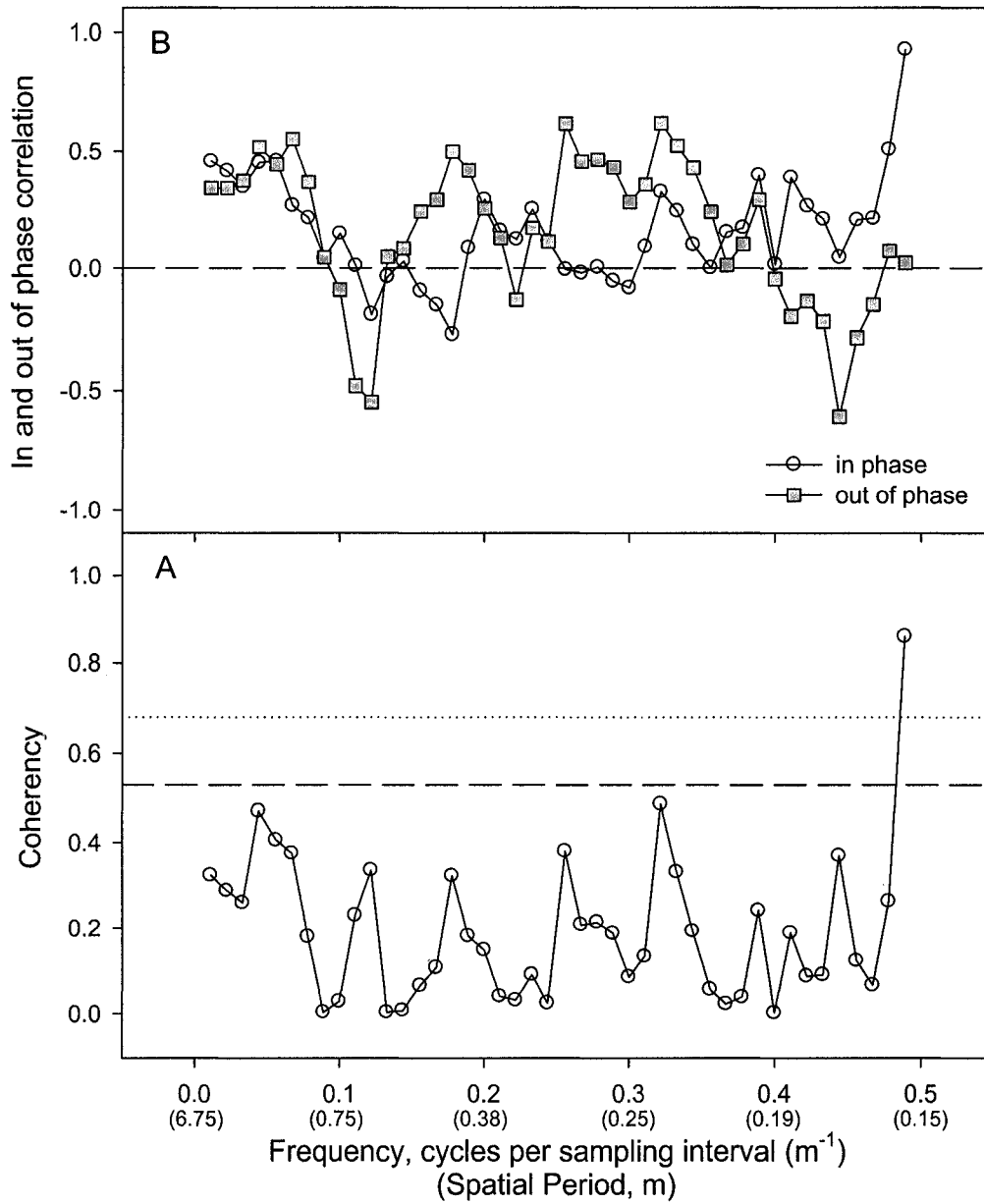
Figure 4-16: Coherency (A), in phase and out phase correlation (B) spectra between $q_{w,A|tr}(10.6)$ and $q_{w,B|tr}(10.6)$
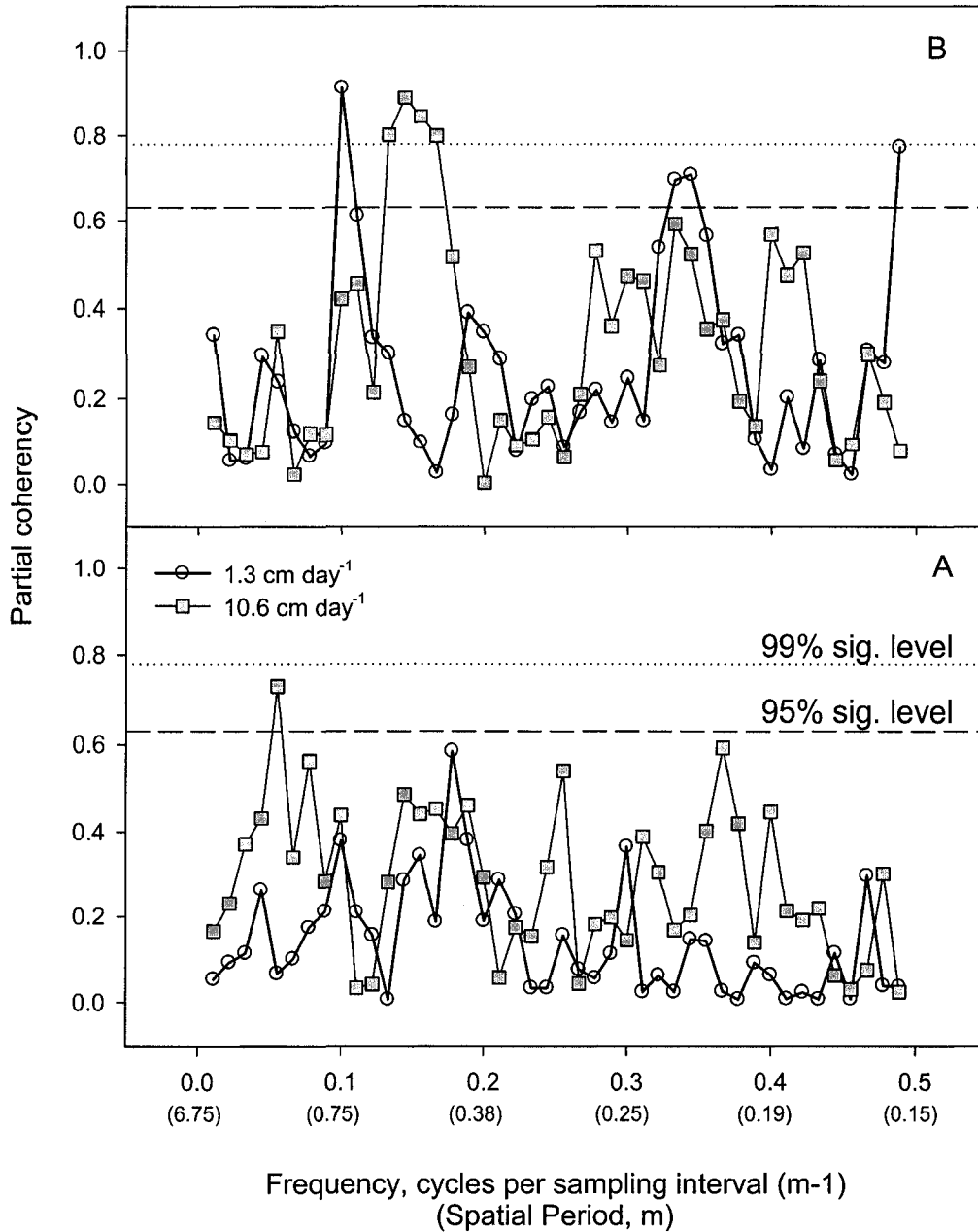
Figure 4-17: (A) Partial coherency between B horizon transient soil water flux and depth to A/B horizon interface, given the input signal, A horizon transient soil water flux. (B) Partial coherency between B horizon transient soil water flux and plan curvature (PLAN), given A horizon flux. Spectra shown for 1.3 and 10.6 cm day^{-1} water application rates.
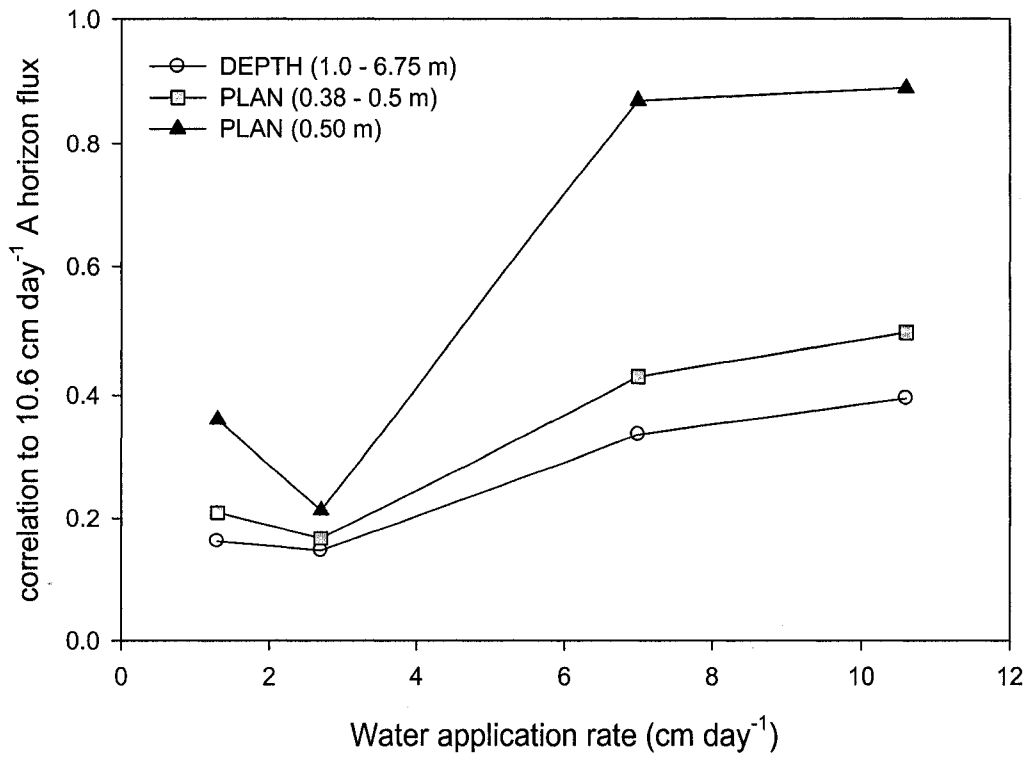
Figure 4-18: Summary of coherency between B horizon flux and layer parameters at selected scales as a function of water application rate.
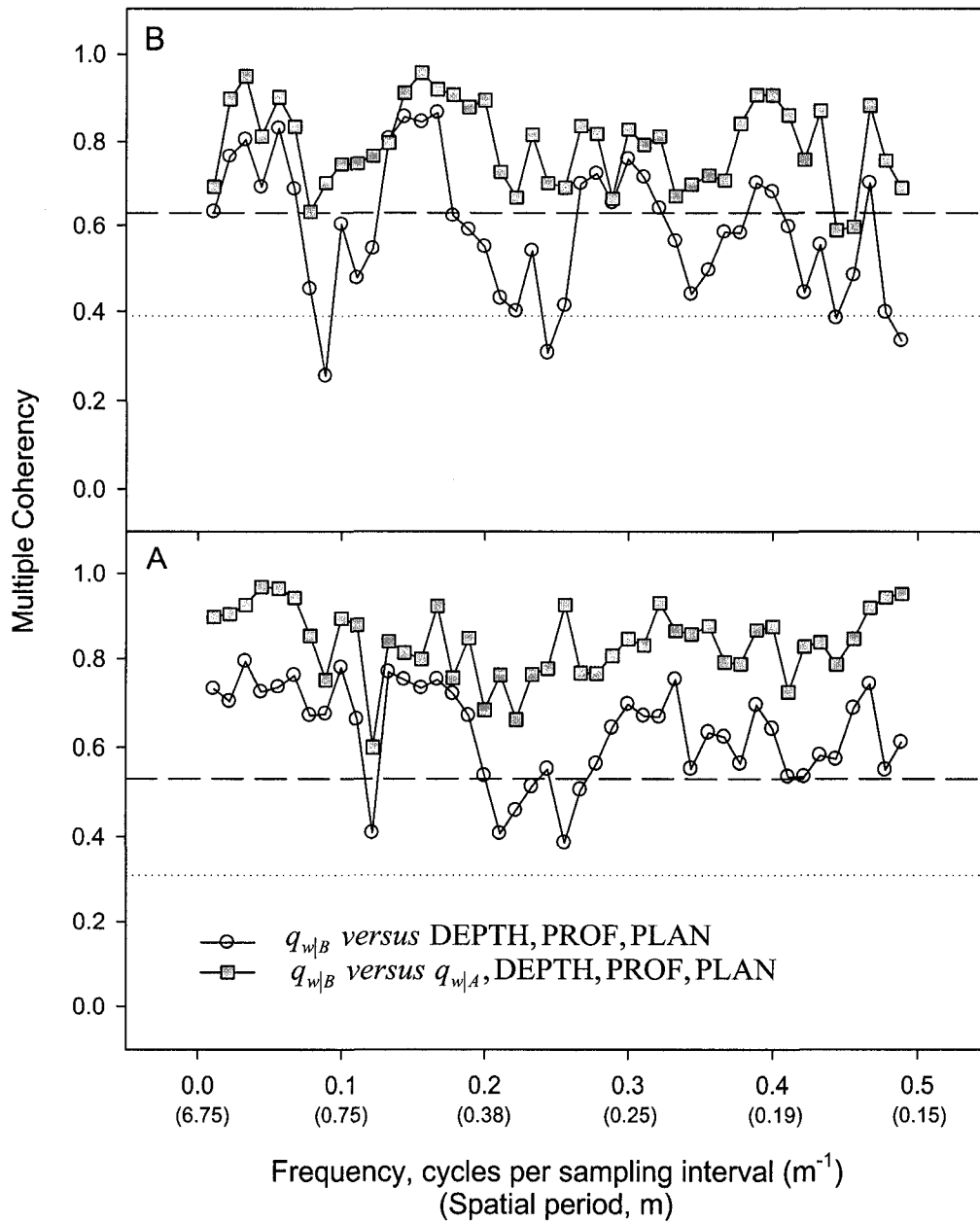
Figure 4-19: Multiple coherency spectra comparing transient (A) and steady state (B) B horizon soil water flux to: 1) soil horizon shape parameters (circles; the dotted line indicates the 95% critical coherency value); and 2) A horizon soil water flux (input pattern) and soil horizon shape parameters (squares; the dashed line indicates the 95% critical coherency value).

5. General Discussion and Conclusion

5.1. Summary and contributions of this PhD thesis

The major objective of this thesis was to better understand the physics of water flow and solute transport in spatially-variable layered soils. In order to achieve this objective, effective one-dimensional flow and transport experiments under known and controlled surface boundary conditions were executed in the field (Section 2). The hydraulic response of the soil and the soil horizon interface under the imposed boundary conditions was measured. The major contributions and conclusions of this thesis are:

1) The TDR methodology described in Sections 2 and 3 extends the work of Parkin et al., (1995) and Si and Kachanoski (2003) to layered soils. The method was shown to be very sensitive to local redistribution of water and solute mass at soil horizon interfaces. When implemented in the field, this methodology can be used to measure the spatial pattern of local soil water flux (transient) above and below a soil horizon interface.

2) Analysis of the measured spatial patterns of local soil water flux revealed a flux-and scale-dependent, spatial covariance relationship between local soil water flux and the soil horizon interface. The nature of this relationship was also dependent on the internal boundary conditions (transient or steady state) at the horizon interface (Section 4).

3) The use of spectral analysis methods quantified the scale-dependent spatial structure of the horizon interface and allowed the scale at which the horizon interface influence the spatial patterns of soil water flux to be resolved. Although the physical mechanisms were different for transient and steady

state boundary conditions, the horizon interface significantly influenced the spatial scale dependence of vertical mass flux continuity. The application of multitaper power, coherency, and multiple and partial coherency analysis to a spatial data set of a soil hydrological process is a unique contribution to the soil science literature.

4) Average multiple coherency spectra showed that the scale-dependent variance of local soil water flux in the B horizon could be explained by a linear, scale-dependent multivariate model with A horizon flux, DEPTH, PROF, and PLAN as independent variables. This result further illustrates the complex, scale-dependent covariance relationship between A and B horizon hydraulic properties and interface shape in the modification of A and B horizon local soil water fluxes.

5.2.   Process based definition of a Pedon

The basic unit of soil, the pedon, is described as the minimum, three-dimensional unit of soil representative of the local scale variability of soil horizon dimensions and morphology. In hydrology, the representative elementary volume (REV) may be thought of as the minimum three-dimensional unit of porous media representative of the local scale variability of the pore space influencing bulk hydraulic properties. The hydrological REV may or may not have the same dimensions as a pedon. In fact, it could be argued that since the REV accounts for pore-scale variability, its dimensions may be smaller than the pedon. Examples of such thinking are in the simulation experiments of Zhang et al. (2003) and Ursino et al. (2000) where a larger domain was discretized into smaller elements or cells (REVs). Each grid or cell of the simulation model may be

thought of as an REV. The overall spatially-discretized domain may be thought of as a pedon. In field soils, pedogenic processes have: 1) created spatially-variable soil horizons and soil horizon interfaces; 2) modified the pore structure within soil horizons such that average hydraulic properties of individual horizons are different (but may be only modestly so); and 3) as a result of 1) and 2) created a scale-dependent, spatial covariance between the hydraulic properties (REV scale) and the shape and of the soil horizons (pedon scale).

Because of the feedbacks between hydraulic properties and soil horizon formation that likely operate during soil genesis (hydrological processes are a major component of pedogenesis), it is reasonable to expect that hydrological processes may show a scale-dependent variance similar to that of the soil horizon dimensions (pedon). In Section 4, the significant coherency between the spatial patterns of the shape of the horizon interface and the local soil water flux, at scales where the horizon and flux patterns showed relatively high variability (0.4 – 0.5 m), is a quantitative example of the complex feedbacks between patterns of soil horizons and soil hydraulic properties. This finding has important practical significance in that the scale at which hydrological processes show the most variability may be predicted by simple observation of the soil horizon interface. It also suggests that the concept of the pedon has hydrological significance like the REV (van Wesenbeeck and Kachanoski, 1991).

5.3.   Future research

This thesis provides a foundation for various future research trajectories. Perhaps the most obvious is further quantification of the nature of the spatial covariance between soil hydraulic properties and the shape of the soil horizon interface, and how that

covariance relationship influences the spatial pattern of observed hydrological processes.

Investigations such as this could be carried out in field experiments or with simulation

models. The data set presented in this thesis could be used to calibrate and/or validate

existing process models. Coupled solute transport and electromagnetic wave (TDR)

models could be used to investigate, in more detail, transport processes measured by

vertical TDR probes in layered soils. Future research may also involve using the

methodology developed in this thesis to investigate other types of soil horizon interfaces,

or the influence of soil disturbances (such as cultivation) on hydrological processes in

layered soils.

5.4.   References

Parkin, G. W., R. G. Kachanoski, D. E. Elrick, and R. G. Gibson. 1995. Unsaturated
    hydraulic conductivity measured by time domain reflectometry under a rainfall
    simulator. Water Resour. Res. 31:447-454.

Si, B. C., and R. G. Kachanoski. 2003. Measurement of local soil water flux during field
    solute transport experiments. Soil Sci. Soc. Am J. 67:730-736.

Ursino, N., K. Roth, T. Gimmi, and H. Flühler. 2000. Upscaling of anisotropy in
    unsaturated Miller-similar porous media. Water Resour. Res. 36:421-430.

van Wesenbeeck, I. J., and R. G. Kachanoski. 1991. Spatial scale dependence of in-situ
    solute transport. Soil Sci. Soc. Am. J. 55:3-7.

Zhang, Z. F., A. L. Ward, and G. W. Gee. 2003. A tensorial connectivity-tortuosity
    concept to describe the unsaturated hydraulic properties of anisotropic soils.
    Vadose Zone J. 2:313-321.

Appendix A: Soil Water Storage Measurements During the 10.6 cm day^{-1} Transient Experiment, 0.45 m Transect

Location

Data from 25 cm Probe:

DOY	TIME	DAYS	Location (m, northing)	Probe Length	T1 (ns)	T2 (ns)	TDR Travel Time (ns)	Apparent Permitivity	Volumetric Water Content	Water Storage
2007204	15:34:00	0.00	0.45	0.25	1.86	7.21	5.35	10.29	0.121	3.01
2007204	16:05:07	0.02	0.45	0.25	1.88	7.40	5.52	10.95	0.129	3.23
2007204	16:31:28	0.04	0.45	0.25	1.88	7.51	5.63	11.39	0.138	3.45
2007204	17:14:17	0.07	0.45	0.25	1.89	7.68	5.79	12.05	0.151	3.77
2007204	17:58:10	0.10	0.45	0.25	1.88	7.86	5.98	12.85	0.166	4.14
2007204	18:44:49	0.13	0.45	0.25	1.91	8.05	6.15	13.59	0.179	4.49
2007204	19:31:22	0.16	0.45	0.25	1.92	8.24	6.32	14.36	0.193	4.83
2007204	20:24:33	0.20	0.45	0.25	1.95	8.45	6.50	15.19	0.208	5.20
2007204	21:28:58	0.25	0.45	0.25	1.94	8.61	6.67	16.00	0.222	5.55
2007204	22:31:57	0.29	0.45	0.25	1.96	8.75	6.79	16.55	0.231	5.78
2007204	23:27:09	0.33	0.45	0.25	1.95	8.86	6.91	17.16	0.241	6.03
2007205	1:32:04	0.42	0.45	0.25	1.96	9.00	7.04	17.81	0.252	6.30
2007205	2:24:20	0.45	0.45	0.25	1.96	9.01	7.05	17.86	0.253	6.32
2007205	3:26:31	0.49	0.45	0.25	1.96	9.02	7.06	17.90	0.253	6.34
2007205	4:32:20	0.54	0.45	0.25	1.97	9.08	7.10	18.15	0.257	6.43
2007205	5:29:36	0.58	0.45	0.25	1.97	9.08	7.11	18.17	0.258	6.44
2007205	6:27:50	0.62	0.45	0.25	1.97	9.12	7.14	18.34	0.260	6.51
2007205	7:33:16	0.67	0.45	0.25	1.96	9.08	7.13	18.26	0.259	6.48
2007205	8:26:28	0.70	0.45	0.25	1.96	9.11	7.16	18.41	0.262	6.54
2007205	10:30:16	0.79	0.45	0.25	1.93	9.07	7.14	18.32	0.260	6.50
2007205	11:22:18	0.83	0.45	0.25	1.93	9.04	7.11	18.15	0.257	6.44
2007205	12:55:54	0.89	0.45	0.25	1.95	9.04	7.09	18.08	0.256	6.41
2007205	14:56:39	0.97	0.45	0.25	1.95	9.00	7.05	17.88	0.253	6.33
2007207	11:12:53	2.82	0.45	0.25	2.04	9.23	7.20	18.62	0.265	6.62
2007207	14:07:05	2.94	0.45	0.25	1.88	8.83	6.94	17.34	0.244	6.10
2007207	17:56:12	3.10	0.45	0.25	1.95	8.56	6.61	15.70	0.217	5.42
2007207	20:43:24	3.21	0.45	0.25	1.99	8.45	6.46	15.01	0.205	5.12
2007208	7:37:49	3.67	0.45	0.25	2.05	8.23	6.18	13.74	0.182	4.55
2007212	13:21:34	7.91	0.45	0.25	1.97	7.43	5.47	10.75	0.125	3.13

152

Data from 60 cm probe:

DOY	TIME	DAYS	Location (m, northing)	Probe Length	T1 (ns)	T2 (ns)	TDR Travel Time (ns)	Apparent Permittivity	Volumetric Water Content	Water Storage
2007204	15:34:00	0.00	0.45	0.6	3.72	15.25	11.53	8.30	0.155	9.29
2007204	16:10:14	0.03	0.45	0.6	3.76	15.47	11.71	8.56	0.159	9.56
2007204	16:36:30	0.04	0.45	0.6	3.76	15.61	11.85	8.76	0.164	9.81
2007204	17:19:31	0.07	0.45	0.6	3.78	15.79	12.01	9.01	0.169	10.11
2007204	18:03:16	0.10	0.45	0.6	3.77	15.99	12.22	9.31	0.175	10.48
2007204	18:49:56	0.14	0.45	0.6	3.82	16.21	12.39	9.58	0.180	10.81
2007204	19:36:37	0.17	0.45	0.6	3.85	16.48	12.63	9.96	0.187	11.25
2007204	20:29:41	0.21	0.45	0.6	3.88	16.74	12.86	10.31	0.194	11.66
2007204	21:35:08	0.25	0.45	0.6	3.88	17.04	13.15	10.80	0.204	12.21
2007204	22:37:05	0.29	0.45	0.6	3.90	17.26	13.36	11.15	0.210	12.61
2007204	23:32:17	0.33	0.45	0.6	3.90	17.57	13.66	11.65	0.219	13.16
2007205	1:37:12	0.42	0.45	0.6	3.91	18.03	14.12	12.44	0.233	14.01
2007205	2:29:35	0.46	0.45	0.6	3.91	18.23	14.32	12.80	0.240	14.38
2007205	3:31:46	0.50	0.45	0.6	3.91	18.40	14.49	13.11	0.245	14.70
2007205	4:38:01	0.54	0.45	0.6	3.92	18.51	14.59	13.28	0.248	14.87
2007205	5:34:44	0.58	0.45	0.6	3.93	18.54	14.61	13.33	0.249	14.92
2007205	6:32:56	0.62	0.45	0.6	3.93	18.62	14.69	13.46	0.251	15.06
2007205	7:38:45	0.67	0.45	0.6	3.90	18.57	14.67	13.44	0.250	15.03
2007205	8:31:36	0.71	0.45	0.6	3.90	18.62	14.72	13.52	0.252	15.11
2007205	9:32:09	0.75	0.45	0.6	3.85	18.60	14.74	13.56	0.253	15.15
2007205	10:36:27	0.79	0.45	0.6	3.85	18.56	14.71	13.50	0.252	15.09
2007205	11:27:47	0.83	0.45	0.6	3.81	18.58	14.77	13.61	0.253	15.20
2007205	13:12:34	0.90	0.45	0.6	3.83	18.58	14.75	13.58	0.253	15.17
2007205	15:11:54	0.98	0.45	0.6	3.85	18.56	14.71	13.50	0.252	15.09
2007206	21:00:11	2.23	0.45	0.6	3.89	19.01	15.11	14.26	0.264	15.84
2007207	11:28:02	2.83	0.45	0.6	3.81	18.63	14.82	13.70	0.255	15.30
2007207	14:24:41	2.95	0.45	0.6	3.78	18.06	14.28	12.73	0.239	14.31
2007207	20:11:17	3.19	0.45	0.6	3.86	17.56	13.70	11.71	0.221	13.23
2007208	7:53:28	3.68	0.45	0.6	3.95	17.12	13.17	10.82	0.204	12.24
2007212	13:53:53	7.93	0.45	0.6	3.86	15.77	11.91	8.85	0.165	9.92

Summary Graph:

0.45 m location

y = 11.02x + 9.42
R² = 1.00

y = 11.48x + 9.29
R² = 1.00

y = 10.97x + 3.01
R² = 1.00

Water Storage (cm)

Time (days)

154
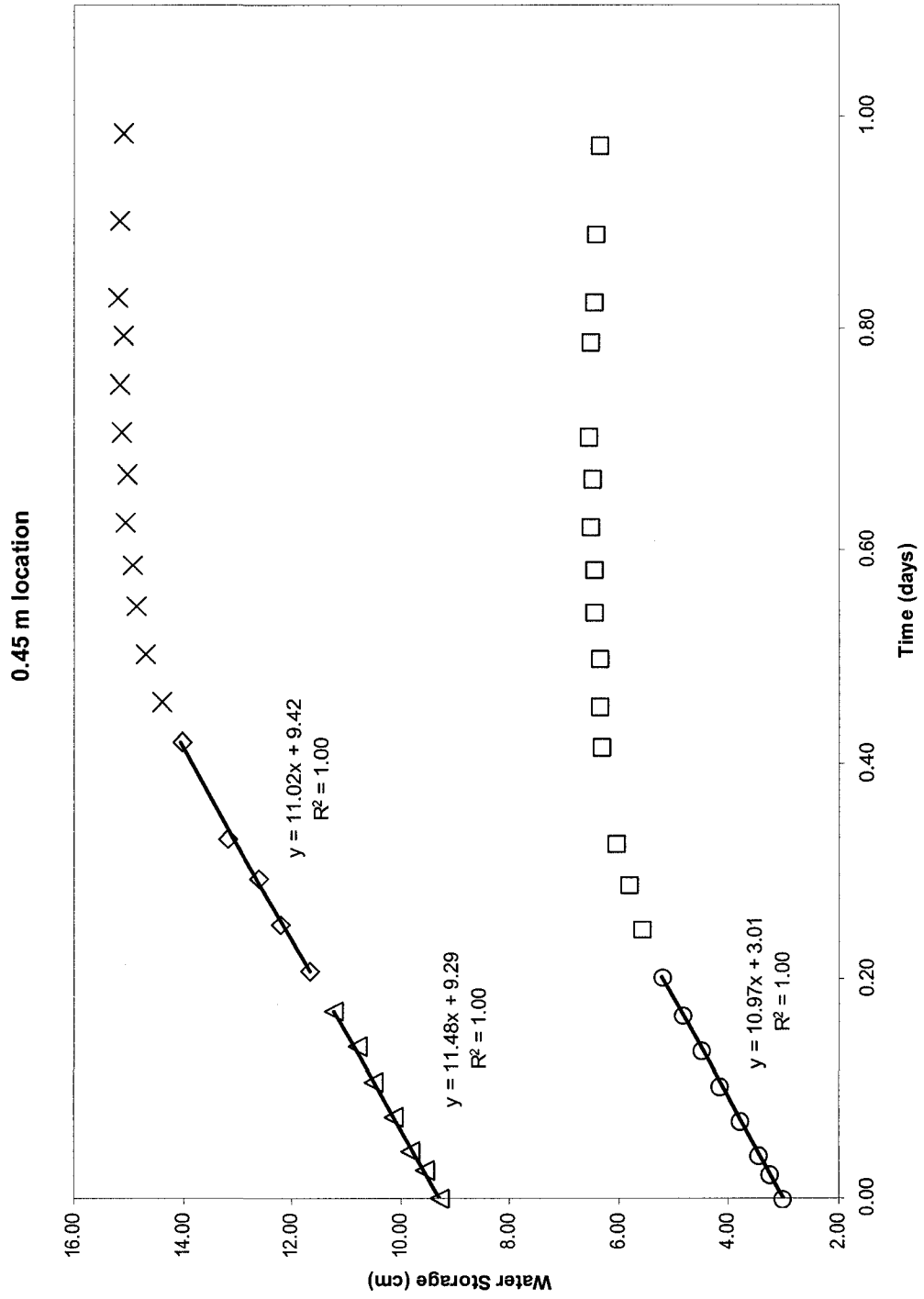
Appendix B: TDR Measured EC During the 2.7 cm day^{-1} Steady State Experiment, 1.8 m Transect Location

Depth to Horizon Interface: 26 cm
A horizon steady state water content: 0.23 cm^3 cm^{-3}
B horizon steady state water content: 0.20 cm^3 cm^{-3}

Data from 25 cm probe:

DOY	TIME	Time (days)	Location (m, northing)	V_o	V_f	V_i	ρ	R_L (Ω)	$1/(R_L - R_{cable})$ (Ω^{-1})	avg soil temp °C	temp correction	$1/(R_L - R_{cable})$ corrected (Ω^{-1})
2006214	20:28:00	0.00	1.80	5455.76	6123.80	3864.56	0.42	122.37	0.0082058	19.03	1.13	0.0092561
2006214	23:34:21	0.13	1.80	5452.44	6155.41	3868.96	0.44	129.84	0.0077317	18.01	1.15	0.0089161
2006215	3:05:15	0.28	1.80	5450.80	6196.14	3864.52	0.47	138.63	0.0072395	17.33	1.17	0.0084736
2006215	6:01:12	0.40	1.80	5445.08	6225.31	3862.04	0.49	147.19	0.0068172	16.88	1.18	0.0080602
2006215	8:57:24	0.52	1.80	5444.08	6250.80	3852.88	0.51	152.84	0.0065644	16.94	1.18	0.0077521
2006215	14:16:21	0.74	1.80	5452.12	6281.31	3853.36	0.52	157.75	0.0063594	18.31	1.15	0.0072848
2006215	17:35:14	0.88	1.80	5442.04	6300.47	3845.92	0.54	166.37	0.0060289	18.70	1.14	0.0068485
2006215	20:51:33	1.02	1.80	5442.12	6325.78	3859.60	0.56	176.44	0.0056836	18.82	1.13	0.0064405
2006215	23:45:48	1.14	1.80	5435.52	6348.69	3854.44	0.58	186.72	0.0053700	17.54	1.17	0.0062574
2006216	3:02:58	1.27	1.80	5440.72	6388.37	3857.32	0.60	199.06	0.0050362	17.22	1.17	0.0059101
2006216	5:59:13	1.40	1.80	5436.40	6415.69	3857.88	0.62	213.42	0.0046965	16.74	1.19	0.0055706
2006216	8:55:37	1.52	1.80	5430.32	6437.80	3849.60	0.64	225.75	0.0044394	16.74	1.19	0.0052658
2006216	12:06:23	1.65	1.80	5431.84	6464.88	3851.24	0.65	238.66	0.0041988	16.58	1.19	0.0049984
2006216	15:01:38	1.77	1.80	5430.56	6481.65	3850.20	0.67	248.59	0.0040308	16.86	1.18	0.0047679
2006216	18:05:30	1.90	1.80	5428.00	6498.33	3837.44	0.67	255.74	0.0039178	17.04	1.18	0.0046157
2006216	20:55:43	2.02	1.80	5431.80	6505.27	3841.60	0.68	257.75	0.0038873	17.41	1.17	0.0045426
2006217	2:09:45	2.24	1.80	5427.04	6521.53	3845.56	0.69	274.75	0.0036464	16.92	1.18	0.0043076
2006217	6:10:59	2.40	1.80	5425.08	6528.18	3847.00	0.70	282.24	0.0035494	15.95	1.21	0.0042868
2006217	9:08:44	2.53	1.80	5426.04	6527.77	3839.44	0.69	277.22	0.0036138	16.33	1.20	0.0043269
2006217	12:02:42	2.65	1.80	5424.92	6518.80	3830.28	0.69	268.45	0.0037321	17.24	1.17	0.0043773
2006217	14:59:00	2.77	1.80	5423.84	6513.90	3829.72	0.68	266.26	0.0037628	18.31	1.15	0.0043112
2006217	18:15:42	2.91	1.80	5428.04	6507.39	3826.72	0.67	256.79	0.0039019	18.79	1.13	0.0044236
2006217	21:16:08	3.03	1.80	5422.88	6507.94	3830.48	0.68	263.87	0.0037969	17.03	1.18	0.0044746
2006218	5:08:01	3.36	1.80	5425.60	6521.96	3847.08	0.69	277.39	0.0036116	15.09	1.23	0.0044492
2006218	12:06:02	3.65	1.80	5424.88	6513.43	3822.68	0.68	261.93	0.0038252	16.49	1.19	0.0045634
2006218	15:02:38	3.77	1.80	5428.76	6510.65	3821.52	0.67	255.94	0.0039149	17.96	1.15	0.0045197
2006218	18:01:49	3.90	1.80	5426.64	6502.14	3818.84	0.67	252.05	0.0039754	18.78	1.13	0.0045082
2006218	20:56:47	4.02	1.80	5423.88	6502.02	3836.08	0.68	261.54	0.0038308	18.49	1.14	0.0043712
2006218	23:45:56	4.14	1.80	5425.56	6508.75	3842.52	0.68	266.70	0.0037566	17.77	1.16	0.0043544
2006219	6:18:08	4.41	1.80	5426.12	6519.98	3846.32	0.69	275.10	0.0036416	16.14	1.20	0.0045786
2006219	9:14:47	4.53	1.80	5429.84	6515.63	3837.28	0.68	264.26	0.0037914	16.28	1.20	0.0045440

DOY	TIME	Time (days)	Location (m, northing)	V_o	V_f	V_i	ρ	R_L (Ω)	$1/(R_L - R_{cable})$ (Ω⁻¹)	avg soil temp °C	temp correction	$1/(R_L - R_{cable})$ corrected (Ω⁻¹)
2006214	20:28:00	0.00	1.80	5485.80	5861.20	3891.20	0.24	80.79	0.0124548	17.41	1.17	0.0145536
2006214	23:49:14	0.14	1.80	5485.68	5883.00	3896.28	0.25	83.33	0.0120729	17.19	1.17	0.0141764
2006215	3:18:40	0.29	1.80	5480.08	5910.04	3896.56	0.27	87.27	0.0115244	17.04	1.18	0.0135774
2006215	6:14:44	0.41	1.80	5478.68	5928.96	3895.16	0.28	89.73	0.0112065	16.83	1.18	0.0132652
2006215	9:12:43	0.53	1.80	5478.64	5946.88	3883.88	0.29	91.57	0.0109811	16.67	1.19	0.0130456
2006215	14:29:40	0.75	1.80	5479.24	5963.14	3881.80	0.30	93.46	0.0107578	17.09	1.18	0.0126620
2006215	17:48:40	0.89	1.80	5473.76	5975.33	3880.80	0.31	95.96	0.0104759	17.19	1.17	0.0123005
2006215	21:04:49	1.03	1.80	5473.84	5994.55	3884.16	0.33	98.71	0.0101821	17.35	1.17	0.0119147
2006215	23:59:42	1.15	1.80	5475.24	6016.94	3888.48	0.34	101.83	0.0098683	17.00	1.18	0.0116367
2006216	3:15:54	1.28	1.80	5469.60	6039.43	3889.44	0.36	106.40	0.0094428	16.91	1.18	0.0111587
2006216	6:12:17	1.41	1.80	5468.68	6063.92	3886.96	0.38	110.34	0.0091042	16.71	1.19	0.0108073
2006216	9:08:43	1.53	1.80	5462.88	6083.51	3881.92	0.39	114.63	0.0087622	16.56	1.19	0.0104354
2006216	15:14:35	1.78	1.80	5462.64	6120.31	3875.08	0.41	120.73	0.0083176	16.43	1.19	0.0099348
2006216	18:18:38	1.91	1.80	5462.28	6134.45	3868.44	0.42	122.93	0.0081679	16.51	1.19	0.0097392
2006216	21:08:46	2.03	1.80	5457.44	6156.55	3873.32	0.44	128.99	0.0077824	16.64	1.19	0.0092517
2006217	2:22:41	2.25	1.80	5454.80	6195.26	3873.12	0.47	138.02	0.0072716	16.47	1.19	0.0086772
2006217	6:24:05	2.41	1.80	5456.88	6216.98	3872.28	0.48	142.19	0.0070577	16.20	1.20	0.0084748
2006217	9:24:55	2.54	1.80	5453.32	6229.57	3859.76	0.49	144.98	0.0069216	16.29	1.20	0.0082950
2006217	12:18:49	2.66	1.80	5454.16	6233.31	3853.88	0.49	144.89	0.0069258	16.57	1.19	0.0082470
2006217	15:12:10	2.78	1.80	5457.16	6235.61	3851.04	0.48	144.05	0.0069661	16.91	1.18	0.0082320
2006217	18:28:44	2.92	1.80	5450.80	6245.61	3853.16	0.50	149.00	0.0067340	17.13	1.18	0.0079187
2006217	21:29:20	3.04	1.80	5448.48	6251.12	3856.80	0.50	151.72	0.0066127	16.16	1.20	0.0079471
2006218	5:21:03	3.37	1.80	5451.04	6286.67	3862.72	0.53	161.02	0.0062298	15.43	1.22	0.0076138
2006218	12:21:37	3.66	1.80	5450.80	6303.04	3840.40	0.53	162.41	0.0061763	15.79	1.21	0.0074864
2006218	15:18:00	3.78	1.80	5447.44	6306.55	3840.76	0.53	164.92	0.0060820	16.42	1.19	0.0072665
2006218	18:14:53	3.91	1.80	5448.36	6308.31	3843.92	0.54	165.51	0.0060602	16.84	1.18	0.0071729
2006218	21:10:03	4.03	1.80	5446.04	6320.14	3850.64	0.55	171.18	0.0058588	16.84	1.18	0.0069344
2006218	23:58:53	4.15	1.80	5448.52	6326.53	3851.84	0.55	172.17	0.0058251	16.63	1.19	0.0069269
2006219	6:31:05	4.42	1.80	5443.84	6356.77	3852.64	0.57	184.60	0.0054320	16.06	1.20	0.0065437
2006219	9:30:02	4.54	1.80	5439.68	6363.22	3843.76	0.58	187.35	0.0053518	16.02	1.21	0.0064531
2006219	13:11:26	4.70	1.80	5451.32	6364.29	3835.56	0.57	179.91	0.0055739	16.57	1.19	0.0066374
2006219	16:42:59	4.84	1.80	5443.36	6359.67	3837.36	0.57	182.86	0.0054837	17.35	1.17	0.0064166

Summary Graph

1.80 m location

The chart shows "1/Ω" on the vertical axis (ranging from 0.0030000 to 0.0170000) and "Time (days)" on the horizontal axis (ranging from 0.00 to 5.00).

$\bar{t}_A = 2.07\ days$

$\bar{t}_{AB} = 4.6\ days$

$\bar{t}_A = 1.92\ days$
adjusted to a depth of 26 cm
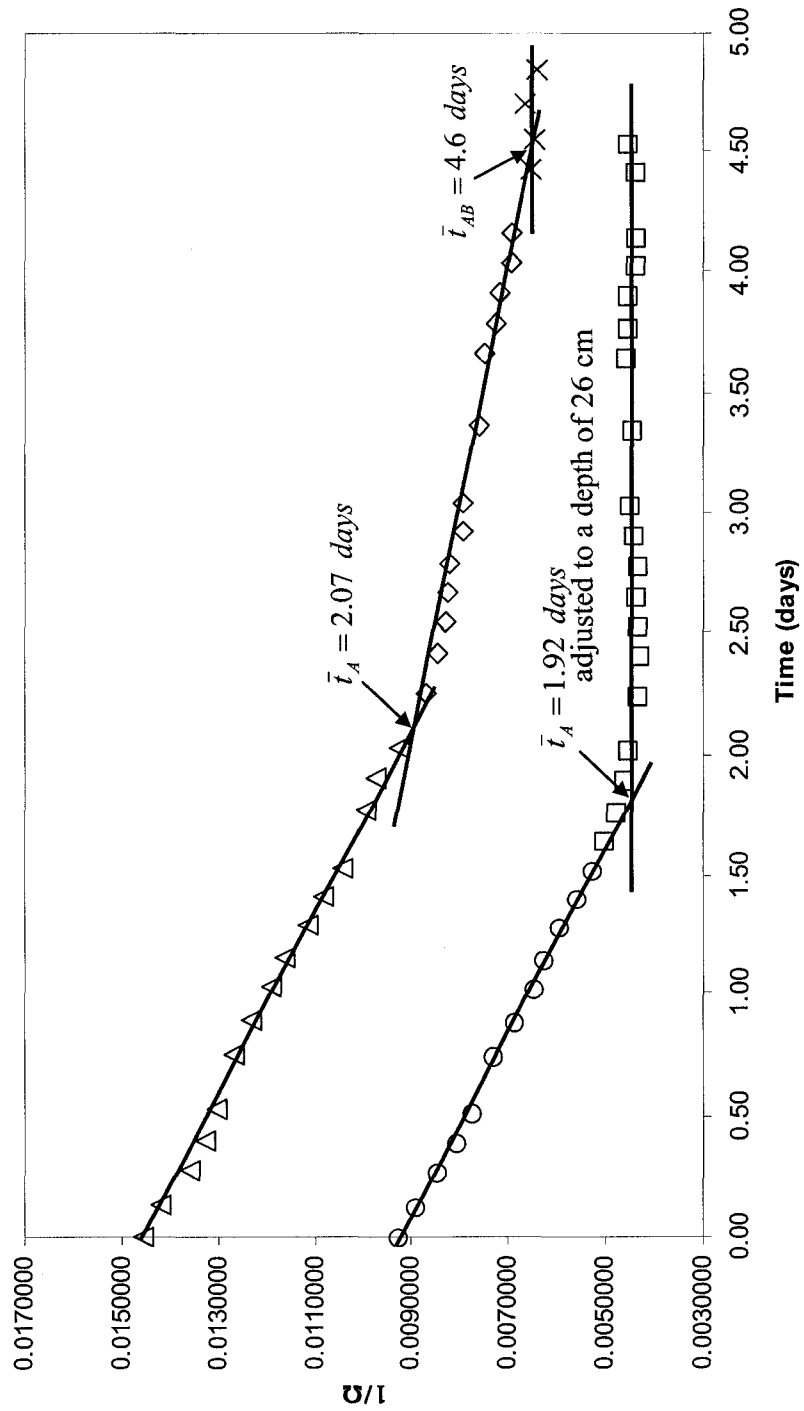
Appendix C: Spatial series of steady state A and B horizon water content, steady state A and B horizon soil water storage, A and B horizon solute travel time, A and B horizon steady state and transient soil water flux.

Northing (m)	DEPTH	PROF	PLAN	$\bar{\theta}_{A,ss}$(2.7)	$\bar{\theta}_{B,ss}$(2.7)	$\theta_{A,ss}$(7.0)	$\theta_{B,ss}$(7.0)	$\theta_{A,ss}$(10.6)	$\theta_{B,ss}$(10.6)	$W_{A,ss}$(2.7)	$W_{B,ss}$(2.7)	$W_{A,ss}$(7.0)	$W_{B,ss}$(7.0)	$W_{A,ss}$(10.6)
0.000	-25	0.0319	-0.1606	0.266	0.190	0.291	0.207	0.305	0.221	6.47	6.79	7.09	7.37	7.43
0.075	-22	0.0047	-0.5470	0.262	0.203	0.284	0.207	0.305	0.221	5.86	7.64	6.35	7.81	6.81
0.150	-20	-0.0079	0.0691	0.251	0.184	0.273	0.205	0.302	0.214	5.35	7.13	5.82	7.92	6.44
0.225	-22	-0.0003	-1.7109	0.203	0.206	0.220	0.222	0.241	0.235	4.46	7.84	4.83	8.42	5.31
0.300	-24	0.0026	0.0657	0.157	0.248	0.168	0.276	0.184	0.288	3.60	9.18	3.87	10.23	4.22
0.375	-23	0.0326	-0.0419	0.193	0.193	0.223	0.198	0.237	0.213	4.70	6.88	5.42	7.06	5.77
0.450	-26	-0.0567	-0.3032	0.228	0.206	0.273	0.211	0.288	0.233	5.01	7.83	6.02	8.02	6.33
0.525	-17	0.0592	0.2422	0.228	0.183	0.265	0.188	0.280	0.206	5.17	6.83	6.01	7.01	6.36
0.600	-25	-0.0342	0.0963	0.223	0.207	0.251	0.220	0.268	0.239	5.21	7.57	5.86	8.06	6.25
0.675	-28	0.0212	-0.4821	0.237	0.189	0.253	0.195	0.269	0.213	6.16	6.44	6.57	6.63	6.99
0.750	-25	0.0390	0.1996	0.252	0.212	0.259	0.232	0.274	0.247	6.80	7.00	6.99	7.65	7.39
0.825	-28	-0.0763	-0.0285	0.236	0.253	0.241	0.268	0.258	0.286	6.44	8.26	6.60	8.76	7.05
0.900	-29	0.0980	0.0723	0.208	0.235	0.223	0.264	0.240	0.274	6.04	7.28	6.46	8.18	6.97
0.975	-30	-0.0229	-0.8510	0.204	0.258	0.217	0.269	0.234	0.283	5.72	8.26	6.08	8.62	6.56
1.050	-25	0.0906	0.0994	0.186	0.224	0.208	0.251	0.224	0.251	4.95	7.47	5.54	8.38	5.97
1.125	-25	-0.0208	-0.4204	0.210	0.188	0.229	0.200	0.245	0.216	5.31	6.51	5.79	6.93	6.20
1.200	-26	-0.0034	0.2512	0.235	0.187	0.251	0.217	0.266	0.230	6.26	6.22	6.69	7.23	7.08
1.275	-29	0.0002	-0.5271	0.221	0.183	0.242	0.206	0.258	0.218	5.61	6.33	6.12	7.14	6.54
1.350	-21	-0.0034	0.2512	0.212	0.207	0.230	0.230	0.249	0.240	5.37	7.17	5.83	7.97	6.31
1.425	-26	0.0051	0.1544	0.190	0.200	0.206	0.208	0.225	0.222	4.55	7.21	4.94	7.48	5.40
1.500	-25	0.0107	-0.1203	0.174	0.167	0.182	0.191	0.201	0.201	4.57	5.63	4.78	6.44	5.29
1.575	-28	-0.0216	-0.3445	0.199	0.201	0.211	0.211	0.228	0.230	5.04	6.96	5.35	7.31	5.78
1.650	-23	0.0585	-0.2123	0.222	0.197	0.238	0.207	0.253	0.224	5.93	6.55	6.35	6.91	6.75
1.725	-29	-0.0406	-0.2942	0.229	0.176	0.251	0.188	0.268	0.198	5.73	6.16	6.28	6.56	6.69
1.800	-23	-0.0058	0.8226	0.233	0.197	0.259	0.209	0.277	0.225	6.14	6.64	6.83	7.03	7.30
1.875	-27	-0.0044	-0.0752	0.230	0.220	0.257	0.222	0.271	0.241	5.97	7.47	6.67	7.55	7.04
1.950	-28	-0.0409	-0.4573	0.222	0.217	0.251	0.220	0.262	0.238	5.98	7.16	6.77	7.27	7.08
2.025	-26	0.0030	0.2531	0.222	0.205	0.242	0.215	0.255	0.231	6.08	6.70	6.60	7.02	6.98
2.100	-28	-0.0264	-0.1073	0.218	0.201	0.233	0.220	0.250	0.241	5.97	6.57	6.36	7.20	6.84
2.175	-28	0.0007	-0.1176	0.219	0.205	0.228	0.217	0.244	0.235	5.77	6.89	6.01	7.31	6.43
2.250	-23	-0.0039	-0.1960	0.215	0.187	0.222	0.209	0.237	0.229	5.95	6.05	6.13	6.77	6.56
2.325	-32	-0.0163	-0.0185	0.220	0.226	0.228	0.225	0.242	0.242	6.15	7.23	6.37	7.19	6.78
2.400	-29	-0.0507	0.0393	0.215	0.207	0.227	0.205	0.242	0.222	6.60	6.06	6.96	6.00	7.41
2.475	-31	-0.0487	-0.0472	0.215	0.224	0.222	0.230	0.237	0.247	6.25	6.95	6.44	7.12	6.87
2.550	-27	0.0578	0.2235	0.206	0.212	0.213	0.227	0.228	0.242	6.47	6.07	6.69	6.51	7.16
2.625	-36	-0.2364	-0.0523	0.203	0.226	0.207	0.237	0.226	0.253	5.81	7.09	5.95	7.44	6.47
2.700	-23	0.0939	0.0356	0.197	0.224	0.198	0.241	0.220	0.256	5.25	7.47	5.28	8.04	5.88
2.775	-21	-0.0087	0.1424	0.177	0.190	0.193	0.195	0.214	0.207	4.13	6.97	4.50	7.14	5.00
2.850	-26	-0.0795	-0.2410	0.164	0.201	0.191	0.208	0.210	0.224	4.14	6.96	4.84	7.22	5.32
2.925	-29	0.0871	0.0422	0.185	0.230	0.197	0.237	0.216	0.250	5.17	7.37	5.51	7.57	6.04
3.000	-29	-0.1283	-0.3400	0.183	0.251	0.199	0.251	0.218	0.264	5.07	8.13	5.50	8.13	6.03
3.075	-25	-0.0234	0.1138	0.192	0.234	0.193	0.254	0.210	0.263	5.25	7.65	5.27	8.29	5.75
3.150	-28	0.0114	0.3247	0.181	0.255	0.189	0.269	0.206	0.284	5.01	8.25	5.22	8.70	5.71
3.225	-30	0.0001	-0.0570	0.194	0.222	0.201	0.233	0.218	0.246	5.69	6.79	5.88	7.14	6.39
3.300	-30	-0.0036	-0.3578	0.183	0.122	0.193	0.130	0.210	0.141	5.75	3.49	6.05	3.73	6.59
3.375	-34	-0.0843	-0.0870	0.195	0.174	0.199	0.190	0.215	0.202	6.30	4.80	6.44	5.26	6.95
3.450	-33	-0.0843	-0.0870	0.199	0.233	0.202	0.240	0.217	0.259	5.97	6.99	6.05	7.21	6.52
3.525	-23	0.0280	-0.0361	0.194	0.234	0.199	0.240	0.215	0.257	4.67	8.41	4.78	8.66	5.16
3.600	-16	0.0140	0.0938	0.197	0.179	0.217	0.181	0.233	0.195	3.75	7.35	4.12	7.40	4.43
3.675	-18	-0.1045	0.1928	0.191	0.184	0.222	0.181	0.238	0.197	3.62	7.54	4.21	7.43	4.52
3.750	-23	0.0363	0.0079	0.198	0.188	0.215	0.192	0.231	0.208	5.14	6.38	5.59	6.53	6.01
3.825	-37	-0.1454	-0.2575	0.201	0.207	0.212	0.222	0.229	0.238	6.31	5.93	6.66	6.36	7.17
3.900	-34	-0.0295	0.0480	0.194	0.215	0.211	0.230	0.228	0.248	6.51	5.67	7.09	6.05	7.68
3.975	-30	-0.0391	-0.1164	0.198	0.213	0.210	0.228	0.226	0.241	5.75	6.61	6.09	7.05	6.56
4.050	-23	0.0192	0.2772	0.193	0.206	0.210	0.217	0.227	0.236	5.01	6.99	5.47	7.37	5.91
4.125	-25	-0.0444	-0.0209	0.185	0.194	0.199	0.204	0.215	0.222	4.56	6.84	4.91	7.21	5.30
4.200	-26	-0.0278	0.0760	0.183	0.230	0.192	0.245	0.207	0.261	4.94	7.60	5.19	8.07	5.60
4.275	-30	0.0035	-0.1319	0.192	0.205	0.200	0.209	0.215	0.226	5.39	6.55	5.60	6.70	6.03
4.350	-28	-0.0591	-0.1372	0.196	0.220	0.212	0.231	0.227	0.246	5.41	7.13	5.86	7.46	6.28
4.425	-25	0.0008	0.0689	0.179	0.221	0.190	0.235	0.205	0.254	4.60	7.58	4.88	8.08	5.27
4.500	-24	0.0152	0.0496	0.157	0.185	0.167	0.189	0.182	0.204	3.76	6.68	4.01	6.79	4.37
4.575	-23	0.0028	0.0651	0.191	0.133	0.198	0.145	0.215	0.164	4.34	4.96	4.49	5.41	4.87
4.650	-21	0.0344	0.0586	0.216	0.129	0.225	0.138	0.246	0.151	4.90	4.82	5.10	5.16	5.57
4.725	-24	0.0080	0.0390	0.201	0.192	0.200	0.210	0.219	0.224	4.90	6.86	4.86	7.50	5.34
4.800	-28	-0.0714	0.0285	0.180	0.198	0.184	0.198	0.202	0.211	4.74	6.66	4.84	6.68	5.33
4.875	-27	-0.0414	0.0180	0.189	0.182	0.198	0.186	0.217	0.199	4.73	6.37	4.95	6.51	5.41
4.950	-20	0.0387	0.0436	0.202	0.205	0.211	0.219	0.230	0.236	4.43	7.81	4.64	8.32	5.07
5.025	-19	0.0156	0.2443	0.181	0.192	0.201	0.199	0.218	0.218	3.81	7.47	4.23	7.77	4.58
5.100	-24	0.0118	-0.0805	0.174	0.209	0.188	0.218	0.204	0.232	4.17	7.53	4.51	7.85	4.89
5.175	-29	-0.0390	-0.0256	0.198	0.167	0.216	0.178	0.233	0.193	5.28	5.58	5.77	5.93	6.22
5.250	-27	-0.0157	-0.4122	0.225	0.178	0.244	0.198	0.263	0.216	6.14	5.80	6.66	6.48	7.18
5.325	-26	-0.0644	-0.0168	0.199	0.233	0.223	0.230	0.242	0.248	4.98	8.17	5.58	8.05	6.04
5.400	-22	0.0749	-0.0149	0.178	0.245	0.191	0.267	0.211	0.278	4.09	9.05	4.39	9.89	4.84
5.475	-21	0.0097	-0.0428	0.176	0.170	0.204	0.165	0.223	0.179	3.75	6.57	4.34	6.40	4.77
5.550	-21	-0.0005	-0.2605	0.185	0.145	0.206	0.153	0.227	0.163	3.94	5.60	4.39	5.93	4.85
5.625	-22	0.0525	0.0078	0.180	0.153	0.201	0.150	0.221	0.162	4.27	5.57	4.75	5.45	5.22
5.700	-28	-0.0816	-0.0982	0.174	0.189	0.198	0.196	0.217	0.207	4.29	6.69	4.88	6.94	5.36
5.775	-24	-0.0078	0.1547	0.189	0.209	0.208	0.213	0.225	0.230	4.84	7.16	5.34	7.32	5.78
5.850	-25	-0.0066	0.1334	0.197	0.211	0.217	0.224	0.233	0.240	4.78	7.52	5.28	7.98	5.67
5.925	-24	0.0725	-0.0741	0.211	0.231	0.226	0.245	0.246	0.257	5.76	7.56	6.17	7.99	6.72
6.000	-33	-0.0683	-0.1152	0.211	0.219	0.230	0.232	0.254	0.240	6.39	6.51	6.99	6.87	7.70
6.075	-34	-0.0914	-0.1824	0.218	0.214	0.239	0.227	0.258	0.236	7.04	5.92	7.71	6.27	8.35
6.150	-30	0.1743	-0.1681	0.213	0.211	0.245	0.214	0.263	0.222	6.66	6.06	7.68	6.12	8.23
6.225	-30	-0.0660	-2.1710	0.231	0.223	0.253	0.222	0.271	0.238	6.32	7.30	6.92	7.24	7.42
6.300	-22	0.0489	-0.0468	0.245	0.195	0.261	0.201	0.279	0.213	5.88	7.02	6.27	7.23	6.69
6.375	-20	0.0107	0.5152	0.227	0.225	0.265	0.223	0.280	0.240	4.62	8.94	5.39	8.83	5.70
6.450	-19	0.0327	-0.0073	0.221	0.239	0.253	0.259	0.270	0.272	4.72	9.26	5.40	10.02	5.75
6.525	-25	-0.0072	-0.0367	0.217	0.249	0.252	0.245	0.268	0.263	5.20	8.96	6.05	8.83	6.42
6.600	-28	-0.0901	-0.0283	0.225	0.212	0.249	0.236	0.264	0.251	6.00	7.08	6.64	7.88	7.04
6.675	-27	-0.0837	0.0244	0.223	0.225	0.249	0.234	0.261	0.249	5.20	8.24	5.81	8.59	6.10
6.750	-15	0.0038	0.0245	0.231	0.206	0.251	0.212	0.261	0.230	4.85	8.05	5.28	8.28	5.48

Northing (m)	$W_{g,ar}$(10.6)	$\bar{t}_A$(2.7)	$\bar{t}_B$(2.7)	$\bar{t}_A$(7.0)	$\bar{t}_B$(7.0)	$\bar{t}_A$(10.6)	$\bar{t}_B$(10.6)	$q_{w|A,ar}$(1.3)	$q_{w|B,ar}$(1.3)	$q_{w|A,ar}$(2.7)	$q_{w|B,ar}$(2.7)	$q_{w|A,ar}$(7.0)	$q_{w|B,ar}$(7.0)	$q_{w|A,ar}$(10.6)
0.000	7.87	1.82	2.26	0.92	1.01	0.57	0.69	1.61	1.67	3.11	2.89	8.09	7.83	12.21
0.075	8.31	2.90	1.29	0.97	0.97	0.64	0.63	1.30	1.27	2.45	3.60	6.90	7.71	10.95
0.150	8.26	2.30	2.07	0.93	1.10	0.67	0.71	1.28	1.23	2.66	2.62	6.39	6.75	12.15
0.225	8.91	2.42	2.00	1.00	1.02	0.80	0.72	1.19	1.26	2.50	2.69	6.58	6.92	10.72
0.300	10.66	1.40	2.52	0.81	1.06	0.53	0.67	1.30	1.44	2.75	3.08	6.75	7.27	10.27
0.375	7.61	2.25	1.99	0.65	1.37	0.64	0.95	1.37	1.15	2.59	2.48	7.98	6.04	10.74
0.450	8.85	2.20	2.24	0.74	1.14	0.71	0.43	1.27	1.35	2.31	2.27	6.90	6.90	11.48
0.525	7.68	2.03	2.82	0.78	1.35	0.57	0.81	1.19	1.09	1.99	2.23	6.56	6.78	9.74
0.600	8.75	1.53	2.53	0.71	1.17	0.56	0.75	1.59	1.25	2.67	2.45	7.65	6.71	12.55
0.675	7.23	2.42	1.81	0.82	1.43	0.89	0.56	1.18	1.40	2.68	2.13	6.43	6.94	10.43
0.750	8.15	1.94	2.22	0.87	1.26	0.59	0.74	1.51	1.54	2.63	2.48	7.20	6.60	11.71
0.825	9.33	2.46	2.09	0.82	1.42	0.83	0.62	1.30	1.18	2.71	2.67	7.39	6.94	11.41
0.900	8.51	2.25	2.31	0.88	1.20	0.75	0.60	1.41	1.25	2.40	2.38	6.94	7.23	10.53
0.975	9.04	2.03	2.23	1.06	1.14	0.57	0.70	1.17	1.33	2.81	3.09	7.02	7.73	11.01
1.050	8.37	1.63	2.95	0.98	1.19	0.58	0.83	1.44	1.47	2.32	2.84	6.85	6.01	10.18
1.125	7.48	2.00	2.15	0.90	1.34	0.58	0.93	1.15	1.10	2.36	1.99	6.85	6.01	10.13
1.200	7.68	2.08	2.52	1.03	1.19	0.74	0.81	1.56	1.12	2.61	2.34	7.50	6.56	11.25
1.275	7.56	2.04	2.39	0.90	1.17	0.63	0.71	1.37	1.27	2.26	2.12	7.45	6.47	9.32
1.350	8.33	2.66	1.61	0.89	1.05	0.69	0.59	1.36	1.56	2.38	2.82	7.19	7.84	10.10
1.425	7.98	2.26	2.17	0.90	1.04	0.51	0.70	1.16	1.11	2.13	2.30	6.80	6.17	9.34
1.500	6.77	2.36	2.33	0.87	1.28	0.57	0.85	1.35	1.24	2.18	2.27	6.23	6.98	9.30
1.575	7.96	2.26	2.17	0.65	1.29	0.63	0.66	1.29	1.40	2.02	2.50	6.48	6.97	10.20
1.650	7.47	2.13	2.01	0.92	0.95	0.66	0.66	1.71	1.30	2.91	2.84	7.05	7.22	10.80
1.725	6.93	2.26	2.17	0.90	1.12	0.57	0.68	1.32	1.24	2.65	1.83	6.55	7.81	9.58
1.800	7.58	2.08	2.52	0.83	1.05	0.64	0.58	1.82	1.25	2.97	2.48	8.77	7.30	11.91
1.875	8.20	2.79	1.64	0.82	0.83	0.63	0.68	1.45	1.38	2.49	1.96	7.35	7.59	11.04
1.950	7.86	2.25	1.63	0.91	0.98	0.57	0.68	1.55	1.44	2.42	2.95	8.18	7.29	11.54
2.025	7.54	1.93	2.49	0.76	1.49	0.57	0.78	1.39	1.31	2.26	2.37	7.97	7.10	10.91
2.100	7.86	2.04	2.57	0.82	1.12	0.55	0.70	1.38	1.15	2.47	2.60	7.19	8.08	11.00
2.175	7.91	2.26	2.05	0.66	1.18	0.58	0.67	1.40	1.39	2.59	2.64	7.69	7.52	10.01
2.250	7.42	2.21	1.90	1.10	0.98	0.57	0.55	1.46	1.34	2.66	2.71	7.09	8.02	10.42
2.325	7.74	2.42	1.84	0.70	1.54	0.57	0.76	1.84	1.40	2.34	2.77	6.50	7.66	10.15
2.400	6.51	2.09	2.26	0.97	1.00	0.63	0.64	1.58	1.49	2.21	2.62	7.23	7.24	11.01
2.475	7.65	2.04	2.20	0.99	1.04	0.57	0.69	1.74	1.44	2.41	2.89	7.50	7.31	9.41
2.550	6.94	2.41	2.07	1.09	1.01	0.66	0.71	1.55	1.68	2.49	2.55	7.15	6.88	10.47
2.625	7.93	2.55	2.30	1.18	1.07	0.64	0.76	1.39	1.36	2.41	2.66	7.74	7.88	11.33
2.700	8.52	2.41	2.24	0.89	1.27	0.62	0.73	1.54	1.56	2.06	2.60	7.42	7.55	11.01
2.775	7.60	2.26	2.60	0.82	1.42	0.69	0.89	1.02	1.16	1.79	1.76	6.19	6.08	8.48
2.850	7.76	1.26	3.57	0.67	1.58	0.47	1.09	1.46	1.37	2.08	1.95	6.84	6.42	10.51
2.925	8.00	1.79	2.64	0.82	1.31	0.52	0.83	1.20	1.24	2.27	2.62	6.86	7.55	9.16
3.000	8.55	2.02	2.06	0.97	1.17	0.55	0.66	1.46	1.22	2.35	2.67	7.17	7.39	9.54
3.075	8.59	2.04	2.67	0.82	1.42	0.51	0.89	1.39	1.36	2.36	2.58	6.98	7.44	10.55
3.150	9.17	2.25	2.01	0.83	1.24	0.53	0.59	1.45	1.65	2.13	2.84	7.12	7.66	10.80
3.225	7.53	1.78	2.93	0.90	1.10	0.81	0.56	1.46	1.11	2.42	2.54	7.35	6.92	10.87
3.300	4.03	2.39	1.66	0.87	0.78	0.60	1.04	1.39	1.10	2.01	1.88	6.65	6.28	10.95
3.375	5.59	2.04	2.16	0.82	0.92	0.62	0.84	1.48	1.13	2.34	2.46	7.19	7.18	11.35
3.450	7.76	2.83	1.21	0.91	0.88	0.62	0.51	1.64	1.47	2.30	3.32	7.20	7.57	11.29
3.525	9.24	2.26	1.90	0.70	1.15	0.32	0.86	1.45	1.37	2.46	3.22	6.79	8.12	10.33
3.600	7.99	1.31	3.18	0.52	1.59	0.32	1.10	1.69	1.51	2.42	2.52	7.44	6.59	11.20
3.675	8.08	2.04	2.39	0.91	1.12	0.75	0.51	1.57	1.15	2.08	2.98	7.25	6.90	10.60
3.750	7.07	2.42	1.92	1.00	1.14	0.75	0.68	1.46	1.56	2.20	3.31	6.50	7.44	10.23
3.825	6.81	2.26	1.97	1.28	0.66	0.57	0.62	1.79	1.58	2.76	2.99	8.43	7.11	12.73
3.900	6.54	2.14	2.20	0.88	0.84	0.63	0.53	1.68	1.50	2.56	2.95	7.60	7.92	12.14
3.975	7.48	2.26	1.95	0.76	1.10	0.57	0.58	1.59	1.46	2.62	2.85	7.79	7.96	11.50
4.050	8.01	2.03	1.51	0.93	1.24	0.45	0.57	1.60	1.57	2.56	2.81	7.15	6.96	10.80
4.125	7.84	2.26	1.90	0.75	1.28	0.51	0.69	1.50	1.61	2.20	2.33	7.13	7.75	11.63
4.200	8.62	2.26	2.18	1.02	1.05	0.58	0.71	1.77	1.39	2.20	2.78	6.54	8.07	10.30
4.275	7.23	2.04	2.12	0.73	1.22	0.65	0.59	1.00	1.01	2.57	2.07	6.86	6.26	10.92
4.350	7.94	3.37	1.25	1.03	1.05	0.66	0.67	1.35	1.36	2.15	2.74	6.62	6.81	10.29
4.425	8.71	1.92	2.93	1.29	0.96	0.87	0.59	1.32	1.39	2.04	2.34	6.44	6.92	9.52
4.500	7.33	2.35	2.35	0.84	1.45	0.53	0.86	1.20	0.99	1.91	2.15	6.09	6.44	8.73
4.575	6.11	1.42	3.01	0.60	1.43	0.44	1.14	0.97	0.94	1.91	1.43	6.09	5.88	9.65
4.650	5.65	1.53	3.07	0.75	1.47	0.50	0.87	1.16	1.00	2.40	2.01	6.22	5.73	10.22
4.725	7.98	2.04	2.23	0.95	1.29	0.63	0.96	0.96	1.15	2.07	2.21	7.10	6.27	10.53
4.800	7.09	1.86	4.01	0.87	1.38	0.68	0.62	1.72	1.14	2.53	2.64	7.08	6.53	10.69
4.875	6.95	1.54	2.66	0.70	1.32	0.57	0.83	1.68	1.37	2.52	2.04	6.66	5.72	9.30
4.950	8.97	1.64	2.37	0.85	1.21	0.40	0.63	1.35	1.61	2.47	2.79	7.40	8.02	10.88
5.025	8.50	2.26	1.96	0.83	1.20	0.45	0.81	1.60	1.06	2.24	2.46	6.62	7.48	10.08
5.100	8.37	2.10	3.31	0.90	0.93	0.44	0.79	1.56	1.56	2.12	3.66	7.29	7.52	10.03
5.175	6.44	2.04	2.39	0.68	1.27	0.51	0.79	1.58	1.37	2.57	2.21	7.42	6.41	11.38
5.250	7.04	2.10	2.47	0.91	1.33	0.63	0.97	1.53	1.64	2.86	3.03	8.16	6.28	11.92
5.325	8.66	2.04	2.82	0.83	1.42	0.75	0.58	1.57	1.47	2.16	3.26	7.04	7.56	10.94
5.400	10.28	1.90	2.68	0.86	0.99	0.50	0.75	1.56	1.66	2.61	2.49	7.49	7.49	10.68
5.475	6.93	2.04	2.39	0.75	1.38	0.38	0.86	1.16	1.11	1.74	2.98	5.29	5.81	11.26
5.550	6.31	1.41	2.83	0.57	1.18	0.43	0.76	1.28	1.00	2.07	2.16	5.98	6.14	9.23
5.625	5.88	2.04	2.12	1.05	1.19	0.70	0.63	1.19	1.04	1.86	2.14	5.74	5.65	8.42
5.700	7.30	1.69	2.41	0.79	1.25	0.48	0.77	1.59	1.23	2.44	1.93	7.67	5.87	11.20
5.775	7.90	2.26	2.07	0.83	1.20	0.51	0.69	1.71	1.54	2.57	2.38	7.40	6.88	10.89
5.850	8.56	1.92	2.73	0.71	1.24	0.47	0.84	1.74	1.84	2.95	2.93	8.32	7.94	12.17
5.925	8.40	2.26	1.85	0.83	1.12	0.57	0.76	1.36	1.28	2.66	3.12	6.67	6.95	11.01
6.000	7.12	1.82	2.76	0.88	1.20	0.78	0.45	1.68	1.62	2.37	3.03	6.55	6.70	9.73
6.075	6.53	2.04	2.82	0.77	1.48	0.66	0.85	1.66	1.15	2.25	3.13	6.35	6.31	9.28
6.150	6.35	1.94	2.78	0.96	1.21	0.63	0.82	1.65	1.35	2.32	2.65	6.64	7.02	9.54
6.225	7.76	1.80	3.06	1.20	1.05	0.60	0.80	1.50	1.44	2.81	2.77	6.33	7.26	11.32
6.300	7.65	1.82	2.52	0.86	1.24	0.55	0.74	1.42	1.76	2.52	3.98	7.26	8.31	11.24
6.375	9.54	2.80	1.77	0.83	1.31	0.58	0.76	1.51	1.37	2.68	3.62	6.27	8.27	11.49
6.450	10.51	1.08	3.35	0.97	1.12	0.49	0.76	2.11	1.76	2.90	4.42	7.99	8.44	13.12
6.525	9.48	1.80	3.06	0.83	1.20	0.58	0.83	1.30	1.42	2.84	3.87	8.14	6.71	11.62
6.600	8.38	2.13	2.09	0.95	1.08	0.59	0.65	1.94	1.30	2.92	2.92	7.42	7.04	11.83
6.675	9.14	1.97	2.19	1.08	1.17	0.58	0.70	1.93	1.27	2.62	3.46	6.40	6.31	10.68
6.750	8.98	2.03	2.15	0.88	1.11	0.57	0.73	1.64	1.74	2.25	4.01	5.38	7.45	8.34

159

Northing (m)	$q_{\alpha|d,xx}(10.6)$	$q_{w|d,xx}(2.7)$	$q_{w|g,xx}(2.7)$	$q_{w|d,xx}(7.0)$	$q_{w|g,xx}(7.0)$	$q_{w|d,xx}(10.6)$	$q_{w|g,xx}(10.6)$
0.000	12.49	3.56	3.00	7.73	7.30	12.97	11.42
0.075	11.16	2.02	5.92	6.53	8.09	10.66	13.11
0.150	11.36	2.32	3.45	6.24	7.22	9.59	11.70
0.225	10.46	1.84	3.91	4.86	8.22	6.67	12.36
0.300	11.56	2.58	3.64	4.75	9.69	7.99	15.84
0.375	9.56	2.08	3.46	8.31	5.16	9.06	7.98
0.450	11.02	2.28	3.50	8.16	7.05	8.88	20.37
0.525	10.76	2.55	2.42	7.72	5.19	11.18	9.44
0.600	11.80	3.40	2.99	8.25	6.90	11.21	11.69
0.675	11.02	2.54	3.55	8.00	4.64	7.82	12.89
0.750	11.14	3.51	3.15	8.03	6.07	12.63	10.97
0.825	11.04	2.61	3.95	8.04	6.16	8.54	15.09
0.900	11.38	2.69	3.15	7.30	6.80	9.31	14.08
0.975	11.35	2.82	3.70	5.71	7.59	11.53	12.97
1.050	10.42	3.04	2.53	5.65	7.02	10.28	10.09
1.125	8.89	2.65	3.02	6.42	5.17	10.62	8.01
1.200	10.56	3.00	2.47	6.51	6.10	9.56	9.50
1.275	11.04	2.75	2.65	6.78	6.12	10.40	10.68
1.350	12.35	2.02	4.47	6.55	7.57	9.15	14.24
1.425	10.50	2.02	3.32	5.47	7.21	10.55	11.44
1.500	9.33	1.94	2.41	5.51	5.04	9.22	8.00
1.575	10.68	2.23	3.20	8.18	5.69	9.19	12.12
1.650	10.46	2.78	3.26	6.88	7.26	10.23	11.39
1.725	9.86	2.54	2.83	6.95	5.87	11.73	10.25
1.800	11.88	2.95	2.63	8.27	6.70	11.38	13.02
1.875	10.65	2.14	4.56	8.11	9.05	11.19	12.10
1.950	11.65	2.66	4.39	7.47	7.40	12.33	11.62
2.025	9.48	3.14	2.69	8.73	4.72	12.23	9.68
2.100	11.91	2.92	2.56	7.77	6.42	12.46	11.28
2.175	11.46	2.56	3.37	9.14	6.22	11.15	11.87
2.250	12.03	2.69	3.18	5.58	6.90	11.51	13.56
2.325	12.34	2.54	3.93	9.11	4.65	11.87	10.23
2.400	12.31	3.16	2.68	7.15	6.03	11.82	10.14
2.475	12.16	3.06	3.17	6.53	6.86	12.04	11.06
2.550	11.30	2.68	2.94	6.13	6.46	10.85	9.76
2.625	11.74	2.28	3.08	5.05	6.96	10.14	10.49
2.700	12.51	2.17	3.34	5.96	6.31	9.43	11.74
2.775	9.20	1.83	2.68	5.47	5.02	7.22	8.51
2.850	10.90	3.28	1.95	7.22	4.56	11.28	7.13
2.925	12.57	2.88	2.80	6.69	5.79	11.53	9.66
3.000	12.10	2.51	3.95	5.68	6.94	10.89	12.86
3.075	11.51	2.57	2.87	6.40	5.83	11.34	9.61
3.150	11.90	2.23	4.10	6.28	7.00	10.78	15.67
3.225	9.91	3.20	2.32	6.50	6.52	7.86	13.49
3.300	9.44	2.40	2.10	6.98	4.76	10.92	3.86
3.375	11.18	3.09	2.23	7.82	5.71	11.24	6.66
3.450	10.10	2.11	5.79	6.68	8.16	10.49	15.20
3.525	11.95	2.07	4.43	6.84	7.52	16.15	10.69
3.600	10.91	2.86	2.31	7.88	4.65	13.76	7.26
3.675	12.20	1.78	3.15	4.65	6.63	6.02	15.75
3.750	11.39	2.13	3.33	5.57	5.73	8.04	10.44
3.825	10.13	2.79	3.01	5.20	9.60	12.52	11.04
3.900	12.29	3.04	2.58	8.05	7.21	12.26	12.42
3.975	12.98	2.55	3.39	8.06	6.44	11.47	12.82
4.050	13.28	2.46	4.63	5.85	5.96	13.09	14.15
4.125	12.46	2.02	3.59	6.55	5.65	10.43	11.32
4.200	11.88	2.18	3.49	5.11	7.67	9.73	12.15
4.275	10.63	2.64	3.09	7.73	5.50	9.24	12.31
4.350	10.90	1.60	5.72	5.67	7.10	9.57	11.83
4.425	12.40	2.39	2.58	3.79	8.43	6.05	14.81
4.500	9.94	1.60	2.84	4.80	4.69	8.32	8.56
4.575	12.25	3.06	1.65	7.53	3.79	10.95	5.34
4.650	9.33	3.20	1.57	6.85	3.51	11.16	6.47
4.725	9.45	2.40	3.08	5.09	5.80	8.44	8.35
4.800	11.01	2.55	1.66	5.57	4.86	7.81	11.38
4.875	9.05	3.06	2.40	7.03	4.92	9.44	8.41
4.950	11.17	2.70	3.29	5.48	6.86	12.65	14.27
5.025	11.32	1.69	3.81	5.12	6.47	10.29	10.49
5.100	12.52	1.98	2.27	5.02	8.49	11.02	10.62
5.175	10.56	2.59	2.33	8.52	4.68	12.21	8.18
5.250	9.89	2.92	2.35	7.33	4.87	11.33	7.28
5.325	11.07	2.44	2.90	6.75	5.66	8.02	14.87
5.400	11.93	2.15	3.38	5.08	10.00	9.61	13.69
5.475	11.07	1.84	2.75	5.79	4.62	12.42	8.02
5.550	10.71	2.80	1.98	7.75	5.01	11.21	8.26
5.625	10.38	2.09	2.63	4.51	4.56	7.50	9.33
5.700	10.83	2.54	2.77	6.18	5.54	11.13	9.44
5.775	11.27	2.14	3.47	6.46	6.09	11.33	11.46
5.850	13.74	2.50	2.75	7.41	6.45	12.15	10.21
5.925	12.69	2.55	4.08	7.46	7.15	11.70	11.03
6.000	10.82	3.52	2.35	7.93	5.75	9.92	15.78
6.075	11.50	3.45	2.10	10.28	4.18	12.67	7.65
6.150	11.13	3.43	2.18	8.02	5.05	13.04	7.72
6.225	12.49	3.52	2.38	5.75	6.92	12.36	9.70
6.300	11.77	3.23	2.78	7.27	5.85	12.27	10.38
6.375	13.27	1.65	5.06	6.51	6.75	9.91	12.53
6.450	12.20	4.36	2.76	5.54	8.92	11.71	13.86
6.525	10.12	2.89	2.93	7.32	7.35	11.16	11.48
6.600	9.69	2.81	3.39	7.01	7.31	11.96	12.85
6.675	10.70	2.63	3.77	5.38	7.34	10.59	13.10
6.750	12.46	2.38	3.75	5.97	7.49	9.65	12.37

160

Appendix D: Soil specific apparent permittivity-volumetric water content calibration

Legend:
- ◆ measured
- Topp equation
- Poly. (measured)

$y = 1.35243E\text{-}06x^3 - 2.66761E\text{-}04x^2 + 2.45187E\text{-}02x - 1.07809E\text{-}01$
$R^2 = 9.48790E\text{-}01$

Y-axis: measured volumetric water content (0, 0.05, 0.1, 0.15, 0.2, 0.25, 0.3, 0.35, 0.4, 0.45)

X-axis: apparent permittivity (5, 10, 15, 20, 25, 30)
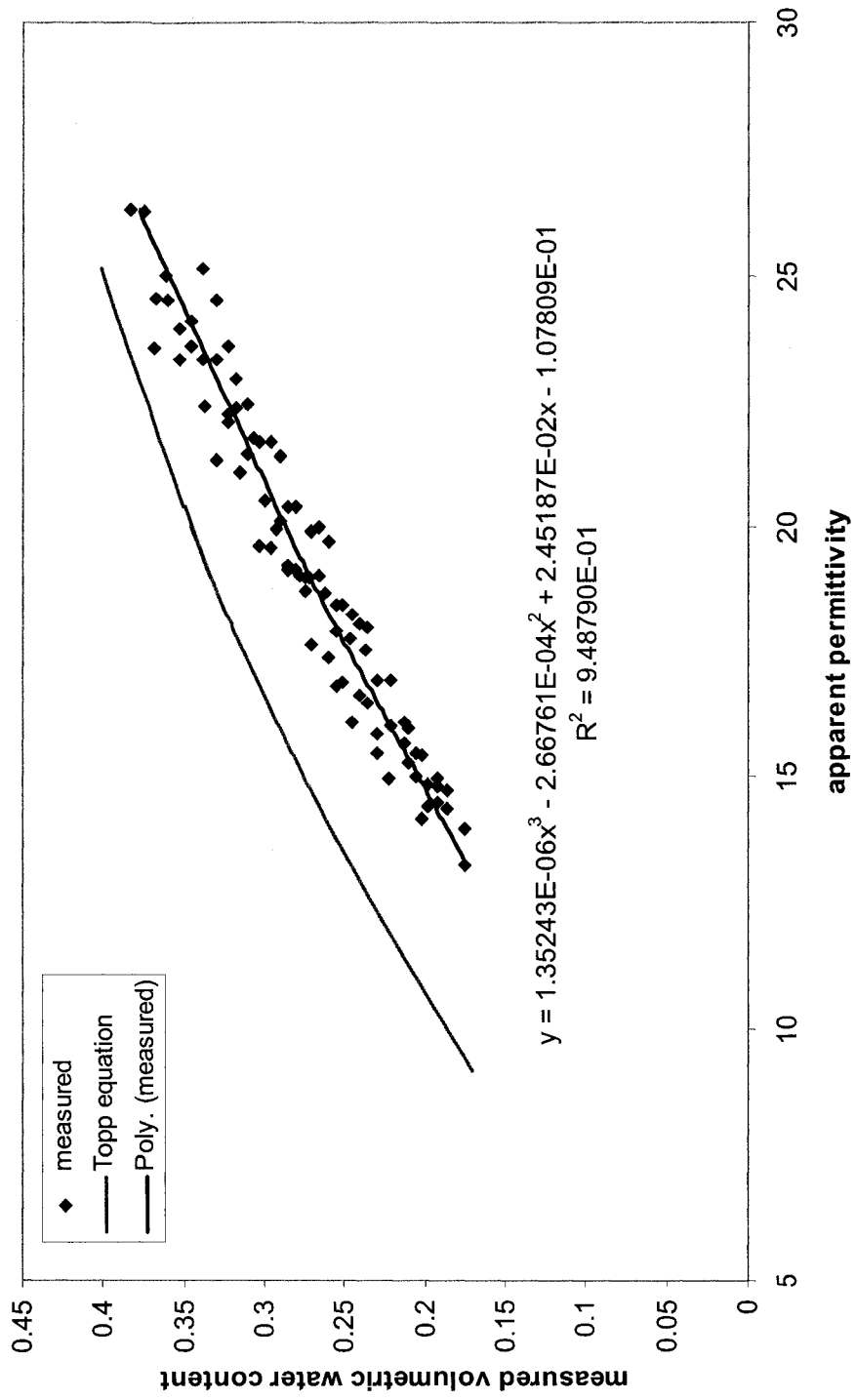
Appendix E: Transfer Functions for transient and steady A and B horizon local soil water flux

Frequency, cycles per sampling interval (m⁻¹)
(Spatial Period, m)
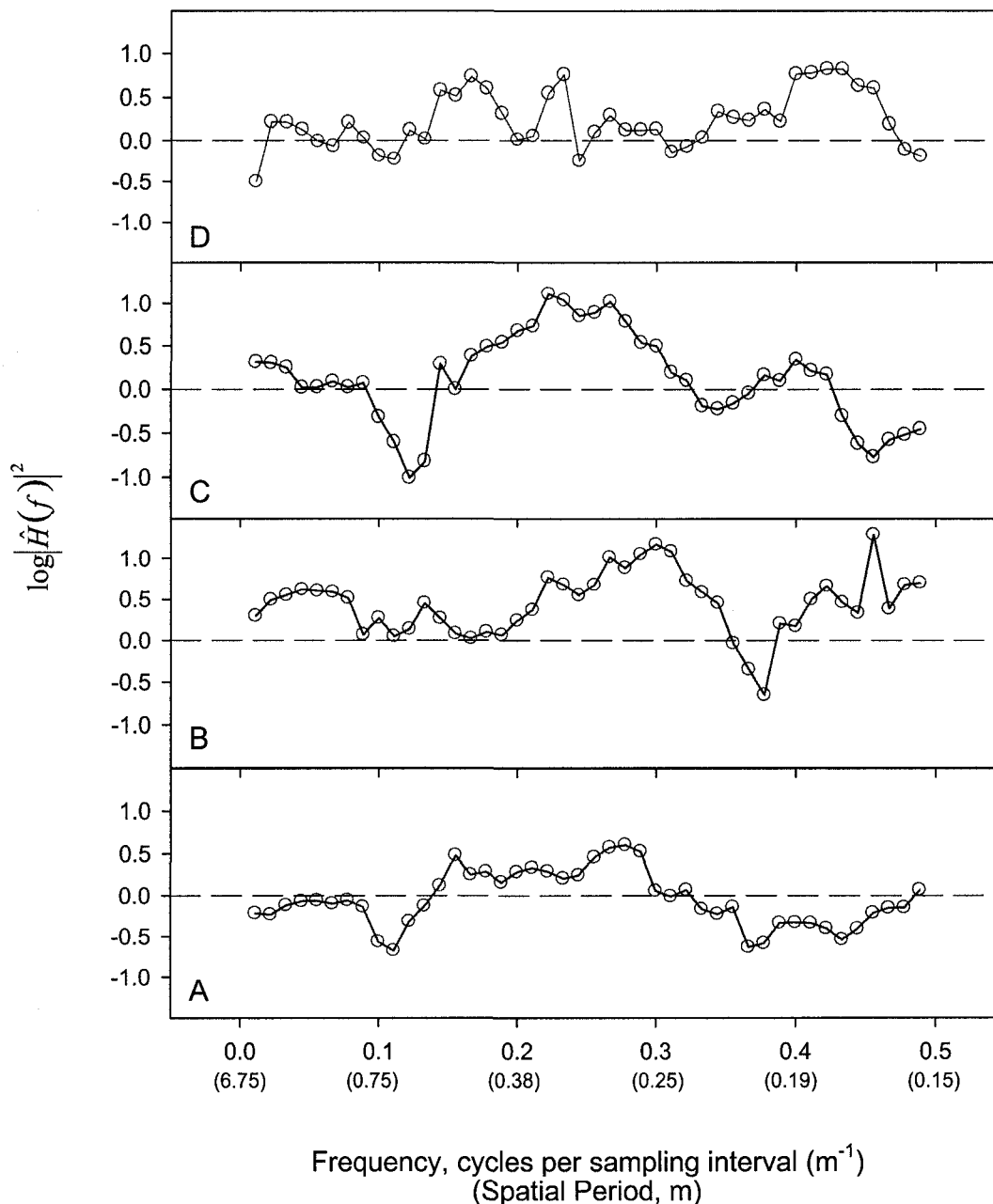
Transfer function of A and B horizon transient local soil water flux for A) 1.3 cm day⁻¹;
B) 2.7 cm day⁻¹; C) 7.0 cm day⁻¹; and D) 10.6 cm day⁻¹ water application rates. Zero
variance transfer is marked as a reference. Calculated with adaptive multitaper power
spectra.
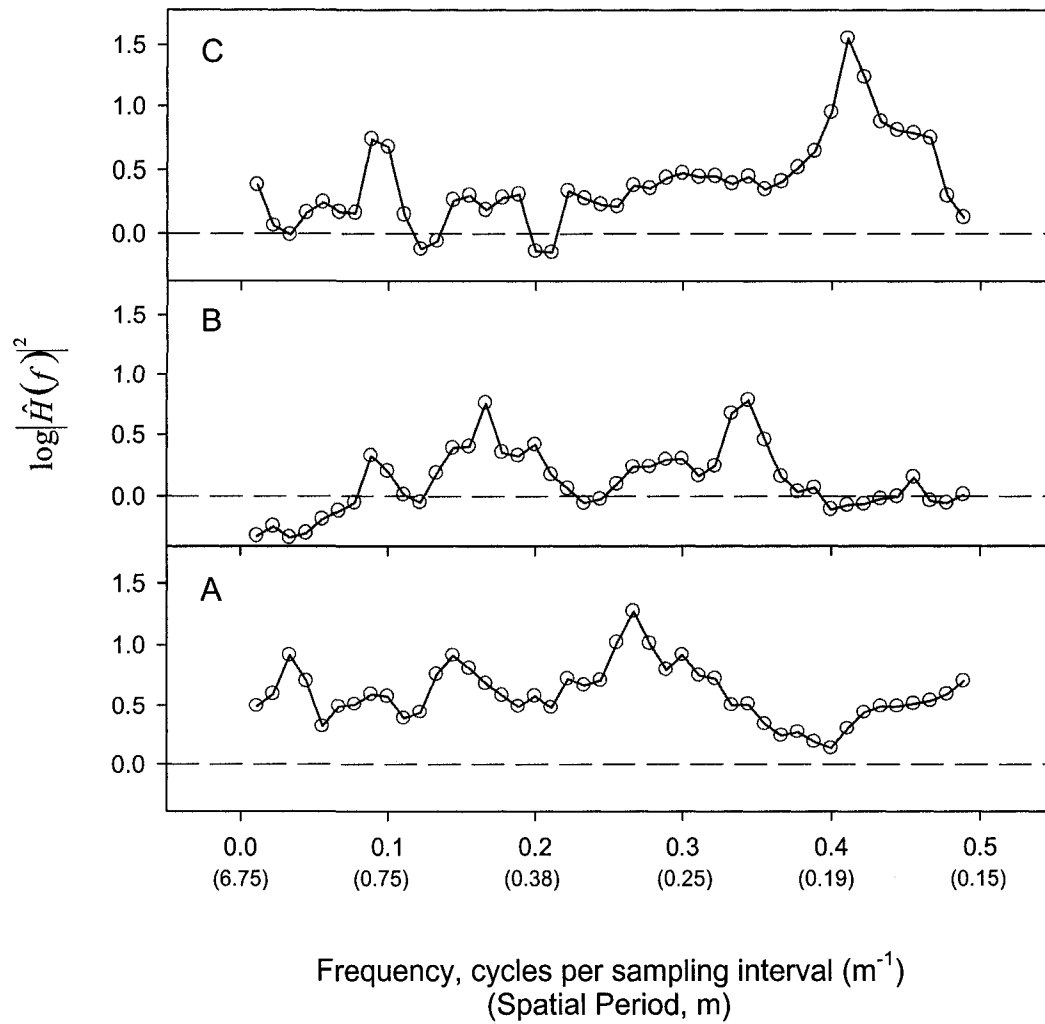
Transfer function of A and B horizon steady state local soil water flux for A) 2.7 cm day^{-1}; B) 7.0 cm day^{-1}; and C) 10.6 cm day^{-1} water application rates. Zero variance transfer is marked as a reference. Calculated with adaptive multitaper power

Appendix F: Pascal code for calculated DPSS tapers

```
{
Program to retrieve eigenvectors that make up Slepian taper functions
for multi-taper spectral analysis. The function, SMatrixTDEVD finds the
eigenvectors and eigen values of symmetrical tridiagonal matrix.
Details for calculating the matrix are in Lees and Park (1995) or Varshney (2004)
This function is not native to Free Pascal. It was downloaded from
http://www.alglib.net/eigen/symmetric/tdevd.php and is part of the AlgLib
library of linear algebra functions. This function is part of the units
"Ap", "blas", "rotations", and "tdevd" originally written for Delphi. The
free pascal switches, ($IFDEF FPC) ($MODE DELPHI) ($ENDIF FPC) must be
added to the unit codes in order to compile under free pascal. There should
be curly braces instead of brackets around the switches. See the "porting
code" section of the free pascal documentation.

These taper functions are symmetric and this program only spits out half of the
function. Some post processing is required to get the right function. It
is best to make sure you have functions that look like the ones in Fig. 1
of Lees and Park, 1995 (Computers and geosciences 21: 199-236). The functions
should then also be normalized such the sum of the squared points = 1. See
Walden, 1990 (Signal Processing 20: 67 - 75) for more details.


References
Lees and Park. 1995. Computers and geosciences 21: 199-236
Walden. 1990. Signal Processing 20: 67-75
Varshney. 2004. http://www.mit.edu/~lrv/cornell/publications/426%Report%201.pdf

Millbot. June 3, 2008

JOIN THE PASCAL REVOLUTION!
}


program Eigens;

uses    CRT,Math,Ap,blas,rotations,tdevd;



type
        maindarray = array of double;
        offdarray = array of double;
        eigenvalarray = array of double;
        eigenvecarray = array of array of double;
```

164

```
var
      mainD: maindarray;
      offD: offdarray;
      eigenvals: eigenvalarray;
      eigenvects: eigenvecarray;
      pie,p: double;

      zneed,i,j,NN: integer;
      keyprs: char;
      diditwork: boolean;
      f: text;


begin


      clrscr;
      diditwork:=false;
      pie:=Pi;
      zneed:=2;
      writeln;
      writeln;
      writeln('this program generates the Slepian tapers by finding the');
      writeln('eigen values and eigen vectors of the special tridiagonal');
      writeln('symmetric matrix.  See Lees and Park, 1995 or Varshney, 2004.');
      writeln;
      writeln;
      writeln('enter the number of samples (size of matrix, integer only), N: ');
      readln(NN);
      writeln;
      writeln;
      writeln('enter p (W=p/N): ');
      readln(p);
      writeln;
      writeln;
      writeln;
      writeln;
      SetLength(mainD,NN);
      SetLength(offD,NN-1);
      SetLength(eigenvals,NN);
      SetLength(eigenvects,NN,NN);


      for i:=0 to NN-2 do begin
            offD[i]:=((i*(NN-i))/2)*-1;
            writeln(offD[i]:0:6);
```

```
end;

for i:=0 to NN-1 do begin
    mainD[i]:=((Power(((NN-1-2*i)/2),2))*cos(2*pie*(p/NN)))*-1;
    writeln(mainD[i]:0:6);
end;

writeln('main and off diagonal vectors generated.  press enter to continue');
readln(keyprs);

diditwork:=SMatrixTDEVD(mainD,offD,NN,zneed,eigenvects);

if diditwork=true then begin
    writeln('success! dumping to file');
    Assign(f,'c:\sims2\eigenvects.txt');
    Rewrite(f);

    for i:=0 to NN-1 do begin
        for j:=0 to NN-1 do
            if j=NN-1 then write(f,eigenvects[i,j]:0:16)
                else write(f,eigenvects[i,j]:0:16,',');
        writeln(f);
    end;
    Close(f);


end else writeln('back to the old drawing board');

writeln;
writeln('press enter to exit');
readln(keyprs);


end.
```

Appendix G: Mathcad program used to calculate multitaper power and coherency spectra

U := READFILE("3 cm theta layers sub mean.xls" , "Excel")

$$NN := last\left(U^{\langle 0 \rangle}\right)$$

$$NN = 90$$

$$UU := U^{T}$$

$$nn := last\left(UU^{\langle 0 \rangle}\right)$$

$$nn = 4$$

P := READFILE("norm slep tapers p3 k5.xls" , "Excel")

$$NNN := last\left(P^{\langle 0 \rangle}\right)$$

$$NNN = 90$$

$$PP := P^{T}$$

$$nK := last\left(PP^{\langle 0 \rangle}\right)$$

$$nK = 4$$

multiply each column of U by the nK data tapers to get a
master matrix of (nK+1)(nn+1) X NN+1

$$B := \begin{array}{|l} \text{for } x \in 0..nn \\ \quad \begin{array}{|l} a \leftarrow U^{\langle x \rangle} \\ \text{for } y \in 0..nK \\ \quad \begin{array}{|l} b \leftarrow P^{\langle y \rangle} \\ \text{for } z \in 0..NN \\ \quad \begin{array}{|l} c_z \leftarrow a_z \cdot b_z \\ m \leftarrow x \cdot (nK + 1) + y \\ A_{z,m} \leftarrow c_z \end{array} \end{array} \end{array} \\ A \end{array}$$

confirm size of master matrix

$$\text{last}\left(B^{\langle 0 \rangle}\right) = 90$$

$$BB := B^T$$

$$nnK := \text{last}\left(BB^{\langle 0 \rangle}\right)$$

$$nnK = 24$$

now calculate the eigen spectra:

$$QQ := \begin{array}{|l} \text{for } x \in 0..nnK \\ \quad \begin{array}{|l} a \leftarrow B^{\langle x \rangle} \\ b \leftarrow CFFT(a) \\ Q^{\langle x \rangle} \leftarrow b \end{array} \\ Q \end{array}$$

finds fourier transfom coeffients

$$PWR := \begin{array}{|l} \text{for } x \in 0..nnK \\ \quad \begin{array}{|l} a \leftarrow QQ^{\langle x \rangle} \\ \text{for } y \in 1..\dfrac{NN}{2} \\ \quad b_y \leftarrow \left(a_y \cdot \overline{a_y}\right) \cdot 2 \\ X^{\langle x \rangle} \leftarrow b \end{array} \\ X \end{array}$$

eigen spectra

take arithmetic average of each eigen spectra to calculate the
simple multi-taper spectral estimate. Examples are shown for A and B
horizon steady state water contetn

$$SIMPLEMT := \begin{array}{|l} \text{for } x \in 0..nn \\ \quad \begin{array}{|l} \text{for } z \in 1..\dfrac{NN}{2} \\ \quad A_{z,x} \leftarrow \dfrac{1}{nK+1} \cdot \displaystyle\sum_{j=x\cdot(nK+1)}^{x\cdot(nK+1)+nK} PWR_{z,j} \end{array} \\ A \end{array}$$

168

$$\underset{\sim}{K} := 1 .. \frac{NN}{2}$$

$$\text{logSIMPLEMT} := \quad \begin{array}{|l} \text{for } x \in 0 .. nn \\[2mm] \quad \text{for } z \in 1 .. \dfrac{NN}{2} \\[3mm] \qquad A_{z,x} \leftarrow \log\left(\text{SIMPLEMT}_{z,x}\right) \\[2mm] A \end{array}$$

$$\frac{\log\left(\text{SIMPLEMT}_{K,0}\right)}{\log\left(\text{SIMPLEMT}_{K,1}\right)}$$

$$\frac{K}{NN}$$

169
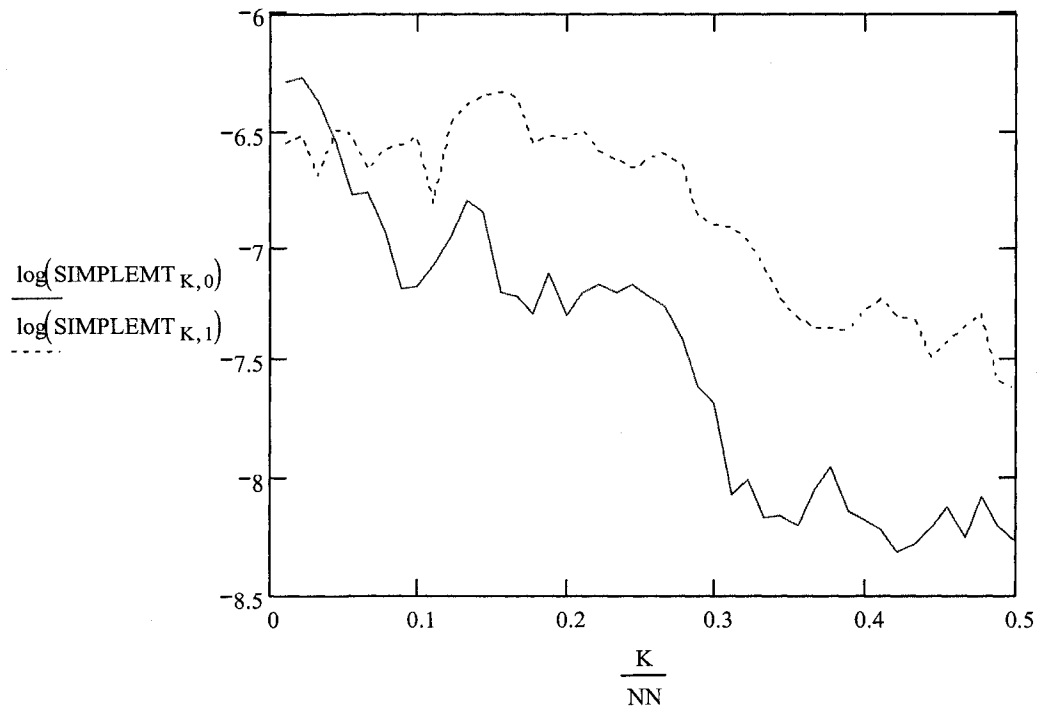
Adaptive weighting calculations

calculation of eigen values:

$p := 3.5$

$$eig := \quad \begin{vmatrix} \text{for } i \in 0..\,nK \\[2em] \begin{vmatrix} a_i \leftarrow \dfrac{\sqrt{2 \cdot \pi}}{i!} \cdot \left(\dfrac{8 \cdot NNN \cdot \sin\left(\pi \cdot \dfrac{p}{NNN} \right)}{\cos\left(\pi \cdot \dfrac{p}{NNN} \right)^2} \right)^{i + \frac{1}{2}} \cdot \left(\dfrac{1 - \sin\left(\pi \cdot \dfrac{p}{NNN} \right)}{1 + \sin\left(\pi \cdot \dfrac{p}{NNN} \right)} \right)^{NNN} \\[2em] b_i \leftarrow 1 - a_i \end{vmatrix} \\[1em] b \end{vmatrix}$$

$$eig = \begin{pmatrix} 0.999999993698122 \\ 0.999999438699362 \\ 0.999975002815945 \\ 0.99925784369512 \\ 0.983474259150804 \end{pmatrix}$$

170

$$\text{WEIGHTS} := \quad \text{for } x \in 0..\,nn$$

$$\sigma \leftarrow \text{var}\!\left(U^{\langle x \rangle}\right)$$

$$\text{for } z \in 1..\frac{NN}{2}$$

$$\text{for } j \in 0..\,100$$

$$\text{start} \leftarrow \frac{PWR_{z,\,[x \cdot (nK+1)]} \cdot eig_0 + PWR_{z,\,[x \cdot (nK+1)+1]} \cdot eig_1}{eig_0 + eig_1}$$

$$Sf \leftarrow \text{start} \quad \text{if } j = 0$$

$$\text{for } y \in 0..\,nK$$

$$d_y \leftarrow \frac{\sqrt{eig_y} \cdot Sf}{eig_y \cdot Sf + \sigma \cdot \left(1 - eig_y\right)}$$

$$\text{newSf} \leftarrow \frac{\displaystyle\sum_{m=0}^{nK} \left[\left(\left|d_m\right|\right)^2 \cdot eig_m \cdot PWR_{z,\,[x \cdot (nK+1)+m]}\right]}{\displaystyle\sum_{q=0}^{nK} \left[\left(\left|d_q\right|\right)^2 \cdot eig_q\right]}$$

$$\text{for } y \in 0..\,nK$$

$$D_{z,\,[x \cdot (nK+1)+y]} \leftarrow d_y$$

$$\text{break if } \left|Sf - \text{newSf}\right| < 0.0000000001$$

$$Sf \leftarrow \text{newSf}$$

$$D$$

calculation of adaptive degrees of freedom

$$
\text{FREEDOM} := \begin{array}{|l}
\text{for } x \in 0 \,..\, nn \\[4pt]
\quad \text{for } z \in 1 \,..\, \dfrac{NN}{2} \\[10pt]
\qquad A_{z,x} \leftarrow 2 \cdot \dfrac{\left[\displaystyle\sum_{m=0}^{nK} \left[\left[\text{WEIGHTS}_{z,[x \cdot (nK+1)+m]} \right]^{2} \cdot eig_{m} \right] \right]^{2}}{\displaystyle\sum_{q=0}^{nK} \left[\left[\text{WEIGHTS}_{z,[x \cdot (nK+1)+q]} \right]^{4} \cdot \left(eig_{q} \right)^{2} \right]} \\[40pt]
A
\end{array}
$$

now calculate power spectra with adaptive weighting. Again spectra for
A and B horizon steady state water contentents are shown

$$
\text{ADAPTMT} := \begin{array}{|l}
\text{for } x \in 0 \,..\, nn \\[4pt]
\quad \text{for } z \in 1 \,..\, \dfrac{NN}{2} \\[10pt]
\qquad A_{z,x} \leftarrow \dfrac{\displaystyle\sum_{m=0}^{nK} \left[\left[\left| \text{WEIGHTS}_{z,[x \cdot (nK+1)+m]} \right| \right]^{2} \cdot eig_{m} \cdot \text{PWR}_{z,[x \cdot (nK+1)+m]} \right]}{\displaystyle\sum_{q=0}^{nK} \left[\left[\left| \text{WEIGHTS}_{z,[x \cdot (nK+1)+q]} \right| \right]^{2} \cdot eig_{q} \right]} \\[40pt]
A
\end{array}
$$

$$\text{logADAPTMT} := \begin{vmatrix} \text{for } x \in 0..\,nn \\ \quad \text{for } z \in 1..\dfrac{NN}{2} \\ \qquad A_{z,x} \leftarrow \log\!\left(\text{ADAPTMT}_{z,x}\right) \\ A \end{vmatrix}$$

$$\frac{\log\!\left(\text{ADAPTMT}_{K,0}\right)}{\log\!\left(\text{ADAPTMT}_{K,1}\right)}$$
- - - - -

$$\frac{K}{NN}$$
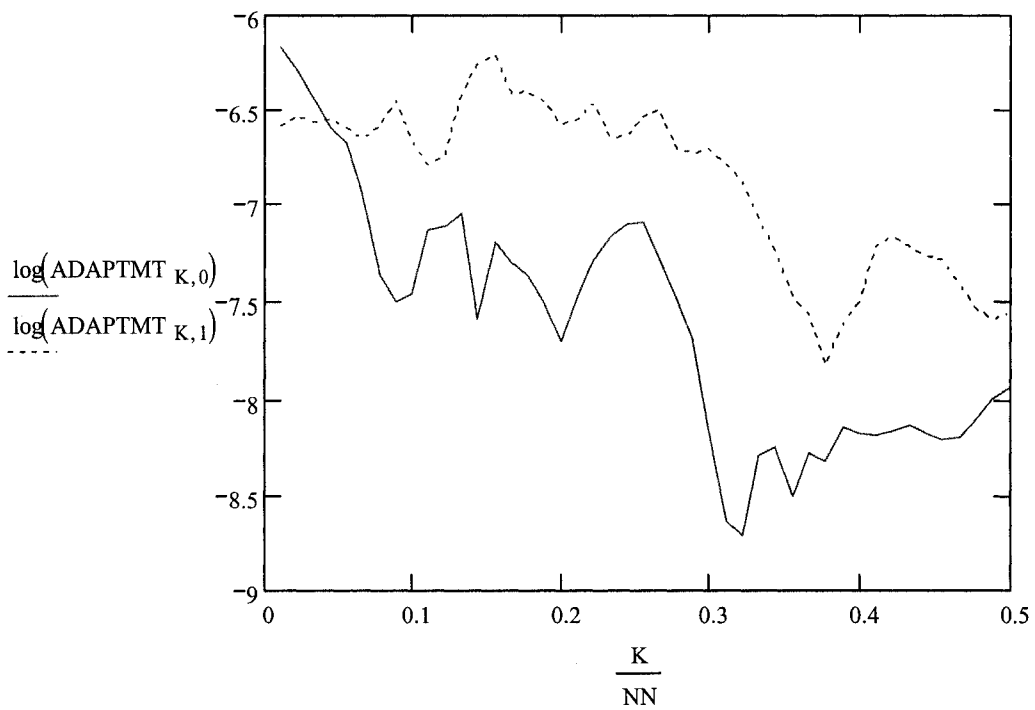
for coherency analysis, calculate the cross spectra. the number of
cross spectra calculated will depend on the comparisons you want to make.
For these examples A and B horizon steady state water contents are
compared to the layer parameters.

$\text{ACROSS} :=$ $\Bigg|$ for $x \in 0 .. \, nn - 1$

    $\Bigg|$ for $y \in 0 .. \, nK$

        $\Bigg|$ $a \leftarrow QQ^{\langle y \rangle}$

        $b \leftarrow QQ^{\langle (nK+1) + x \cdot (nK+1) + y \rangle}$

        $\Bigg|$ for $z \in 1 .. \, \dfrac{NN}{2}$

            $A_{z, [x \cdot (nK+1) + y]} \leftarrow \left(a_z \cdot \overline{b_z} \right) \cdot 2$

  A

$\text{BCROSS} :=$ $\Bigg|$ for $x \in 0 .. \, nn - 2$

    $\Bigg|$ for $y \in 0 .. \, nK$

        $\Bigg|$ $a \leftarrow QQ^{\langle (nK+1) + y \rangle}$

        $b \leftarrow QQ^{\langle 2 \cdot (nK+1) + x \cdot (nK+1) + y \rangle}$

        $\Bigg|$ for $z \in 1 .. \, \dfrac{NN}{2}$

            $A_{z, [x \cdot (nK+1) + y]} \leftarrow \left(a_z \cdot \overline{b_z} \right) \cdot 2$

  A

$$\text{AVGACROSS} := \begin{vmatrix} \text{for } x \in 0 \ldots nn - 1 \\[4pt] \quad \text{for } z \in 1 \ldots \dfrac{NN}{2} \\[10pt] \qquad A_{z,x} \leftarrow \dfrac{1}{nK + 1} \cdot \displaystyle\sum_{j = x \cdot (nK+1)}^{x \cdot (nK+1) + nK} \text{ACROSS}_{z,j} \\[10pt] A \end{vmatrix}$$

$$\text{AVGBCROSS} := \begin{vmatrix} \text{for } x \in 0 \ldots nn - 2 \\[4pt] \quad \text{for } z \in 1 \ldots \dfrac{NN}{2} \\[10pt] \qquad A_{z,x} \leftarrow \dfrac{1}{nK + 1} \cdot \displaystyle\sum_{j = x \cdot (nK+1)}^{x \cdot (nK+1) + nK} \text{BCROSS}_{z,j} \\[10pt] A \end{vmatrix}$$

175

$$\text{ACOHERE} := \left| \begin{array}{l} \text{for } x \in 0..\, nn - 1 \\[6pt] \quad \left| \begin{array}{l} a \leftarrow \text{AVGACROSS}^{\langle x \rangle} \\[6pt] \text{for } z \in 1..\dfrac{NN}{2} \\[12pt] \quad \left| \; A_{z,x} \leftarrow \dfrac{a_z \cdot \overline{a_z}}{\text{SIMPLEMT}_{z,0} \cdot \text{SIMPLEMT}_{z,(x+1)}} \right. \end{array} \right. \\[12pt] A \end{array} \right.$$

$$\text{AINPHASE} := \left| \begin{array}{l} \text{for } x \in 0..\, nn - 1 \\[6pt] \quad \left| \begin{array}{l} a \leftarrow \text{Re}\left(\text{AVGACROSS}^{\langle x \rangle}\right) \\[6pt] \text{for } z \in 1..\dfrac{NN}{2} \\[12pt] \quad \left| \; A_{z,x} \leftarrow \dfrac{a_z}{\sqrt{\text{SIMPLEMT}_{z,0} \cdot \text{SIMPLEMT}_{z,(x+1)}}} \right. \end{array} \right. \\[12pt] A \end{array} \right.$$

$$\text{AOUTPHASE} := \left| \begin{array}{l} \text{for } x \in 0..\, nn - 1 \\[6pt] \quad \left| \begin{array}{l} a \leftarrow \text{Im}\left(\text{AVGACROSS}^{\langle x \rangle}\right) \\[6pt] \text{for } z \in 1..\dfrac{NN}{2} \\[12pt] \quad \left| \; A_{z,x} \leftarrow \dfrac{a_z}{\sqrt{\text{SIMPLEMT}_{z,0} \cdot \text{SIMPLEMT}_{z,(x+1)}}} \right. \end{array} \right. \\[12pt] A \end{array} \right.$$

$$\text{ACOHERE} := \begin{array}{|l} \text{for } x \in 0..nn - 1 \\ \quad \begin{array}{|l} a \leftarrow \text{AVGACROSS}^{\langle x \rangle} \\ \text{for } z \in 1..\dfrac{NN}{2} \\ \quad \begin{array}{|l} A_{z,x} \leftarrow \dfrac{a_z \cdot \overline{a_z}}{\text{SIMPLEMT}_{z,0} \cdot \text{SIMPLEMT}_{z,(x+1)}} \end{array} \end{array} \\ A \end{array}$$

$$\text{AINPHASE} := \begin{array}{|l} \text{for } x \in 0..nn - 1 \\ \quad \begin{array}{|l} a \leftarrow \text{Re}\left(\text{AVGACROSS}^{\langle x \rangle}\right) \\ \text{for } z \in 1..\dfrac{NN}{2} \\ \quad \begin{array}{|l} A_{z,x} \leftarrow \dfrac{a_z}{\sqrt{\text{SIMPLEMT}_{z,0} \cdot \text{SIMPLEMT}_{z,(x+1)}}} \end{array} \end{array} \\ A \end{array}$$

$$\text{AOUTPHASE} := \begin{array}{|l} \text{for } x \in 0..nn - 1 \\ \quad \begin{array}{|l} a \leftarrow \text{Im}\left(\text{AVGACROSS}^{\langle x \rangle}\right) \\ \text{for } z \in 1..\dfrac{NN}{2} \\ \quad \begin{array}{|l} A_{z,x} \leftarrow \dfrac{a_z}{\sqrt{\text{SIMPLEMT}_{z,0} \cdot \text{SIMPLEMT}_{z,(x+1)}}} \end{array} \end{array} \\ A \end{array}$$

example of B horizon stead state state water content versus profile
curvature coherency

and in and out of phase correlation

178
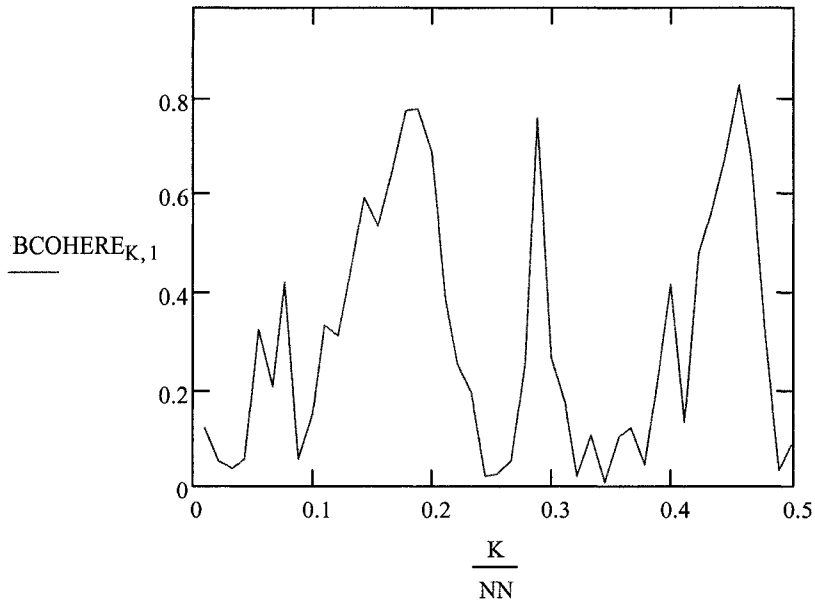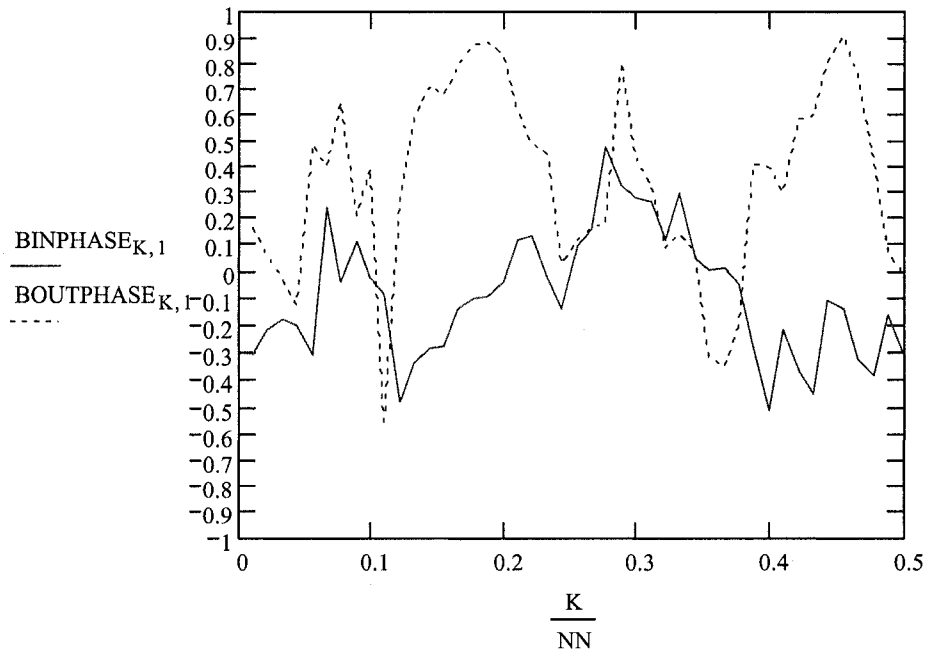
example of multiple coherency calculation for B horizon volumetric water content
versus depth, profile and plan curvature

$$
\text{multcohereBlayers} := \left|
\begin{array}{l}
\text{for } z \in 1..\dfrac{NN}{2} \\[2ex]
R_z \leftarrow \dfrac{\left(\text{AVGBCROSS}_{z,0} \quad \text{AVGBCROSS}_{z,1} \quad \text{AVGBCROSS}_{z,2}\right) \cdot \begin{pmatrix} \dfrac{\text{SIMPLEMT}_{z,2}}{\text{AVGLAYERCROSS}_{z,0}} & \text{AVGLAYERCROSS}_{z,0} & \text{AVGLAYERCROSS}_{z,1} \\[2ex] \overline{\text{AVGLAYERCROSS}_{z,0}} & \text{SIMPLEMT}_{z,3} & \text{AVGCURVCROSS}_z \\[2ex] \overline{\text{AVGLAYERCROSS}_{z,1}} & \overline{\text{AVGCURVCROSS}_z} & \text{SIMPLEMT}_{z,4} \end{pmatrix}^{-1} \begin{pmatrix} \overline{\text{AVGBCROSS}_{z,0}} \\[2ex] \overline{\text{AVGBCROSS}_{z,1}} \\[2ex] \overline{\text{AVGBCROSS}_{z,2}} \end{pmatrix}}{\text{SIMPLEMT}_{z,1}} \\[4ex]
R
\end{array}
\right.
$$

$\text{multcohereBlayers}_K$

$\dfrac{K}{NN}$
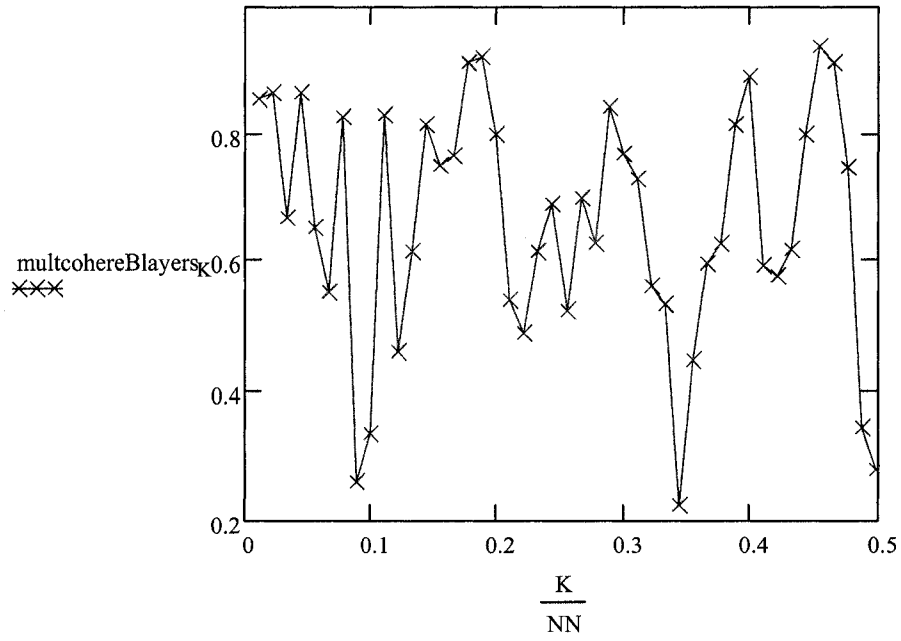
example of partial coherency between B horizon water content and profile curvature given depth

$$\text{partspecBprof} := \left| \begin{array}{l} \text{for } z \in 1..\dfrac{NN}{2} \\[2em] a_z \leftarrow \text{AVGBCROSS}_{z,1} - \dfrac{\overline{\text{AVGACROSS}_{z,0} \cdot \text{AVGACROSS}_{z,2}}}{\text{SIMPLEMT}_{z,0}} \\[2em] a \end{array} \right.$$

$$\text{partspecBB} := \left| \begin{array}{l} \text{for } z \in 1..\dfrac{NN}{2} \\[2em] a_z \leftarrow \text{SIMPLEMT}_{z,1} - \dfrac{\overline{\text{AVGACROSS}_{z,0} \cdot \text{AVGACROSS}_{z,0}}}{\text{SIMPLEMT}_{z,0}} \\[2em] a \end{array} \right.$$

$$\text{partspecprofprof} := \left| \begin{array}{l} \text{for } z \in 1..\dfrac{NN}{2} \\[2em] a_z \leftarrow \text{SIMPLEMT}_{z,3} - \dfrac{\overline{\text{AVGACROSS}_{z,2} \cdot \text{AVGACROSS}_{z,2}}}{\text{SIMPLEMT}_{z,0}} \\[2em] a \end{array} \right.$$

$$\text{partialBprof} := \left| \begin{array}{l} \text{for } z \in 1..\dfrac{NN}{2} \\[2em] a_z \leftarrow \dfrac{\overline{\text{partspecBprof}_z \cdot \text{partspecBprof}_z}}{\text{partspecBB}_z \cdot \text{partspecprofprof}_z} \\[2em] a \end{array} \right.$$

180
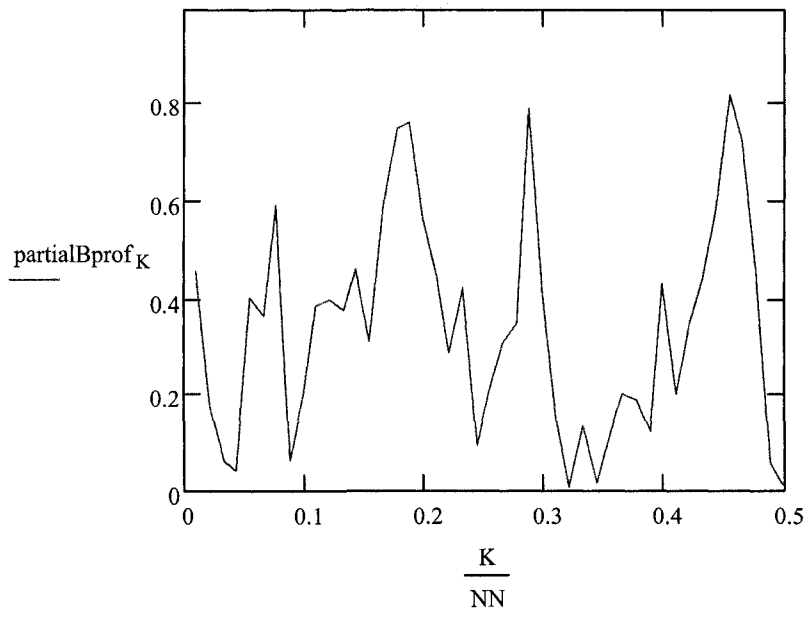
Appendix H: Spatial series of steady state soil water flux estimates
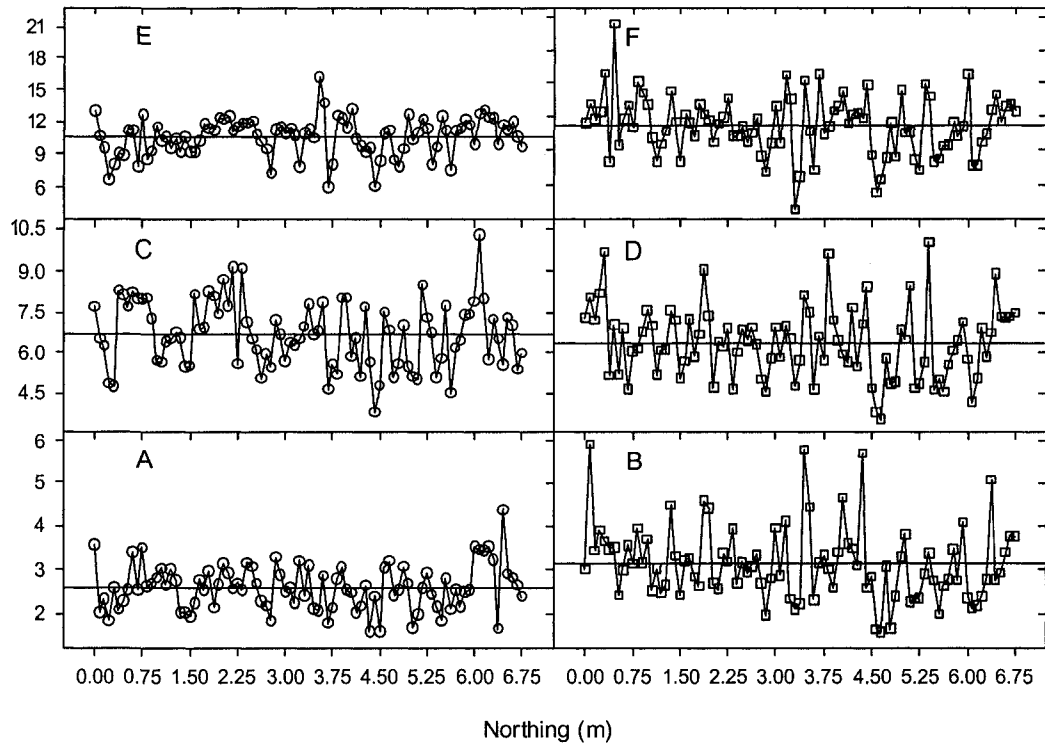
Spatial pattern of A and B horizon steady state local soil water flux. A) & B) A and B horizon 2.7 cm day^{-1} water application rate; C) & D) A and B horizon 7.0 cm day^{-1} water application rate; E) & F) A and B horizon 10.6 cm day^{-1} water application rate.